Design and Optimisation of Polymer Nanoparticles for Advanced Healthcare Applications

Saweta Garg

Thesis submitted to Newcastle University in candidature for the degree of

Doctor of Philosophy

Faculty of Science, Agriculture and Engineering

October 2024

Abstract

The World Health Organisation has highlighted widening health inequalities and increased pressure on healthcare systems as major global health challenges. Key contributors to these disparities are uneven distribution of specialised instruments in centralised laboratories and expensive pharmaceuticals in resource-limited settings, resulting in delayed disease diagnosis and treatment. This emphasises the urgent need for developing low-cost, robust point-of-care (PoC) sensors and affordable, effective and precision targeted pharmaceuticals. To address these issues and reduce the healthcare inequalities, this thesis aims to develop polymer-based solutions that are suitable for both diagnostics and pharmaceuticals.

This thesis is organised into seven chapters. The extensive literature review of different polymers for the sensors/therapeutics is given in chapter 1. Chapter 2 details the chemicals/monomers used to prepare the polymers/polymeric nanoparticles and methodologies employed for sensing and drug delivery application. The design and optimisation of electroactive molecularly imprinted polymeric nanoparticles (nanoMIPs) as recognition element for PoC electrochemical glucose sensor (chapter 3). The glucose detection is demonstrated in both diabetic patient serum samples and in artificial interstitial fluids indicating its potential for wearable technology applications. The protein imprinting is crucial for separation and detection of the range of proteins. Therefore, chapter 4 explores the synthesis of full protein lysozyme (major allergic protein in eggs) imprinted nanoMIPs and optimising them for developing lysozyme impedimetric/thermal sensors. Given the intriguing application of imprinted polymers in drug delivery, chapter 5 is dedicated to developing targeted drug nanocarriers using double imprinting approach for breast cancer treatment.

The drug delivery of hydrophobic silymarin drug is investigated using mixed Pluronics micelles (commercial surface-active polymers) in chapters 6. Different mixed micellar formulations are studied for their effect on solubilisation of silymarin. Further different solubilisation methods and drug loading capacities of various polymeric micelles are investigated for the delivery of two poorly water-soluble nutraceuticals (naringenin and baicalein) in chapter 7. This thesis demonstrates the diverse applications of imprinted and surface-active polymers for diagnostic and drug delivery, offering more robust and cost-effective solutions to overcome the healthcare inequalities.

Acknowledgment

First and foremost, I would like to thank and bow in gratitude to **Lord Krishna** for his goodness and showers of blessings which are boundless in both good times and in bad times.

While my name may be alone on the front cover of this thesis, I am by no means its sole contributor. Rather, there are several people behind this piece of work who deserve to be both acknowledged and thanked here. At the very outset, I express my deepest sense of gratitude to my esteemed supervisors, **Dr Shayan Seyedin**, Newcastle University, and **Prof Marloes Peeters**, University of Manchester for the continuous support, sagacious advice, immense knowledge, sustained enthusiasm, and exemplary guidance throughout the course of my doctoral research. I would like to thank my co-supervisor **Prof Katarina Novakovic**, School of Engineering, Newcastle University, Newcastle. Without their invaluable guidance, kind co-operation, incisive criticism, deep faith, vital encouragement and dynamic assistance, the present work would not have seen the light of this day. I also cherish the amount of freedom I have enjoyed during the research work under them. I am fortunate and grateful to have such a wonderful supervisor as my research guide. My cordial thanks to them for grooming me as a successful research assistant and PhD student.

Thanks to industrial collaboration MIP Discovery (Dr Francesco Canfarotta), Kablefree (Mr Tommy Lovell) and Cambridge medical technology (Mrs Alexandria Moseley) for research support in research project and expert advice/perspective in many scientific areas.

I am grateful to my research project academic collaborators Prof Craig E Banks and Dr Robert Crapnell (Manchester Metropolitan University), Prof RK Mahajan (GNDU, India), Dr Shoba Amarnath (Newcastle University), Prof Eirini Velliou (University College London), Prof Tim Witney (Kings college London), Prof Nick Turner (University of Sheffield), Dr Bartek Papiez, (University of Oxford) and Prof Robert Rintoul (University of Cambridge) for their excellent support in research work and help at the time of need.

My acknowledgement would be incomplete without thanking the biggest source of my strength, my family. The blessings of my parents Mrs Usha Rani and Dr Ram Chander Garg as well as my in-laws, Mrs Santosh Singla and Mr Krishan Kumar have been invaluable throughout this journey. The love and care of my loving brother Dr Lovedeep

Garg, sister Dr Priyanka Garg and sisters-in-law*s,* Mrs Menka and Mrs Shampy, have been a constant source of strength. A special thanks to my husband Dr Pankaj Singla for helping me to get through difficult times and for the emotional support, cooperation and care throughout this academic and professional journey.

My heartfelt thanks to my fellow research colleagues at Newcastle University, University of Manchester and beyond including Dr Jake McClements, Dr Oliver Jamieson, Dr Joshua Saczek, Dr Robert Crapnell, Dr Sarbjeet Kaur, Amy Dann, Jack Reeder, Rachel Lee, Alexander Stokes, Ushna Khalid, Gajanand Verma, Viji for their suggestions, co-operation and moral support.

I would also like to express my gratitude for the funding and salary support provided by Northern Accelerator grant (grant number NACCF248) and MRC research grant (ARIaL: MR/Y008421/1).

Table of Contents

List of Figures

List of Tables

List of Equations

List of Abbreviations

^{1}H-NMR	Proton nuclear magnetic resonance
3D	Three dimensional
AA	Acrylic acid
Ab	Antibody
Abs	Antibodies
AD	Alzheimer disease
ADCs	Antibody drug conjugates
ADME	Absorption, distribution, metabolism, and elimination
ADR	Adriamycin
AISF	Artificial interstitial fluid
AMX	Amoxicillin sodium
APBA	Amino phenylboronic acid
APS	Ammonium persulfate
ATR	Attenuated total reflection
ATRP	Atom transfer radical polymerisation
Au	Gold
AuNPs	Gold nanoparticles
Au-SPE	Gold-screen printed electrode
BAC	Baicalein
BASF	Blood brain barrier
BBB	Breast cancer
BCA	Bicinchoninic acid
BSA	Bovine serum albumin
BS-NPs	Biodegradable silica NPs
C_4-HSL	C_4-homoserine lactone
CA125	Colleagues synthesised cancer antigen 125
Ca^{2+}	Calcium
CDs	Communicable diseases
CE	Counter electrode
CFQ	Cefquinome
Cl^-	Chloride
CLSM	Confocal laser scanning microscopy
CMC	Critical micelle concentration
CMT	Critical micelle temperature
CNTs	carbon nanotubes
CPs	Conducting polymers
cTnI	Cardiac biomarker troponin I
CUR	Curcumin
CV	Cyclic voltammetry
CVDs	Cardiovascular diseases
D.D.M.	Direct dissolution method
DAPI	4',6-diamidino-2-phenylindole
DCHA	3,5-dichlorohydroxyacetophenone
DDSs	Drug delivery systems
D_h	Hydrodynamic diameter

DI	Deionised
DL	Drug loading
DLC	Drug loading capacity
DLE	Drug loading efficiency
DLS	Dynamic light scattering
DM	Diabetes mellitus
DMEM	Dulbecco's Modified Eagle Medium
DNA	Deoxyribonucleic acid
DOX	Doxorubicin
DOX-nanoMIPs	Doxorubicin -loaded doubly molecularly imprinted nanoparticles
DPPH	2,2-diphenyl-1-picrylhydrazyl
DPSV	Differential pulse stripping voltammetry
DPV	Differential pulse voltammetry
ECM	Extracellular matrix
EGFR	Epidermal growth factor receptor
EGFR	Epidermal growth factor receptor
EIS	Electrochemical impedance spectroscopy
ELISA	Enzyme-linked immunosorbent assays
eMIPs	Electroactive molecularly imprinted polymers
eNIPs	Electroactive non-imprinted polymers
eNIPs-SPEs	eNIPs functionalised SPEs
EPR	Enhanced permeability and retention
ER	Estrogen receptor
ER-α	Estrogen receptor alpha
FA	Folic acid
FBS	Foetal bovine serum
FDA	Food and Drug Administration
FETs	Field-effect transistors
FLU	Fluorescein
FLU-DOX-nanoMIPs	Fluorescein-tagged DOX-imprinted nanoparticles
FLU-DOX-NIPs	Fluorescein-tagged DOX-non imprinted nanoparticles
FLU-nanoMIPs	Fluorescein-tagged imprinted nanoparticles
FLU-NIPs	Fluorescein-tagged non imprinted nanoparticles
FRAP	Ferric reducing antioxidant power
FR-α	Folate receptor-α
$FSiO_2$ nanoparticles	Fluorescent silica nanoparticles
FTIR	Fourier transform infrared
GA	Glutaraldehyde
gC1qR	Receptor of the globular head of C1q
GOx	Glucose oxidase enzyme
GSH	Glutathione
HLB	Hydrophilic–lipophilic balance
HMGB1	Anti-high-mobility group box 1
HPLC	High-performance liquid chromatography
HS	Human serum
HTM	Heat-Transfer Method

IARC	International Agency for Research on Cancer
IARC	International Agency for Research on Cancer
IC50	Inhibitory concentration 50 (%)
IF	Imprinting factor
IgG	Immunoglobulin G
ISF	Interstitial fluids
ITO	Indium/tin oxide
IUPAC	International Union of Pure and Applied Chemistry
IV	Intravenous
IVCIA	*In vitro* comparative immunogenicity assessment
K^+	Potassium
K_D	Binding affinity
KP	Korsmeyer-Peppas
LOD	limit of detection
LYZ	lysozyme
MDR	Multidrug-resistant
MFI	Mean fluorescence intensity
MIPs	Molecularly imprinted polymers
MRE	Molecular recognition element
mRNA	Messenger ribonucleic acid
MTT	3-(4,5-dimethylthiazol-2-yl)-2,5-diphenyltetrazolium bromide
MTX	Methotrexate
MW	Molecular weight
MWCO	Molecular weight cut-off
Na^+	Sodium
nanoMIPs	MIPs nanoparticles
NAR	Naringenin
NCDs	Non-communicable diseases
NICE	National Institute for Health and Care Excellence
Ni-NPs	Nickel nanoparticles
NIPAM	N-Isopropylacrylamide
NIPs	Non-imprinted nanoparticles
NMP	Nitrous oxide mediated polymerisation
NMs	Nanomaterials
NPs	Nanoparticles
nTBA	N-tert-Butylacrylamide
NUTs	Nutraceuticals
P	Partition coefficient
PAA	Poly(acrylic acid
PANi	Polyaniline
PBS	Phosphate buffered saline
PBST	Phosphate-Buffered Saline with Tween 20
PCa	Prostate cancer
PDI	Polydispersity index
PEDOT	Poly(3,4-ethylenedioxythiophene)
PEG	Polyethylene glycol

PEG-FA	Polyethylene glycol-folic acid
PEO	Polyethylene oxide
PID	Proportional-integral-derivative
PLA	Poly(lactic acid)
PMMA	Poly(methyl methacrylate)
PoC	Point-of-care
PPO	Polypropylene oxide
PPy	Polypyrrole
PSA	Prostate specific antigen
PT	Polythiophene
PVA	Polyvinyl acetate
RAFT	Reversible addition-fragmentation chain transfer polymerisation
R_{CT}	Charge transfer resistance
RI	Reverse iontophoresis
RSD	Relative standard deviation
RT	Room temperature
SA	Sialic acid
SAILs	Surface-active ionic liquids
SD	Standard deviation
SZ	Schizophrenia
ΔG°	Gibbs free energy of solubilisation

List of Publications

I hereby declare that the list of published works included in this thesis consists of publications that are the result of my original research. I confirm that appropriate permissions and consent have been obtained from all co-authors for including these publications as part of my thesis submission. All works cited have been duly acknowledged and referenced.

1. **S. Garg,** P. Singla, F. Canfarotta, E. Velliou, J. Dawson, N. Kapur, N. Warren, S. Amarnath, M. Peeters, Analysis and future perspectives on the automation and biocompatibility of molecularly imprinted polymers for healthcare applications (invited perspective), *Macromolecules*, 2025, 58, 1157−1168. **(Editor's Choice)**

2. **S. Garg**, P. Singla, S. Kaur, R.D. Crapnell, C.E. Banks, S. Seyedin, M. Peeters, Electroactive Molecularly Imprinted Polymer Nanoparticles (eMIPs) for Label-free Detection of Glucose: Toward Wearable Monitoring, *Small***,** 2024, 2403320. [IF: 13.3].

3. P. Singla, T. Broughton, M. V. Sullivan, **S. Garg**, R. Berlinguer-Palmini, P. Gupta, F. Canfarotta, N. W. Turner, E. Velliou, S. Amarnath, M. Peeters, Double Imprinted Nanoparticles for Sequential Membrane-to-Nuclear Targeted Drug Delivery of Chemotherapeutic Drugs, *Advanced Science,* 2024, 2309976.

4. **S. Garg**, A. Sachdeva, M. Peeters, J. McClements, Point-of-Care Prostate Specific Antigen Testing: Examining Translational Progress toward Clinical Implementation, 2023, *ACS Sensors,* 8(10), 3643-58.

5. P. Singla, S. Kaur, O. Jamieson, A. Dann, **S. Garg**, C. Mahon, R.D. Crapnell, C.E. Banks, I. Kaur, M. Peeters, Electrochemical and thermal detection of allergenic substance lysozyme with molecularly imprinted nanoparticles, *Analytical and Bioanalytical Chemistry*, 2023, 415(18), 4467-78.

6. P. Singla, H. Kaur, **S. Garg**, N. Kaur, F. Canfarotta, R. K. Mahajan, M. Peeters, Early detection of SARS-CoV-2 with functionalized gold and molecularly imprinted polymeric nanoparticles: a mini review, 2023, Molecular Systems Design & Engineering, 8, 1337-1354.

7. P. Singla, G. Parokie, **S. Garg**, S. Kaur, I. Kaur, R.D. Crapnell, C.E. Banks, U. Rinner, C. Wills, M. Peeters, Enhancing encapsulation of hydrophobic phyto-drugs naringenin and baicalein in polymeric nano-micelles, *Journal of Drug Delivery Science and Technology*, 2023, 83,104403.

8. **S. Garg**, M. Peeters, R. K. Mahajan, P. Singla, Loading of Hydrophobic Drug Silymarin in Pluronic and Reverse Pluronic Mixed Micelles, *Journal of Drug Delivery Science and Technology*, 2022, 75: 103699.

Chapter 1: Introduction

1.1 Healthcare burden of non-communicable diseases (NCDs)

Healthcare systems around the globe face increasing strain due to rise in ageing populations, workforce shortages, capacity constraints, and fragmented systems. These issues still exist even in highly developed countries like the US and the UK, which emphasises the need for innovative solutions and policy reforms to enhance healthcare delivery (Jones and Dolsten, 2024).

Non-communicable diseases (NCDs) comprise chronic conditions such as cancer, cardiovascular diseases, chronic respiratory diseases including chronic obstructive pulmonary disease, diabetes, and neurological disorders. NCDs are not contagious and are caused by genetic, environmental, or lifestyle factors ((WHO), 2024a; BBC, 2024). NCDs are responsible for around half of all diseases globally and accounts for 41 million deaths annually (or 74% of all fatalities globally) (Organization, 2023). NCDs are the leading cause of death in adults worldwide and around 86% of the 17 million premature deaths are attributed to the NCDs especially in low- and middle-income countries. There are ~18 million deaths occur each year due to coronary heart disease alone, followed by cancer, chronic obstructive pulmonary disease (4.1 million deaths), and type 2 diabetes (Mohan et al., 2023; Muka et al., 2015). Both the United Nations and the WHO predict that NCDs will be the leading causes of death worldwide by 2030, surpassing infectious diseases such as cholera, malaria and tuberculosis (D'Antona et al., 2024). These NCDs pose major challenges to healthcare systems worldwide which have disproportionate effect on people life depending upon their economy, nationality and other factors (Islam et al., 2014). One of the primary reasons for the delayed diagnosis and treatment of NCDs is the "know-do gap," which refers to the discrepancy between healthcare providers' knowledge and their actual clinical practices. Furthermore, these challenges also lead to economic implications, strained healthcare resources, and disparities in access to quality care.

Diabetes is the 9th leading cause of death worldwide (~2 million deaths annually with type 2 diabetes only) and has been established as a common, chronic metabolic syndrome (Bhilare et al., 2024a). Moreover, high blood sugar (>7 mM) in diabetes can damage tissues resulting in multi-morbidities such as renal failure, retinopathy, neuropathy, and cardiovascular diseases (Acosta-Patino et al., 2001; Harding et al., 2019). The timely and

continuous measurement of glucose levels in blood is a key for the effective treatment of diabetes, for the past 50 years, finger-prick glucose testing has been the gold standard method for measuring glucose. However, this invasive approach often leads to patient non-compliance due to the need for frequent pricks and can be affected by substances like galactose, fructose, and ascorbic acid, which can impact test accuracy (Inzucchi, 2012; Olansky and Kennedy, 2010). Moreover, advancement in the medical technology led to the development of wearable glucose sensors for continuous monitoring of glucose in the market for instance Abbott libre, Dexcom (Healthline, 2024a; Healthline, 2024b). However, they are still out of reach for poor population in developing and underdeveloped countries due to their cost. Therefore, there is still race for developing cost effective glucose sensors and additionally, there is need to replace enzymes used in these sensors. Non-invasive enzymatic sensors (based on reverse iontophoresis for sample extraction etc.) are gaining popularity as alternative options to finger prick tests; but currently face challenges such as stability, limited sensitivity due to the susceptibility of glucose oxidase to deactivation and the need to address various regulatory hurdles (Gao et al., 2019). Consequently, there is industrial and scientific demand to develop non-enzymatic glucose sensing platform or non-enzymatic recognition elements (REs) for glucose. These non-enzymatic platforms can be integrated into existing and new sensor technologies to more effectively monitor glucose and develop next generation glucose sensors.

Cancer is a significant public health challenge and contributor to one in every six NCDs related deaths worldwide ((WHO), 2024b). According to the International Agency for Research on Cancer (IARC), ~ 20 million new cancer cases with 9.7 million deaths were reported in 2022 and these cases are expected to rise to 35 million by 2035. Breast cancer (~12% of all cancer cases) and lung cancer (~12%) in women and men respectively, were the most common and lethal cancers (Bray et al., 2024). Traditional therapies like chemotherapy and radiation have imposed significant physical and psychological burdens on cancer patients (Liu et al., 2024). Moreover, the non-specific targeting of cancer cells has rendered these approaches ineffective for a significant number of patients. To improve the existing therapies and for the targeted chemotherapy, antibody drug conjugates (ADCs) have been developed and successfully used in clinical practice for several cancers (Drago et al., 2021). However, there are still number of cancers where ADCs cannot be used such as glioblastoma (Anami et al., 2022), are expensive (*e.g.,* Enhertu, ~$100,000 per treatment) and have limited *in vivo* stability

(CARE and (NICE), 2021).

On the other hand, nanoparticles (NPs) with unique properties, have been researched extensively for the drug delivery applications. The most common used NPs are metallic NPs (gold, silver/magnetic) and polymeric NPs (Gavas et al., 2021). To make them efficient for targeted therapy, functionalisation of these NPs with antibodies (Abs), aptamers or peptides is being explored and offer several advantages over conventional therapies/ADCs by reducing unwanted side effects and cost (Bahrami et al., 2017). However, there is still a room for the advancement and improvement in the treatment modalities that offer both personalised and precise tumour targeting for most aggressive and untreated cancers such as blood/brain cancer.

Oxidative stress play an important role in the development of NCDs (Camps and García-Heredia, 2014); specifically in the pathogenesis of neurodegenerative disorders (*e.g.,* schizophrenia), cardiovascular diseases, cancer, neuropathic pain, and inflammation (Oktay et al., 2003). Consequently, for NCD treatment, researchers are developing therapeutic strategies by targeting oxidative stress. Drugs of plant origin or natural products such as flavonoids or coumarins etc. have abundant active ingredients, multiple therapeutic effects and minimal side effects (Zhang et al., 2024). However, hydrophobic (poor water solubility) nature of most of the natural drugs hinder their use for pharmaceutical and biological applications (Coimbra et al., 2011). Improving the water solubility/physiochemical properties of these drugs with different materials, can overcome these disadvantages (Chaudhary et al., 2012). Therefore, different formulations for natural products/drugs can be explored to targeting the oxidative stress pathway for the treatment of NCDs.

1.1.1 Need for effective diagnosis and treatment

Early detection and effective therapeutic treatments are critical in controlling these conditions (Omotayo et al., 2024). Early diagnosis allows for timely intervention, and suitable therapeutic treatments aid in illness management and patient outcomes. Conventional methods of diagnosing diseases, which depend on centralised laboratories and sophisticated equipment, can lead to a delayed diagnosis and worsening patient outcomes. In emergency, ambulatory, and distant settings, where prompt intervention is critical, the delay in diagnosis is especially troublesome (Srinivas and Kale, 2023).

Furthermore, low-concentration indicators seen in the early stages of illnesses present a challenge to traditional diagnostic methods. There is an urgent need for more efficient and accessible diagnostic techniques that can detect biomarkers at low concentrations, particularly during the asymptomatic transition period of illnesses. In this regard, conventional approaches are frequently insufficient, emphasising the need for innovative options (Chandra, 2023).

In addition to diagnosis, the treatment of the diseases is one of the key components of a healthcare system. There remain several challenges in drug delivery of pharmaceuticals due to their physiochemical and biological properties (Ezike et al., 2023). Moreover, the human body is a complex structure, and a drug molecule needs to pass through various biological barriers before it reaching to the site of action. Therefore, there is a continuous need for drug delivery carriers for these therapeutic agents such as drug solubilizers for poorly water-soluble drugs (van Hoogevest et al., 2011). Targeted drug delivery is especially crucial in the treatment of cancer and autoimmune diseases, where highly toxic drugs (chemotherapy drugs) should selectively target cancer cells while sparing healthy cells to minimise severe side effects (Manzari et al., 2021). For the therapeutic delivery various drug delivery vehicles including polymers, NPs, surface active materials have been used, out of which polymers hold a unique position due to their various advantages (cost effectiveness, easy fabrication process, versatile nature and minimal toxicity etc.) over others (Bodoki et al., 2019; Ding et al., 2024; Mitchell et al., 2021; Prasad et al., 2018).

1.2 Polymers, their types and biomedical applications

A polymer is a substance composed of macromolecules (The International Union of Pure and Applied Chemistry, IUPAC) (Jenkins et al., 1996). Polymers are composed of many monomeric repeating subunits and their properties vary depending on the arrangement and connections of these subunits (Aida and Meijer, 2020; Su, 2013). Polymers can be categorised into homopolymers (consist of a single repeating subunit (monomer)), and copolymers, (consists of two or more different monomers) (Ratner, 2004; Stevens, 1990). The synthetic polymer poly(methyl methacrylate) reported for medical use, was first introduced by a British ophthalmologist Sir Nicholas Harold in 1949 for making intraocular lenses to replace damaged corneas (Hussain and Thomas, 2021). Biostability and biodegradability are critical considerations when choosing a polymer for biomedical

applications (Ulery et al., 2011). For example, ventricular assist devices made of polyurethane were first used in clinical settings in the 1960s (Eisen, 2019; Robinson et al., 2001). This polymer not only improved safety but also lowered the costs, increasing the availability of these devices. However, this prolonged the waiting period for a suitable match for the approximately 18,000 individuals who were not able to receive a donor heart right away each year. Polymers, with their outstanding characteristics and engineering versatility, have been employed for a variety of biomedical applications **(Figure 1.1)** such as biomaterials, implants, and drug delivery systems, offering a low-cost alternative to expensive treatments (Robinson et al., 2001).

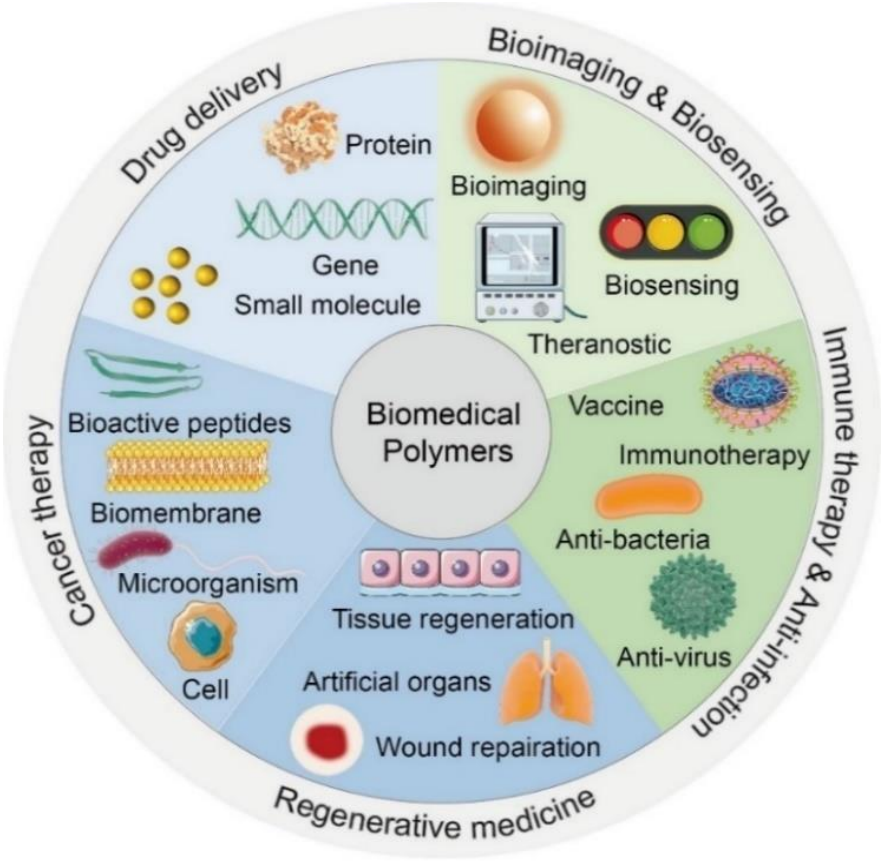

Figure 1.1: Schematic illustration of polymers for biomedical applications (W.-H. Chen et al., 2022). Reprinted with permission from Springer Nature (5992500612373), Copyright 2024.

Biomedical polymers including both natural and synthetic, have revolutionised biomedical technology by serving as alternative for tissue engineering, drug delivery, and medical devices development (Annabi et al., 2014; Satchanska et al., 2024; Tian et al., 2012). Natural polymers (*e.g.,* proteins and polysaccharides) are biodegradable and

interact with cells but have limited mechanical properties and potential immunogenicity (W.-H. Chen et al., 2022). Synthetic polymers have better composition, structure, and mechanical properties but lack natural bioactivity and further divided into biodegradable and non-biodegradable types. Polymers that do not degrade in the human body, like polymethacrylate derivatives due to their stability and inertness, are used in permanent implants and prostheses. For example, poly(ether-urethane-urea) has FDA approval for vascular grafts and a PU-based implant was approved by FDA as a meniscal substitute (Dang et al., 2014). On the other hand, biodegradable polymers (such as aliphatic polyesters and poly(ortho esters)) discompose safely in the body after achieving their functions and are employed for drug delivery, tissue regeneration, and wound closure devices (Shelton et al., 1971). The other most exciting class of the polymers is conducting polymers (CPs), which are extensively studied due to their outstanding properties, including tuneable electrical property, high mechanical properties, easy synthesis and high environmental stability over conventional inorganic materials. CPs possess alternating single (σ) and double (π) bonds, with π-conjugated systems that enable them optical, electrochemical, and electrically conductive properties. CPs such as polypyrrole (PPy), polyaniline (PANi), polythiophene (PT), poly(3,4-ethylenedioxythiophene) (PEDOT) have a wide range of applications in sensors/biosensors, neural probes, tissue engineering scaffolds and drug delivery (Le et al., 2017; Namsheer and Rout, 2021). Apart from that biocompatibility and biodegradability of polymers is essential for most of the biomedical applications, specifically in therapeutic and drug delivery (Gayathry et al., 2022). However, biocompatibility is more important than biodegradability in sensing applications (including wearable sensors), as robustness is crucial for extended sensor use.

1.2.1 Point of care sensors

PoC biosensor and smart wearable sensing systems offer a promising solution to the challenges posed by traditional diagnostic methods (Qazi and Raza, 2020). By providing rapid and accurate results, PoC biosensors empower the patient to detect the diseases and consultation with healthcare professionals and decrease the turnaround time, ultimately improving patient outcomes, reducing healthcare costs (Sharma et al., 2021). In the development of PoC, various transducers can be used depending on the type of physicochemical signal produced which can be electrochemical, mass-based, thermal, or

optical. The transduction elements can take various forms, such as electrodes for amperometric and potentiometric detection, field-effect transistors, piezoelectric quartz (Quartz Crystal Microbalance), thermistors, optical fibres/optoelectronic systems, and colorimetric indicators (Hughes and Fatoyinbo, 2012). Depending on the transducer, various techniques such as electrochemical methods, spectrophotometry, and surface plasmon resonance (SPR) can be used. Furthermore, to improve and enhance the signal to the transducer, during or after the binding event, NPs/nanomaterials (NMs) can serve as effective signal transducers **(Figure 1.2)** (Khan et al., 2024).

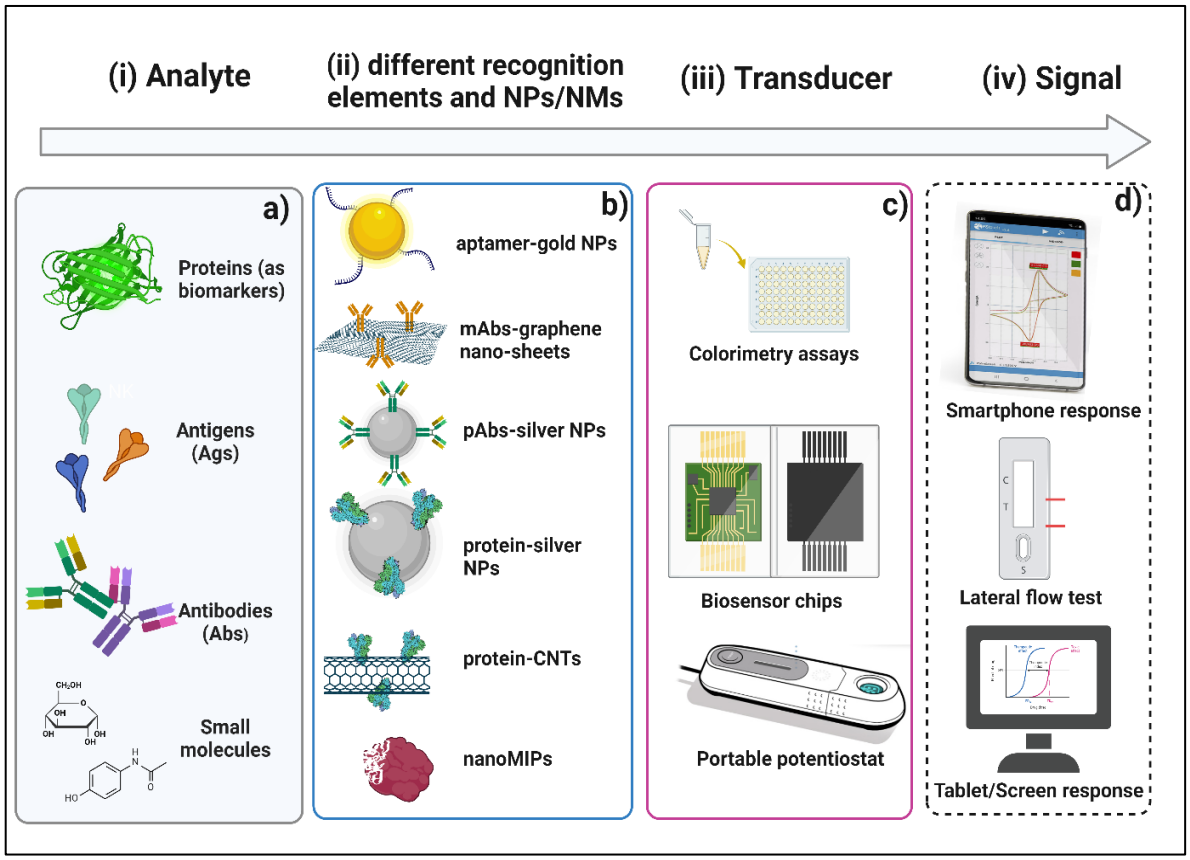

Figure 1.2: Various components of bioreceptor/ molecular recognition element (MRE) functionalised NPs/NMs based PoC sensors **(a)** Analyte such as SARS-CoV-2 virus and antigens (spike proteins), **(b)** a bioreceptor (*e.g.,* enzymes, Abs, proteins) also known as MRE conjugated NPs/NMs, **(c)** a transducer that converts the physicochemical signal and **(d)** a signal processor to interpret the converted information.

PoC biosensors fill the gap in disease diagnosis, particularly in resource-limited settings such as lateral flow test for cancer biomarkers (ColoAlert test for colorectal cancer) and more advanced wearable glucose sensor, for instance Abbott's Free Style

Libre (Abbott, 2024; ColoAlert, 2024). PoC diagnostics (portable and ultra-sensitive) can detect biomarkers even at low concentrations, enabling early diagnosis and intervention (Mondal et al., 2020; Parihar et al., 2020)**.** Despite tremendous advancement in biosensors, there is an urgent need for further improvements in selectivity, accuracy, and calibration. In addition, long-term stability remains a vital issue in wearable sensors (Kim et al., 2019; A. Sharma et al., 2022). For example, wearable devices rely mostly on natural recognition elements (REs) which are not stable at various temperature range and wearable potentiometric probes need calibration procedures, storage, and other procedures that are not appropriate in wearable platforms (Parrilla et al., 2019). Therefore, the selectivity, stability, accuracy, and adaptability of a sensor play a major role in the development of the suitable wearable sensors. There are three different biorecognition elements and based on their origin, they can be classified into natural, pseudo-natural and synthetic origin (Kalita et al., 2023; Morales and Halpern, 2018). Natural biorecognition elements such as enzymes, Abs, subcellular components (i.e., organelles) impart the naturally evolved physiological interactions to achieve analyte specificity. Pseudo-natural biorecognition elements (*e.g.,* aptamers, peptides) are artificially engineered supramolecular modalities having natural subunits such as nucleic acids, amino acids and have both natural and synthetic characteristics (Morales and Halpern, 2018). Synthetic biorecognition elements such as molecularly imprinted polymers (MIPs) are engineered artificially to mimic the physiologically defined interactions of their natural counterparts such as Abs (Vaneckova et al., 2020). Amongst these biorecognition elements, synthetic and pseudo biorecognition elements are more stable, robust and cost-effective than natural biorecognition elements. Moreover, they can exhibit similar selectivity, specificity and sensitivity. One can argue that polymeric supramolecular materials are the most appropriate for the biosensors and wearable devices because of precise structure, stability and robustness.

1.2.2 Drug delivery systems

Drug delivery systems (DDSs) played a paramount importance in the delivery of drugs, also known as active pharmaceutical ingredients. Depending upon the physiochemical properties of drugs and mode of deliveries, these drug delivery agents have been used from more than a century (Aitken et al., 2014). Moreover, there is further demand of DDSs to improve the delivery of biopharmaceuticals such as proteins, genes (including siRNA,

mRNA etc.), nucleic acids, Abs for their protection from enzymes such as proteases, nucleases, improving bioavailability, and specificity (Tibbitt et al., 2016). In the light of advancement in the science and technology, innovative and improved delivery methods have been developed for new and existing drugs in order to enhance their safety and efficacy (Brunton et al., 2011). There are several DDSs such as excipients (bulking agents, emulsifiers and solubilisers), controlled release, targeted DDSs and many more. There are still many drawbacks associated with these DDSs like uncontrolled and burst release, and stability. Moreover, for the cytotoxic drugs such as anticancer drugs, targeted DDSs are required to target specifically cancer or diseased cells, while sparing healthy cells to avoid the unwanted toxicities and side effects. To address these challenges, targeted DDSs have been explored employing different materials and chemical approaches. A DDS can be formulation or device that deliver the therapeutic agents into the body while enhancing their efficacy and safety by controlling the drug's release rate, timing, and location (Jain, 2020). There are various NPs-based drug delivery vehicles *viz.* micelles, including polymeric micelles, nanocapsules, nanoshells and nanospheres, niosomes, magnetic NPs including Au NPs, iron oxide NPs, liposomes, and dendrimers (**shown in Figure 1.3**) (Begines et al., 2020; Chan et al., 2010; Silindir Gunay et al., 2016). Natural and synthetic polymers based DDSs are rapidly growing in pharmaceutical industries and offer flexibility in shape, size, and surface properties (Sung and Kim, 2020; Uhrich et al., 1999). Early synthetic polymeric systems, such as polyglycolic acid, sparked interest in biodegradable polymers (Pillai and Panchagnula, 2001). Polymers are widely used in DDSs such as in many dosage forms (*e.g.,* tablets, capsules, films, gels and suspensions), osmotic DDSs, and controlled release systems (Borandeh et al., 2021; Gandhi et al., 2012). Moreover, polymeric systems at nano/micro levels have been explored in the applications of targeted DDSs and gene delivery. Polymeric NPs based DDSs offer great potential for clinical applications because they improve drug encapsulation and delivery, prolong circulation time, and allow for sustained drug release, thereby enhancing drug efficacy and reducing therapeutic side effects (Khalid and El-Sawy, 2017). The versatility and adaptability of polymeric micelles with small size (~100 nm), strong core-shell structures, and kinetic stability, make them particularly promising for delivering insoluble or poorly soluble drugs (Negut and Bita, 2023). Additionally, innovations like molecular imprinting, supercritical fluid technology, and nanoscale engineering are expected to further advance DDSs performance.

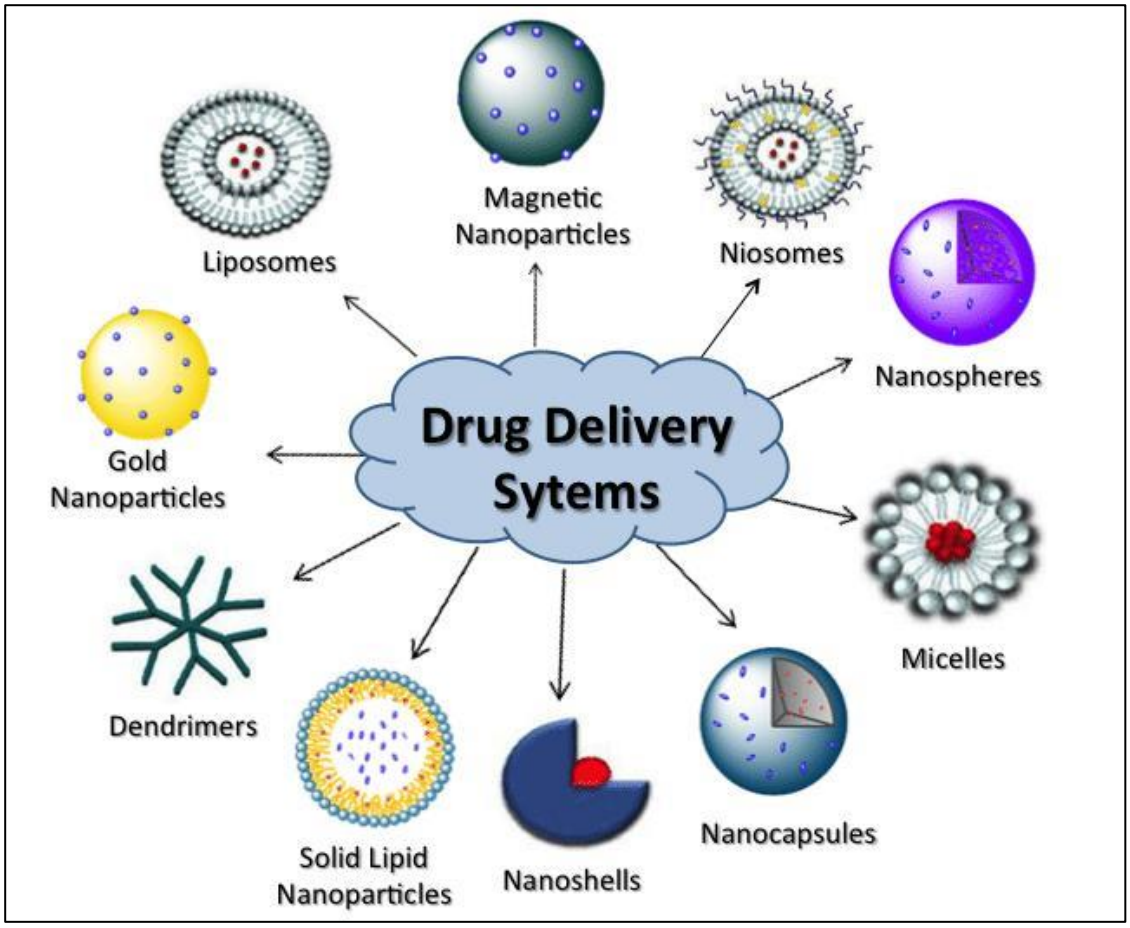

Figure 1.3: Different nanoparticles (NPs)-based drug delivery systems (Silindir Gunay et al., 2016). Reproduced under Creative Commons Attribution-Non-Commercial 4.0 International Public License (CC BY-NC 4.0).

1.3 Molecularly imprinted polymers (MIPs) and their classification

Molecularly imprinted polymers (MIPs) also known as "*plastic or artificial Abs*" which have specific cavities within a three dimensional (3D) polymeric network complementary to the size, shape and chemical functionality of the chosen compounds to be imprinted (called "template") (**Figure 1.4**) (Ertürk and Mattiasson, 2017). This "lock and key" mechanism enables MIPs to mimic the binding properties of natural Abs, along with several distinct advantages such as lower production costs and the ability to target a broader range of molecules, regardless of their size or immunogenicity (BelBruno, 2018).

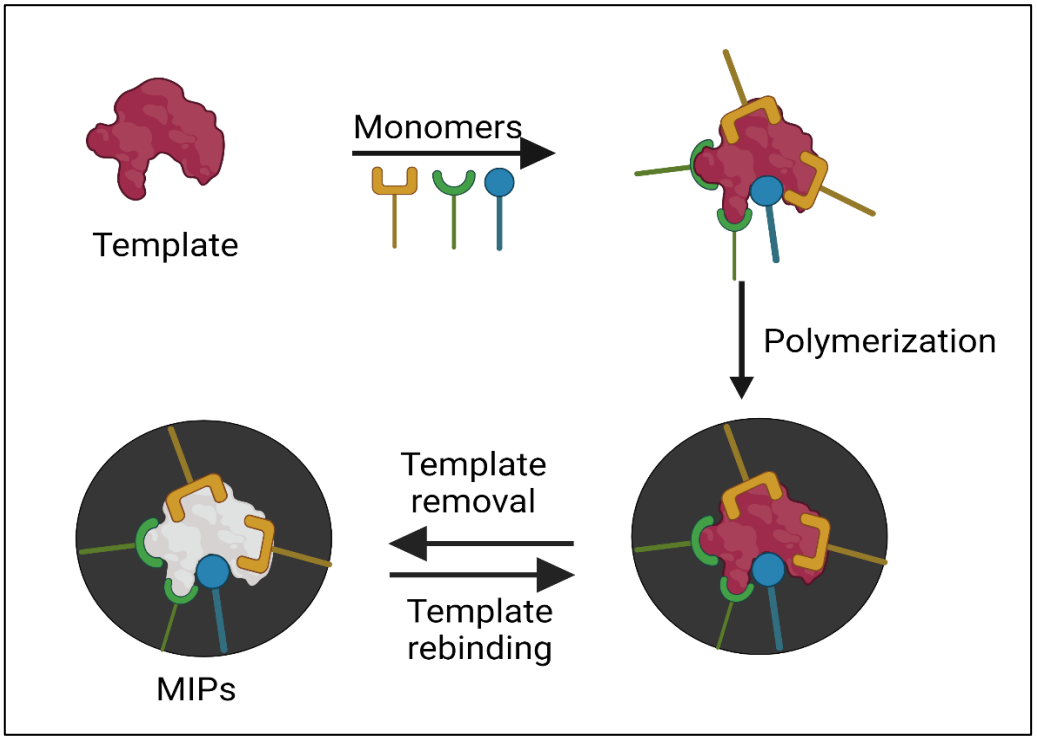

Figure 1.4: The schematic representation illustrating core principles of MIPs synthesis and extraction.

The first scientific mention of molecular imprinting technique was nearly 100 years ago when Polyakov in 1931 discovered that silica gels (made in the presence of another molecule) selectively absorbing the specific molecule. In 1949, Pauling presented experiments by Dickey which demonstrated that silica gels had been prepared by "procedures analogous to the formation of Abs" (Dickey, 1949; Polyakov, 1931). MIPs also known as synthetic biorecognition elements or synthetic Abs mainly emerged about 40 years ago when Wulff and Klotz independently proposed the first examples of molecular imprinting in the 1970's in synthetic organic polymers (Takagishi and Klotz, 1972) (Wullf, 1972). Since then, MIPs have been explored for various applications due to their excellent properties including high selectivity and specificity, robustness, high affinity and can withstand to extremes of temperature and pH conditions. MIPs have emerged as a revolutionary class of synthetic receptors with high selectivity and affinity for their target molecules. Once the template is removed, the synthesised polymer can selectively bind to the target, which can be the analyte itself. The template can be removed using different methods including mechanical grinding and solid phase extraction through extended washing steps using protic solvents (Joseph W Lowdon et al., 2020). Unlike the complex and costly production of monoclonal Abs, MIPs can be fabricated with easy, scalable and

cost-effective approaches, without the need for preclinical development or animal testing (Altintas et al., 2016; Altintas et al., 2015; R. Liu et al., 2017; Nguyen et al., 2024).

1.4 Polymerisation mechanisms for MIPs

1.4.1 Free radical polymerisation

The free radical polymerisation is most used method to synthesise the MIPs. This polymerisation is performed under mild reaction conditions (such as atmospheric pressure and ambient temperature) in solvent or bulk (Włoch and Datta, 2019). The mechanism of free radical polymerisation involves of initiation, propagation and termination as shown in **Figure 1.5.**

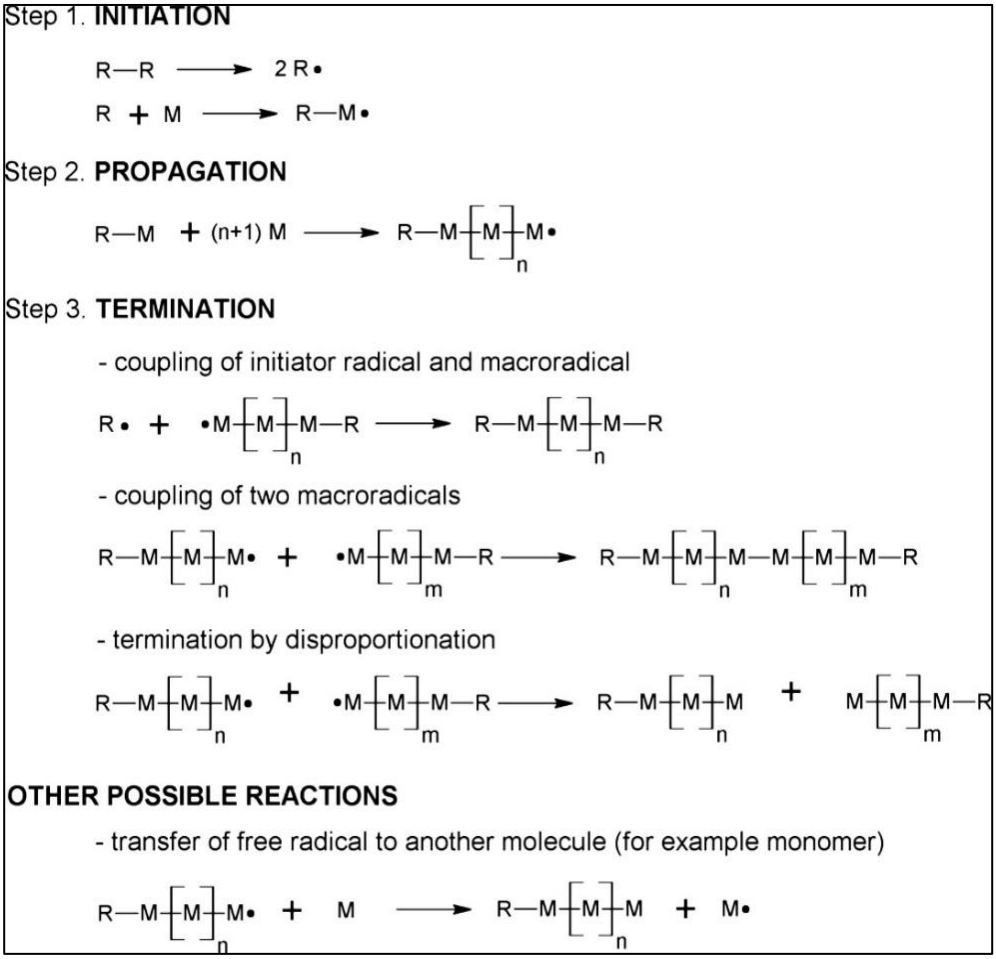

Figure 1.5: Mechanism of free radical polymerisation, where M represents the monomer, R and R• denotes the chemical group and free radical of that chemical group respectively (Panagiotopoulou et al., 2015).

1.4.2 Controlled and living radical polymerisation

In recent years, heat- and UV light-initiated polymerisations have been utilised for the synthesis of MIPs. However, the ongoing interest to optimise polymerisation protocols has led to the emergence of new techniques, such as microwave-assisted synthesis initiation and controlled living radical polymerisation methods, including atom transfer radical polymerisation (ATRP) and reversible addition-fragmentation chain transfer polymerisation (RAFT). These polymerisation strategies have been predominantly used for fabricating MIP films or core-shell MIP NPs. A significant advantage of living radical polymerisation over conventional free-radical polymerisation is the ability to control the thickness of the MIP film, which is essential for developing composite NPs.

a. Atom transfer radical polymerisation (ATRP)

ATRP is a robust polymerisation technique introduced by Matyjaszewski's group in 1995 (Wang and Matyjaszewski, 1995). Additionally, ATRP method uses metal ion catalysts (copper ions), to facilitate the interactions involved in forming the monomer-template conjugate and the overall polymerisation reaction (Di Lena and Matyjaszewski, 2010; Matyjaszewski, 2012a). The main advantage of this strategy is the equilibrium of the reaction, and the metal ions used and allows the precise control of the polymerisation process. However, uses of the metal ions have disadvantage in ATRP such as the removal of these metal ion after the polymerisation reaction and need various sophisticated purification steps.

b. Reversible addition-fragmentation chain transfer polymerisation (RAFT)

Chiefari *et al.* were the first to report RAFT polymerisation in 1998 (Chiefari et al., 1998; Chiefari et al., 2003). This living free-radical polymerisation process, across a broad spectrum of monomers and reaction conditions allow the synthesis of polymers with controlled molecular weight with exceptionally low polydispersity (generally <1.2) (Gregory and Stenzel, 2011; Moad et al., 2000). Furthermore, this polymerisation method enables the fabrication of block copolymers and other polymers (from linear to dendrimers like polymers) of complex architectures that are difficult to synthesise using other methods. To achieve a controlled free-radical polymerisation, specific reagents such as trithiocarbonates and xanthates are used which enable the cycled addition-fragmentation chain-transfer during polymerisation (Chiefari et al., 2003; Chong et al., 2003). For

instance, in core-shell MIP NPs synthesis, a RAFT agent is immobilised on the surface of core particles (*e.g.,* polystyrene, silica) (Xu et al., 2011). Grafting and precipitation methods via RAFT results in the formation of homogenous MIP shells having high affinity and selectivity, while also allowing the adjustment to the polymer's thickness formed. Even though these both ATRP and RAFT methods are relatively new for MIPs synthesis but can serve as a starting point to further optimise polymerisation methods.

c. Iniferter polymerisation

In iniferter polymerisation method, iniferters (chemical agents such as dithiocarbamates) act as initiator-transfer agent-terminator, enabling precise control over the polymerisation process and resulting in well-defined MIPs with specific binding sites (Otsu and Yoshida, 1982). The method involves mainly three steps: a radical initiator (which generates radicals to start polymerisation), a functional group (which interacts with the target molecule), and a termination group (which ends the polymerisation process).

d. Nitrous oxide mediated polymerisation

Nitrous oxide mediated polymerisation (NMP) works on a reversible termination mechanism, where the growing propagating (macro)radical is temporary terminated by the nitroxide, acting as a control agent. This led to the formation of (macro)alkoxyamine as the predominant species. In NMP, no additional catalyst or chain transfer reagent is needed and a single NMP initiator (for instance, 3-(4-tert-butylphenyl)-1,1-dimethyl-3-(2,2,6,6-tetramethylpiperidinooxy)propyl cyanide) is enough to obtain the reaction control (Boonpangrak et al., 2006; Matyjaszewski, 2012b). There are only few reports on the use of NMP for the synthesis of MIPs so far. In this context, Boonpangrak and colleagues developed the cholesterol-imprinted MIPs using NMP (Boonpangrak et al., 2006). These MIPs showed greater selective binding for cholesterol binding than that synthesised by a traditional radical polymerisation. Kouki and co-workers reported the preparation of MIPs for adsorbing 3,5-dichlorohydroxyacetophenone (DCHA) using NMP and by conventional free radical polymerization (Kouki et al., 2022). NMP MIPs was found to be better as they showed the improved adsorption due to a higher density of molecular imprints, not a stronger affinity for DCHA.

1.5 Approaches to MIPs synthesis

MIPs can be synthesised in several formats, for instance as films or membranes, microparticles or NPs. The molecular imprinting consists of three main steps: (i) forming the monomer-template complexes, (ii) polymerisation, and (iii) removing the template and collecting the MIPs. Traditional MIP typically synthesised heterogeneous microparticles, which often struggle with low affinity, template leaching, and slow binding kinetics (Refaat et al., 2019). However, these MIPs due to their low-cost and enhanced robustness, have been widely adopted in commercial applications for purification and separation where capacity is prioritised over sensitivity (Tchekwagep et al., 2022). MIPs NPs, compared to other formats, offer several advantages including a much higher surface-to-volume ratio and a larger total surface area per weight unit of polymer. This increased surface area allows analytes to access the imprinted cavities more easily, improving binding kinetics and template removal, and ultimately enhancing their recognition capabilities (Tokonami et al., 2009).

Synthetic polymer-based imprinting approaches are typically classified into three categories: covalent, non-covalent, and semi-covalent protocols, depending on the type of the interaction between the template and functional monomer(s). There are several polymerisation strategies such as bulk, emulsion, suspension, precipitation, multi-step swelling, surface imprinting polymerisation and solid-phase synthesis (Capek, 2010; Zhang, 2020) using different approaches (*e.g.,* free radical) to produce MIPs NPs **(Figure 1.6)** (Gkika et al., 2024).

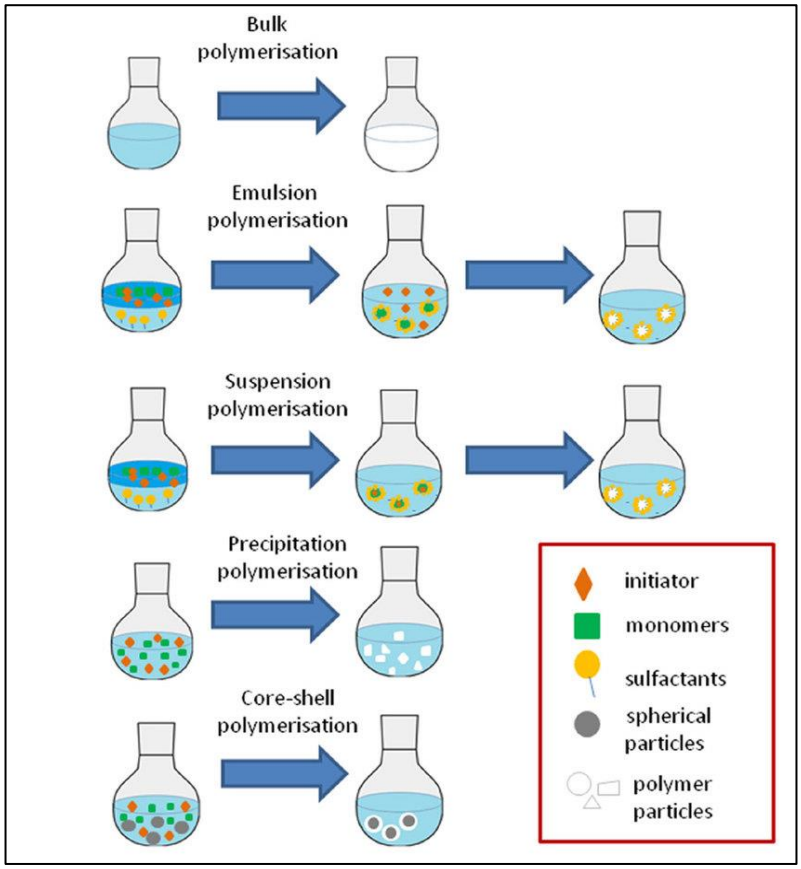

Figure 1.6: Different approaches and strategies for synthesis of molecularly imprinted polymer particles (MIPs) (Kwaśniewska et al., 2015). Reproduced under Creative Commons Attribution-NonCommercial-NoDerivs 3.0 License.

1.5.1 Bulk polymerisation

Bulk polymerisation is a fast, simple and most widely used method in which only functional monomer, template, cross-linker, and initiator is needed. However, particles obtained (in non-aqueous solvents) from this method require crushing, grinding, and sieving, which is a time taking and labour-intensive procedure (Mohajeri et al., 2011). In addition, due to grinding, non-uniform particles (shapes and size) are obtained and sieving often results in loss of prepared polymer (L. Wang et al., 2019). Furthermore, the particles demonstrate limited access to binding sites and low mass transfer kinetics towards the target molecule. This method generally exhibits poor reproducibility and selectivity (Turiel et al., 2005).

1.5.2 Suspension polymerisation

Suspension polymerisation is also a simple method used to synthesise spherical particles and is suitable for different templates/analytes like proteins, metal ions or drugs (Andaç et al., 2007; Ansell and Mosbach, 1997). In this method, each droplet serves as a mini bulk

reactor which enable the formation of spherical beads ranging from micrometres to millimetres in size (Yemiş et al., 2013). This polymerisation is performed in water, but mineral oil or perfluorocarbon can be used as continuous phase. The excellent heat dispersion is one of the major advantages of this method making it ideal for industrial scale-up without limitations of heat transfer.

1.5.3 Emulsion polymerisation

Emulsion polymerisation is the method to obtain high yield and uniform spherical MIP NPs and involves dissolving the template-conjugated functional monomers and organic cross-linking monomers in organic solvents (Poma et al., 2010). This process consists of a high-shear homogenisation step and an aqueous solution containing surfactants and stabilisers (*e.g.,* sodium dodecyl sulphate, SDS) to obtain MIP NPs with size of 50-500 nm (Van Herk and Monteiro, 2002). Moreover, a polymeric surfactant monomer can also be used to produce MIP NPs. Emulsion polymerisation generally can be categorised into mini- and micro-emulsion polymerisation depending upon the size of the emulsified droplet produced. Mini-emulsion approach utilizes the co-surfactant or surfactant monomers and, eventually, a co-stabiliser is added to produce NPs with uniform size (30-500 nm) (Vaihinger et al., 2002). The unique aspect of mini-emulsion polymerisation is the ability to synthesize semi covalently imprinted NPs. In this process, pre-polymerisation complex of monomers and the template forms through covalent bonds while the target binding relies on non-covalent interactions. Moreover, MIP NPs obtained via this method demonstrate high affinity and selectivity towards their target molecule. The synthesis of MIP NPs employing emulsion polymerisation was first reported by Whitcombe and co-workers in 2000 and to synthesise MIPs for proteins, viruses and other small templates (Zhang, 2020). On the contrary, micro emulsion polymerisation produces the particles of 5-50 nm diameter and typically take place under more complex conditions involving the presence of water, oil, one or more surfactants and thermodynamically stable system (Slomkowski et al., 2011; Ye, 2013).

This process utilizes lower concentration of monomers, and a higher surfactant concentration compared to the mini-emulsion method (Ye, 2013). Additionally, spherical MIPs NPs can be produced employing various methods. One innovative approach exploit adding monomers or peptides conjugated with fatty acid chains to enhance the confinement of the template on the surface of the growing MIP NPs (Zeng et al., 2010).

Although emulsion polymerisation process has several advantages such as high yield, homogeneous monodispersed NPs, but has major downside is the use of surfactant (SDS) and other chemicals. The presence of surfactants and stabilisers in solution can interfere with monomer-target recognition, necessitating several washing steps that may reduce the reaction yield and compromise the efficacy and uniformity of the MIP NPs.

1.5.4 Precipitation polymerisation

Precipitation polymerisation is the fastest and straightforward method for producing monodispersed NPs (with high yield) within the various techniques used to synthesize MIP NPs. Typically, this approach relies on a free-radical polymerisation taking place in highly diluted monomer mixtures. The “growing” pre-polymer continuously incorporates monomers until its size causes the polymer to become insoluble and precipitate. This process produces the spherical and uniform NPs with high yield and minimal consumption of reagents. However, the major disadvantage of this method is the diluted solution of monomers, which can reduce the interaction of the active monomers and template molecule. This reduction results in formation of less efficient monomer-template pre-polymerisation complex which in turn decreases the selectivity of the produced MIP NPs. Furthermore, increasing concentration of monomers results in larger and less uniform MIP NPs (Li et al., 2003). Precipitation polymerisation is generally carried out using organic solvents, however; it is also possible to precipitate MIP NPs from aqueous solutions by adding a surfactant (low concentration) to the monomer mixture. Following synthesis, it is essential to remove both the template and the surfactant. There are several parameters that critically influence this polymerisation, thereby affecting the quality of the resulting MIP NPs. For example, the ratio/concentration of different reagents including the template, and the type of solvent can affect the MIP NPs and the yield. The use of precipitation polymerisation for MIP NPs synthesis was first reported by Ye and colleagues using both thermo- and UV-initiated traditional free-radical polymerisation methods (Ye et al., 1999). Theophyline- and 17b-estradiol-imprinted MIP NPs (200 and 300 nm diameter) were synthesised and showed high specificity towards their template and higher binding site densities as compared to MIPs generated through bulk polymerisation method. Overall, this approach is a cost-effective and time-efficient for producing nano or micro sized MIPs. Moreover, this facilitates the synthesis of uniform, spherical MIP NPs and even their properties can be tuned.

1.5.5 Core-shell polymerisation

It is used to prepare the imprinted polymeric layer around the various NPs such as gold NPs, mesoporous NPs and magnetic NPs (i.e. Fe_3O_4 NPs) etc. where NPs act as a "core materials" and imprinted layer as a shell (Tan and Tong, 2007). In this, emulsion polymerisation is mostly used to assemble core-shell MIPs.

1.5.6 Multi-step swelling polymerisation

Multi-step swelling polymerisation (known as seed polymerisation) allows the production of monodisperse and uniform sized MIPs which can be directly synthesised in the form of beads (water is usually used as dispersive solvent) with controlled diameter (Nakamura et al., 2017). However, this method is laborious and complicated due to the requirement of specific reaction conditions. MIPs produced by this method can be used for the chromatographic applications as show better separation ability (Liu et al., 2007). The application of this method involves the aqueous emulsions preparation, that can affect the imprinting process and the selectivity of the produced MIPs.

1.5.7 Surface imprinting polymerisation

Surface imprinting polymerisation involves surface grafting of thin and monodisperse MIP layers onto solid phase matrixes or beads with recognition sites located on the outer layer or exterior surface of the solid substrates. This method has gained extensive attention and has been employed in different fields including sensors, catalysis, biomedical, separation and purification (Dong et al., 2021; Xuan et al., 2014).

1.5.8 Solid phase synthesis

A popular method to synthesise molecularly imprinted polymeric NPs (nanoMIPs) is solid-phase approach in which template of interest is immobilised on the solid surface and polymerisation can be performed with different monomer mixtures using different polymerisation techniques mentioned above (section 1.5.1 to 1.5.3). Canfarotta *et al.* reported a general synthesis protocol for nanoMIPs using this solid phase synthesis method (Francesco Canfarotta et al., 2016a). In this approach, the template is covalently bound to a solid phase like micrometre-size beads (is used as an affinity medium) which facilitates the separation and collection of uniformly sized nanoMIPs with high binding affinity (Poma et al., 2013). Generally, the microbeads used as solid phase are glass

beads and to further link these with a template, silanization of these glass beads is needed with chemicals having specialised functional moieties. Various methods based on the functional group present on the template, can be used to immobilise the template onto the glass beads. For example, if template to be immobilised has –SH group, beads are pre-functionalised with succinimidyl iodoacetate and for –NH2 and –COOH group bearing templates, EDC/NHS chemistry can be used (Francesco Canfarotta et al., 2016a). Currently used imprinting techniques have several drawbacks in which imprinting binding sites are developed in the polymer because template is free in solution. On the other hand, binding sites in case of solid phase are present on the NPs, therefore, target molecule can access the surface more easily. Furthermore, other imprinting methods impart the "polyclonal" distribution of binding sites, low capacity and has poor performance in water particularly with hydrophilic targets. Due to the oriented immobilisation of the template in solid phase approach, this overcomes the abovementioned disadvantages associated with currently used imprinting techniques (F Canfarotta et al., 2018).

The schematic for nanoMIPs synthesis using different templates of interests *viz*. protein, epitope or small molecules is shown in **Figure 1.7** (Singla et al., 2024; Singla et al., 2023b). The unreacted monomers and low-affinity nanoMIPs are removed with low-temperature elution, followed by purification of high-affinity nanoMIPs at an elevated temperature (60°C). Moreover, high-affinity nanoMIPs produced using this approach are template-free, and the covalent immobilisation of the template/epitope ensures specific orientation, resulting homogeneous binding site affinity, similar to that of monoclonal Abs. **Figure 1.7a** summarises this solid-phase approach for small scale production in flask in the lab, in addition to highlighting an innovative double imprinting approach (**1.7b**) where two templates (double imprinted) are introduced at the stage of the pre-polymerisation complex.

Due to the high affinity (similar to Abs) and different applications including *in vitro* and *in vivo* assays, nanoMIPs has gained attention from big companies. Therefore, it is crucial to have a scale approach in place that can produce particles with precisely defined size and molecular weight as well as in high yields. Piletsky and colleagues were the first who proposed the automated reactor for nanoMIPs synthesis (F Canfarotta et al., 2018).

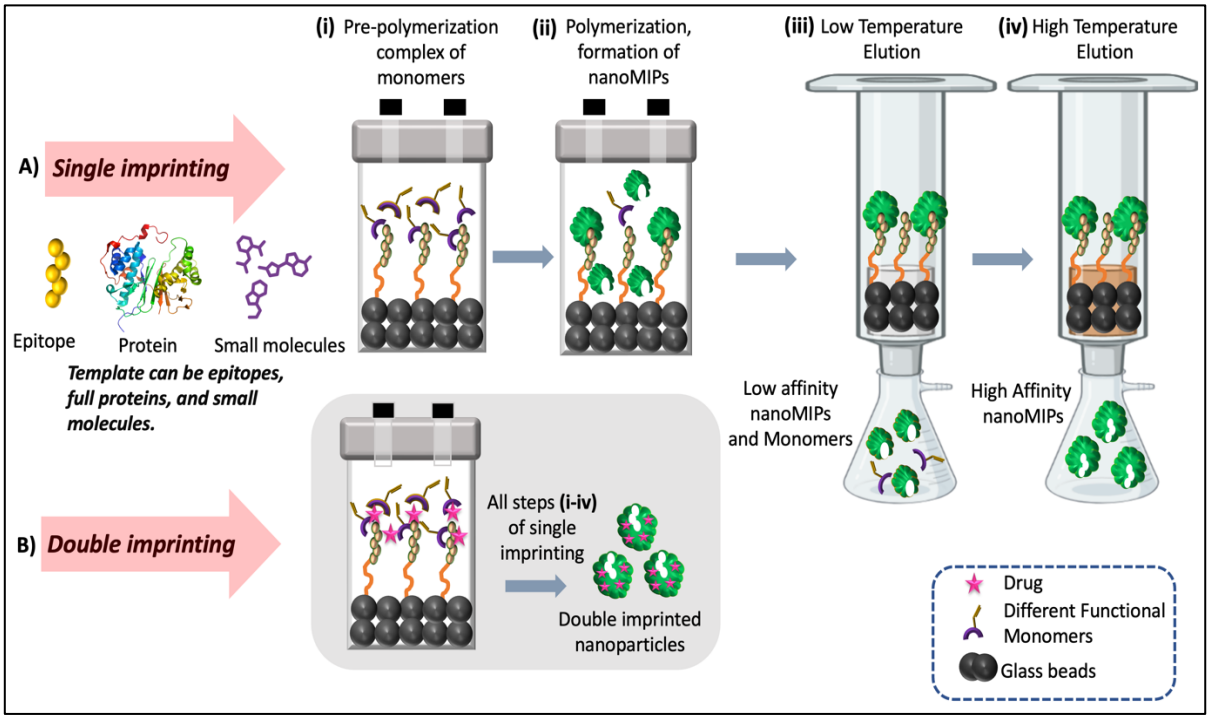

Figure 1.7: Solid phase synthesis of a) single imprinted and b) double imprinted nanoMIPs for different templates for examples small molecules, proteins, and larger macromolecules such as virus particles.

MIPs can be designed and imprinted for different targets including low molecular weight molecules (*e.g.,* ions, peptides), high molecular weight macromolecules (*e.g.,* proteins, nucleic acids, polysaccharides) or even whole cells (viruses, bacteria, etc.) (El-Schich et al., 2020). The most intriguing application of solid phase approach is protein imprinting, most of the proteins are expensive and need to be recycled which is possible with this approach. Moreover, protein imprinted MIPs have gained more attention because of their potential to replace Abs in sensors, diagnostics, or molecular biology. Additionally, it will give all the advantages of solid phase synthesis such as monodisperse and high affinity nanoMIPs, enable imprinting on the surface of NPs, affordable, easy fabrication and purification etc.

Protein are large macromolecules (generally has a molecular weight of a few thousand Daltons) and has an extended surface with multiple interaction sites. Various bonding including hydrogen, hydrophobic, electrostatic, or coordinative collectively enable strong interactions between the template and recognition cavities resulting in high affinity and selective binding. However, the heterogeneity and abundance of these interactions give

rise to multiple difficulties. Due to heterogeneity, the formed cavities will vary in their physicochemical and recognition properties, leading to differences in their affinity and binding kinetics with the template. The presence of abundant interaction sites can sites often bind to numerous non-imprinted areas, which reduces specificity and selectivity (He and Lin, 2022). To overcome these issues, epitope of a protein can be used (epitope imprinting approach) as a template instead of using whole protein molecule. An epitope (also known as an antigenic determinant) is a specific region or sequence on a protein or antigen that is recognized by the immune system, particularly by antibodies or binding ligands (Atassi, 1984). The concept of epitope imprinting was first coined by Rachkov *et al.* where a peptide (as epitope) with 5-30 amino acids residue was imprinted (Rachkov and Minoura, 2001). The use of epitopes offers several advantages, such as the ability to use organic solvents or harsher conditions during synthesis and are more cost-effective to synthesize and purify compared to whole proteins (Teixeira et al., 2021). Moreover, small templates like epitope, with a smaller number of possible interactions, can lead to more specific and homogenous binding sites. In addition, it is easier to remove and rebind a smaller template peptide due to its ease of diffusion in a polymer matrix. The epitope template can be either the N- or C-terminus, where N-terminus is the starting end with a free amine ($-NH_2$) group, while the C-terminus is the ending end with a free carboxyl (-COOH) group (Westwood and Hay, 2001). However, the C-terminus is more commonly used since it is less susceptible to post-translational modifications that can reduce recognition efficiency. The template peptides are usually linear chains, but they can also have circular structures or more complex structures (*e.g.,* α-helixes or β-turns) (Pasquardini and Bossi, 2021).

1.6 Diagnostic applications of MIPs and electroactive MIPs (eMIPs)

Early diagnosis for various conditions such as cancer, infectious diseases, cardiovascular diseases, autoimmune diseases and inflammatory diseases is necessary. Different biomarkers including proteins, Abs, hormones, and cytokines for disease like cancer are greatly explored (Polanski and Anderson, 2006). MIPs have been widely used in sensing, bioimaging and medical assays due to their ability to mimic the function of their natural counterparts (like Abs) and are more stable, cost-effective and have easy fabrication process (Joseph W Lowdon et al., 2020).

1.6.1 Electrochemical sensing

Electrochemical techniques are among the most used techniques in wearable and PoC sensor applications owing to their high sensitivity, quick response times, low cost, and portability. Wearable electronics combined with electrochemical detection improve the diagnostic results and allow for non-invasive and real-time biomarker monitoring. In electrochemical sensors, various REs including biological counterparts like aptamers and Abs can be used in conjunction with redox probes for signal response. However, eMIPs as their name suggests, possess intrinsic redox properties that eliminate the need for a redox probe, while also being robust, stable, and cost-effective.

The first eMIPs were developed by Piletsky *et al.* using solid phase synthesis approach using various monomers composition and have explored it for analysis of various biomarkers/protein. In this work, five distinct analytes *viz*. trypsin, glucose, paracetamol, C4-homoserine lactone, and THC were detected using differential pulse voltammetry (DPV, measures the current before and after applying the pulse and calculate the difference in current) (Venton and DiScenza, 2020). In these experiments, gold screen printed electrodes (SPEs) as the working electrode (WE), platinum as the counter electrode (CE), and silver as the reference electrode (RE) were employed. In other work, the Mazzotta and Piletsky groups generated eMIPs (solid phase synthesis, 2016) specific to the antibiotic vancomycin and carried out the electrochemical detection using cyclic voltammetry (CV). The same research team next used redox active eMIPs to measure glyphosate in spiked river water samples (2023) by using DPV (Lach et al., 2023). The impact of integrating multi-walled carbon nanotubes with eMIPs for the electrochemical detection of the antibiotic cefquinome, which is found in milk, was another area of interest to researchers. According to Moro *et al.* (2019), the eMIPs sensor demonstrated great sensitivity and selectivity for cefquinome detection. Furthermore, the researchers used DPV (2021) to determine the presence of paracetamol in spiked serum samples using an electroactive nanoMIPs-based SPE sensor (Alanazi et al., 2021). Additionally, Cruz and Piletsky conducted studies that used an eMIPs-based DPV sensor to detect sitagliptin, a drug used to treat type 2 diabetes mellitus, in human plasma. Haq *et al.* reported that this sensor exhibited a limit of detection (LOD) of 0.06 pM for sitagliptin, along with good selectivity and sensitivity (32.5 ± 0.6 nA pM^{-1}). Moreover, electro-polymerisation methods have been used to prepare an imprinting polymer layer on the electrodes. However, this often leads to a low utilisation of imprinted cavities, other limitations such as reproducibility

issues, non-uniformity of the layer which restricts the commercial scalability (R. Sharma et al., 2022). Many literature reports show the versatility of the eMIPs production using solid phase synthesis utilising a range of targets from small (*e.g.,* paracetamol) to large molecules such as proteins (*e.g.,* trypsin). Although this solid phase synthesis using multi monomer approach is a useful technique, its production is cumbersome for small organic molecules such as glucose. Therefore, free radical polymerisation of conductive monomers (such as aniline, pyrrole, thiophene) can be used as an alternative approach to develop eMIPs for the small molecules such as creatinine, uric acid, and glucose.

1.6.2 Wearable sensing

While blood and blood serum are the main biofluids and are widely considered the best methods for identifying various biomarkers, their extraction necessitates the use of invasive hypodermic needles and expertise to ensure patient safety (Frank and Hargreaves, 2003; Samant et al., 2020). This limitation makes frequent blood sample and biochemical tests difficult outside of clinical settings, with a few exceptions, such as finger-pricking for blood glucose monitoring. Researchers have been actively looking for new methods over time that minimize procedure complexity and invasiveness while maintaining accuracy. These investigations focus to find a blood like biofluid which is readily obtainable and do not require invasive methods, to act as a revolutionary game-changer in diagnostic processes. The biofluids including interstitial fluids (ISF), saliva, sweat and tears are being explored to determine both small (*e.g.,* glucose, lactate, and amino acids) and large (*e.g.,* drugs, proteins, and hormones) molecules biomarker (Kim et al., 2015; Kim et al., 2017; Samant et al., 2020). ISF due to its abundance, minimal bio-interference, and therapeutic significance stands out to be better among these biofluids. Moreover, serum and ISF differ in biomarker abundance due to their physiological roles. Serum, rich in proteins like albumin and immunoglobulins, is widely used for disease diagnostics but can mask low-abundance biomarkers. ISF, surrounding tissue cells, has fewer plasma proteins but better reflects local tissue conditions, making it useful for monitoring diseases like cancer. Although, ISF biomarkers are present at lower concentrations but offer localized and real-time insights into tissue-specific conditions, making them valuable for wearable and minimally invasive sensing technologies. ISF contains key biomarkers, such as ions (*e.g*., sodium (Na^+), potassium (K^+), chloride (Cl^-), and calcium (Ca^{2+})), small molecules (*e.g*., glucose, lactate, uric acid, peptides and

ammonia) and proteins (Yuan et al., 2023). Many literature studies show that the average Na^+ concentration is 141.2 mM in blood and 135.7 mM in ISF, while K^+ averages 4.37 mM in blood and 3.97 mM in ISF. Similarly, glucose, lactate, and other biomarker concentrations are nearly identical in both fluids (Friedel et al., 2023). A lot of research has been done on the most reliable, easy, and minimally invasive ways to extract information from ISF sensors in order to fully utilise them for supporting healthcare applications as shown in **Figure 1.8**. Along with different methods like reverse iontophoresis (RI), micro-dialysis and microneedles to sample or access ISF, ISF biomarkers are also investigated for diagnosis and treatment purposes (Sang et al., 2023; B. Yang et al., 2022; Yao et al., 2021).

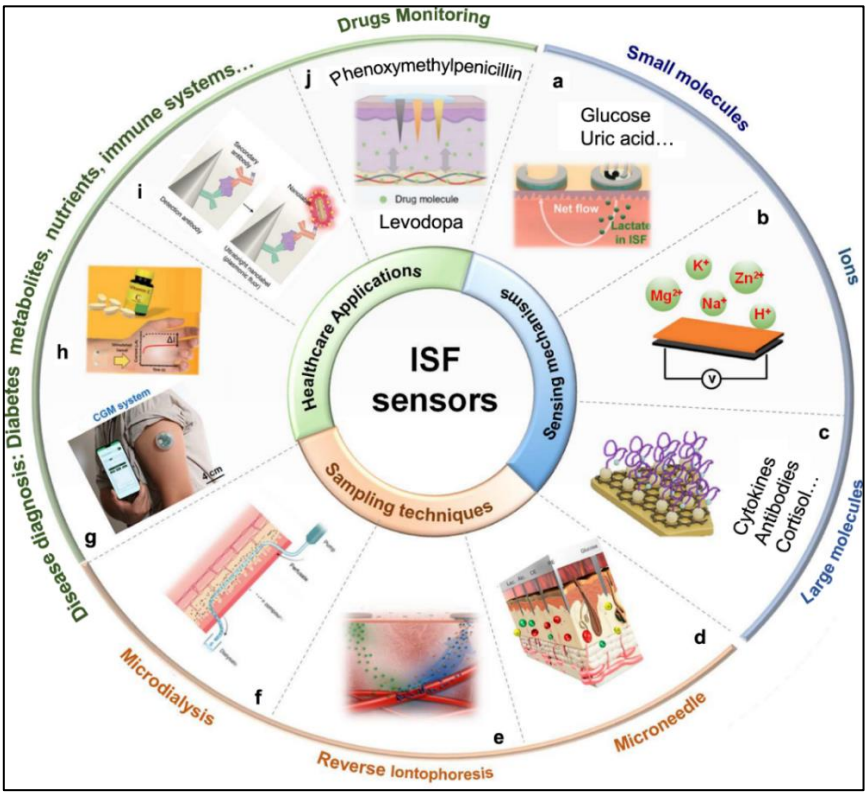

Figure 1.8: Different application of ISF sensors in wearable technology (Wu et al., 2024). Reproduced under the Creative Commons CC BY-NC 4.0 license.

1.6.3 Sampling techniques to collect biofluids or ISF

ISF analysis is promising in diagnosis as it is less invasive, which reduces concerns about clotting and interference from blood cells. ISF is difficult to sample or access for efficient detection, even though it contains important biomarkers with considerable clinical

promise. Many sample techniques, such as microneedles, RI, and microdialysis, have been proposed to overcome this. These methods use in-body sensors placed inside the tissue for in-situ real-time analysis, or they collect ISF from the human body for external examination.

a. Microneedles

These sampling methods employ array of microneedles to penetrate the skin, establishing fluid pathways for the extraction of ISF (**Figure 1.9a**). Based on their composition and morphology, microneedles can be categorised as solid, hollow, porous, or hydrogel.

Solid microneedles, generally shaped like pyramids or cones with sharp tips, are easier to fabricate, more mechanically robust, and less expensive than other types (Aldawood et al., 2021). They generate microchannels when they are pressed into and released from the skin that allow ISF to flow in due to osmotic and concentration gradients, passively transporting solutes like electrolytes (Na^+, K^+, Cl^-, and Ca^{2+}), glucose, lactate, amino acids, and drug metabolites. The ISF components can then be analysed by sensors close to the channels (J. Yang et al., 2022). Furthermore, functional materials can be added to solid microneedles to enable in situ biomarker detection (Tehrani et al., 2022). These microneedles integrated with electronics, can be used to identify various biomarkers, including glucose, medications, and even multiple biomarkers (Liu et al., 2021; Wu et al., 2022). Hollow microneedles have the same form and materials as solid ones, but their hollow lumen serves two functions: generating microchannels for ISF extraction and acting as a conduit for drug delivery. ISF extraction is facilitated by capillary flow, which creates a concentration gradient in the lumen that makes it easier to collect ISF for analysis (Mishra et al., 2020; Yang et al., 2023). Porous microneedles with several capillary channels are composed of inorganic, metal, or polymer materials (Gao et al., 2022). They can extract ISF from the dermis and transfer it to a sensing chamber for evaluation when they combine it with iontophoresis (Li et al., 2021).

Hydrogel microneedles are a new type of microneedle that remains rigid when dry but swells upon skin penetration (GhavamiNejad et al., 2023; Mandal et al., 2018). Hydrogel microneedles can also function as reservoirs, necessitating additional processes to remove the gathered ISF (Chang et al., 2017).

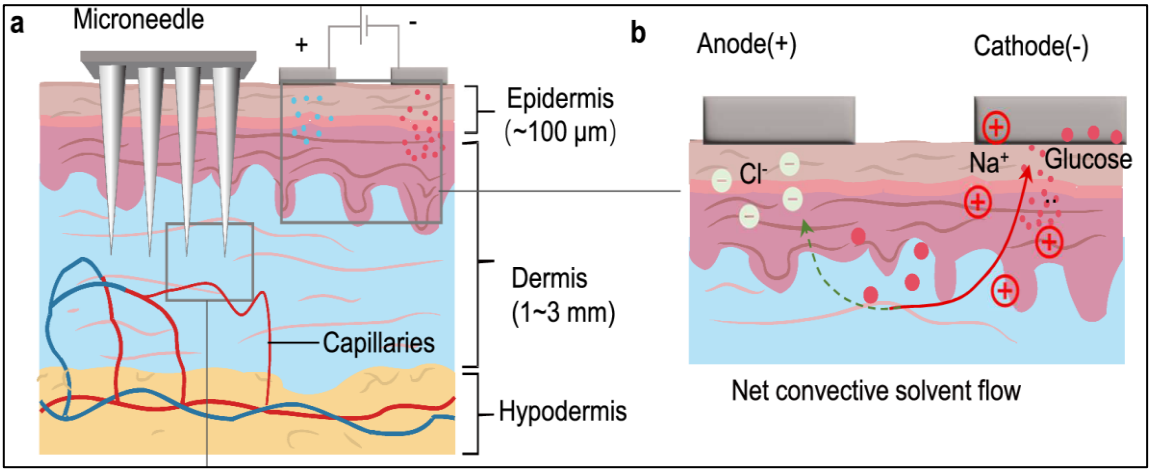

Figure 1.9: Schematic illustration of the **a)** skin structure, bioenvironment, and typical methods to access ISF, **b)** reverse iontophoresis-based ISF sampling method (Wu et al., 2024). Reproduced under the Creative Commons CC BY-NC 4.0 license.

b. Reverse iontophoresis (RI)

The RI method uses an electric voltage to drive positively charged ions through the epidermis, causing an electroosmotic flow to occur, which extract molecules from the skin **(Figure 1.8b)** (Moore, 2022). The RI approach is totally non-invasive because it doesn't involve epidermal penetration to obtain ISF, unlike microneedles that are utilised for ISF extraction (Zhu et al., 2023). RI was used in the commercially available GlucoWatch to provide continuous real-time glucose monitoring (Ma et al., 2022). However, following concerns about irritation from overuse of current, it was eventually taken off the market. By using a much lower current density, Bandodkar et al. addressed the earlier issues with their tattoo-based glucose sensor, which also used RI for ISF sampling (Bandodkar et al., 2015). They used a modified Prussian Blue transducer with glucose oxidase to enable selective amperometric biosensing with a reduced working. But it gathers biomarkers in a highly diluted way, which leads to the extraction of a lower level of biomarkers.

c. Microdialysis

An invasive method of obtaining ISF is called microdialysis, which involves inserting a catheter with a semipermeable membrane into the skin. The fluid in the membrane, which is later analysed externally, interacts with small analytes in the ISF. The device can remain in place for hours or even weeks, depending on what's required. However, the isoenzyme derived from microdialysis is often diluted five to ten times, rendering it less effective for biosensing in comparison to alternative methods (Korf et al., 2010).

1.7 Therapeutic and drug delivery applications of MIPs

As previously discussed, the importance of polymers in DDSs (**in section, 1.2.2**), this section focussed on the use of MIPs and nanoMIPs in the therapeutic deliveries of drugs and biopharmaceuticals. NanoMIPs offer several advantages such as low cost, easy preparation, non-toxic, biocompatible and multiple routes of administration (*e.g.,* oral or intravenous) making them an attractive alternative drug delivery carrier (He et al., 2021). One of the key benefits of nanoMIPs in targeted drug delivery as well as their ability to provide site-specific and controlled release of therapeutic agents. This can minimize off-target adverse effects and enhances the therapeutic index of drugs (Shevchenko et al., 2022). There are recent developments in MIP technology to use them in advanced therapeutic delivery in nanomedicine (Esfandyari-Manesh et al., 2016; Shevchenko et al., 2022). Recent studies have demonstrated the potential of nanoMIPs in the delivery of chemotherapeutic agents and immunotherapeutic agents (Suna et al., 2021). These advancements are crucial to improve the efficacy and safety of therapeutic agents, particularly in the treatment of chronic and complex diseases such as cancer (Puoci et al., 2011). In addition to cancer therapy, nanoMIPs have shown potential in treating a wide range of chronic diseases, including diabetes, atherosclerosis, and neurodegenerative disorders (Li and Zhaosheng, 2021).

In this context, Wu and colleagues (in 2015) reported the preparation and evaluation of amoxicillin sodium (AMX) loaded dual MIP NPs for anti-H. pylori therapy. MIPs were designed for targeting Lpp20 lipoproteins, a conserved outer membrane protein in all H. pylori strains, for AMX delivery. The NQA fragment of Lpp20 and AMX were co-imprinted using inverse microemulsion polymerisation. Batch rebinding tests showed a preferential affinity of NQA for the Dual-MIPs. *In vivo* fluorescence imaging revealed prolonged residence of these dual-MIPs in the stomach of H. pylori-infected mice after intragastric administration. H. pylori clearance tests demonstrated that dual-MIPs were more effective than bare AMX (Wu et al., 2015). This is the only report in which MIPs have been used for bacteria-targeting drug delivery. However, several subsequent reports have focused primarily on the application of MIPs for cancer-targeted drug delivery, as discussed below. A pH and thermosensitive magnetic imprinted NPs were developed for the targeted DOX delivery to cancer cells by Kaamyabi and colleagues (in 2016). They polymerised N-isopropylacrylamide with methacrylate functionalised Fe_3O_4 NPs in the

presence of DOX and formulations showed the controlled DOX release. Additionally, the developed NPs showed a lower critical solution temperature of 40 °C, which could be advantageous for cancer drug delivery. This is because the temperature of cancer cells is typically higher than that of healthy cells, allowing for selective release of DOX in cancerous tissues (Kaamyabi et al., 2016). The downside of this study is that the researchers performed only physicochemical and in vitro release studies; there was no evidence of targeted DOX delivery to cancer cells or tumours, either *in vitro* or *in vivo*. Kubo *et al.* (in 2018) reported a stimulus-responsive drug delivery system using Fe_3O_4 NPs coated with MIP layer via a polymerisation method for the effective release of methotrexate (MTX). The MIP-coated NPs exhibited superparamagnetic properties and selective MTX adsorption. At 60 °C, 80% of MTX was released due to hydrogen bond cleavage. MTX release under an AC magnetic field was successfully demonstrated within 10 minutes (Kubo et al., 2018).

DOX imprinted photoluminescent polymer on graphene quantum dots were designed by Javanbakht *et al.* (in 2020) as a pH-responsive nanocarrier, via the precipitation free-radical polymerisation strategy. DOX binding kinetics identified specific recognition sites in the photoluminescent MIP. *In vitro,* the nanocarriers released DOX in a pH-controlled, sustained manner and showed effective anticancer activity against A549 lung adenocarcinoma cell (Javanbakht et al., 2020). Peng *et al.* (in 2020) reported dual-template imprinting polymeric NPs with a core-shell structure, in which fluorescent silica NPs were the core and the imprinted polymer layers were formed the outer shell. These NPs also carrying gadolinium-doped silicon quantum dots and photosensitizers (Ce6). The imprinted layer was designed and constructed via free-radical precipitation approach on the surface of fluorescent silica NPs. During the polymerisation process, two template molecules *viz.* epitope of CD59 protein and antitumor agent were introduced into the monomer mixtures. The embedded Ce6 generates toxic $^1O_2$ under 655 nm laser irradiation to kill cancer cells, while the loaded DOX provides a synergistic (cytotoxic) effect. Additionally, the inclusion of gadolinium-doped silicon quantum dots, Ce6, and DOX enables targeted fluorescence and MR imaging. *In vitro* and *in vivo* experiments of this study demonstrated excellent targeting ability and effective treatment with minimal toxicity to healthy tissues and organs (Peng et al., 2020). Lu *et al.* developed (in 2021) novel drug delivery carrier for cytotoxic ribonuclease A (RNase A) using sialic acid (SA)-imprinted biodegradable silica NPs (BS-NPs). The matrix of disulfide-hybridised silica NPs

(encapsulation efficiency of ~64%) is encapsulated with RNase A and were further functionalised with cancer targeting capability via surface imprinting using SA template. These imprinted NPs selectively targeted the SA-overexpressed tumour cells, enhanced cellular uptake and led to increased cytotoxicity. Additionally, *in vivo* results showed the specific tumour-targeting ability and high therapeutic efficacy of RNase A in a xenograft tumour model with these NPs (Lu et al., 2021).

The hybrid core-shell systems were developed by Qin *et al.* where fluorescent NPs loaded with DOX were coated with MIPs to facilitate targeted drug delivery to cell-specific receptors on breast cancer (Qin et al., 2020). Manesh *et al,* developed PTX loaded polyethylene glycol (PEG)-FA MIPs (prepared using mini-emulsion polymerisation) for the targeted delivery to folate positive tumours. Researchers used two different cancer cell lines *viz*. MDA-MB-231 (folate positive) and A549 (folate negative) to screen the anticancer activity of PTX loaded PEG-FA MIPs. Moreover, PTX loaded PEG-FA-MIPs showed higher cytotoxicity to MDA-MB-231 cells as compared to MIP and PTX (Esfandyari-Manesh et al., 2016). Han and colleagues synthesised cancer antigen 125 (CA125) imprinted MIPs on the surface of graphene oxide for the delivery of DOX to liver cancer cells (Han et al., 2019). DOX loaded MIPs showed the higher cytotoxicity to SMMC-7721 (tumour cell line) as compared to HEK293 cells (normal cells). Furthermore, amygdalin (anticancer drug) imprinted nanoMIPs incubation (2 days) with MDA-MB-231 cells reduced the cell viability significantly as compared to amygdalin loaded non-imprinted NPs (Korde et al., 2019).

The double imprinted nanoMIPs were used by Canfarotta *et al.* (in 2018*)* for the first time where DOX drug delivery was explored to target membrane proteins EGFR in the cancer cells (Francesco Canfarotta et al., 2018b). Furthermore, Piletsky and colleagues reported different nanoMIPs against extracellular and intracellular epitopes of EGFR to target cancers expressing high levels of EGFR. Moreover, MIPs targeting the intracellular domain of EGFR showed the cytotoxicity towards EGFR positive cells, demonstrating the use of MIPs directly as therapeutic agents. Whilst double imprinting is a promising approach for the targeted drug delivery for water soluble drugs, complications might arise when using this system for the delivery of hydrophobic drugs that are not water-soluble. Therefore, hydrophobic drugs can be delivered using other polymer-based vehicles such as surface-active polymers.

1.8 Surface active copolymers for drug delivery applications

Surface-active polymers are made up of two distinct blocks of the polymers one is hydrophilic (water-attracting) and other is hydrophobic (water-repelling), which enable their surfactant properties. As they contain two or more different polymer, therefore, known as copolymers. These copolymers can alter surface and interfacial properties, which make them a centre of attraction for different applications, including emulsifiers, detergents, foaming agents, and dispersants in food and pharmaceutical industry.

Surface-active copolymers are divided into several classes, most used class is block-copolymers. These consist of distinct blocks of hydrophilic and hydrophobic segments. These blocks can be arranged in various ways such as AB (monomer A is hydrophilic, and B is hydrophobic) block copolymers, for example, polystyrene-b-polyethylene glycol and ABA (two hydrophilic blocks separated by a hydrophobic block) block copolymers, for example, polystyrene-b-polyethylene oxide-b-polystyrene (El Jundi et al., 2020; Karayianni and Pispas, 2021). Other classes of copolymers are graft copolymers (one type of polymer is grafted with side chains of another polymer type). The side chains can be hydrophilic or hydrophobic, leading to complex surface-active properties. For example, poly(methyl methacrylate)-g-polyethylene glycol (PMMA-g-PEG) (Neugebauer, 2007). Further classes of copolymers are random copolymers (randomly distributed hydrophilic and hydrophobic monomers) (L. Li et al., 2014), alternating copolymers (hydrophilic and hydrophobic monomers alternate in the polymer chain) and janus copolymers (two distinct regions with different chemical properties on the same polymer chain) (Guo et al., 2018; Huang and Turner, 2017).

Pluronics also known as Poloxamers is the most common commercially available example of ABA-type copolymers. These copolymers consist of polyethylene oxide (PEO) and polypropylene oxide (PPO) units arranged in a PEO-PPO-PEO structure (Xiong et al., 2012). They are made up of a group of over fifty amphiphilic, water-soluble molecules and the first letter of their name represents their physical state: L, P and F for liquid, paste, and flake, respectively as shown in **Figure 1.10** (Khimani et al., 2020).

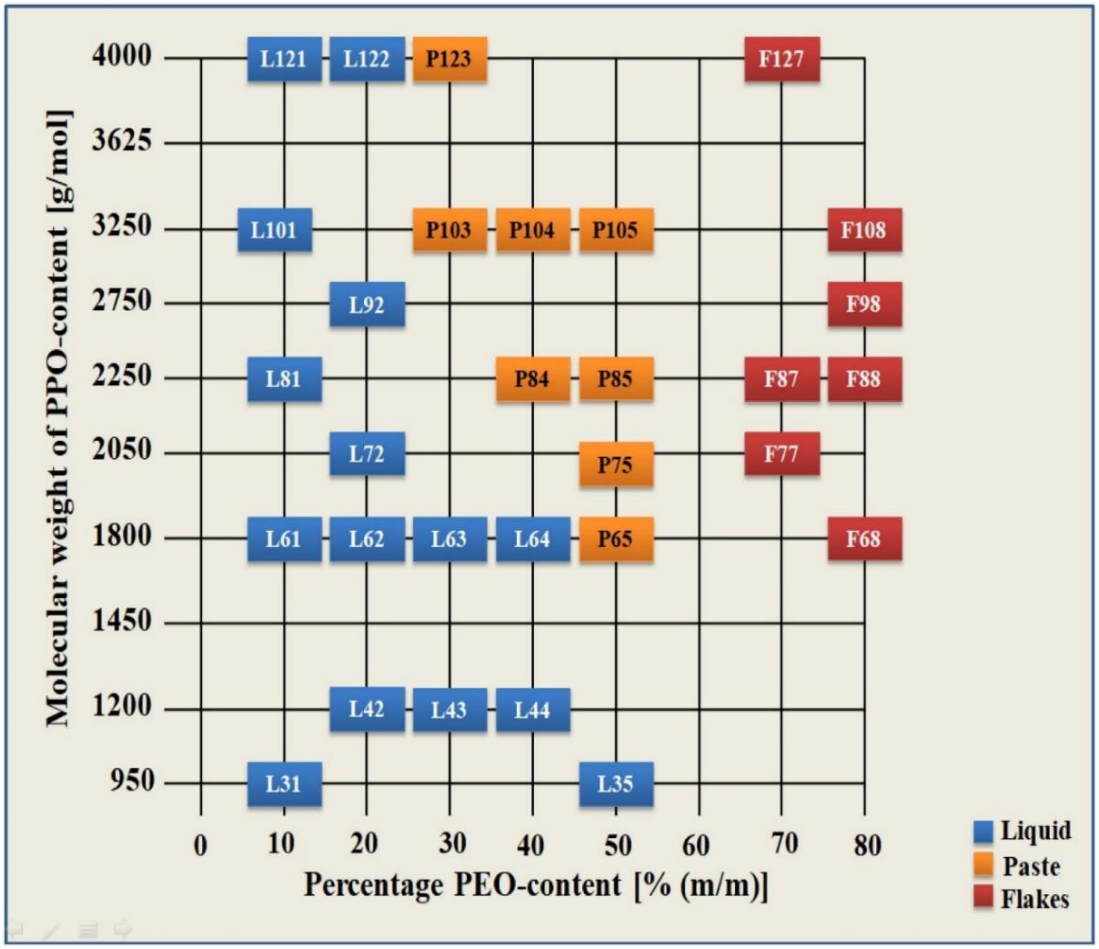

Figure1.10: Pluronic PEO-PPO-PEO copolymers arranged in the "Pluronic grid". The vertically aligned copolymers have the same PPO/PEO composition ratio, while the horizontal copolymers lines have PPO blocks of the same length (Singla et al., 2022b).

Pluronic solutions exhibit temperature-dependent self-assembly, with micellization being extensively studied in aqueous media. At low temperatures and concentrations, Pluronic molecules remain homogeneously dissolved. However, increasing temperature or concentration makes water a poor solvent for PPO moieties, prompting them to minimise unfavourable interactions by forming micellar aggregates. In these structures, the hydrophobic PPO segments form the core, while the hydrophilic PEO segments occupy the shell (as illustrated in **Figure 1.11**). The hydrophilic PEO and hydrophobic PPO blocks of Pluronic polymers enable the formation of micelles at or above the critical micelle concentration (*cmc*) and critical micelle temperature (*cmt*) (Raval et al., 2017). This process is dynamic, reversible, and highly endothermic. Water molecules bend and break hydrogen bonds to accommodate Pluronic unimers (Di Spirito et al., 2024c). As unimers associate into micelles, water molecules regain freedom, increasing system entropy.

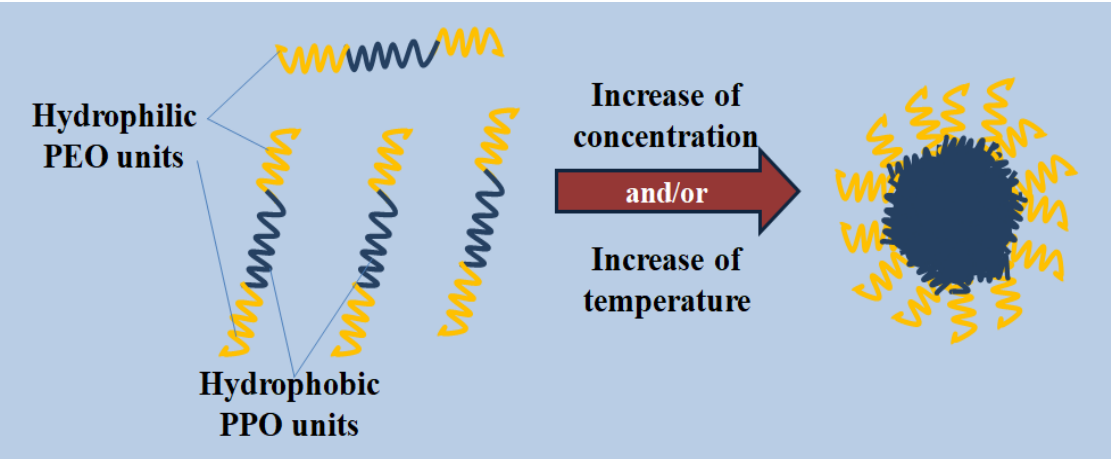

Figure 1.11: Schematic of Pluronic Micelle Formation in Aqueous Medium: A diagram depicting the micellization of Pluronic, where unimers arrange into micellar aggregates once the temperature exceeds the critical micellar temperature (*cmt*) and the concentration surpasses the critical micellar concentration (*cmc*).

Despite the positive enthalpy of micellization, the entropy contribution dominates, resulting in a negative Gibbs free energy, ensuring spontaneous micelle formation (Pitto-Barry and Barry, 2014). Consequently, Pluronic micellization is an entropically driven process with an endothermic enthalpy. The resulting Pluronic structures have broad applications, including hydrophobic drug encapsulation and controlled delivery in aqueous environments (Di Spirito et al., 2024a; Marin et al., 2002). Notably, *cmt* and *cmc* values vary with Pluronic type, solvent, temperature, and concentrations. The critical packing parameter of the amphiphilic unimer dictates the morphology of the resulting aggregates. This parameter depends on the molecular structure, including the volume and length of the hydrophobic chain and the area of the polar block (Israelachvili et al., 1976). In addition to micellar aggregates, Pluronic water solutions at sufficiently high concentrations and temperatures can spontaneously form thermodynamically stable, long-lasting supramolecular structures. These structures exhibit a diverse polymorphism in solution, encompassing not only micellar aggregates of various shapes but also hexagonal phases, lamellar structures, and crystalline lattices. The phase boundaries between different structural forms are typically investigated experimentally by constructing equilibrium phase diagrams as a function of temperature and concentration (Alexandridis et al., 1996).

1.8.1 Pluronics in the Presence of External Additives

Pluronic-based nanotechnology is rapidly expanding, gaining significant interest across various technological and biomedical fields, including drug delivery, cosmetics, and

nanomedicine (Di Spirito et al., 2024c; Figueiras et al., 2022). For instance, Pluronics serve as supportive vehicles for the storage, protection, and controlled release of drug molecules, acting as stable, long-lasting depots capable of retaining large drug quantities (Di Spirito et al., 2023). Other approaches focus on the functionalisation of Pluronic systems to improve their physicochemical properties and overcome limitations such as rapid dissolution, weak mechanical strength, and short residence time in biological environments (de Freitas et al., 2023). While unmodified Pluronic solutions are often effective for various applications, functionalization can be essential in certain cases to enhance stability, prolong efficacy, and introduce stimuli-responsive properties. To this end, Pluronics have been functionalised with a diverse range of external additives, including drugs, nanoparticles, metals, pH-sensitive moieties, antibodies, and conductive materials. Such modifications impart novel properties, transforming Pluronic-based systems into stimuli-responsive and active platforms. Numerous studies have explored the potential of functionalised Pluronics for applications such as tumor targeting, drug delivery, antimicrobial activity, hydrogel enhancement, and the development of sensitive, responsive systems **(Figure 1.12)** (Li et al., 2020; Liang et al., 2015).

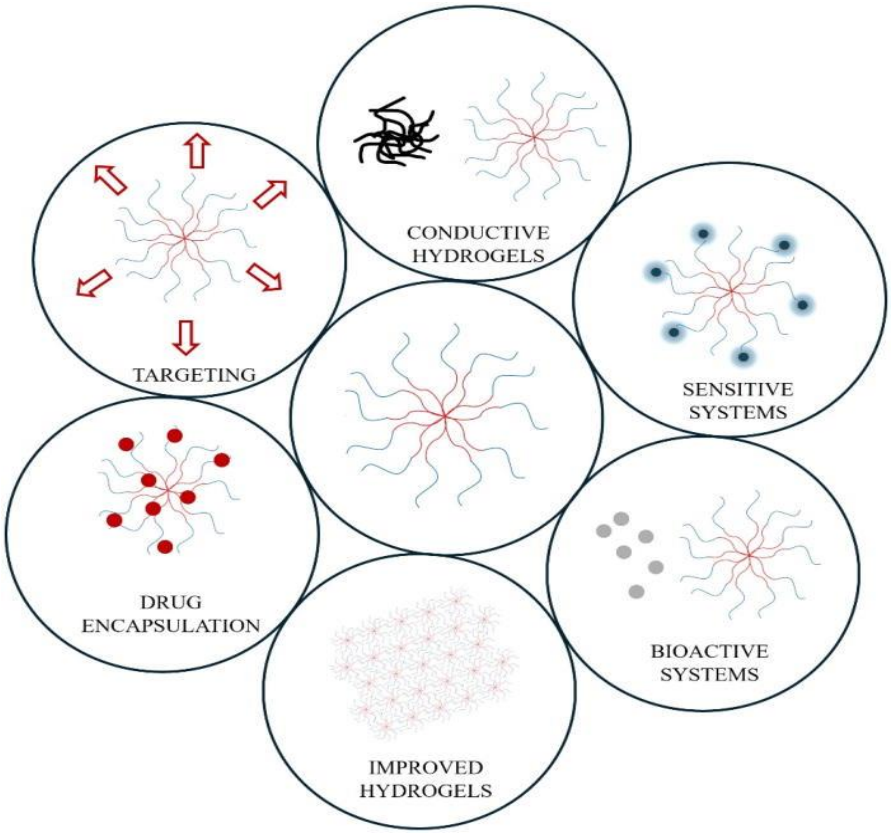

Figure 1.12: Examples of functionalisation strategies of Pluronics (Di Spirito et al., 2024c). Adapted with permission from AIP Publishing, Copyright 2025 (5992470240635).

Pluronic-based systems are highly sensitive to the addition of external additives, which can significantly affect their phase transitions and supramolecular structures. The ionic strength and pH of the surrounding environment can influence the behavior of Pluronic solutions when external additives, such as salts, are introduced. Generally, the absence of ionizable molecules within the Pluronic solution leads to a lower sensitivity to pH changes, except in extremely alkaline or acidic conditions (Foster et al., 2009; Park et al., 2007). In contrast, the introduction of ionizable molecules into Pluronic solutions seems to enhance the system's responsiveness to pH variations .

Barım *et al.* demonstrated that combining hydrated lithium salts with Pluronics results in the formation of lyotropic liquid crystalline mesophases, which are influenced by the salt concentration (Barım et al., 2014). Lopez-Barron and colleagues investigated the self-assembly of an end-functionalized Pluronic, featuring acrylic end groups, in a protic ionic liquid (López-Barrón et al., 2016). They discovered that cross-linking the polymer imparts conductivity to the gel-like material. Furthermore, the release of diclofenac sodium, an anti-inflammatory drug, from Pluronic F68 hydrogels was studied, revealing that high drug concentrations disrupt the ability of the Pluronic solution to undergo any liquid-to-solid phase transition, affecting both macroscopic and microscopic properties **(Figure 1.13)** (López-Barrón et al., 2016).

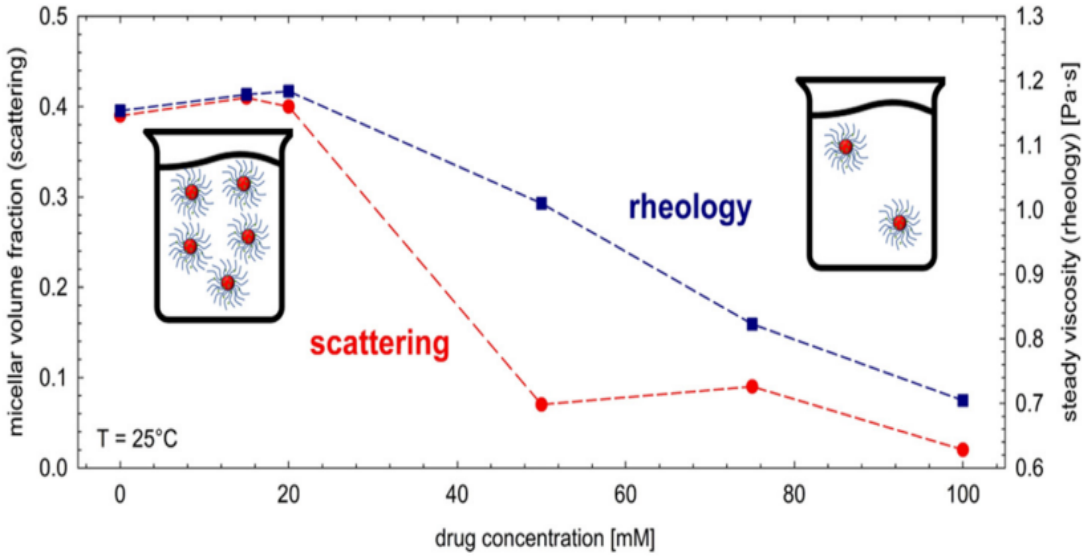

Figure. 1.13: Inhibition of Pluronic micellization due to high drug concentration. Reproduced under Creative Commons Attribution (CC BY) license (Di Spirito et al., 2024b).

Covalent functionalization of Pluronics is another critical strategy, where Pluronic molecules are used as initiators in polymerization processes. Additionally, a growing trend in chemical modification of Pluronics aims to overcome the common limitations of high *cmc*, low stability, and weak mechanical strength of physically cross-linked hydrogels (Xiong et al., 2006). Bromberg *et al.* copolymerized Pluronics with poly(acrylic acid) (PAA), enhancing the strength of the resulting hydrogels by cross-linking the PAA chains with the Pluronic polymer (Bromberg, 1998). Xiong and colleagues developed novel block copolymers by grafting poly(lactic acid) (PLA) onto the ends of Pluronic F127, and their aggregation behavior revealed that these copolymers could form bi-layer or onion-like vesicles (Xiong et al., 2003). Furthermore, Pluronic F68 was modified by reacting it with chloroacetyl chloride and then treating the modified polymer with triethylamine, triphenyl phosphine, and tributyl phosphine (Kenawy et al., 2023). This modification introduced quaternary ammonium and phosphonium salts into the polymer chain, resulting in environmentally friendly and antimicrobial materials.

Pluronics have several advantages such as high surface-activity, high loading capacity, low-toxicity, low immunogenicity with excellent biocompatibility and biodegradability over conventional block copolymers (Kabanov and Alakhov, 2002; Singla et al., 2022b). Pluronics can act as efficient drug delivery vehicles due to their intrinsic property to accommodate drugs both in the core (formed by PPO block) and corona (formed by PEO block) region, as well as preventing degradation of drugs in biological media. Additionally, the PEO (hydrophilic region) increase the circulation time in the body by providing steric stability (Singla et al., 2019b; Wang et al., 2016).

Pluronics are typically regarded as inert carriers for drug delivery applications, but they can function as biological response modifier and increase the transport of drugs across tissues, into cells, blood brain and intestinal barriers. For instance, Pluronics can sensitise multidrug resistance cancer cells by inhibiting drug efflux proteins, multiple resistant proteins and alter the micro-viscosity through their incorporation into the membrane (Batrakova et al., 2001; J. Yu et al., 2021). Pluronic-based nanotechnology is rapidly growing and highly promising area in the pharmaceutical research. The properties of Pluronics such as size, structure and adsorption make them suitable for use in a broad range of applications such as drug delivery, cosmetics, emulsion formulations and NPs synthesis (Singla et al., 2018a; Torcello-Gomez et al., 2013). Some of the Pluronics are

FDA approved for the drug delivery excipients. Pluronic formulations for different applications are in clinical trials and some are already in market (Singla et al., 2018a). For instance, Pluronic F127 mixed system with hyaluronic acid and chondroitin sulphate (trade name ZIVEREL®) is in clinical trials for the treatment of esophagitis induced by radiotherapy in cancer patients (de Castro et al., 2023). Mediclore, an anti-adhesive hydrogel formulation consisting of Pluronic and chitosan, is already on the market (Kang et al., 2023). These ongoing clinical trials and marketed formulations indicate that Pluronics hold great potential as commercially viable and efficient drug delivery vehicle.

1.8.2 Pluronic micelles as DDSs

Pluronic-based nanotechnology is rapidly growing and one of the most attractive fields of pharmaceutical research. Pluronics possess various properties such as size, biodegradability, adsorption properties and structure which make them ideal for wide array of applications such as drug delivery, sensing, cosmetics, emulsion formulations, hydrogels, and NPs synthesis **(Figure 1.14)** (de Castro et al., 2023; Singla et al., 2018a; Torcello-Gomez et al., 2013).

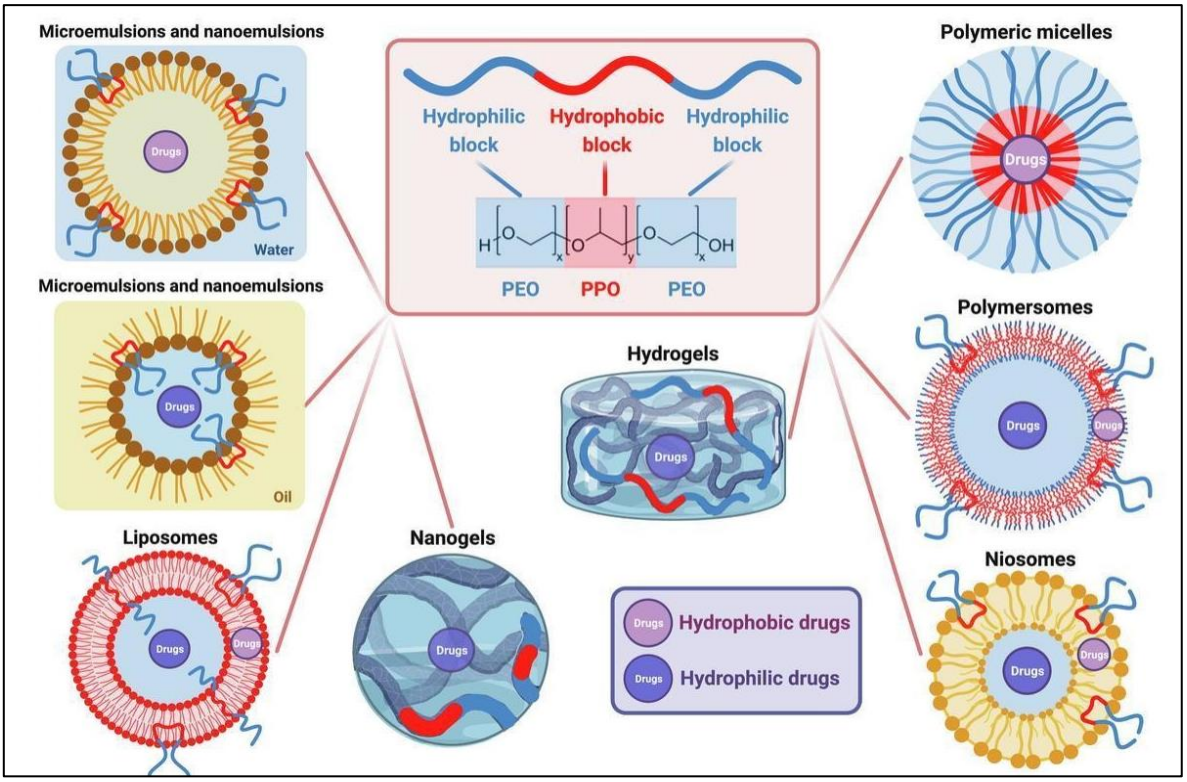

Figure 1.14: Pluronics (surface active copolymer) based nano-formulations for therapeutic/drug delivery applications (de Castro et al., 2023).

In the past two decades, extensive research has been carried out to explore the drug delivery applications of these Pluronics for various therapeutic and hydrophobic molecules (Singla et al., 2023c) **(Figure 1.15)**. For instance, the curcumin loading, its interaction and photophysical properties in the Pluronic (P123 and F127) micelles were investigated by various characterisation techniques. It was observed that curcumin encapsulated in Pluronic micelles exhibited a significantly lower hydrolytic degradation rate compared to the aqueous system (Ghosh et al., 2014). Similarly, Alexander *et al.* reported the different Pluronic (P103, P123, and L43) micelles for the solubilisation of poorly water soluble flurbiprofen drug. The results observed that Pluronic P123 was able to solubilise more drug as compared to other Pluronics investigated in this study (Alexander et al., 2011). In another study, the solubilisation of poorly water-soluble oxcarbazepine was explored in Pluronics F108, F127, and P84 and higher solubilisation capacity was observed with Pluronic P84 than F108 and F127 (Singla et al., 2016).

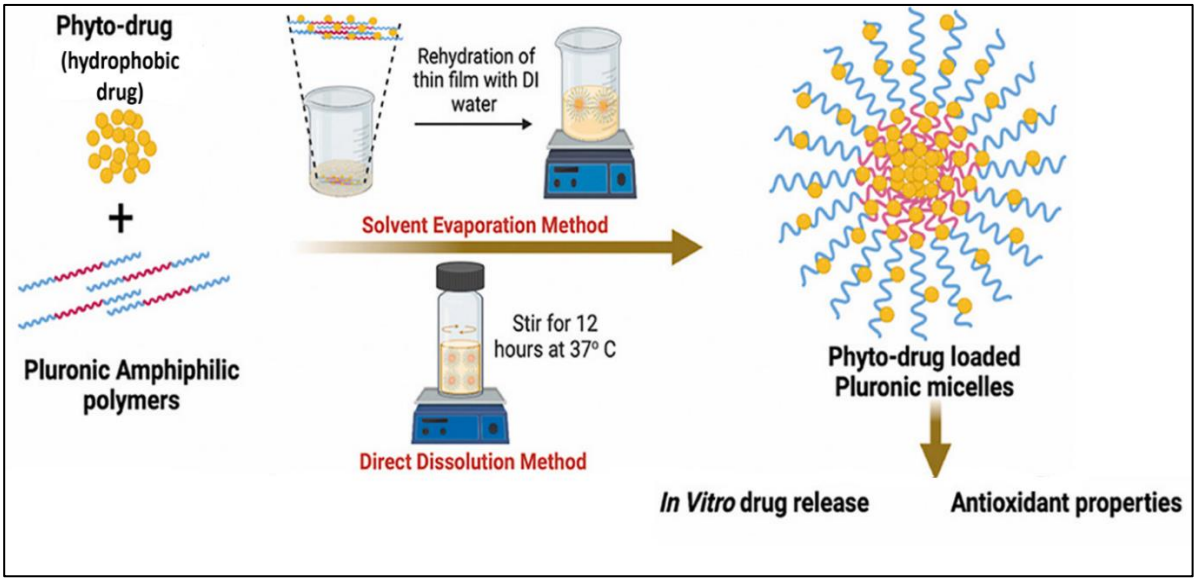

Figure 1.15: Pluronic based formulation for the solubilisation of poorly water soluble phyto-drug to improve the drug release and antioxidant properties (Singla et al., 2023c).

Additionally, researchers are conjugating targeting moieties such as Abs, aptamers, folic acid (FA) with Pluronics, to modulate its properties and targeted drug delivery applications. As an example, Liu *et al.*, loaded the natural polyphenolic anticancer drug resveratrol in Pluronic F127-SS-α-tocopherol polymeric micelles (Y. Liu et al., 2017).

Resveratrol loaded Pluronic micelles showed significantly higher cytotoxicity in breast cancer (BC) cells (MCF-7 and MDA-MB-231) compared to free resveratrol. Wang *et al.* conjugated FA with Pluronic P105/L101 for the targeted drug delivery of Paclitaxel (PTX), as folate receptors are overexpressed in several cancers (Wang et al., 2007). In MCF-7/ADR human breast cancer cells, the uptake of FA-conjugated P105/L101 micellar PTX was nearly 3 times higher than that of PTX loaded in pure P105/L101 micelles. Additionally, a significant reduction in PTX's IC_{50} (inhibitory concentration) in multidrug-resistant (MDR) cells was observed compared to free PTX, demonstrating greater cytotoxicity and increased susceptibility of MDR cells to Pluronic micellar PTX. Song *et al.* targeted stomach cancer cells using PTX loaded Pluronic P123 micelles conjugated with an anti-HIF-1α Ab, showing significant cytotoxicity to MGC-803 stomach cancer cells while sparing normal cells (Song et al., 2010). For targeting MCF-7/ADR breast cancer cells, CD44 Abs were conjugated to dendrimer-Pluronic P123 for delivering anti-MDR1 shRNA-encoding plasmid DNA (Gu et al., 2015). Similarly, anti-GPC3 Ab-functionalised Pluronic NPs were used for targeted sorafenib delivery in HepG2 human liver cells (Gan et al., 2018). Andrade *et al.* developed niclosamide loaded Pluronic F127 micelles functionalised with CD44v6 Abs, which enhanced internalisation in CD44v6+ colorectal cancer stem cells. *In vivo* studies showed a reduction in circulating tumour cells following administration of these functionalised micelles (Andrade et al., 2021).

Jindal *et al.* explored the loading behaviour of the drug nevirapine in mixed micelles of poloxamer 407 and Pluronic P123, concluding that these mixed micellar formulations demonstrate high entrapment efficiency and sustained release behaviour *in vitro* (Jindal and Mehta, 2015). In other study, Pluronic F68 coupled with linoleic acid were used for the delivery of anticancer drug brusatol to different cancer cell lines (J. Zhang et al., 2018). Dash and colleagues also investigated mixed micelles composed of Pluronic F108 and Pluronic L81 for the solubilisation of ciprofloxacin using various techniques. A significantly higher solubility of ciprofloxacin was observed in the mixed Pluronic micelles compared to the pure Pluronic micelles (Senthilkumar et al., 2019). Zhang *et al.* observed increased drug loading capacity and enhanced anti-cancer activity in Pluronic P123-F127 mixed micelles loaded with PTX (Zhang et al., 2010). Similarly, Singla *et al.* documented improved solubilisation of hydrophobic drugs like clozapine and oxcarbazepine in mixed micelles of low and high molecular weight Pluronics (Singla et al., 2020). The combination

of standard Pluronic with reverse Pluronic 10R5 has been reported to stabilize micelles and reduce the critical micelle concentration (*cmc*). For example, Naskar *et al.* investigated the solution behaviour of a binary mixture of Pluronic L44 and 10R5, suggesting that this combination could serve as a template for nanoparticle synthesis.

It is well documented in the literature that mixed surfactant or micellar formulations of Pluronics with ionic liquids (salt in the liquid state at ambient conditions) such as surface-active ionic liquids (SAILs) and other additives like reverse Pluronics and bile salts exhibit synergistic effects. This results in the improved surface activity and lower *cmc* values compared to single Pluronic micelles. Additionally, mixed micelles provide significant advantages, such as enhanced thermodynamic and kinetic stability, along with higher drug-loading capacities (Jindal and Mehta, 2015). In this context, Vashishat *et al.* investigated the solubilisation of the poorly water-soluble drug phenothiazine in mixed micellar media composed of SAILs and bile salts. The solubility of phenothiazine in these mixed micelles was found to be dependent on the micelles' hydrophobicity and size. Similarly, Singla et al., also studied the solubilisation of quercetin in Pluronic F108 and SAILs mixed micelles. UV-visible spectroscopy revealed that the F108-SAIL mixed micellar system had a higher solubilisation capacity for quercetin, with improved solubility, loading efficiency, and partition coefficient compared to F108 alone (Singla et al., 2018b).

1.9 Aim and objectives

As thoroughly discussed, the healthcare burden of NCDs and the importance of timely diagnosis as well as treatment in the healthcare, this thesis aims to develop the novel polymeric platforms for the point of care sensor, targeted drug delivery therapeutics and drug delivery carriers for the hydrophobic drugs. The straightforward and low-cost approach, ease of synthesis, robust nature and high stability makes MIPs an attractive alternative for developing sensors and efficient drug delivery carriers. There is a gap in the literature regarding the use of electroactive imprinted polymers for direct biomarker detection. Additionally, dual-functional, double-imprinted nanoMIPs targeting new molecules like BC for imaging and targeted delivery have yet to be reported. Despite their advantages, these nanoMIPs are limited to hydrophilic drug delivery, highlighting the need for alternatives to deliver hydrophobic drugs and nutraceuticals. The use of hydrophobic drugs or nutraceuticals is often restricted due to their poor water solubility and, consequently, their low bioavailability. To address these challenges, Pluronic copolymers

that are easy to fabricate without sophisticated techniques, can be effectively used for the delivery of hydrophobic drugs. Therefore, this research work focussed to find out the more sustainable, affordable healthcare solutions, which can impact and inspire the research in these imprinted and surface-active polymers. Therefore, in the light of the aim of developing novel point of care sensor and drug delivery carriers using polymers the main objectives of this research are:

Objective 1: Design and synthesis of eMIPs for the detection of glucose, which serves as a model compound for sensing of small molecules with eMIPs. eMIPs-based sensor will be developed for the electrochemical detection of glucose in clinical diabetic samples and artificial interstitial fluid, thus demonstrating its intended application in wearable sensors.

Objective 2: Examination of the development of high affinity nanoMIPs against the full protein structure of lysozyme, as most of the biomarkers are proteins and lysozyme is a well-known model protein compound. Furthermore, these nanoMIPs will be utilised for the impedimetric and thermal detection of lysozyme.

Objective 3: To investigate the dual functionality of nanoMIPs using a double imprinting approach, which can facilitate specific detection of cell proteins and subsequent localised drug delivery. As proof-of-concept, nanoMIPs will be develop for the targeted drug delivery of anticancer drug doxorubicin (DOX) to the estrogen receptor alpha (ERα) that is commonly overexpressed in breast cancer. This study will demonstrate that it is possible to target nuclear receptors with nanoMIPs and showcase their working in “patient-like” environment, which includes sophisticated 3D cancer models.

Objective 4: To optimise drug delivery vehicles for hydrophobic drugs via employing pure Pluronic (surface active copolymers) formulations as well as mixed micelles containing Pluronics and reverse Pluronics. As proof-of-concept, drug delivery will be demonstrated with the natural agent silymarin naringenin and baicalein.

1.10 References

(WHO), W. H. O. (2024a). *Communicable and noncommunicable diseases, and mental health*: WHO. Available at: https://www.who.int/our-work/communicable-and-noncommunicable-diseases-and-mental-health.

(WHO), W. H. O. (2024b). *World cancer day 2024*: WHO. Available at: https://www.emro.who.int/media/news/world-cancer-day-2024.html.

Abbott (2024). *Freestyle libre 3*. Available at: https://www.abbott.com/corpnewsroom/strategy-and-strength/freeStyle-libre-3-worlds-smallest-sensor-is-here.html.

Acosta-Patino, J., Jimenez-Balderas, E., Juarez-Oropeza, M. & Dıaz-Zagoya, J. (2001). 'Hypoglycemic action of cucurbita ficifolia on type 2 diabetic patients with moderately high blood glucose levels' *Journal of Ethnopharmacology*, 77 (1), pp. 99-101.

Aitken, M., et al. (2014). 'Global outlook for medicines through 2018' *IMS Institute for Healthcare Informatics*, 100.

Aldawood, F. K., Andar, A. & Desai, S. (2021). 'A comprehensive review of microneedles: Types, materials, processes, characterizations and applications' *Polymers*, 13 (16), p. 2815.

Alexander, S., Cosgrove, T., Prescott, S. W. & Castle, T. C. (2011). 'Flurbiprofen encapsulation using pluronic triblock copolymers' *Langmuir*, 27 (13), pp. 8054-8060.

Alexandridis, P., Zhou, D. & Khan, A. (1996). 'Lyotropic liquid crystallinity in amphiphilic block copolymers: Temperature effects on phase behavior and structure for poly (ethylene oxide)-b-poly (propylene oxide)-b-poly (ethylene oxide) copolymers of different composition' *Langmuir*, 12 (11), pp. 2690-2700.

Altintas, Z., et al. (2016). 'Ultrasensitive detection of endotoxins using computationally designed nanomips' *Analytica Chimica Acta*, 935 pp. 239-248.

Altintas, Z., et al. (2015). 'Detection of waterborne viruses using high affinity molecularly imprinted polymers' *Analytical chemistry*, 87 (13), pp. 6801-6807.

Anami, Y., et al. (2022). 'Homogeneity of antibody-drug conjugates critically impacts the therapeutic efficacy in brain tumors' *Cell reports*, 39 (8).

Andaç, M., et al. (2007). 'Ion-imprinted beads for molecular recognition based mercury removal from human serum' *International Journal of Biological Macromolecules*, 40 (2), pp. 159-166.

Andrade, F., et al. (2021). 'Polymeric micelles targeted against cd44v6 receptor increase niclosamide efficacy against colorectal cancer stem cells and reduce circulating tumor cells in vivo' *Journal of Controlled Release*, 331 pp. 198-212.

Annabi, N., et al. (2014). '25th anniversary article: Rational design and applications of hydrogels in regenerative medicine' *Advanced materials*, 26 (1), pp. 85-124.

Ansell, R. J. & Mosbach, K. (1997). 'Molecularly imprinted polymers by suspension polymerisation in perfluorocarbon liquids, with emphasis on the influence of the porogenic solvent' *Journal of Chromatography A*, 787 (1-2), pp. 55-66.

Atassi, M. Z. (1984). 'Antigenic structures of proteins: Their determination has revealed important aspects of immune recognition and generated strategies for synthetic mimicking of protein binding sites' *European journal of biochemistry*, 145 (1), pp. 1-20.

Bahrami, B., et al. (2017). 'Nanoparticles and targeted drug delivery in cancer therapy' *Immunology letters*, 190 pp. 64-83.

Bandodkar, A. J., et al. (2015). 'Tattoo-based noninvasive glucose monitoring: A proof-of-concept study' *Analytical chemistry*, 87 (1), pp. 394-398.

Barım, G. z., Albayrak, C., Yılmaz, E. & Dag, O. m. (2014). 'Highly conducting lyotropic liquid crystalline mesophases of pluronics (p65, p85, p103, and p123) and hydrated lithium salts (licl and lino3)' *Langmuir*, 30 (23), pp. 6938-6945.

Batrakova, E., et al. (2001). 'Mechanism of sensitization of mdr cancer cells by pluronic block copolymers: Selective energy depletion' *British journal of cancer*, 85 (12), pp. 1987-1997.

BBC (2024). *Non-communicable diseases - different types of diseases*: BBC. Available at: https://www.bbc.co.uk/bitesize/guides/z8pcsrd/revision/1#:~:text=types%20of%20diseases-,Diseases,measles%2C%20food%20poisoning%20and%20malaria.

Begines, B., et al. (2020). 'Polymeric nanoparticles for drug delivery: Recent developments and future prospects' *Nanomaterials*, 10 (7), p. 1403.

BelBruno, J. J. (2018). 'Molecularly imprinted polymers' *Chemical reviews*, 119 (1), pp. 94-119.

Bhilare, N. V., Shedge, R., Tambe, P. M. & More, A. (2024). 'Unveiling the potential of prodrug and drug-conjugate strategies in treatment of diabetes mellitus and its complications' *Medicinal Chemistry Research*, 33 (3), pp. 337-353.

Bodoki, A. E., Iacob, B.-C. & Bodoki, E. (2019). 'Perspectives of molecularly imprinted polymer-based drug delivery systems in cancer therapy' *Polymers*, 11 (12), p. 2085.

Boonpangrak, S., et al. (2006). 'Preparation of molecularly imprinted polymers using nitroxide-mediated living radical polymerization' *Biosensors and Bioelectronics*, 22 (3), pp. 349-354.

Borandeh, S., van Bochove, B., Teotia, A. & Seppälä, J. (2021). 'Polymeric drug delivery systems by additive manufacturing' *Advanced drug delivery reviews*, 173 pp. 349-373.

Bray, F., et al. (2024). 'Global cancer statistics 2022: Globocan estimates of incidence and mortality worldwide for 36 cancers in 185 countries' *CA: a cancer journal for clinicians*, 74 (3), pp. 229-263.

Bromberg, L. (1998). 'Novel family of thermogelling materials via c− c bonding between poly (acrylic acid) and poly (ethylene oxide)-b-poly (propylene oxide)-b-poly (ethylene oxide)' *The Journal of Physical Chemistry B*, 102 (11), pp. 1956-1963.

Brunton, L., Chabner, B. & Knollmann, B. (2011). Goodman and gilman's the pharmacological basis of therapeutics. Twelfth. New York, NY: McGraw-Hill.

Camps, J. & García-Heredia, A. (2014). 'Introduction: Oxidation and inflammation, a molecular link between non-communicable diseases' *Oxidative Stress and Inflammation in Non-communicable Diseases-Molecular Mechanisms and Perspectives in Therapeutics*, pp. 1-4.

Canfarotta, F., Cecchini, A. & Piletsky, S. (2018). 'Nano-sized molecularly imprinted polymers as artificial antibodies'.

Canfarotta, F., et al. (2018). 'Specific drug delivery to cancer cells with double-imprinted nanoparticles against epidermal growth factor receptor' *Nano letters*, 18 (8), pp. 4641-4646.

Canfarotta, F., Poma, A., Guerreiro, A. & Piletsky, S. (2016). 'Solid-phase synthesis of molecularly imprinted nanoparticles' *Nature protocols*, 11 (3), pp. 443-455.

Capek, I. (2010). 'On inverse miniemulsion polymerization of conventional water-soluble monomers' *Advances in colloid and interface science*, 156 (1-2), pp. 35-61.

CARE, N. I. F. H. A. & (NICE), E. (2021). *Trastuzumab deruxtecan for treating her2-positive unresectable or metastatic breast cancer after 2 or more anti-her2 therapies*: NICE. Available at: https://www.nice.org.uk/guidance/ta704/documents/final-appraisal-determination-document#:~:text=2.3%20The%20company's%20list%20price,company%20has%20a%20commercial%20arrangement.

Chan, J. M., et al. (2010). 'Polymeric nanoparticles for drug delivery' *Cancer nanotechnology: Methods and protocols*, pp. 163-175.

Chandra, P. (2023). 'Personalized biosensors for point-of-care diagnostics: From bench to bedside applications' *Nanotheranostics*, 7 (2), p. 210.

Chang, H., et al. (2017). 'A swellable microneedle patch to rapidly extract skin interstitial fluid for timely metabolic analysis' *Advanced Materials*, 29 (37), p. 1702243.

Chaudhary, A., et al. (2012). 'Enhancement of solubilization and bioavailability of poorly soluble drugs by physical and chemical modifications: A recent review' *Journal of Advanced Pharmacy Education and Research*, 2 (1-2012), pp. 32-67.

Chen, W.-H., et al. (2022). 'Biomedical polymers: Synthesis, properties, and applications' *Science China Chemistry*, 65 (6), pp. 1010-1075.

Chiefari, J., et al. (1998). 'Living free-radical polymerization by reversible addition-fragmentation chain transfer: The raft process' *Macromolecules*, 31 (16), p. 5559.

Chiefari, J., et al. (2003). 'Thiocarbonylthio compounds (sc (z) s− r) in free radical polymerization with reversible addition-fragmentation chain transfer (raft polymerization). Effect of the activating group z' *Macromolecules*, 36 (7), pp. 2273-2283.

Chong, Y., et al. (2003). 'Thiocarbonylthio compounds [sc (ph) s− r] in free radical polymerization with reversible addition-fragmentation chain transfer (raft polymerization). Role of the free-radical leaving group (r)' *Macromolecules*, 36 (7), pp. 2256-2272.

Coimbra, M., et al. (2011). 'Improving solubility and chemical stability of natural compounds for medicinal use by incorporation into liposomes' *International journal of pharmaceutics*, 416 (2), pp. 433-442.

ColoAlert (2024). *The colorectal cancer screening test that takes a closer look*. Available at: https://www.coloalert.com/.

D'Antona, S., Porro, D., Gallivanone, F. & Bertoli, G. (2024). 'Characterization of cell cycle, inflammation, and oxidative stress signaling role in non-communicable diseases: Insights into genetic variants, micrornas and pathways' *Computers in Biology and Medicine*, 174 p. 108346.

Dang, T. T., Nikkhah, M., Memic, A. & Khademhosseini, A. (2014). 'Polymeric biomaterials for implantable prostheses', *Natural and synthetic biomedical polymers*: Elsevier, pp. 309-331.

de Castro, K. C., et al. (2023). 'Pluronic® triblock copolymer-based nanoformulations for cancer therapy: A 10-year overview' *Journal of Controlled Release*, 353 pp. 802-822.

de Freitas, C. F., et al. (2023). 'Recent advances of pluronic-based copolymers functionalization in biomedical applications' *Biomaterials Advances*, 151 p. 213484.

Di Lena, F. & Matyjaszewski, K. (2010). 'Transition metal catalysts for controlled radical polymerization' *Progress in Polymer Science*, 35 (8), pp. 959-1021.

Di Spirito, N. A., et al. (2024a). 'Drug release from pluronic f68 hydrogels' *Physics of Fluids*, 36 (3).

Di Spirito, N. A., et al. (2023). 'Phase transitions of aqueous solutions of pluronic f68 in the presence of diclofenac sodium' *International Journal of Pharmaceutics*, 644 p. 123353.

Di Spirito, N. A., et al. (2024b). 'Pluronic f68 micelles as carriers for an anti-inflammatory drug: A rheological and scattering investigation' *Langmuir*, 40 (2), pp. 1544-1554.

Di Spirito, N. A., Grizzuti, N. & Pasquino, R. (2024c). 'Self-assembly of pluronics: A critical review and relevant applications' *Physics of Fluids*, 36 (11).

Dickey, F. H. (1949). 'The preparation of specific adsorbents' *Proceedings of the national academy of sciences*, 35 (5), pp. 227-229.

Ding, L., et al. (2024). 'Polymer-based drug delivery systems for cancer therapeutics' *Polymers*, 16 (6), p. 843.

Dong, C., et al. (2021). 'Molecularly imprinted polymers by the surface imprinting technique' *European Polymer Journal*, 145 p. 110231.

Drago, J. Z., Modi, S. & Chandarlapaty, S. (2021). 'Unlocking the potential of antibody–drug conjugates for cancer therapy' *Nature Reviews Clinical Oncology*, 18 (6), pp. 327-344.

El-Schich, Z., et al. (2020). 'Molecularly imprinted polymers in biological applications' *Biotechniques*, 69 (6), pp. 406-419.

El Jundi, A., et al. (2020). 'Double hydrophilic block copolymers self-assemblies in biomedical applications' *Advances in colloid and interface science*, 283 p. 102213.

Ertürk, G. & Mattiasson, B. (2017). 'Molecular imprinting techniques used for the preparation of biosensors' *Sensors*, 17 (2), p. 288.

Esfandyari-Manesh, M., et al. (2016). 'Paclitaxel molecularly imprinted polymer-peg-folate nanoparticles for targeting anticancer delivery: Characterization and cellular cytotoxicity' *Materials science and engineering: C*, 62 pp. 626-633.

Ezike, T. C., et al. (2023). 'Advances in drug delivery systems, challenges and future directions' *Heliyon*, 9 (6).

Figueiras, A., et al. (2022). 'New advances in biomedical application of polymeric micelles' *Pharmaceutics*, 14 (8), p. 1700.

Foster, B., Cosgrove, T. & Espidel, Y. (2009). 'Pfgse-nmr study of ph-triggered behavior in pluronic− ibuprofen solutions' *Langmuir*, 25 (12), pp. 6767-6771.

Frank, R. & Hargreaves, R. (2003). 'Clinical biomarkers in drug discovery and development' *Nature reviews Drug discovery*, 2 (7), pp. 566-580.

Friedel, M., et al. (2023). 'Opportunities and challenges in the diagnostic utility of dermal interstitial fluid' *Nature Biomedical Engineering*, 7 (12), pp. 1541-1555.

Gan, H., et al. (2018). 'Enhanced delivery of sorafenib with anti-gpc3 antibody-conjugated tpgs-b-pcl/pluronic p123 polymeric nanoparticles for targeted therapy of hepatocellular carcinoma' *Materials Science and Engineering: C*, 91 pp. 395-403.

Gandhi, K. J., Deshmane, S. V. & Biyani, K. R. (2012). 'Polymers in pharmaceutical drug delivery system: A review' *Int J Pharm Sci Rev Res*, 14 (2), pp. 57-66.

Gao, G., et al. (2022). 'Porous microneedles for therapy and diagnosis: Fabrication and challenges' *ACS Biomaterials Science & Engineering*, 9 (1), pp. 85-105.

Gao, W., et al. (2019). 'Flexible electronics toward wearable sensing' *Accounts of chemical research*, 52 (3), pp. 523-533.

Gavas, S., Quazi, S. & Karpiński, T. M. (2021). 'Nanoparticles for cancer therapy: Current progress and challenges' *Nanoscale research letters*, 16 (1), p. 173.

Gayathry, G., Komath, M. & Velayudhan, S. (2022). 'Biomaterials for medical products', *Biomedical product and materials evaluation*: Elsevier, pp. 25-62.

GhavamiNejad, P., et al. (2023). 'A conductive hydrogel microneedle-based assay integrating pedot: Pss and ag-pt nanoparticles for real-time, enzyme-less, and electrochemical sensing of glucose' *Advanced Healthcare Materials*, 12 (1), p. 2202362.

Ghosh, S., et al. (2014). 'Organic additive, 5-methylsalicylic acid induces spontaneous structural transformation of aqueous pluronic triblock copolymer solution: A spectroscopic investigation of interaction of curcumin with pluronic micellar and vesicular aggregates' *The Journal of Physical Chemistry B*, 118 (39), pp. 11437-11448.

Gkika, D. A., et al. (2024). 'Application of molecularly imprinted polymers (mips) as environmental separation tools' *RSC Applied Polymers*, 2 (2), pp. 127-148.

Gregory, A. & Stenzel, M. H. (2011). 'The use of reversible addition fragmentation chain transfer polymerization for drug delivery systems' *Expert opinion on drug delivery*, 8 (2), pp. 237-269.

Gu, J., Fang, X., Hao, J. & Sha, X. (2015). 'Reversal of p-glycoprotein-mediated multidrug resistance by cd44 antibody-targeted nanocomplexes for short hairpin rna-encoding plasmid DNA delivery' *Biomaterials*, 45 pp. 99-114.

Guo, Z. H., et al. (2018). 'Janus graft block copolymers: Design of a polymer architecture for independently tuned nanostructures and polymer properties' *Angewandte Chemie International Edition*, 57 (28), pp. 8493-8497.

Han, S., et al. (2019). 'A molecularly imprinted composite based on graphene oxide for targeted drug delivery to tumor cells' *Journal of materials science*, 54 (4), pp. 3331-3341.

Harding, J. L., et al. (2019). 'Global trends in diabetes complications: A review of current evidence' *Diabetologia*, 62 pp. 3-16.

He, S., et al. (2021). 'Advances of molecularly imprinted polymers (mip) and the application in drug delivery' *European Polymer Journal*, 143 p. 110179.

He, Y. & Lin, Z. (2022). 'Recent advances in protein-imprinted polymers: Synthesis, applications and challenges' *Journal of Materials Chemistry B*, 10 (35), pp. 6571-6589.

Healthline (2024a). *The 10 best glucose meters and continuous glucose monitors of 2024*: Healthline. Available at: https://www.healthline.com/health/diabetes/best-glucose-monitors#1.

Healthline (2024b). *A 2024 review of the dexcom g6 vs. Abbott freestyle libre: How do these cgms compare?*: Healthline. Available at: https://www.healthline.com/diabetesmine/dexcom-vs-abbott-freestyle-libre-cgm-function-accuracy-and-cost.

Huang, J. & Turner, S. R. (2017). 'Recent advances in alternating copolymers: The synthesis, modification, and applications of precision polymers' *Polymer*, 116 pp. 572-586.

Hughes, M. & Fatoyinbo, H. (2012). 'Biosensors', *Encyclopedia of nanotechnology*: Springer.

Inzucchi, S. E. (2012). 'Diagnosis of diabetes' *New England Journal of Medicine*, 367 (6), pp. 542-550.

Islam, S. M. S., et al. (2014). 'Non-communicable diseases (ncds) in developing countries: A symposium report' *Globalization and health*, 10 pp. 1-8.

Israelachvili, J. N., Mitchell, D. J. & Ninham, B. W. (1976). 'Theory of self-assembly of hydrocarbon amphiphiles into micelles and bilayers' *Journal of the Chemical Society, Faraday Transactions 2: Molecular and Chemical Physics*, 72 pp. 1525-1568.

Jain, K. K. (2020). 'An overview of drug delivery systems' *Drug delivery systems*, pp. 1-54.

Javanbakht, S., et al. (2020). 'Doxorubicin imprinted photoluminescent polymer as a ph-responsive nanocarrier' *ACS Applied Bio Materials*, 3 (7), pp. 4168-4178.

Jenkins, A., Kratochvíl, P., Stepto, R. & Suter, U. (1996). 'Glossary of basic terms in polymer science (iupac recommendations 1996)' *Pure and applied chemistry*, 68 (12), pp. 2287-2311.

Jindal, N. & Mehta, S. (2015). 'Nevirapine loaded poloxamer 407/pluronic p123 mixed micelles: Optimization of formulation and in vitro evaluation' *Colloids and Surfaces B: Biointerfaces*, 129 pp. 100-106.

Jones, C. H. & Dolsten, M. (2024). 'Healthcare on the brink: Navigating the challenges of an aging society in the united states' *npj Aging*, 10 (1), p. 22.

Kaamyabi, S., Habibi, D. & Amini, M. M. (2016). 'Preparation and characterization of the ph and thermosensitive magnetic molecular imprinted nanoparticle polymer for the cancer drug delivery' *Bioorganic & medicinal chemistry letters*, 26 (9), pp. 2349-2354.

Kabanov, A. V. & Alakhov, V. Y. (2002). 'Pluronic® block copolymers in drug delivery: From micellar nanocontainers to biological response modifiers' *Critical Reviews™ in Therapeutic Drug Carrier Systems*, 19 (1).

Kalita, N., Gogoi, S., Minteer, S. D. & Goswami, P. (2023). 'Advances in bioelectrode design for developing electrochemical biosensors' *ACS Measurement Science Au*, 3 (6), pp. 404-433.

Kang, S. I., et al. (2023). 'Double-layer adhesives for preventing anastomotic leakage and reducing post-surgical adhesion' *Materials Today Bio*, 23 p. 100806.

Karayianni, M. & Pispas, S. (2021). 'Block copolymer solution self-assembly: Recent advances, emerging trends, and applications' *Journal of Polymer Science*, 59 (17), pp. 1874-1898.

Kenawy, E.-R., Abdelhady, S. & Azaam, M. M. (2023). 'Chemical modification, electrospinning and biological activities of pluronic f68' *Polymer Bulletin*, 80 (5), pp. 5725-5740.

Khalid, M. & El-Sawy, H. S. (2017). 'Polymeric nanoparticles: Promising platform for drug delivery' *International journal of pharmaceutics*, 528 (1-2), pp. 675-691.

Khan, A. R., Hussain, W. L., Shum, H. C. & Hassan, S. U. (2024). 'Point-of-care testing: A critical analysis of the market and future trends' *Frontiers in Lab on a Chip Technologies*, 3 p. 1394752.

Khimani, M., et al. (2020). 'Self-assembly of stimuli-responsive block copolymers in aqueous solutions: An overview' *Polymer Bulletin*, 77 pp. 5783-5810.

Kim, J., Campbell, A. S., de Ávila, B. E.-F. & Wang, J. (2019). 'Wearable biosensors for healthcare monitoring' *Nature biotechnology*, 37 (4), pp. 389-406.

Kim, J., et al. (2015). 'Wearable salivary uric acid mouthguard biosensor with integrated wireless electronics' *Biosensors and Bioelectronics*, 74 pp. 1061-1068.

Kim, J., et al. (2017). 'Wearable smart sensor systems integrated on soft contact lenses for wireless ocular diagnostics' *Nature communications*, 8 (1), p. 14997.

Korde, B. A., Mankar, J. S., Phule, S. & Krupadam, R. J. (2019). 'Nanoporous imprinted polymers (nanomips) for controlled release of cancer drug' *Materials science and engineering: C*, 99 pp. 222-230.

Korf, J., Huinink, K. D. & Posthuma-Trumpie, G. A. (2010). 'Ultraslow microdialysis and microfiltration for in-line, on-line and off-line monitoring' *Trends in biotechnology*, 28 (3), pp. 150-158.

Kouki, S., et al. (2022). 'The enhanced adsorption properties of molecular imprinted polymer material prepared using nitroxide-mediated radical deactivation reversible polymerization' *Polymer*, 249 p. 124841.

Kubo, T., et al. (2018). 'Magnetic field stimuli-sensitive drug release using a magnetic thermal seed coated with thermal-responsive molecularly imprinted polymer' *ACS Biomaterials Science & Engineering*, 5 (2), pp. 759-767.

Kwaśniewska, K., Gadzała-Kopciuch, R. & Buszewski, B. (2015). 'Magnetic molecular imprinted polymers as a tool for isolation and purification of biological samples' *Open Chemistry*, 13 (1), p. 000010151520150137.

Le, T.-H., Kim, Y. & Yoon, H. (2017). 'Electrical and electrochemical properties of conducting polymers' *Polymers*, 9 (4), p. 150.

Li, L., et al. (2014). 'Self-assembly of random copolymers' *Chemical communications*, 50 (88), pp. 13417-13432.

Li, M. & Zhaosheng, L. (2021). 'Mip as drug delivery systems for special application' pp. 179-200. DOI: 10.1007/978-981-16-0227-6_9 Available at: https://consensus.app/papers/drug-delivery-systems-special-application-ma/fd793133646a558da7b6b576d86a67da/.

Li, P., et al. (2020). 'Dual responsive oligo (lysine)-modified pluronic f127 hydrogels for drug release of 5-fluorouracil' *RSC advances*, 10 (41), pp. 24507-24514.

Li, P., Rong, F. & Yuan, C. (2003). 'Morphologies and binding characteristics of molecularly imprinted polymers prepared by precipitation polymerization' *Polymer international*, 52 (12), pp. 1799-1806.

Li, X., et al. (2021). 'A fully integrated closed-loop system based on mesoporous microneedles-iontophoresis for diabetes treatment' *Advanced Science*, 8 (16), p. 2100827.

Liang, Y., Su, Z., Yao, Y. & Zhang, N. (2015). 'Preparation of ph sensitive pluronic-docetaxel conjugate micelles to balance the stability and controlled release issues' *Materials*, 8 (2), pp. 379-391.

Liu, B., et al. (2024). 'Exploring treatment options in cancer: Tumor treatment strategies' *Signal Transduction and Targeted Therapy*, 9 (1), p. 175.

Liu, R., et al. (2017). 'Preparation of sialic acid-imprinted fluorescent conjugated nanoparticles and their application for targeted cancer cell imaging' *ACS applied materials & interfaces*, 9 (3), pp. 3006-3015.

Liu, X., et al. (2007). 'Uniform-sized molecularly imprinted polymer for metsulfuron-methyl by one-step swelling and polymerization method' *Talanta*, 71 (3), pp. 1205-1210.

Liu, Y., et al. (2017). 'Preparation, characterization and anticancer activities of resveratrol loaded redox-sensitive f127-ss-toc micelles' *RSC advances*, 7 (74), pp. 47091-47098.

Liu, Y., et al. (2021). 'Continuous monitoring of diabetes with an integrated microneedle biosensing device through 3d printing' *Microsystems & Nanoengineering*, 7 (1), p. 75.

López-Barrón, C. R., Chen, R., Wagner, N. J. & Beltramo, P. J. (2016). 'Self-assembly of pluronic f127 diacrylate in ethylammonium nitrate: Structure, rheology, and ionic conductivity before and after photo-cross-linking' *Macromolecules*, 49 (14), pp. 5179-5189.

Lowdon, J. W., et al. (2020). 'Mips for commercial application in low-cost sensors and assays–an overview of the current status quo' *Sensors and Actuators B: Chemical*, 325 p. 128973.

Lu, H., et al. (2021). 'Redox-responsive molecularly imprinted nanoparticles for targeted intracellular delivery of protein toward cancer therapy' *ACS nano*, 15 (11), pp. 18214-18225.

Ma, R., et al. (2022). 'Recent advancements in noninvasive glucose monitoring and closed-loop management systems for diabetes' *Journal of Materials Chemistry B*, 10 (29), pp. 5537-5555.

Mandal, A., et al. (2018). 'Cell and fluid sampling microneedle patches for monitoring skin-resident immunity' *Science translational medicine*, 10 (467), p. eaar2227.

Manzari, M. T., et al. (2021). 'Targeted drug delivery strategies for precision medicines' *Nature Reviews Materials*, 6 (4), pp. 351-370.

Marin, A., et al. (2002). 'Drug delivery in pluronic micelles: Effect of high-frequency ultrasound on drug release from micelles and intracellular uptake' *Journal of Controlled Release*, 84 (1-2), pp. 39-47.

Matyjaszewski, K. (2012a). 'Atom transfer radical polymerization (atrp): Current status and future perspectives' *Macromolecules*, 45 (10), pp. 4015-4039.

Matyjaszewski, K. (2012b). 'Fundamentals of controlled/living radical polymerization' *Encyclopedia of Radicals in Chemistry, Biology and Materials*.

Mishra, R. K., et al. (2020). 'Continuous opioid monitoring along with nerve agents on a wearable microneedle sensor array' *Journal of the American Chemical Society*, 142 (13), pp. 5991-5995.

Mitchell, M. J., et al. (2021). 'Engineering precision nanoparticles for drug delivery' *Nature reviews drug discovery*, 20 (2), pp. 101-124.

Moad, G., et al. (2000). 'Living free radical polymerization with reversible addition–fragmentation chain transfer (the life of raft)' *Polymer International*, 49 (9), pp. 993-1001.

Mohajeri, S. A., Karimi, G., Aghamohammadian, J. & Khansari, M. R. (2011). 'Clozapine recognition via molecularly imprinted polymers; bulk polymerization versus precipitation method' *Journal of Applied Polymer Science*, 121 (6), pp. 3590-3595.

Mohan, S., Khunti, K. & Prabhakaran, D. (2023). 'Principles for the prevention and control of non-communicable disease' *Nature Medicine*, 29 (7), pp. 1598-1600.

Mondal, S., Zehra, N., Choudhury, A. & Iyer, P. K. (2020). 'Wearable sensing devices for point of care diagnostics' *ACS Applied Bio Materials*, 4 (1), pp. 47-70.

Moore, K. (2022). 'Novel applications of reverse iontophoresis'.

Morales, M. A. & Halpern, J. M. (2018). 'Guide to selecting a biorecognition element for biosensors' *Bioconjugate chemistry*, 29 (10), pp. 3231-3239.

Muka, T., et al. (2015). 'The global impact of non-communicable diseases on healthcare spending and national income: A systematic review' *European journal of epidemiology*, 30 pp. 251-277.

Nakamura, Y., et al. (2017). 'Preparation of molecularly imprinted polymers for warfarin and coumachlor by multi-step swelling and polymerization method and their imprinting effects' *Journal of Chromatography A*, 1516 pp. 71-78.

Namsheer, K. & Rout, C. S. (2021). 'Conducting polymers: A comprehensive review on recent advances in synthesis, properties and applications' *RSC advances*, 11 (10), pp. 5659-5697.

Negut, I. & Bita, B. (2023). 'Polymeric micellar systems—a special emphasis on "smart" drug delivery' *Pharmaceutics*, 15 (3), p. 976.

Neugebauer, D. (2007). 'Graft copolymers with poly (ethylene oxide) segments' *Polymer International*, 56 (12), pp. 1469-1498.

Nguyen, M.-H., et al. (2024). 'Electrochemical degradation of molecularly imprinted polymers for future applications of inflammation sensing in cochlear implants' *ACS omega*.

Oktay, M., Gülçin, İ. & Küfrevioğlu, Ö. İ. (2003). 'Determination of in vitro antioxidant activity of fennel (foeniculum vulgare) seed extracts' *LWT-Food Science and Technology*, 36 (2), pp. 263-271.

Olansky, L. & Kennedy, L. (2010). Finger-stick glucose monitoring: Issues of accuracy and specificity. Am Diabetes Assoc.

Omotayo, O., et al. (2024). 'The rise of non-communicable diseases: A global health review of challenges and prevention strategies' *International Medical Science Research Journal*, 4 (1), pp. 74-88.

Organization, W. H. (2023). *Noncommunicable diseases*: WHO. Available at: https://www.who.int/news-room/fact-sheets/detail/noncommunicable-diseases.

Otsu, T. & Yoshida, M. (1982). 'Role of initiator-transfer agent-terminator (iniferter) in radical polymerizations: Polymer design by organic disulfides as iniferters' *Die Makromolekulare Chemie, Rapid Communications*, 3 (2), pp. 127-132.

Panagiotopoulou, M., et al. (2015). 'Initiator-free synthesis of molecularly imprinted polymers by polymerization of self-initiated monomers' *Polymer*, 66 pp. 43-51.

Parihar, A., et al. (2020). 'Point-of-care biosensor-based diagnosis of covid-19 holds promise to combat current and future pandemics' *ACS applied bio materials*, 3 (11), pp. 7326-7343.

Park, S. Y., et al. (2007). 'Temperature/ph-sensitive hydrogels prepared from pluronic copolymers end-capped with carboxylic acid groups via an oligolactide spacer' *Macromolecular rapid communications*, 28 (10), pp. 1172-1176.

Parrilla, M., Cuartero, M. & Crespo, G. A. (2019). 'Wearable potentiometric ion sensors' *TrAC Trends in Analytical Chemistry*, 110 pp. 303-320.

Pasquardini, L. & Bossi, A. M. (2021). 'Molecularly imprinted polymers by epitope imprinting: A journey from molecular interactions to the available bioinformatics resources to scout for epitope templates' *Analytical and Bioanalytical Chemistry*, 413 (24), pp. 6101-6115.

Peng, H., et al. (2020). 'Epitope molecularly imprinted polymer nanoparticles for chemo-/photodynamic synergistic cancer therapy guided by targeted fluorescence imaging' *ACS applied materials & interfaces*, 12 (11), pp. 13360-13370.

Pillai, O. & Panchagnula, R. (2001). 'Polymers in drug delivery' *Current opinion in chemical biology*, 5 (4), pp. 447-451.

Pitto-Barry, A. & Barry, N. P. (2014). 'Pluronic® block-copolymers in medicine: From chemical and biological versatility to rationalisation and clinical advances' *Polymer Chemistry*, 5 (10), pp. 3291-3297.

Polanski, M. & Anderson, N. L. (2006). 'A list of candidate cancer biomarkers for targeted proteomics' *Biomarker insights*, 1 p. 117727190600100001.

Polyakov, M. (1931). 'Adsorption properties and structure of silica gel' *Zhur Fiz Khim*, 2 pp. 799-805.

Poma, A., et al. (2013). 'Solid-phase synthesis of molecularly imprinted polymer nanoparticles with a reusable template–"plastic antibodies"' *Advanced functional materials*, 23 (22), pp. 2821-2827.

Poma, A., Turner, A. P. & Piletsky, S. A. (2010). 'Advances in the manufacture of mip nanoparticles' *Trends in biotechnology*, 28 (12), pp. 629-637.

Prasad, M., et al. (2018). 'Nanotherapeutics: An insight into healthcare and multi-dimensional applications in medical sector of the modern world' *Biomedicine & Pharmacotherapy*, 97 pp. 1521-1537.

Puoci, F., et al. (2011). 'Molecularly imprinted polymers in drug delivery: State of art and future perspectives' *Expert Opinion on Drug Delivery*, 8 pp. 1379-1393. DOI: 10.1517/17425247.2011.609166 Available at: https://consensus.app/papers/molecularly-polymers-drug-delivery-state-future-puoci/8751a3b373d656fba5de872d8ed18ee8/.

Qazi, S. & Raza, K. (2020). 'Smart biosensors for an efficient point of care (poc) health management', *Smart biosensors in medical care*: Elsevier, pp. 65-85.

Qin, Y.-T., et al. (2020). 'Tumor-sensitive biodegradable nanoparticles of molecularly imprinted polymer-stabilized fluorescent zeolitic imidazolate framework-8 for targeted imaging and drug delivery' *ACS applied materials & interfaces*, 12 (22), pp. 24585-24598.

Rachkov, A. & Minoura, N. (2001). 'Towards molecularly imprinted polymers selective to peptides and proteins. The epitope approach' *Biochimica et Biophysica Acta (BBA)-Protein Structure and Molecular Enzymology*, 1544 (1-2), pp. 255-266.

Raval, A., Pillai, S. A., Bahadur, A. & Bahadur, P. (2017). 'Systematic characterization of pluronic® micelles and their application for solubilization and in vitro release of

some hydrophobic anticancer drugs' *Journal of Molecular Liquids*, 230 pp. 473-481.

Refaat, D., et al. (2019). 'Strategies for molecular imprinting and the evolution of mip nanoparticles as plastic antibodies—synthesis and applications' *International journal of molecular sciences*, 20 (24), p. 6304.

Samant, P. P., et al. (2020). 'Sampling interstitial fluid from human skin using a microneedle patch' *Science translational medicine*, 12 (571), p. eaaw0285.

Sang, M., et al. (2023). 'Fluorescent-based biodegradable microneedle sensor array for tether-free continuous glucose monitoring with smartphone application' *Science advances*, 9 (22), p. eadh1765.

Satchanska, G., Davidova, S. & Petrov, P. D. (2024). 'Natural and synthetic polymers for biomedical and environmental applications' *Polymers*, 16 (8), p. 1159.

Senthilkumar, M., Sheelarani, B., Joshi, R. & Dash, S. (2019). 'Solubilization and interaction of ciprofloxacin with pluronics and their mixed micelles' *New Journal of Chemistry*, 43 (42), pp. 16530-16537.

Sharma, A., Badea, M., Tiwari, S. & Marty, J. L. (2021). 'Wearable biosensors: An alternative and practical approach in healthcare and disease monitoring' *Molecules*, 26 (3), p. 748.

Sharma, A., Singh, A., Gupta, V. & Arya, S. (2022). 'Advancements and future prospects of wearable sensing technology for healthcare applications' *Sensors & Diagnostics*, 1 (3), pp. 387-404.

Shelton, J. R., Lando, J. B. & Agostini, D. E. (1971). 'Synthesis and characterization of poly (β-hydroxybutyrate)' *Journal of Polymer Science Part B: Polymer Letters*, 9 (3), pp. 173-178.

Shevchenko, K., et al. (2022). 'Nano-molecularly imprinted polymers (nanomips) as a novel approach to targeted drug delivery in nanomedicine' *RSC Advances*, 12 pp. 3957-3968. DOI: 10.1039/d1ra08385f Available at: https://consensus.app/papers/nanomolecularly-polymers-nanomips-approach-targeted-shevchenko/75c63e3dff65579688c198363ac2de23/.

Silindir Gunay, M., Yekta Ozer, A. & Chalon, S. (2016). 'Drug delivery systems for imaging and therapy of parkinson's disease' *Current neuropharmacology*, 14 (4), pp. 376-391.

Singla, P., et al. (2024). 'Double imprinted nanoparticles for sequential membrane-to-nuclear drug delivery' *Advanced Science*, p. 2309976.

Singla, P., Chabba, S. & Mahajan, R. K. (2016). 'A systematic physicochemical investigation on solubilization and in vitro release of poorly water soluble oxcarbazepine drug in pluronic micelles' *Colloids and Surfaces A: Physicochemical and Engineering Aspects*, 504 pp. 479-488.

Singla, P., et al. (2020). 'Solubilization of hydrophobic drugs clozapine and oxcarbazepine in the lower and higher molecular weight pluronic mixed micelles-a physicochemical, in vitro release and in vitro anti-oxidant study' *Journal of Molecular Liquids*, 317 p. 113816.

Singla, P., et al. (2022). 'Advances in the therapeutic delivery and applications of functionalized pluronics: A critical review' *Advances in Colloid and Interface Science*, 299 p. 102563.

Singla, P., et al. (2023a). 'Electrochemical and thermal detection of allergenic substance lysozyme with molecularly imprinted nanoparticles' *Analytical and bioanalytical chemistry*, 415 (18), pp. 4467-4478.

Singla, P., et al. (2023b). 'Enhancing encapsulation of hydrophobic phyto-drugs naringenin and baicalein in polymeric nano-micelles' *Journal of Drug Delivery Science and Technology*, 83 p. 104403.

Singla, P., et al. (2018a). 'Sodium deoxycholate mediated enhanced solubilization and stability of hydrophobic drug clozapine in pluronic micelles' *Spectrochimica Acta Part A: Molecular and Biomolecular Spectroscopy*, 191 pp. 143-154.

Singla, P., Singh, O., Chabba, S. & Mahajan, R. K. (2018b). 'Pluronic-sails (surface active ionic liquids) mixed micelles as efficient hydrophobic quercetin drug carriers' *Journal of Molecular Liquids*, 249 pp. 294-303.

Singla, P., et al. (2019). 'Temperature-dependent solubilization of the hydrophobic antiepileptic drug lamotrigine in different pluronic micelles—a spectroscopic, heat transfer method, small-angle neutron scattering, dynamic light scattering, and in vitro release study' *ACS omega*, 4 (6), pp. 11251-11262.

Slomkowski, S., et al. (2011). 'Terminology of polymers and polymerization processes in dispersed systems (iupac recommendations 2011)' *Pure and Applied Chemistry*, 83 (12), pp. 2229-2259.

Song, H., et al. (2010). 'Anti-hif-1α antibody-conjugated pluronic triblock copolymers encapsulated with paclitaxel for tumor targeting therapy' *Biomaterials*, 31 (8), pp. 2302-2312.

Srinivas, S. & Kale, D. (2023). 'New approaches to learning and regulation in medical devices and diagnostics: Insights from indian cancer care' *Innovation and Development*, 13 (2), pp. 361-384.

Suna, H., et al. (2021). 'Advances of molecularly imprinted polymers (mip) and the application in drug delivery' *European Polymer Journal*, 143 p. 110179. DOI: 10.1016/j.eurpolymj.2020.110179 Available at: https://consensus.app/papers/advances-molecularly-imprinted-polymers-drug-delivery-he/bce3da55598050afbdd17026a16afaa1/.

Sung, Y. K. & Kim, S. W. (2020). 'Recent advances in polymeric drug delivery systems' *Biomaterials Research*, 24 (1), p. 12.

Takagishi, T. & Klotz, I. M. (1972). 'Macromolecule-small molecule interactions; introduction of additional binding sites in polyethyleneimine by disulfide cross–linkages' *Biopolymers: Original Research on Biomolecules*, 11 (2), pp. 483-491.

Tan, C. J. & Tong, Y. W. (2007). 'Molecularly imprinted beads by surface imprinting' *Analytical and bioanalytical chemistry*, 389 pp. 369-376.

Tchekwagep, P. M. S., et al. (2022). 'A critical review on the use of molecular imprinting for trace heavy metal and micropollutant detection' *Chemosensors*, 10 (8), p. 296.

Tehrani, F., et al. (2022). 'An integrated wearable microneedle array for the continuous monitoring of multiple biomarkers in interstitial fluid' *Nature Biomedical Engineering*, 6 (11), pp. 1214-1224.

Teixeira, S. P., et al. (2021). 'Epitope-imprinted polymers: Design principles of synthetic binding partners for natural biomacromolecules' *Science Advances*, 7 (44), p. eabi9884.

Tian, H., et al. (2012). 'Biodegradable synthetic polymers: Preparation, functionalization and biomedical application' *Progress in Polymer Science*, 37 (2), pp. 237-280.

Tibbitt, M. W., Dahlman, J. E. & Langer, R. (2016). 'Emerging frontiers in drug delivery' *Journal of the American Chemical Society*, 138 (3), pp. 704-717.

Tokonami, S., Shiigi, H. & Nagaoka, T. (2009). 'Micro-and nanosized molecularly imprinted polymers for high-throughput analytical applications' *Analytica chimica acta*, 641 (1-2), pp. 7-13.

Torcello-Gomez, A., Maldonado-Valderrama, J., Jódar-Reyes, A. B. n. & Foster, T. J. (2013). 'Interactions between pluronics (f127 and f68) and bile salts (natdc) in the aqueous phase and the interface of oil-in-water emulsions' *Langmuir*, 29 (8), pp. 2520-2529.

Turiel, E., Tadeo, J., Cormack, P. & Martin-Esteban, A. (2005). 'Hplc imprinted-stationary phase prepared by precipitation polymerisation for the determination of thiabendazole in fruit' *Analyst*, 130 (12), pp. 1601-1607.

Uhrich, K. E., Cannizzaro, S. M., Langer, R. S. & Shakesheff, K. M. (1999). 'Polymeric systems for controlled drug release' *Chemical reviews*, 99 (11), pp. 3181-3198.

Vaihinger, D., et al. (2002). 'Molecularly imprinted polymer nanospheres as synthetic affinity receptors obtained by miniemulsion polymerisation' *Macromolecular Chemistry and Physics*, 203 (13), pp. 1965-1973.

Van Herk, A. M. & Monteiro, M. (2002). 'Heterogeneous systems' *Handbook of radical polymerization*, pp. 301-331.

van Hoogevest, P., Liu, X. & Fahr, A. (2011). 'Drug delivery strategies for poorly water-soluble drugs: The industrial perspective' *Expert opinion on drug delivery*, 8 (11), pp. 1481-1500.

Vaneckova, T., et al. (2020). 'Application of molecularly imprinted polymers as artificial receptors for imaging' *Acta Biomaterialia*, 101 pp. 444-458.

Venton, B. J. & DiScenza, D. J. (2020). 'Voltammetry' *Electrochemistry for Bioanalysis*, pp. 27-50.

Wang, J.-S. & Matyjaszewski, K. (1995). 'Controlled/" living" radical polymerization. Atom transfer radical polymerization in the presence of transition-metal complexes' *Journal of the American Chemical Society*, 117 (20), pp. 5614-5615.

Wang, L., et al. (2019). 'Molecularly imprinted polymers for gossypol via sol–gel, bulk, and surface layer imprinting—a comparative study' *Polymers*, 11 (4), p. 602.

Wang, M., et al. (2016). 'Poly (ester amine) constructed from polyethylenimine and pluronic for gene delivery in vitro and in vivo' *Drug Delivery*, 23 (9), pp. 3224-3233.

Wang, Y., et al. (2007). 'Difunctional pluronic copolymer micelles for paclitaxel delivery: Synergistic effect of folate-mediated targeting and pluronic-mediated overcoming multidrug resistance in tumor cell lines' *International journal of pharmaceutics*, 337 (1-2), pp. 63-73.

Westwood, O. M. & Hay, F. C. (2001). *Epitope mapping: A practical approach*. Oxford University Press, USA.

Włoch, M. & Datta, J. (2019). 'Synthesis and polymerisation techniques of molecularly imprinted polymers', *Comprehensive analytical chemistry*: Elsevier, pp. 17-40.

Wu, Y., et al. (2022). 'Microneedle aptamer-based sensors for continuous, real-time therapeutic drug monitoring' *Analytical Chemistry*, 94 (23), pp. 8335-8345.

Wu, Z., et al. (2015). 'Preparation and evaluation of amoxicillin loaded dual molecularly imprinted nanoparticles for anti-helicobacter pylori therapy' *International journal of pharmaceutics*, 496 (2), pp. 1006-1014.

Wu, Z., et al. (2024). 'Interstitial fluid-based wearable biosensors for minimally invasive healthcare and biomedical applications' *Communications Materials*, 5 (1), p. 33.

Wullf, G. (1972). 'The use of polymers with enzyme-analogous structures for the resolution of racemates' *Angrew. Chem. Int. Ed.*, 11 pp. 341-341.

Xiong, X.-B., Binkhathlan, Z., Molavi, O. & Lavasanifar, A. (2012). 'Amphiphilic block co-polymers: Preparation and application in nanodrug and gene delivery' *Acta biomaterialia*, 8 (6), pp. 2017-2033.

Xiong, X., Tam, K. & Gan, L. (2003). 'Synthesis and aggregation behavior of pluronic f127/poly (lactic acid) block copolymers in aqueous solutions' *Macromolecules*, 36 (26), pp. 9979-9985.

Xiong, X., Tam, K. & Gan, L. (2006). 'Polymeric nanostructures for drug delivery applications based on pluronic copolymer systems' *Journal of nanoscience and nanotechnology*, 6 (9-10), pp. 2638-2650.

Xu, S., Li, J. & Chen, L. (2011). 'Molecularly imprinted core-shell nanoparticles for determination of trace atrazine by reversible addition–fragmentation chain transfer surface imprinting' *Journal of Materials Chemistry*, 21 (12), pp. 4346-4351.

Xuan, G. S., Sun, Q. Y. & Zheng, X. (2014). 'A new molecularly imprinted polymer prepared by surface imprinting technique for selective adsorption towards rhodamine b' *Advanced Materials Research*, 998 pp. 19-22.

Yang, B., Kong, J. & Fang, X. (2022). 'Programmable crispr-cas9 microneedle patch for long-term capture and real-time monitoring of universal cell-free DNA' *Nature communications*, 13 (1), p. 3999.

Yang, J., et al. (2023). 'Development of smartphone-controlled and microneedle-based wearable continuous glucose monitoring system for home-care diabetes management' *ACS sensors*, 8 (3), pp. 1241-1251.

Yang, J., et al. (2022). 'Masticatory system–inspired microneedle theranostic platform for intelligent and precise diabetic management' *Science Advances*, 8 (50), p. eabo6900.

Yao, Y., et al. (2021). 'Integration of interstitial fluid extraction and glucose detection in one device for wearable non-invasive blood glucose sensors' *Biosensors and Bioelectronics*, 179 p. 113078.

Ye, L. (2013). *Molecular imprinting: Principles and applications of micro-and nanostructure polymers*. CRC press.

Ye, L., Cormack, P. A. & Mosbach, K. (1999). 'Molecularly imprinted monodisperse microspheres for competitive radioassay' *Analytical Communications*, 36 (2), pp. 35-38.

Yemiş, F., Alkan, P., Yenigül, B. & Yenigül, M. (2013). 'Molecularly imprinted polymers and their synthesis by different methods' *Polymers and Polymer Composites*, 21 (3), pp. 145-150.

Yu, J., et al. (2021). 'Polymeric drug delivery system based on pluronics for cancer treatment' *Molecules*, 26 (12), p. 3610.

Yuan, X., et al. (2023). 'Epidermal wearable biosensors for the continuous monitoring of biomarkers of chronic disease in interstitial fluid' *Micromachines*, 14 (7), p. 1452.

Zeng, Z., et al. (2010). 'Synthetic polymer nanoparticles with antibody-like affinity for a hydrophilic peptide' *ACS nano*, 4 (1), pp. 199-204.

Zhang, H. (2020). 'Molecularly imprinted nanoparticles for biomedical applications' *Advanced Materials*, 32 (3), p. 1806328.

Zhang, J., et al. (2018). 'Redox-sensitive micelles composed of disulfide-linked pluronic-linoleic acid for enhanced anticancer efficiency of brusatol' *International Journal of Nanomedicine*, pp. 939-956.

Zhang, L., et al. (2024). 'New perspectives on the therapeutic potential of quercetin in non-communicable diseases: Targeting nrf2 to counteract oxidative stress and inflammation' *Journal of Pharmaceutical Analysis*, 14 (6), p. 100930.

Zhang, W., et al. (2010). 'Enhanced antitumor efficacy by paclitaxel-loaded pluronic p123/f127 mixed micelles against non-small cell lung cancer based on passive

tumor targeting and modulation of drug resistance' *European journal of pharmaceutics and biopharmaceutics*, 75 (3), pp. 341-353.

Zhu, W., et al. (2023). 'Effect of interstitial fluid ph on transdermal glucose extraction by reverse iontophoresis' *Biosensors and Bioelectronics*, 235 p. 115406.

Chapter 2. General Methodologies and Chemicals

The following is a discussion and explanation of the methodologies used throughout this thesis research. The experiments were carried out in the manner disclosed in this chapter unless otherwise stated in an individual chapter.

2.1 General chemicals

A summary of chemicals/reagents used within this thesis research work, and their commercial sources are presented in **Table 2.1.** All the chemicals and solvents were high-performance liquid chromatography (HPLC)/analytical grade and were used without any further purification. Deionised (DI) water was used with the resistivity of 18.2 Ωcm.

Table 2.1. General chemicals used throughout the presented thesis.

Chemical	Grade	Source
Pyrrole (Py)	Analytical	Sigma Aldrich (Gillingham, UK)
Iron (III) chloride hexahydrate	Analytical	
Potassium hexacyanoferrate (II) trihydrate	Analytical	
Potassium ferricyanide (III)	Analytical	
D-glucose	Analytical	
Fructose	Analytical	
Galactose	HPLC	
Human serum (HS)	Sterile-filtered	
Calcium Chloride ($CaCl_2$)	Analytical	
HEPES (2-[4-(2-hydroxyethyl)piperazin-1-yl]ethanesulfonic acid)	Analytical	
Sodium Chloride (NaCl)	Analytical	
Sodium phosphate monobasic dihydrate (NaH_2PO_4)	Analytical	
N-(3-aminopropyl) methacrylamide hydrochloride (APMA)	Analytical	
N-tert-butylacrylamide (TBAm)	Analytical	
N,N′-methylenebisacrylamide (BIS)	Analytical	
N-Isopropylacrylamide (NIPAM)	Analytical	
N,N,N′,N′-tetramethylethylenediamine (TEMED)	Analytical	
Acrylic acid (AAc)	Analytical	
Lysozyme (LYZ, from chicken egg white)	Analytical	
(3-aminopropyl) trimethoxysilane (APTMS)	Analytical	
Glutaraldehyde (GA)	Analytical	
Fluorescein O-methacrylate	Analytical	
3-[4, 5-dimethylthiazol-2-yl]-2,5-diphenyltetrazolium bromide (MTT)	Analytical	
Dialysis cartridges (Vivaspin® 20, 3 k-Da MWCO polyethersulfone)		

Supelco polypropylene solid-phase extraction tubes (60 mL)		
Potassium chloride	Analytical	Fisher Scientific (Loughborough, UK)
Oxoid phosphate buffered saline (PBS) tablets		
PierceTM BCA Protein Assay Kit		
Sodium hydroxide (NaOH)	Analytical	
Acetonitrile (ACN)	Analytical	
Acetone	Analytical	
Hydrochloric acid (33%, HCl)		
1-ethyl-3-(3-dimethylaminopropyl) carbodiimide (EDC)	Analytical	
Sodium nitrite	Analytical	
Succinimidyl iodoacetate (SIA)		
Ammonium persulfate (APS)	Analytical	
4-aminobenzoic acid (4-ABA)	Analytical	
N-hydroxysuccinimide (NHS)	Analytical	
Sodium acetate	Analytical	
Live/Dead Viability/Cytotoxicity Kit (Molecular Probes)		
DAPI		
Superclonal secondary antibody (Goat anti-Mouse IgG Alexa Fluor 488)		
Alexa Fluor 594 Wheat Germ Agglutinin (WGA)		
Invitrogen ERα primary monoclonal antibody (MA1-310)		
Pluronic P84		Gift samples from BASF, Germany.
Pluronic P85		
Pluronic F127		
Pluronic F108		
Reverse Pluronic 10R5		Sigma Aldrich (USA)
2,2′-azino-bis(3-ethylbenzthiazoline-6-sulfonic acid) (ABTS)	HPLC	
Silymarin (SLY)		
1,1-diphenyl-2-picryl-hydrazyl (DPPH)		
3-(2-pyridyl)-5,6-bis (4-phenyl-sulfonic acid)-1,2,4-triazine (Ferrozine)	Analytical	
Trichloroacetic acid (TCA)	ACS reagent	
Ethanolamine	Analytical	Sigma Aldrich (Dorset, UK)
Disodium phosphate	Analytical	
Tween 20		
Naringenin (NAR)	Analytical	Alfa-Aesar (Heysham, UK)
Baicalein (BAC)	Analytical	
Glass beads (53–106-µm diameter, Spheriglass 2429 CP00)		Blagden Chemicals (Kent, UK)
Human recombinant ERα protein (A15674)		

2.2 Methods

2.2.1 Production of electroactive molecularly imprinted polymeric nanoparticles (eMIPs)

Polypyrrole (PPy), compared to other CPs, has gained more attention in the fabrication of MIPs based electrochemical sensors due to their tuneable conductivity, excellent optical, thermoelectric, and electrical properties, easy polymerisation procedure, and environmental stability. Therefore, PPy based electroactive molecularly imprinted polymeric nanoparticles (eMIPs) were synthesised using the chemical (free radical) or oxidative polymerisation method where pyrrole (Py) served as an electroactive/conductive monomer, glucose (free in the solution) as a template, and Pluronic P84 as a surface-active agent (Crapnell et al., 2021). The structure of Py and PPy (after polymerisation in described in **Figure 2.1** (Aarab et al., 2019; Stejskal et al., 2021).

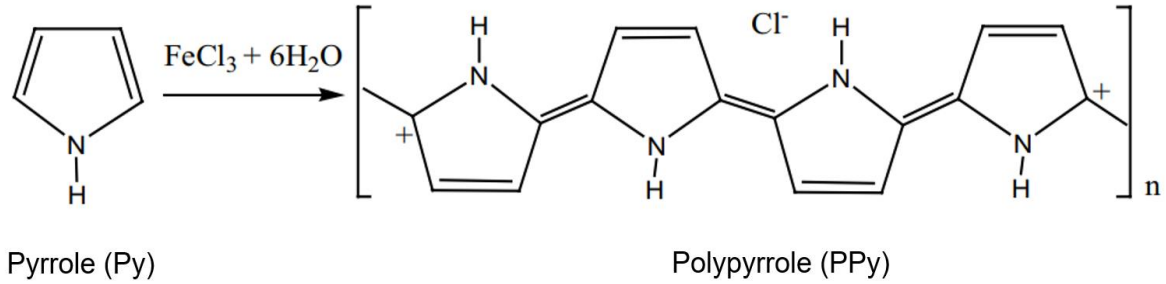

Figure 2.1: Simple polymerisation reaction of pyrrole (Py)

Briefly, 2.3 g of Pluronic P84 (a surfactant) and glucose (0.1 M) mixture in DI water (230 mL) were stirred for 3 h at 40 °C, Py (0.1 M) was then added to the above mixture and stirred for 1 h at 20 °C. The rationale for the simultaneous addition of surfactant and glucose is that Pluronic P84 facilitates glucose solubilisation and micelle formation, ensuring uniform dispersion and effective molecular imprinting. Subsequently, the polymerisation was initiated with $FeCl_3$ (0.3 M) and the mixture (colour changed from yellow to black) was kept at stirring for additional 6 h at 20 °C. The obtained polypyrrole (PPy) based eMIPs were then washed (3X) to remove unreacted monomer and $FeCl_3$ and then refluxed with 50:50 mixture of methanol and water (3X). The mixture was taken off reflux after every 12 h and separated via a Buchner funnel to remove the template (glucose) from eMIPs. Finally, these glucose imprinted eMIPs were collected by filtering the solution through a sintered funnel and drying overnight at 60 °C under vacuum. Non-

imprinted polymeric nanoparticles (eNIPs) were produced using the same process without the addition of template and served as a reference material.

2.2.2 Production of nanoMIPs using solid phase synthesis

(i) Preparation of epitope and lysozyme (LYZ) derivatised glass beads: To prepare the template (epitope/LYZ) derivatised glass beads, 60 g (per template) of glass beads (53-106 µm) were activated by boiling in 2 M NaOH (24 mL) for 15 min. Afterward, these activated glass beads were washed with double-distilled water (8 ×100 mL) until the pH of the washed solution reached ~7.4 and then rinsed twice with acetone (100 mL) and dried at 80 °C for 2 h. Subsequently, the activated glass beads were incubated in a 24 mL solution of 2%, v/v APTMS in anhydrous toluene for 12 h for the silanization step. After the incubation step, the glass beads were transferred into a sintered funnel and washed with acetone (8 × 50 mL) and methanol (3 × 50 mL), and subsequently dried under vacuum. Then, silanized glass beads were placed in a solution of SIA (0.2 mg mL^{-1} in ACN) and GA (7% v/v in PBS, pH 7.4) for epitope (cysteine modified at C-terminal) and LYZ respectively in the dark (0.4 mL solution/g glass beads) for 2 h. For epitope derivatisation, SIA modified glass beads were washed with 400 mL of ACN in a sintered glass funnel and incubated with 7 mg of cysteine-modified peptide epitope (primary template) in 40 mL of deoxygenated 1X PBS containing 5 mm EDTA (pH 8.2). On the other hand, GA-modified glass beads were washed with DI water (eight volumes) and incubated overnight with 12 mg of LYZ (0.5 mg mL^{-1}) in 24 mL of 1X PBS (pH 7.4) solution. Bicinchoninic assay (BCA) was performed to confirm the covalent immobilisation of the epitope/LYZ on the SIA/GA silanized beads, respectively.

(ii) Synthesis of nanoMIPs/NIPs against ERα and LYZ*:* The synthesis protocol was adapted from previous reports of Canfarotta and colleagues (Canfarotta et al., 2016). To synthesize nanoMIPs against ERα, a monomer mixture containing NIPAM (39 mg), Bis (2 mg), nTBA (33 mg, pre-dissolved in ethanol 1 mL), APMA (5.8 mg), AA (2.2 µL), and Fluorescein O-methacrylate (FLU, 2.6 mg) was dissolved in 100 mL of PBS (5 mm, pH = 7.4). Further, to fabricate DOX-loaded doubly molecularly imprinted nanoparticles (DOX-nanoMIPs) and fluorescein-tagged DOX-nanoMIPs (FLU-DOX-nanoMIPs), 3 mg of DOX was added to the above monomer mixture. Fluorescein-tagged nanoMIPs without DOX (unloaded) are named as FLU-nanoMIPs. Non-imprinted nanoparticles (NIPs) were produced according to the aforementioned method, except for the substitution of epitope-

derivatised beads with silanized beads. Similarly, LYZ imprinted nanoMIPs were prepared using the same monomer composition used to synthesize nanoMIPs against ERα (mentioned above) except for the addition of Fluorescein O-methacrylate monomer and DOX. Afterwards, the solution containing the monomer mixture was degassed under a vacuum sonicated for 10 min, and purged with N_2 for 30 min.

Then, ERα epitope and LYZ derivatised glass beads (60 g each) were added to their respective monomer's mixture solution under continuous N_2 purging, and polymerisation was initiated by adding a mixture containing 800 µL of APS aqueous solution (60 mg mL^{-1}) and 24 µL of TEMED. This mixture was kept for 4 h at room temperature (RT) for polymerisation, and afterward, poured into a solid-phase extraction (SPE) cartridge (60 mL) fitted with a frit (20 µm porosity). The removal of low affinity nanoMIPs, polymer, and unreacted monomers was achieved by washing with distilled water (9 × 20 mL) at RT. Following that, 20 mL of distilled water pre-warmed at 65 °C was poured into the SPE cartridge and placed in a water bath at 65 °C for 15 min. This step was repeated five times until ~100 mL of high affinity nanoMIPs solution were collected. Concentrated nanoMIPs were obtained by evaporating the dispersion solvent in an oven for 24 h at 60 °C. The obtained nanoMIPs were further purified using a centrifugal dialysis cartridge fitted with a membrane of 3 kDa MWCO (Vivaspin® 20, 3-kDa MWCO polyethersulfone). Five washes with DI water (10 mL) were performed and obtained nanoMIPs were re-suspended in 50 mL of DI water.

2.2.3 Dynamic light scattering (DLS)

The hydrodynamic diameter (D_h) of all the polymeric imprinted nanoparticles (NPs) and Pluronics based formulations (in above mentioned sections) was determined using Malvern Zetasizer Nano-ZS by employing DLS technique. The instrument was operated with a He–Ne laser (λ = 632.8 nm) at a scattering angle of 173° (**Figure 2.2**). The temperature of the instrument was controlled by built-in-temperature controller having an accuracy of ± 0.1 ℃. The formulations were filtered through 0.2 µm millipore filters to remove the contaminants prior to sample measurements. All the experiments were performed in triplicate. Additionally, *in vitro* stability of nanoMIPs was performed by mixing nanoMIPs with DMEM (GIBCO) low glucose media consisting of 10% foetal bovine serum (FBS, GIBCO) at 1:1 and incubated for different time intervals (0. 0.5, 4, 8, 12 and 24 hours) at 37 °C. Stability of nanoMIPs was determined with same instrument employed

for DLS measurements.

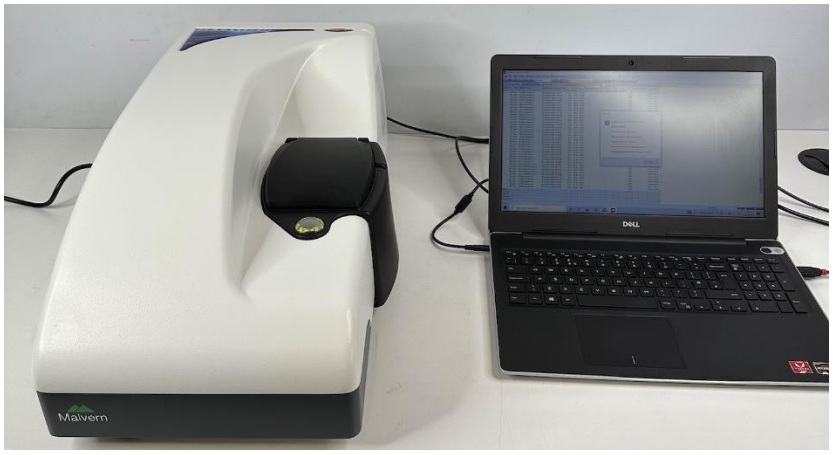

Figure 2.2: Malvern Zetasizer Nanoseries Nano-ZS

In DLS analysis, the D_h is determined by observing the Brownian motion of particles in a solution using optical methods. The random movement or diffusion of these particles is caused by collisions with thermally agitated liquid molecules. According to the Stokes-Einstein equation, the rate of diffusion is inversely related to the size of the particles. From DLS outputs, diffusion coefficients of the NPs/micelles in solution were obtained and corresponding D_h values were calculated using Stoke-Einstein relationship as per **Eq. 2.1**.

$$D = k_B T / 3\pi \eta D_h \quad \textbf{(Eq. 2.1)}$$

where D is diffusion coefficient, η is the viscosity of solvent, T is absolute temperature and k_B is the Boltzmann constant.

2.2.4 Scanning electron microscopy (SEM)

SEM measurements were performed to analyse the morphology and size of the imprinted (NPs) including nanoMIPs and eMIPs. For the nanoMIPs, different nanoMIPs *viz.* such as ERα nanoMIPs, ERα and DOX nanoMIPs, LYZ nanoMIPs, nanoMIP solutions were drop-casted and dried on the glass chips (1 × 1 cm) and measurements were performed using a Tescan Vega 3LMU (Kohoutovice Czech Republic) machine with tungsten filament Samples were mounted onto aluminium SEM pin stubs (12-mm diameter). In addition to that SEM measurements were performed to confirm the functionalisation of eMIPs on screen-printed electrode (SPEs) and compare with Bare SPEs using Carl Zeiss Sigma VP

FEG-SEM (Germany) shown in **Figure 2.3**.

Figure 2.3: Carl Zeiss Sigma VP FEG-SEM (Germany) SEM machine

2.2.5 Transmission electron microscopy (TEM) measurement

TEM measurements were performed for the morphology and particle size determination of the various nanoMIPs and eMIPs using Hitachi HT7800 120kV TEM machine (Japan) shown in **Figure 2.4**. Briefly, eMIPs/eNIPs (2 µg mL^{-1}) and nanoMIP (40 µg mL^{-1}) solution in PBS (pH 7.0) was sonicated using RS pro ultrasonicator (at a frequency of 40 kHz with an ultrasonic power rating of 70 W) for 1 min and subsequently applied to a copper grid using drop-casting.

Figure 2.4: Hitachi HT7800 120kV TEM machine (Japan).

2.2.6 Fourier transform infrared (FTIR) spectroscopy

The obtained eMIPs powder was subjected to FTIR analysis using an attenuated total reflection (ATR)-FTIR spectrometer (Perkin Elmer UATR Spectrum Two, UK) photograph depicted in **Figure 2.5**. FTIR spectra were recorded to identify the formation of the PPy polymeric material, and the functional groups present in the polymer network.

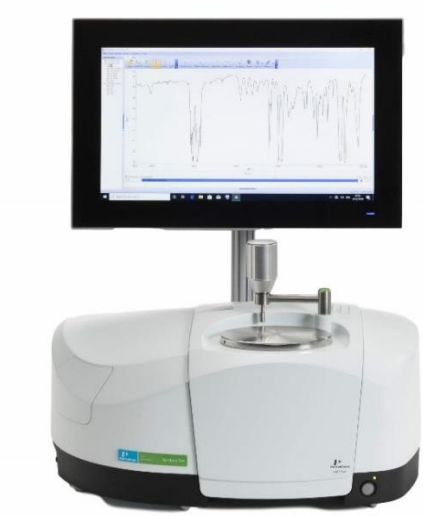

Figure 2.5: Perkin Elmer UATR Spectrum Two, UK.

2.2.7 Potentiometric experiments

Two different potentiostat instruments viz. PalmSens4 (PalmSens, the Netherlands, shown in **Figure 2.6**) and Reference 3000™ (Gamry Instruments, USA) (electrochemical workstation) were used to perform electrochemical experiments.

Figure 2.6: Photograph of potentiostat (electrochemical workstation), PalmSens4 (PalmSens, the Netherlands).

The graphite SPEs with a diameter = 3.1 mm were fabricated in-house (produced and provided by our collaborator Prof Craig E. Banks group at Manchester Metropolitan University, Manchester) with appropriate stencil designs using a microDEK 1760RS screen-printing machine (DEK, Weymouth, UK). Firstly, a carbon-graphite ink formulation (Product Code: C2000802P2; Gwent Electronic Materials Ltd, UK) was printed onto a polyester (Autostat, 250 micron thickness) substrate. This layer was then cured in a fan oven at 60 °C for 30 min. Finally, a dielectric paste (Product Code: D2070423D5; Gwent Electronic Materials Ltd, UK) was then printed onto the polyester substrate to cover the connections. After curing 60 °C for 30 min, the screen-printed electrodes are ready to be used. The reproducibility of the batch of screen-printed electrode was found to correspond to less than 4.2% RSD towards the redox probe, $[Ru(NH_3)]^{2+/3+}$/0.1 M KCl. This was followed by curing at 60 °C for 30 min with a dielectric material, which was used to define the rectangular shape of the SPE for easy handling. These SPEs had an average connection length of 32 mm with a working electrode resistance of 2.16 ± 0.06 kΩ (Crapnell et al., 2021). The LYZ-nanoMIPs were functionalised onto SPEs using an electrografting procedure established in our lab (McClements et al., 2022). Briefly, electrografting method involved preparing a solution of 2 mM 4-ABA and sodium nitrite in an aqueous HCl solution (0.5 M). The SPEs were then submerged in this solution, and CV was performed from +0.2 V to −0.6 V at a scan rate of 100 mV s^{-1} using an Ag/AgCl RE. Following this, the carboxyl groups of 4-ABA on the SPEs were activated by incubating with a solution of EDC (100 mM) and NHS (20 mM) in PBS buffer (pH 5). A total of 8 µL of the EDC/NHS solution was drop-casted onto the WE of the SPEs. After 1 h, 8 µL of the nanoMIP solution was drop-casted to the WE and incubated for additional 3 h. Then, the SPEs were rinsed with deionised water, dried with a gentle stream of nitrogen, and stored in PBS at 4 °C until use.

(i) Glucose detection: CV measurements were performed using PalmSens4 (PalmSens, the Netherlands) for glucose detection. The custom-made SPE was used as working electrode (WE), Ag/AgCl as reference electrode (RE), and a platinum wire (Pt) as a counter electrode (CE) at the potential range of -1.2 to +1.2 V (*vs.* Ag/AgCl) and a fixed scan rate of 50 mV s^{-1}. 20 µL of eMIPs solution (2 mg mL^{-1} in PBS, pH 7.0) was drop cast onto SPEs and dried for 10 min at RT (25 °C), with the resulting SPEs referred to as eMIPs functionalised SPEs (eMIPs-SPEs). To determine the optimal response of eMIPs-SPEs (*via* CV measurements), four different buffered solutions: buffer 1 (0.1 M PBS, pH 7.0),

buffer 2 (0.1 M PBS, 0.1 M KCl, pH 7.0), buffer 3 (10 mM PBS, 0.1 M Na_2SO_4, pH 7.0), and buffer 4 (0.1 M PBS containing 0.1 M KCl and 3.0 mM $[Fe(CN)_6]^{3-/4-}$ pH 7.0) were employed. These eMIPs-SPEs were washed with DI water and incubated with 5 µL of 1 µM to 10 mM concentration of glucose (in PBS, pH 7.0) for 5 min prior to the CV measurements (in best optimal buffer).

As mentioned earlier, glucose-imprinted polypyrrole (PPy) particles were synthesized using ferric chloride ($FeCl_3$) as the oxidizing agent. During the polymerization process, Fe^{3+} oxidizes pyrrole to initiate chain formation, while chloride ions (Cl^-) from $FeCl_3$ act as dopant anions, embedding into the PPy backbone to ensure electrical conductivity. The resulting electroactive polymer supports reversible redox interactions with $[Fe(CN)_6]^{3-}/[Fe(CN)_6]^{4-}$, generating characteristic redox peaks in CV.

Upon the incubation of glucose (in a concentration dependent manner), specific binding occurs at the complementary cavities present in the PPy based eMIPs. This interaction alters the electrode surface environment-either by hindering the diffusion of redox probe ions to the electrode or modifying the charge transport properties of PPy. As a result, a measurable decrease in peak current is observed in the CV, which correlates with the amount of glucose bound (**Figure 2.7)**. This current change serves as the electrochemical transduction mechanism for glucose detection.

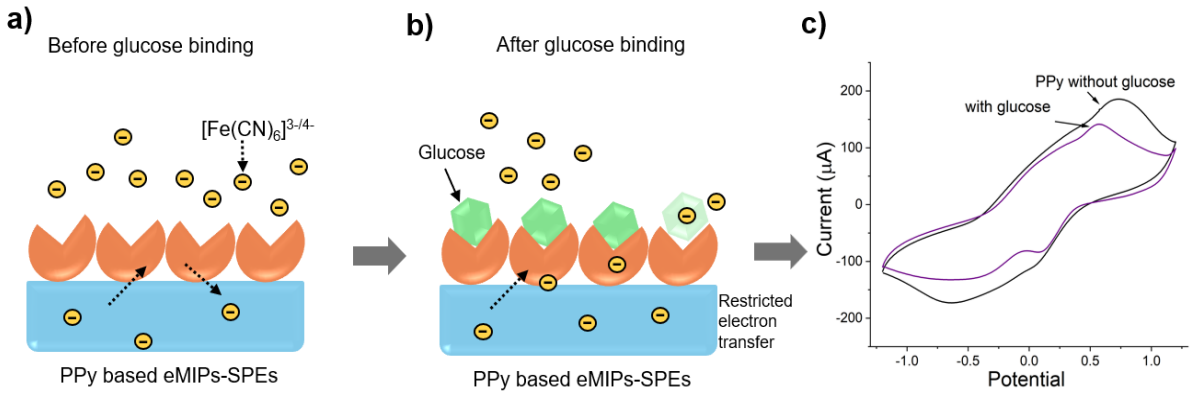

Figure 2.7: (a) The electrode surface has vacant glucose-imprinted cavities in the PPy layer. Ferri/ferrocyanide ions $[Fe(CN)_6]^{3-/4-}$ shown as yellow circles with minus signs) can freely access the electrode. This allows efficient electron transfer, resulting in high redox current in cyclic voltammetry (CV). **(b)** The binding of glucose molecules to the imprinted cavities partially blocking the access of the redox probe to the electrode surface. As a result, **(c)** the peak current (after glucose binding) decreases in the CV scan.

The calibration curve was obtained by plotting different concentrations of glucose (1 µM-10 mM) on the x-axis *vs.* changes in current (Δ*I*) on the y-axis. Selectivity studies have also been performed using different interferents such as galactose, fructose, sucrose and ascorbic acid at different concentrations (5 µL of 1 µM-10 mM in PBS, pH 7.0). eNIPs functionalised SPEs were used to evaluate the specificity of eMIPs-SPEs sensors. CV measurements were also performed in a two-electrode set up constructed by using the same WE and CE used in the three-electrode system. The minimum working volume of glucose to be determined with eMIPs sensor was 5 µL for all the experiments.

(a) Estimation of glucose in real and artificial interstitial fluid (AISF) samples: Interstitial fluid (ISF) glucose levels typically correlate with blood glucose levels but exhibit a slight delay (5-10 min) due to glucose diffusion from capillaries into the ISF (Rebrin et al., 2010). The normal range of ISF glucose is approximately 3.9-6.6 mM and 1.99-22.2 in non-diabetic and diabetic individuals respectively, similar to blood glucose levels (Freckmann et al., 2007; Sun et al., 2024). Therefore, eMIPs sensor was tested with 5 µL of glucose (1 µM-10 mM) spiked human serum (100X diluted HS) samples and real serum samples from five different diabetic patients (100X diluted) using CV measurements. The concentration of glucose in the diabetic serum samples was determined using the calibration curve constructed by plotting glucose concentrations (1 µM to 10 mM) on the x-axis *vs.* Δ*I* for glucose spiked HS on the y-axis. Similar experiments were performed in artificial interstitial fluid (AISF). To prepare the AISF, 2.5 mM $CaCl_2$, 10 mM HEPES (2-[4-(2-hydroxyethyl)piperazin-1-yl]ethanesulfonic acid), 3.5 mM KCl, 0.7 mM $MgSO_4$, 123 mM NaCl, 1.5 mM NaH_2PO_4, 7.4 mM saccharose (sucrose) were mixed, and the pH of the solution was adjusted to pH 7.4 (Bollella et al., 2019). All solutions were prepared with DI water with a resistivity of ≥18.2 MΩ cm.

***(b) Robustness, stability and reproducibility studies*:** To observe the effect of temperature on eMIPs sensor, eMIPs-SPEs (prepared according to method mentioned in section **2.2.7 i**) were kept at different temperatures (20-120 °C) in a temperature-controlled oven for 30 min. Afterwards, these eMIPs-SPEs were incubated with 5 µL of glucose (1 µM) and CV measurements were subsequently performed. For stability studies, eMIPs-SPEs were tested with 5 µL of glucose (1 µM) at different time intervals over a period of one year (1st, 15th, 30th, 60th, 120th, 240th, 360th day). The capability of the eMIPs sensor to withstand various pH values (*i.e.*, pH 5.0, 7.0, and 9.0) was investigated

at minimum and maximum glucose concentrations (1 µM and 10 mM). All the experiments were performed in triplicates (n=3). Additionally, to determine the reproducibility of the developed sensor, CV measurements were performed with six different eMIPs-SPEs (prepared under the same conditions) incubated with 1 µM concentration of glucose. The relative standard deviation (RSD) in percentage was calculated to observe the reproducibility of the developed sensor.

(ii) LYZ detection: CV and electrochemical impedance spectroscopy (EIS) measurements were carried out using Reference 3000™ (Gamry Instruments, USA) potentiostat (electrochemical workstation) for the detection of LYZ, an allergic substance in egg samples. A three-electrode system was used, consisting of SPE as the WE, a platinum wire as the auxiliary electrode, and an Ag/AgCl electrode as the RE. All the measurements were performed in 1 mM $[Fe(CN)_6]^{3-/4-}$ (1:1) mixture in 0.1 M KCl and PBS. CV studies were performed in the potential range from − 0.2 to 0.6 V with a scan rate of 50 mV/s. EIS measurements were performed in a wide frequency range from 0.02 Hz to 100 kHz with an amplitude of 10 mV at open circuit potential. To construct dose-response curve, a SPE functionalised with nanoMIPs was exposed to PBS solutions with increasing concentrations of LYZ (0-1 mM). Measurements to construct dose–response curves to monitor the corresponding charge transfer resistance (RCT) values at certain concentrations of LYZ were calculated by fitting equivalent circuits to Nyquist plots corresponding to each EIS measurement.

(a) Proof-of-application impedimetric detection in an egg white sample

The proposed impedimetric sensor was applied to detect LYZ in an egg white sample. The following steps were taken to prepare the hen egg sample for use: first, the egg white and yolk were separated, and then, the egg white was diluted with 10 mM PBS buffer solution (pH 7.5) in a 1:50 ratio. The sample was further diluted to 5000 times and EIS was employed to determine the concentration of LYZ. The hen eggs were obtained from the local Co-op supermarket, Newcastle, UK.

2.2.8 Heat transfer method (HTM) analysis

In tandem, thermal analysis was conducted with the HTM, which is based on monitoring the heat transfer resistance at the solid–liquid interface of the functionalised SPE.

A measurement chamber with an internal volume of 150 µL, as designed in (Figueiredo et al., 2022), was 3D-printed using an Anycubic Photon printer (Shenzhen, China).

Functionalised SPEs were mounted onto a copper heat sink, which was sealed off with an O-ring and a copper lid to prevent leakage and subsequently placed on top of the measurement chamber (**Figure 2.8**).

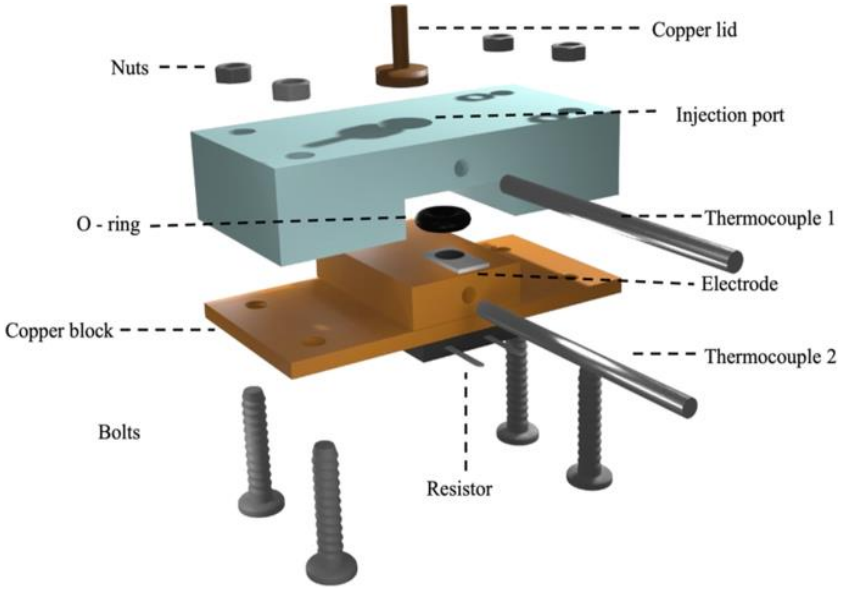

Figure 2.8: Schematic design of the fully assembled measurement chamber, which includes the 3D-printed cell, a copper lid, the functionalised SPE, and a copper heat sink to which a resistor is attached to control the temperature. The thermocouples measure the temperature of the copper and the temperature of the liquid inside the cell.

The measurement set up was coupled to an in-house designed thermal device (Van Grinsven et al., 2012). For all experiments, the thermal measurement device was controlled using LabView software and a proportional-integral-derivative (PID) controller attached to a power resistor (22 Ω). The PID parameters were optimised for this experiment and included P = 1, I = 40, and D = 0.3. The temperature of the copper heat sink was kept at 37 ± 0.02 °C via the PID controller. The temperature of the liquid in the measurement cell (T_2) was recorded via a type-K thermocouple (RS Components, UK) placed at 1.7 mm above the electrode surface. The thermal resistance (R_{th}, °C/W) can then be calculated (**Eq. 2.2**) via dividing the temperature gradient ($T_1 - T_2$) by the power input (P) required to keep the heat sink at the desired temperature.

$$R_{th} = (T_1 - T_2)/P \quad (\textbf{Eq. 2.2})$$

First, a PBS solution (150 µL) was introduced into measurement cell containing a MIP-

functionalised SPE and allowed to stabilize until a stable temperature signal was recorded. Subsequently, this PBS solution was withdrawn, and a PBS solution (150 µL) spiked with a known concentration of LYZ was added. The impact on the R_{th} was determined when the signal had stabilised (after 15–20 min), with binding of the LYZ to the MIP layer expecting to increase the thermal resistance as determined by the pore blocking model (Peeters et al., 2013). LYZ concentrations were measured in a wide range starting at 10 pM, to 1 nM, 0.1 µM, 10 µM, and finally 1 mM. Each MIP-functionalised SPE was used for two measurements. The limit of detection (LOD) was determined via the three-sigma method.

2.2.9 UV-visible spectroscopy

UV-visible spectrophotometer with a quartz cuvette of path length 1 cm was used to record the absorption spectra of various samples. Jenway 7200 UV-visible spectrophotometer (**Figure 2.9**) was employed for the loading and release study of various drugs including DOX, silymarin (SLY), naringenin (NAR) and baicalin (BAC).

Figure 2.9: Jenway 7200 UV-visible spectrophotometer

On the other hand, UV-1800 Shimadzu spectrophotometer (**Figure 2.10**) was used to determine the amount of SLY (hydrophobic drug) solubilised in Pluronic and Pluronic mixed micelles and SLY drug release from different Pluronic micellar formulations.

Figure 2.10: Shimadzu UV-1800 UV-visible Spectrophotometer

2.2.10 Determination of DOX loading and release in nanoMIP formulations

A stock solution of DOX (100 µg mL^{-1}) was prepared in water and further diluted in DI water to the concentration of 1, 2.5, 5, 7.5, and 10 µg mL^{-1}. UV-visible spectra were recorded between 200 and 600 nm using a Jenway 7200 UV-visible spectrophotometer. The DOX calibration curve was plotted using absorbance (λ_{max} 254 nm) versus concentration (**Figure A.2,** Appendix A), and the linear calibration curve equation (*y = mx+b)* was used to estimate the DOX within the nanoMIPs. The calibration curve was plotted in the UV region at 254 nm because in the visible region, the fluorescein-o-methacrylate peak overlaps with the visible region peaks of DOX. The percent drug loading capacity (DLC) was calculated by taking the ratio of the amount of DOX encapsulated and the weight of nanoMIPs.

DLC (%) = Encapsulated DOX / Total weight of nanoMIPs or NIPs x 100 ***(Eq. 2.3)***

DLE of DOX loaded into nanoMIPs have been calculated with following formula.

DLE = Encapsulated DOX in nanoMIPs / amount of DOX fed initially x 100 ***(Eq. 2.4)***

DOX-loaded nanoMIPs and NIPs (2 mL each, polymer concentration was 1 mg mL^{-1}) were poured into a dialysis bag (Spectrum Spectra/Por dialysis membrane with MWCO 12–14 kDa) and subsequently placed in 8 mL release medium of phosphate buffer saline (PBS, pH 7.4). The dialysis system was kept at a temperature of 37 ± 0.2 °C with constant stirring at 120 rpm. Aliquots (0.5 mL) were taken from the release medium at predetermined time intervals and replenished with the same volume of fresh release medium. The concentration of DOX release was estimated using a UV–vis spectrophotometer, using a respective calibration curve of DOX. The cumulative %

release was calculated using the following **Eq. 2.5**.

Cumulative % release = amount of DOX present in release medium / Total encapsulated DOX in nanoMIPs x 100 ***(Eq. 2.5)***

2.2.11 Solubilisation of drugs in Pluronic micelles

Different Pluronic micellar formulations were investigated for the solubilisation of various natural drugs including SLY, NAR and BAC. For this study, direct dissolution method (D.D.M.) for SLY and two different methods *viz.* (D.D.M.) and solvent evaporation method (S.Ev.M.) were adopted to solubilise the NAR and BAC.

(i) Direct dissolution method: The solubilisation of SLY was performed in the mixed micelles of different normal Pluronics (F108, F127, P85 and P84) with reverse Pluronic 10R5. Different Pluronics were dissolved in 5 mL double distilled water and then SLY (20 mg) was added to it. Similarly, different Pluronics (F108, F127 and P84) micellar solution (1-5% w/v in case of NAR; 6 and 12% w/v in case of BAC) were prepared to solubilise NAR and BAC. 40 mg for NAR and BAC was added to different Pluronics solutions which is pre-dissolved in 2 mL of DI water. This method of solubilising drugs directly to the micellar solution by simple dissolution is called the D.D.M. Afterwards, these solutions were kept on stirring (400 rpm) and maintained at the temperature of 37 ± 0.1 °C. For SLY, the stirring time was 24 hours, while for NAR/BAC, it was 12 hours.

Afterwards, the solutions were filtered using millipore filters (0.2 µm Polytetrafluoroethylene (PTFE) syringe filters) to remove the remaining undissolved drugs. The solubilised amount of SLY in mixed micelles of 10R5 with different normal Pluronics and NAR/BAC in normal Pluronics was calculated using absorbance measurements made on Shimadzu, UV-1800 UV-visible spectrophotometer. All experiments were performed in triplicates to ensure the repeatability of the results.

(ii) Solvent evaporation method (S.Ev.M.)*:* In S.Ev.M., excess amount of phyto-drugs (40 mg for NAR and BAC) and different Pluronics at variable concentrations (1-5% w/v in case of NAR; 6 and 12% w/v in case of BAC) were mixed and dissolved in vial containing 2mL of ethanol and afterwards, the mixture was evaporated at 60°C until a thin film was obtained. DI water (2 mL) was poured in the vial containing thin film and sonicated using RS pro ultrasonicator (for 10 min) at frequency of 40 kHz with ultrasonic power rating of 70W. After that, solutions were thoroughly stirred at 37°C for 2 hours to completely dissolve the thin film. The solution was filtered through 0.2 µm PTFE syringe filters (Fisher

Scientific, Heysham, UK) to remove the unloaded phyto-drugs from the solutions. The samples of empty micelles produced via S.Ev.M for DLS and SEM measurements were prepared using the above-mentioned method without adding the phyto-drugs.

The Drug loading efficiency (DLE) was defined as the %age of SLY loaded from the SLY fed initially in mixed micelles during formulation process and has been computed from **Eq. 2.6**.

$$DLE\ (\%) = Drug\ in\ Pluronic\ micelles\ /\ Drug\ fed\ initially\ x\ 100 \quad \textbf{(Eq. 2.6)}$$

The percent drug loading capacity (DLC) was calculated by taking the ratio of amount of Phyto-drug encapsulated (determined using UV-vis) and weight of Pluronic used.

$$DLC\ (\%) = Encapsulated\ phyto\text{-}drugs\ /\ Total\ weight\ of\ Pluronic\ x\ 100 \quad \textbf{(Eq. 2.7)}$$

The partition coefficient (*P*) is the ratio of the drug encapsulated in the micellar phase to the drug solubilised in aqueous phase. It is an important property regarding the encapsulation of drugs in micelles.

$$P = S_{tot} - S_w / S_w \quad \textbf{(Eq. 2.8)}$$

where S_w is the solubility of the drug in water and S_{tot} is the total solubility of the drug.

From the partition coefficient, the Gibbs free energy (ΔG°) of drug encapsulation has been calculated using the formula below:

$$\Delta G^\circ = -RT \ln P \quad \textbf{(Eq. 2.9)}$$

where *R* is the gas constant, *T* is the temperature in Kelvin and *P* is the Partition Coefficient.

(iii) In vitro drug release: Dialysis method was employed to determine the *in vitro* release of SLY and NAR/BAC from mixed micellar formulation and normal Pluronics. Dialysis tubing (Spectra/Por dialysis membrane with MWCO-12-14 kDa) filled with 2 mL of different drug (SLY, NAR and BAC) loaded micellar formulations were submerged in 100 mL of buffer release medium (PBS, pH 7.4) to provide sink condition. The buffer solutions were prepared by dissolving one PBS tablet (acquired from Fisher Bioreagents™). The typical composition of buffer was 137 mM Sodium Chloride, 10 mM Phosphate Buffer [potassium dihydrogen phosphate (8.1 mM) and disodium hydrogen phosphate (1.9 mM)] and 2.7 mM potassium chloride. The dialysis system was maintained at 37 °± 0.5 C with constant stirring at 120 rpm. Samples (1 mL) were

withdrawn after specified time intervals and replenished with equal volume of fresh release medium. The concentration of drug release was estimated using a UV/Visible spectrophotometer, using respective molar absorption coefficient of SLY, NAR and BAC. Cumulative percentage release was calculated using **Eq. 2.5**.

2.2.12 Surface Plasmon Resonance (SPR)

(i) Immobilisation of nanoMIPs onto the SPR sensor surface: Carboxymethyl dextran hydrogel-coated Au chips, purchased from Reichert Technologies (Buffalo, USA) were installed onto a Reichert 2 SPR (**Figure 2.11**), following the manufacturer's instructions. The sensor surface was then preconditioned by running buffer PBST (PBS pH 7.4 and 0.01% Tween 20) at 10 µL min^{-1} until a stable baseline was obtained. The flow rate of 10 µL min^{-1} was maintained throughout the immobilisation process. To activate carboxyl groups on the surface of the sensor chip, a freshly prepared aqueous solution (1 mL) of EDC (40 mg) and NHS (10 mg) was injected onto the sensor chip surface for 6 min.

To the activated surface, 300 µg of the nanoMIPs dissolved in 1 mL of the running buffer (PBST) and 10 mm sodium acetate were injected only to the left channel of the surface for 1 min. Finally, a quenching solution (1 M ethanolamine, pH 8.5) was injected for 8 min to deactivate carboxyl groups and wash away the unbound nanoMIPs. A continuous flow of running buffer (PBST) at 10 µL min^{-1} was maintained after nanoMIPs immobilisation. SPR measurements were carried out after a stable baseline was achieved. The left channel was the working channel, and the right channel was the reference.

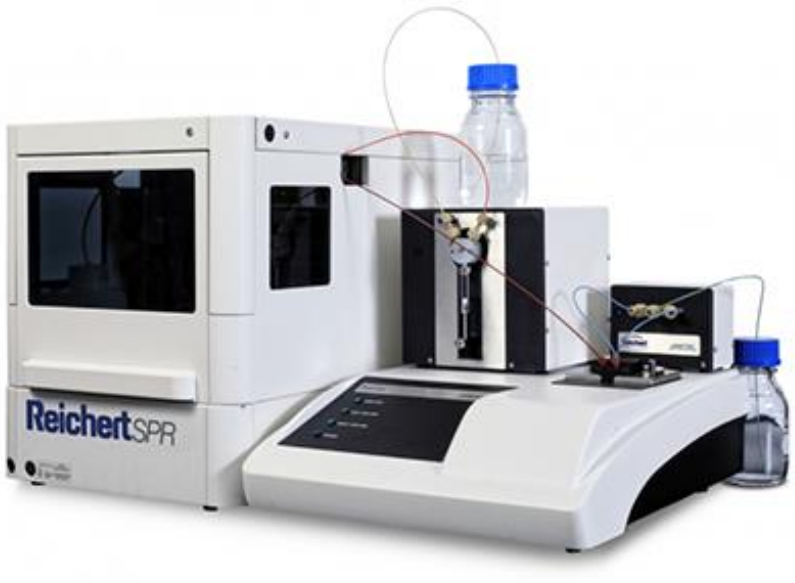

Figure 2.11: Reichert 2 Surface Plasmon Resonance (SPR)

(ii) Kinetic analysis using SPR: Kinetic analysis was initiated by injection of the running buffer PBST (blank) onto the nanoMIPs immobilised sensor surface for 2 min, followed by PBST for 5 min. The binding kinetics of individual nanoMIPs to the selected target were determined from serial dilutions (five concentrations in the 4-64 nm range) of the selected target under study. Each dilution was injected for 2 min (association) followed by PBST for 5 min (dissociation). After dissociation, the target was removed from the immobilised surface by injecting regeneration buffer (10 mm Glycine-HCl, pH 2) for 1 min followed by PBST for 1 min. The same procedures were repeated for the remaining four dilutions of the target. After the analysis were completed, signals from the left channel were subtracted from signals from their respective reference channel (the right channel).

The SPR responses from five concentrations of the target compound (4–64 nm) were fitted to a 1:1 bio-interaction (BI) model (Langmuir fit model) utilising TraceDrawer software. Association rate constants (k_{on}), dissociation rate constants (k_{off}), and maximum binding (B_{max}) were fitted globally, whereas the BI signal was fitted locally. The equilibrium dissociation constant (K_D) was calculated from the ratio k_{off}/k_{on}.

2.2.13 Fluorescence measurements

A Hitachi F-4600 spectrophotometer with a quartz cuvette of 1 cm path length was used for steady-state fluorescence measurements (**Figure 2.12**). The spectrophotometer was employed to determine the critical micelle concentration (*cmc*) and micropolarity measurements.

Figure 2.12: Hitachi F-4600 Fluorescence Spectrophotometer

(i) cmc measurements: The *cmc* values of the mixed micelles of different Pluronics were determined using Hitachi F-4600 Fluorescence Spectrophotometer at 37 °C. Pyrene was used as probe. Variation in ratio of first and third vibronic peak of pyrene with polymer concentration was monitored as a function of micellar concentration. Fluorescence titrations were performed by successive addition of concentrated stock solutions to pyrene solution. The temperature was controlled using an automated thermostat from ORBIT RS with an accuracy of ± 0.01 °C.

(ii) Micropolarity measurements: The locus of solubilised SLY in Pluronic micelles and reverse Pluronic-10R5 mixed micelles was determined using photoluminescence quenching of pyrene. The probe labelled blank micelles were titrated against SLY loaded Pluronic micelles/mixed micelles. The ratio of first to third vibronic peaks (I_1/I_3) of the pyrene emission spectrum reveal the polarity of the medium in which it is dissolved and are instrumental in determining the location of encapsulated SLY in Pluronic micelles/mixed micelles.

2.2.14 ^{1}H NMR (Proton nuclear magnetic resonance)

To determine the binding and interactional behaviour of phyto-drugs (NAR/BAC) with Pluronics, the ^{1}H NMR studies were performed on a Bruker Avance III HD 700 MHz nuclear magnetic resonance spectrometer with a Prodigy TCI cryoprobe operating at 700.13 MHz. Chemical shifts are reported in parts per million (ppm). For the interactional studies, phyto-drugs were first dissolved in the DMSO-d_6 and further diluted in D_2O with final ratio of 5% (w/v) DMSO-D_2O.

2.2.15 In vitro cell binding by flow cytometry

MCF-7 and MDA-MB-231 were cultured in DMEM (GIBCO) low glucose media supplemented with 10% foetal bovine serum (FBS, GIBCO) and 1% penicillin/streptomycin (P/S). The cells were incubated in a humidified atmosphere of 5% CO_2 and 95% air at 37 °C.

In vitro, cell binding of different nanoMIPs with cancer cells was determined using a BD LSRFortessa X-20 flow cytometer. Cells were gently scraped, after washing with PBS, and resuspended in flow cytometry buffer (1×PBS, 0.5% BSA, 0.1% NaN_3) at concentration 1×10^6 cells in 100 µL. Prior to treatment, nanoMIPs were sonicated (10 min) and added to the cell suspension with the final concentration of 10 µg mL^{-1} and

40 µg mL^{-1}. Following the 2-h incubation, the cells were centrifuged, washed, and dispersed in a flow cytometry buffer, and subsequently, binding analysis was performed using a flow cytometer. Each experiment was done in triplicate. Data was analysed using flowJo software, version 10.

2.2.16 In vitro cytotoxicity assessment

The MTT assay was used to evaluate the *in vitro* cytotoxicity of various nanoMIPs and pure DOX in MCF-7 and MDA-MB-231 cells (Surapaneni et al., 2018). For each experiment, 5000 cells per well were seeded into 96-well plates and incubated for 24 h. The cells were then treated with the synthesised nanoMIPs and pure DOX at a concentration of 10 µg mL^{-1} for 24, 48, and 72 h. 2.5 mg of MTT was dissolved in 500 µL of phosphate-buffered saline (PBS) and diluted to 5 mL with serum-free DMEM medium. 200 µL of the MTT solution was added to each well of the plates after 24, 48, and 72 h of nanoMIPs treatment respectively, and the plate wrapped in aluminium foil were incubated at 37 °C for 4 h. After that, the media containing unbound MTT and dead cells was removed from each well, and 200 µL of DMSO was added to each well. The plates were shaken on an orbital shaker at 70 rpm for 30 min, and the absorbance was measured at dual wavelengths of 550 and 630 nm using a Spectramax M5^{e} (Molecular Devices, CA) multi-mode automated microplate reader. The results were expressed as percentage cell viability, assuming the viability of control cells as 100%. Three independent experiments were performed for each study, and all measurements were performed in triplicate.

2.2.17 Confocal laser scanning microscopy (CLSM) imaging

The nanoMIPs binding as well as cellular uptake in MCF-7 and MDA-MB-231 cell lines was assessed at different time points (1 and 24 h). The cells were seeded at 20,000 cells per well (300 µL) in µ-Slide 8 Well high ibiTreat chamber slides (Thistle Scientific, Uddingston, Glasgow, UK) and kept for 24 h to achieve 70–80% confluency. Prior to the treatment, nanoMIPs were washed with ethanol (70%) and then with PBS (two times) before adding to the cells, using centrifugation cartridges.

After 24 h, the medium was pipetted out and the nanoMIPs suspension (10 µg mL^{-1}, in full media) was added to the chamber plates; then the plates were incubated for 1 or 24 h. Following the treatment, the chamber plates were washed three times with PBS (pre-warmed) to remove the unbounded nanoMIPs. Afterward, the treated cells were fixed

using 4% PFA solution prepared in PBS for 20 min at room temperature. PFA fixed chamber wells were then incubated with wheat germ agglutinin (WGA) with Alexa Fluor 594 (catalogue no. W11262) for 10 min (dilution 1:200) to stain the plasma membrane. After washing the chamber wells with PBS (three times, 10 min each), DAPI (1:200 in PBS) was added for 20 min followed by the washing with PBS (three times). For the control experiment, MCF-7 and MDA-MB-231 cells were fixed with 10% formalin incubated for 15 min at room temperature and permeabilised with Triton X-100 (0.1% in PBS). The cells were blocked with 5% goat serum (in PBS) and stained overnight with 10 µg mL^{-1} of ERα primary antibody (MA1-310 in 2.5% goat serum in PBS) at 4 °C. Afterward, the samples were washed twice with 1 mL of PBS, incubated with Alexa Fluor 488 secondary antibody (1:1000 in 2.5% goat serum in PBS) for 30 min, stained with 1 mL DAPI (1:10000 in PBS) for 5 min and finally the slides were mounted with media.

The images were taken with a confocal laser scanning microscope Zeiss 880 inverted confocal microscope (Zeiss Europe, shown in **Figure 2.11**) and Leica TCS SP8 STED 3× (Leica microsystems, Germany) using the following lasers i) 405 nm for DAPI (blue), ii) 488 nm for fluorescein tagged nanoMIPs and Alexa Fluor 488 secondary antibody (green) and iii) 561 nm for Alexa Fluor 594 (red). The images were analysed using Image J software (Wayne Rasband, NIH, Bethesda, MD, USA).

Figure 2.13: Confocal laser scanning microscope Zeiss 880 inverted confocal microscope (Zeiss Europe)

2.2.18 3D scaffold preparation and cell culture

The thermal-induced phase separation method was utilised to synthesize 3D porous polyurethane (PU)-based scaffolds, which were then sterilised, and surface modified (coated) with Collagen I, as per the methodology described in (Gupta et al., 2022; Totti et al., 2019).

The MCF-7 cell lines were seeded onto 3D cancer models measuring 5 × 5 × 5 mm^3 at a seeding density of 0.5 × 10^6 cells per scaffold. The cells were cultured for a duration of 5 weeks. Subsequently, incubated with various treatments, including FLU-nanoMIPs, FLU-DOX-nanoMIPs, and DOX (10 µg mL^{-1}) lasting 72 h, and the treatment was removed. After treatment, the scaffolds were characterised through sectioning, staining, and image analysis via CLSM.

2.2.19 Spatial evaluation of live and dead cells via imaging

To assess the spatial distribution of live and dead cells before and after treatment, model-specific methods were employed. 3D cancer models were obtained at appropriate time intervals, snap-frozen in liquid nitrogen (15 min), and subsequently, stored at -80 °C for further analysis. This preservation technique, widely utilised in tissue engineering, ensures sample integrity without compromising cell viability (Provenzano et al., 2008; Totti et al., 2019). These scaffolds were sectioned and washed two times with PBS prior to analysis. A Live/Dead Viability/Cytotoxicity Kit (Molecular Probes, Thermo Scientific, Loughborough, UK) was utilised for live/dead cell analysis. The sections of the 3D scaffold were stained with 2 µm of Calcein-AM (from a 4 mm stock) and 4 µm of ethidium homodimer (from a 2 mm stock), and incubated for 1 h at 37 °C. The solution was subsequently removed, and the sections were washed twice with PBS and images were taken using a Zeiss 880 inverted confocal microscope (Zeiss Europe).

2.2.20 Antioxidant assays

(i) 1, 1-diphenyl-2-picryl-hydrazil (DPPH) free radical scavenging activity: To determine the free radical scavenging capacity of the SLY loaded mixed micelles of P84:10R5 (4:1 %w/v), SLY loaded pure micelles of P84 and SLY alone; DPPH free radical scavenging assay was employed (Oktay et al., 2003). The preparation of 0.1 mmol/L solution of DPPH reagent in methanol was carried out. Mixed micellar formulation (3 mL) at various concentrations (20–100 µg/mL) were mixed with 1 mL of the DPPH solution.

Absorbance was measured at 517 nm after 30 min. A decrease in absorbance is indicative of free radical scavenging activity. The percentage of DPPH scavenging activity was calculated from the given **Eq. 2.10**.

$$DPPH\ scavenging\ activity\ (\%) = (1-A_s/A_c) \times 100 \quad \textbf{(Eq. 2.10)}$$

where, A_s and A_c indicate the absorbance of the test and control respectively.

(ii) Metal chelating activity: The method described by Dinis *et al.* was used to calculate the ferrous ion chelation by the SLY loaded mixed micelles of P84:10R5 (4:1 %w/v), SLY loaded pure micelles of P84 and SLY alone (Dinis et al., 1994). Briefly, different dilutions of the formulations ranging 20–100 µg/mL were added to a solution of 2 mM $FeCl_2$ (0.05 mL). This was proceeded by addition of 5 mM ferrozine (0.2 mL) and thorough stirring of mixture after which it was kept for 10 min at the room temperature. Thereafter, the absorbance of the solution was noted at 562 nm. The %age inhibition of ferrozine-Fe^{2+}complex formation was calculated from the below mentioned **Eq. 2.11**.

$$\%\ Inhibition = [(A_0 - A_1)/A_0] \times 100 \quad \textbf{(Eq.2.11)}$$

where A_0 and A_1 stands for absorbance of control and SLY loaded micellar formulations respectively.

(iii) Assay of nitric oxide (NO) scavenging activity: Method of Garrat *et al.* has been used for the estimation of NO scavenging activity of SLY loaded mixed micelles of P84:10R5 (4:1 %w/v), SLY loaded pure micelles of P84 and SLY alone (Garg et al., 2022). The reaction mixture consisting different concentrations of SLY mixed micelles and sodium nitroprusside in phosphate buffered saline was incubated for 3 h. The above reaction mixture containing the equivalent amount of water instead of drug was taken as control. Further, 0.5 mL of Griess reagent was added after the incubation period. The absorbance of the formed complex was noted at 546 nm. Inhibition of nitrite formation by the SLY loaded mixed micellar formulation and SLY alone was calculated relative to the control using **Eq. 2.12**.

$$NO\ scavenging\ activity\ (\%) = [(A_0 - A_1)/A_0] \times 100 \quad \textbf{(Eq. 2.12)}$$

where A_0 and A_1 stands for absorbance of control and SLY loaded micellar formulations respectively.

(iv) ABTS$^{\cdot+}$ radical scavenging assay: Method of Subhasree *et al.* was used with a slight modification to determine the antioxidant activity of pure natural-drugs, SLY, NAR and BAC loaded pure Pluronic micelles, SLY loaded mixed micelles of P84:10R5 (4:1 %w/v) (Subhasree et al., 2009). In this method, ABTS solution (7 mM in ethanol) was mixed with 2.45 mM of aqueous ammonium persulfate solution to prepare ABTS radical solution. This solution was kept in the dark for 12–16 h at room temperature and solution turned into dark green due to the formation of ABTS$^{\cdot+}$ radical cations. Prior to measurement, the ABTS radical solution was diluted in phosphate buffer (pH 7.4) to obtain an absorbance of 0.700 ± 0.02 at 734 nm. Thereafter, 0.5 mL of Pluronic micellar formulation of phyto-drugs was added to 4.5 mL of ABTS$^{\cdot+}$ solution. The absorbance was taken 1 min after mixing and up to 6min. The percentage ABTS$^{\cdot+}$ radical scavenging activity was determined for each dilution relative to a blank sample with no scavenger. The intensity of decolourisation indicated the percentage decrease in absorbance. The percentage of ABTS$^{\cdot+}$ radical scavenging activity was calculated according to **Eq. 2.13**.

$$ABTS^{\cdot+}\ radical\ scavenging\ (\%) = [(A_0 - A_1)/A_0] \times 100 \quad \textbf{(Eq. 2.13)}$$

where A_0 and A_1 stands for the absorbance of control and the absorbance of natural drug loaded micellar formulations respectively.

(v) Ferric cyanide (Fe^{3+}) reducing antioxidant power assay

Oyaizu' s method was adapted to determine the ferric reducing antioxidant power (FRAP) of SLY loaded mixed micelles of P84:10R5 (4:1 %w/v), SLY loaded pure micelles of P84 and SLY alone (Oyaizu, 1986). This method is based on the ferricyanide reduction in stoichiometric excess comparative to antioxidants. A mixture was prepared containing SLY loaded mixed micelles (20–100 µg/ml) and 0.2 M of sodium phosphate buffer (pH 6.6). Further,1% of potassium ferricyanide [$K_3Fe(CN)_6$] was incubated with the aforementioned reaction mixture at a temperature of 50 °C for 20 min. This was followed by the acidification of above reaction mixture with 2.5 mL of trichloroacetic acid (10%). Thereafter, 2.5 mL of the acidified sample was added to distilled water and 0.1% of $FeCl_3$ (0.5 mL). The absorbance of the resultant was noted at 700 nm. The absorbance of the reaction mixture is the measure of the reduction potential, with an increase in absorbance indicating greater reduction potential.

2.3 References

Aarab, N., et al. (2019). 'Experimental and dft studies of the removal of pharmaceutical metronidazole from water using polypyrrole' *International Journal of Industrial Chemistry*, 10 pp. 269-279.

Bollella, P., et al. (2019). 'Minimally invasive glucose monitoring using a highly porous gold microneedles-based biosensor: Characterization and application in artificial interstitial fluid' *Catalysts*, 9 (7), p. 580.

Canfarotta, F., Poma, A., Guerreiro, A. & Piletsky, S. (2016). 'Solid-phase synthesis of molecularly imprinted nanoparticles' *Nature protocols*, 11 (3), pp. 443-455.

Crapnell, R. D., et al. (2021). 'Electrospun nylon fibers with integrated polypyrrole molecularly imprinted polymers for the detection of glucose' *Analytical Chemistry*, 93 (39), pp. 13235-13241.

Dinis, T. C., Madeira, V. M. & Almeida, L. M. (1994). 'Action of phenolic derivatives (acetaminophen, salicylate, and 5-aminosalicylate) as inhibitors of membrane lipid peroxidation and as peroxyl radical scavengers' *Archives of biochemistry and biophysics*, 315 (1), pp. 161-169.

Figueiredo, L. F., et al. (2022). 'Influence of design and material characteristics on 3d printed flow-cells for heat transfer-based analytical devices' *Microchimica Acta*, 189 (2), p. 73.

Freckmann, G., et al. (2007). 'Continuous glucose profiles in healthy subjects under everyday life conditions and after different meals' *Journal of diabetes science and technology*, 1 (5), pp. 695-703.

Garg, S., Peeters, M., Mahajan, R. K. & Singla, P. (2022). 'Loading of hydrophobic drug silymarin in pluronic and reverse pluronic mixed micelles' *Journal of Drug Delivery Science and Technology*, 75 p. 103699.

Gupta, P., et al. (2022). 'A systematic comparative assessment of the response of ovarian cancer cells to the chemotherapeutic cisplatin in 3d models of various structural and biochemical configurations—does one model type fit all?' *Cancers*, 14 (5), p. 1274.

McClements, J., et al. (2022). 'Molecularly imprinted polymer nanoparticles enable rapid, reliable, and robust point-of-care thermal detection of sars-cov-2' *ACS sensors*, 7 (4), pp. 1122-1131.

Oktay, M., Gülçin, İ. & Küfrevioğlu, Ö. İ. (2003). 'Determination of in vitro antioxidant activity of fennel (foeniculum vulgare) seed extracts' *LWT-Food Science and Technology*, 36 (2), pp. 263-271.

Oyaizu, M. (1986). 'Antioxidative activities of browning reaction prepared from glucosamine' *Jpn. J. Nutr.*, 44 pp. 307-315.

Peeters, M., et al. (2013). 'Heat-transfer-based detection of l-nicotine, histamine, and serotonin using molecularly imprinted polymers as biomimetic receptors' *Analytical and bioanalytical chemistry*, 405 pp. 6453-6460.

Provenzano, P. P., et al. (2008). 'Collagen density promotes mammary tumor initiation and progression' *BMC medicine*, 6 pp. 1-15.

Rebrin, K., Sheppard Jr, N. F. & Steil, G. M. (2010). Use of subcutaneous interstitial fluid glucose to estimate blood glucose: Revisiting delay and sensor offset. SAGE Publications Sage CA: Los Angeles, CA.

Stejskal, J., et al. (2021). 'Conversion of conducting polypyrrole nanostructures to nitrogen-containing carbons and its impact on the adsorption of organic dye' *Materials Advances*, 2 (2), pp. 706-717.

Subhasree, B., et al. (2009). 'Evaluation of antioxidant potential in selected green leafy vegetables' *Food chemistry*, 115 (4), pp. 1213-1220.

Sun, T., Liu, J. & Chen, C. J. (2024). 'Calibration algorithms for continuous glucose monitoring systems based on interstitial fluid sensing' *Biosensors and Bioelectronics*, p. 116450.

Surapaneni, S. K., Bashir, S. & Tikoo, K. (2018). 'Gold nanoparticles-induced cytotoxicity in triple negative breast cancer involves different epigenetic alterations depending upon the surface charge' *Scientific reports*, 8 (1), p. 12295.

Totti, S., et al. (2019). 'A novel versatile animal-free 3d tool for rapid low-cost assessment of immunodiagnostic microneedles' *Sensors and Actuators B: Chemical*, 296 p. 126652.

Van Grinsven, B., et al. (2012). 'Heat-transfer resistance at solid–liquid interfaces: A tool for the detection of single-nucleotide polymorphisms in DNA' *ACS nano*, 6 (3), pp. 2712-2721.

Chapter 3: Electroactive Molecularly Imprinted Polymer Nanoparticles (eMIPs) for Label-free Detection of Glucose: Toward Wearable Monitoring

*(Published as **S. Garg**, P. Singla, S. Kaur, R.D. Crapnell, C.E. Banks, S. Seyedin, M. Peeters, Small, 2024, 2403320)*

This first-author publication presents the development of eMIPs for low-cost and rapid glucose measurement without relying on enzymes as recognition elements. I designed and conducted the majority of the experiments and wrote the manuscript. Pankaj Singla and Sarbjeet Kaur assisted with the electrochemistry experiments and data analysis. Dr Banks and Crapnell has provided the SPEs for sensor development. Dr Shayan and Prof Peeters offered their expert advice in conceptualising the work and helped to in review & editing the manuscript.

3.1 Abstract

The diagnosis of diabetes mellitus affecting 537 million adults worldwide, relies on invasive and costly enzymatic methods that have limited stabilities. We have developed electroactive polypyrrole (PPy)-based molecularly imprinted polymer nanoparticles (eMIPs) that rival the affinity of enzymes whilst being low-cost, highly robust, and facile to produce. By drop-casting eMIPs onto low-cost disposable screen-printed electrodes (SPEs), we have manufactured sensors that can electrochemically detect glucose in a wide dynamic range (1 µM-10 mM) with a limit of detection of 26 nM. The eMIPs sensors exhibit no cross reactivity to similar compounds (galactose, fructose, and ascorbic acid) and negligible glucose binding with non-imprinted polymeric nanoparticles. Measurements of serum samples of diabetic patients demonstrate excellent correlation (>0.93) between our eMIPs sensor and the current gold standard Roche blood analyser test. Finally, the eMIPs sensors are highly durable and reproducible (storage >12 months), showcasing excellent robustness and high thermal and chemical stability. Proof-of-application is provided via measuring glucose using our eMIPs sensor in a two-electrode configuration and in spiked artificial interstitial fluid, highlighting its potential for non-invasive and wearable monitoring. Due to the versatility of the eMIPs that can be adapted to virtually any target, this platform technology holds high promise for sustainable healthcare applications via providing rapid detection, low-cost, and inherent robustness.

3.2 Introduction

Diabetes mellitus (DM) has been established as a common, chronic metabolic syndrome and is the 9th leading cause of death worldwide (Bhilare et al., 2024b). According to the International Diabetes Federation, over 537 million adults (aged 20-79) had diabetes in 2021 with projections indicating a rise to 643 million by 2030 ((IDF), 2021; H. Sun et al., 2022). Moreover, high blood sugar (>7 mM) in diabetes can damage tissues resulting in comorbidities such as renal failure, retinopathy, neuropathy, and cardiovascular and cerebrovascular diseases (Harding et al., 2019; Picconi et al., 2017). Therefore, it is crucial to develop a rapid and precise glucose sensing platform to effectively manage, monitor, and mitigate the progression of diabetes and its related complications (K. M et al., 2024; Xue et al., 2023). The alarming increase in global incidence of diabetes has spurred a significant expansion in the market for glucose biosensors. In 2022, the global market for glucose biosensors was valued at US$12.9 billion which is projected to rise exponentially to US$40 billion by 2032 (Inc., 2023).

Over the last 50 years, finger-prick glucose testing, relying on enzymes such as glucose oxidase, has remained the preferred method for the majority of individuals with diabetes (Olansky and Kennedy, 2010). However, this method is invasive and often leads to non-compliance among patients who need to undergo multiple finger pricks throughout the day to manage their glucose levels. Furthermore, the interference with certain substances presents in blood, such as galactose, fructose and ascorbic acid, also affects the accuracy of testing (Inzucchi, 2012; Olansky and Kennedy, 2010). Enzyme-based sensors have been used for many years due to their excellent selectivity and sensitivity (Wilson and Turner, 1992). However, they pose significant challenges such as poor stability (<6 months and requiring storage at low temperatures, *i.e.*, 4 ℃), limited shelf life and low tolerance against environmental conditions (*e.g.*, loss of activity above 40 ℃) (Li et al., 2007; Park et al., 2006). Non-invasive sampling methods, such as sweat and saliva-based analysis, are gaining popularity as alternative options to finger prick tests due to improving patient comfort (Gao et al., 2019). Enzymatic sensors currently face challenges in achieving adequate sensitivity due to the susceptibility of glucose oxidase to deactivation for detecting low glucose levels in non-invasive samples. Non-enzymatic sensors have also been widely explored which typically utilize transition metal-based nanomaterials, noble metals, or non-noble transition metals as synthetic receptors (Luo et al., 2012).

However, such sensors are costly due to the use of metals or require harsh electrolyte conditions (alkaline media, pH>11) to work, which do not facilitate direct blood sample measurements without significant sample pre-treatment (Adeel et al., 2020; Hassan et al., 2021). Recently, wearable glucose sensors have emerged as a viable alternative to existing finger prick sensors due to their real-time continuous monitoring capabilities and convenience for frequent testing but are still invasive and expensive (Chang et al., 2022; Hanna et al., 2022). Furthermore, due to the correlation of the blood glucose level with that in other fluids including interstitial fluid (ISF), wearable sensors for glucose testing in ISF offer a potential alternative to traditional finger prick tests (Corrie et al., 2015; Lee et al., 2018). For instance, Dexcom G6 and Abbott Free Style Libre are the popular continuous glucose monitoring systems in ISF but they are not accessible to the general population due to its high-cost (for instance, Dexcom G6 costs $237 for G6 transmitter and $349 for a three-pack of sensors) and limited lifetime of two weeks (Ajjan et al., 2018; Healthline; Kudva et al., 2018).

One promising approach to reducing the costs of the wearable glucose sensors is to replace enzymes with alternative recognition elements. Molecularly imprinted polymers (MIPs) are promising synthetic receptors that have been employed for the development of robust and inexpensive electrochemical sensors due to their high specificity for the chosen template (Alexander et al., 2017b; Piletsky and Turner, 2002). MIPs are porous materials containing high affinity binding for their respective targets and have gained significant interest due to their economical and straightforward preparation, reusability, robustness, biocompatibility, versatility, and specific target recognition in complex matrices (Francesco Canfarotta et al., 2018a; Zeng et al., 2010). Previous literature reports demonstrated that several molecules including different biomarkers (lipids, proteins, and serum amyloid A), glucose, and interleukin-6 can be molecularly imprinted within conventional (*i.e.*, non-electroactive) polymers via electrochemical detection (Chen et al., 2020; Gonçalves et al., 2021; Silva et al., 2016). Electrochemical measurements have gained widespread use in glucose monitoring due to their high sensitivity, excellent selectivity, and straightforward operation. For instance, polypyrrole (PPy) among other conductive polymers, has been widely utilised in the fabrication of electroactive MIPs (eMIPs) based sensors since it offers a high electrical conductivity (~10^5 S cm^{-1}), environmental stability, long term stability (≥1 year), and straightforward polymerisation procedure (H. Chen et al., 2008; Omastová et al., 1996; Ramanavičius et al., 2022). PPy-

based eMIPs sensors have been used for the electrochemical detection of different small and large molecules or drugs such as ethanethiol, L-tryptophan, SARS-CoV-2 spike glycoprotein, and *Klebsiella. pneumonia*, showed excellent selectivity, sensitivity and a low limit of detection (LOD) in real samples.(Alonso-Lomillo and Domínguez-Renedo, 2023; Ratautaite et al., 2022; R. Sharma et al., 2022). However, most studies on PPy-based eMIPs sensors employed a synthesis method that involved direction deposition of the MIP layer on the surface. This often results in a low utilisation of imprinted cavities, non-uniformity of the layer, and slow adsorption rates, thus leading to poor reproducibility and limiting commercial scalability (R. Sharma et al., 2022).

Conventional electrodes such as glassy carbon, platinum, and gold, and have been widely used for the development of eMIPs based glucose electrochemical sensor. However, current electrochemical methods often require a multi-step process involving the pretreatment with nanomaterials such as gold nanoparticles (AuNPs), graphene oxide, electro-polymerisation of various monomers including aminophenylboronic acid (APBA) and pyrrole (Py) to achieve electrochemical sensing. Uygun *et al.* developed eMIPs-based glucose sensors by modifying bespoke platinum screen-printed electrodes (PtE) with electrochemical polymerisation of APBA and Py.(Onur Uygun and Ertuğrul Uygun, 2020) The sensor was used to detect glucose employing chronoimpedimetry exhibiting a LOD of 0.3 mM. Yang *et al.* also developed eMIPs based glucose sensor by electropolymerizing eMIPs micelles and achieved an upper detection limit of 10 mM. However, the eMIPs micelles were prepared using photo-cross linkable amphiphilic copolymer which involved a complicated multistep manufacturing method (Yang et al., 2011). AuNPs coated MIPs were synthesised using free radical polymerisation and electrodeposited on the gold (Au) electrodes in the presence of glucose as a template with a LOD of 3 pM (Zhao et al., 2018). The development of the AuNPs-MIP-based glucose sensor involved a time consuming, tedious and costly fabrication process that required cross-linking for electrodeposition, thus lacking scalability.

This work introduces an innovative enzyme free PPy-eMIPs nanoparticles based SPEs sensor for rapid electrochemical detection of glucose in both serum samples of diabetic patients and artificial interstitial fluid (AISF). The novel, straightforward, one-pot synthesis of eMIPs and deposition onto inexpensive SPEs (<$0.1) eliminate the need for complex electrode modifications, offering significant cost reductions and scalability potential (Crapnell et al., 2021; Jake McClements et al., 2022). We demonstrate the

selective binding of glucose with eMIPs sensor with a LOD of ~26 nM which is significantly lower compared to other glucose sensors (LOD of ~0.3M) (Sehit and Altintas, 2020). Additionally, the unique electroconductivity of PPy-based eMIPs enables high sensitivity, fast response time (<30 s), high selectivity (no significant change in current with other sugars, ascorbic acid and dopamine), and specificity (no response with control particles, *i.e.*, non-imprinted polymers, eNIPs). The eMIPs sensors exhibit exceptional robustness as they could operate at extremes of temperature (20-120 °C), pH (5.0, 7.0 and 9.0) and possess long-term stability (≥360 days) at room temperature (RT). When used in a two-electrode setup, a LOD of 132 nM is achieved for glucose detection highlighting the potential for use in wearable applications. The eMIPs sensor is capable of determining glucose levels in spiked human serum (HS) samples and serum samples of different diabetic patients. Furthermore, we observed a strong correlation (correlation coefficient >0.9) between the results obtained from diabetic serum samples using our eMIPs sensor and those from the gold standard Roche blood analyser. In addition, the ability of the developed eMIPs sensor to measure glucose levels in AISF samples (LOD ~44 nM) with a high correlation (correlation coefficient = 0.99) to serum results, make it compatible with non-invasive monitoring through wearable technology. Overall, our approach offers versatility beyond traditional electrode substrates and its adaptability allows for comfortable, discreet, and user-friendly glucose monitoring solutions, catering to diverse needs of individuals managing diabetes. The high selectivity and versatility of the eMIPs sensor, along with its ability to function in clinical samples, highlight its potential for detecting other biomarkers such as creatinine, urea, and dopamine. This will contribute to the advancement of wearable sensors for patients with multi-morbidities like chronic kidney and, coronary artery disease that require simultaneous monitoring.

3.3 Experimental

3.3.1 Materials

The major chemicals used in study were Pyrrole (Py), iron (III) chloride hexahydrate, D-glucose, fructose, galactose, sucrose, potassium ferricyanide (III), potassium hexacyanoferrate (II) trihydrate, and human serum (HS), Pluronic P84 (MW = 4200 g mol^{-1}), Potassium chloride, PBS tablets and methanol. The serum samples of different diabetic patients were obtained from the NovoPath Biobank (ethical approval number is 22/NE/0054, project ID is 314763) Newcastle upon Tyne Hospital Trust (UK). All

chemicals and solvents used were high-performance liquid chromatography (HPLC) or analytical grade and were used without any further purification (information in **Chapter 2**). PBS solutions were prepared with deionised (DI) water with a resistivity of ≥18.2 MΩ cm. The chemical composition used for AISF preparation is provided in **Chapter 2.**

3.3.2 Methods and Equipment

The synthesis of eMIPs and eNIPs was carried out in a similar manner as described in **Chapter 2** using chemical (free radical) polymerisation method. Fourier transform infrared (FTIR) analysis using ATR-FTIR spectrometer (Perkin Elmer UATR Spectrum Two, UK). FTIR spectra were recorded to identify the formation of the PPy polymeric material, and the functional groups present in the polymer network. DLS experiments were conducted using Malvern Zetasizer Nano ZS to measure the D_h of eMIPs and eNIPs at 25 °C. TEM measurements were conducted using Hitachi HT7800 120kV TEM machine (Japan) to observe the morphology and particle size determination of eMIPs and eNIPs. Briefly, a 2 mg mL^{-1} solution of eMIPs and eNIPs in PBS (pH 7.0) was sonicated using RS pro ultrasonicator (at a frequency of 40 kHz with an ultrasonic power rating of 70 W) for 1 min and subsequently applied to a copper grid using drop-casting. For SEM analysis, eMIPs functionalised SPEs were prepared by drop-casting eMIPs solution (2 mg mL^{-1} in PBS) onto the SPEs and eMIPs-SPEs were kept for drying at RT (25 °C) for 10 min. The morphology of the bare and eMIPs-SPEs was studied using SEM. Cyclic voltammetry (CV) measurements were carried out with a PalmSens4 potentiostat (PalmSens, the Netherlands) using custom-made SPEs as working electrode (WE), Ag/AgCl as reference electrode (RE), and a platinum wire (Pt) as a counter electrode (CE) at the potential range of -1.2 to +1.2 V (*vs.* Ag/AgCl) and a fixed scan rate of 50 mV s^{-1}. The calibration curve was obtained by plotting different concentrations of glucose (1 µM to 10 mM) on the x-axis *vs.* changes in current (ΔI) on the y-axis. Selectivity studies have also been performed using different interferents such as galactose, fructose, sucrose and ascorbic acid at different concentrations (1 µM-10 mM, PBS, pH 7.0). eNIPs functionalised SPEs were used to evaluate the specificity of eMIPs-SPEs sensors. CV measurements were also performed in a two-electrode set up constructed by using the same WE and CE used in the three-electrode system to further explore the potential of the prepared sensor for real-time monitoring of glucose in a wearable device. Robustness, stability and reproducibility studies were performed at different temperatures (20-120 °C), over a period of one year

and various pH values (*i.e.*, pH 5.0, 7.0, and 9.0). All the experiments were performed in triplicates (n=3). eMIPs sensors was further investigated in glucose spiked human serum samples, serum samples of diabetic patients and glucose spiked AISF solutions (composition is explained in section **2.2.7 (a), Chapter 2**).

3.4 Results and discussion

3.4.1 Synthesis and characterisation of eMIPs

eMIPs have been produced through free-radical polymerisation using pyrrole (Py) as an electroactive monomer, glucose as a template and Pluronic P84 as a surface-active agent (**Figure 3.1**). Similarly, eNIPs were synthesised employing the same synthesis method used for eMIPs synthesis without the addition of glucose (**Chapter 2**).

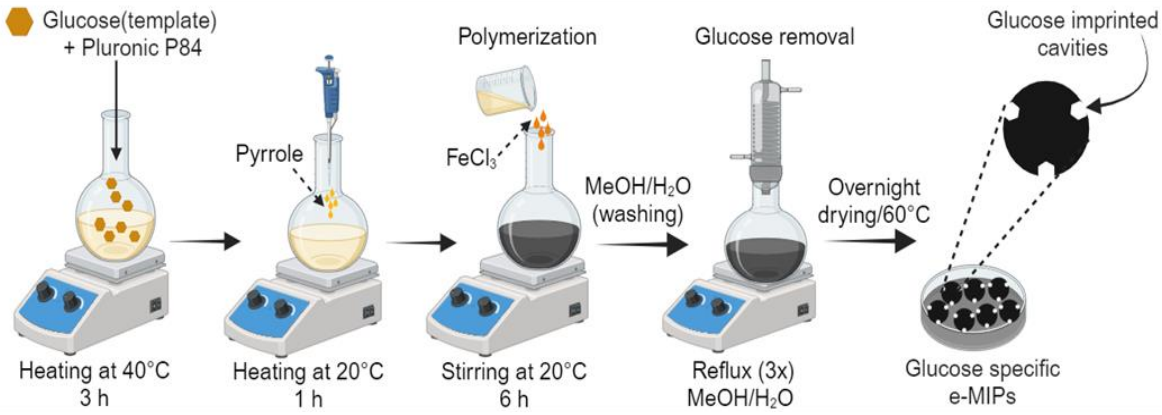

Figure 3.1: Schematic representation of the synthesis of glucose imprinted electroactive MIPs (eMIPs).

The resulting eMIPs were characterised for their size, morphology, and imprinting using different techniques such as DLS, TEM and FTIR spectroscopy. To confirm the synthesis of PPy, samples were characterised by FTIR and the results were in agreement with literature findings (Umer et al., 2020). **Figure 3.2a** showed that the bands observed at 1546 and 1474 cm^{-1} were attributed to the fundamental vibrations of the PPy ring, while those at 1290 and 1034 cm^{-1} corresponded to the =C-H in-plane vibrations, and the band at 1167 cm^{-1} was associated with the C-N stretching vibrations. DLS results showed a hydrodynamic diameter (D_h) of 91 ± 0.9 and 122 ± 0.1 nm for eMIPs and eNIPs respectively (**Figure 3.2b**). The polydispersity index (PDI) values for eMIPs and eNIPs of ~0.3 demonstrated that the nanoparticles had low polydispersity and were homogenous. Homogeneous particles are particularly important as they can be distributed evenly over

the electrode area to enhance the sensor's performance (Singla et al., 2023c).

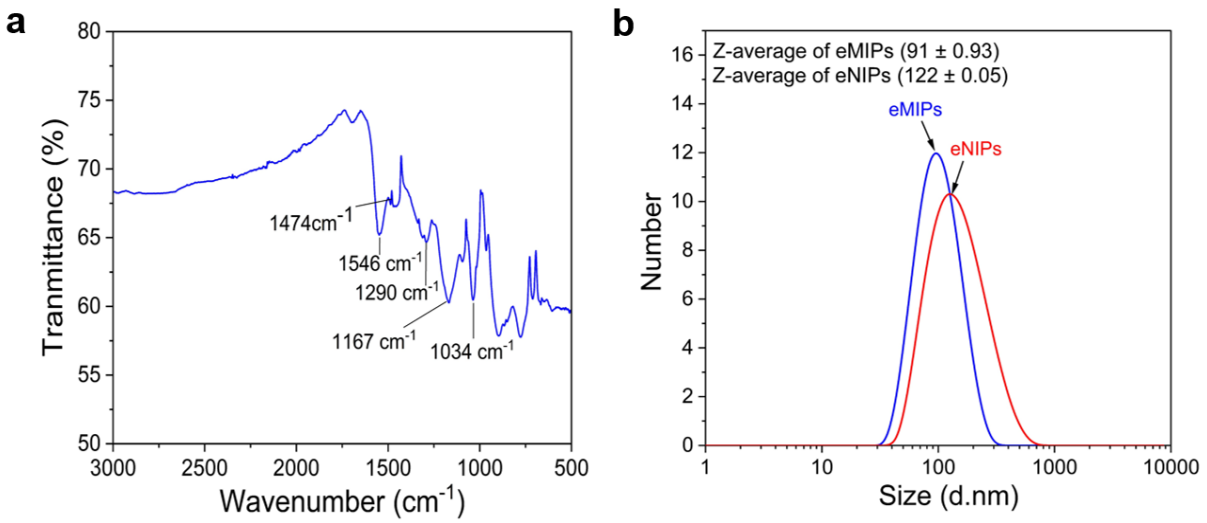

Figure 3.2: (a) FTIR spectrum of PPy-eMIPs. **(b)** eMIPs and non-imprinted polymer (eNIPs) particle size distribution (number *vs.* size in nm) measured by dynamic light scattering (DLS).

TEM results revealed that eMIPs (**Figure 3.3a**) and eNIPs (**Figure 3.3b**) were spherical in shape due to the use of Pluronic P84 in the synthesis process. Pluronic P84, known for its surfactant properties, exhibits a tendency to self-assemble into spherical micelles when introduced into aqueous solutions. Consequently, it is postulated that the alignment of Py monomers with the spherical structure of Pluronic P84 micelles facilitates the formation of spherical PPy particles (Singla et al., 2019a). The size distribution histogram constructed from TEM results showed an average particle size of 63 ± 11 nm (**Figure 3.3c**) and 69 ± 16 nm (**Figure 3.3d**) for eMIPs and eNIPs, respectively.

Moreover, the particle sizes measured by TEM were consistently smaller than those obtained from the DLS measurements for both eMIPs and eNIPs. This disparity could be attributed to the differing physical states of the nanoparticles during the measurements. In TEM, eMIPs/eNIPs were in a dry state whereas these were in solution during DLS measurements, causing them to swell and thus increase in size. Moreover, DLS measures the D_h, which includes the hydration sphere (where water molecules surround the surface of nanoparticles) of eMIPs/eNIPs, thus larger particle size is observed compared to TEM (Singla et al., 2023a).

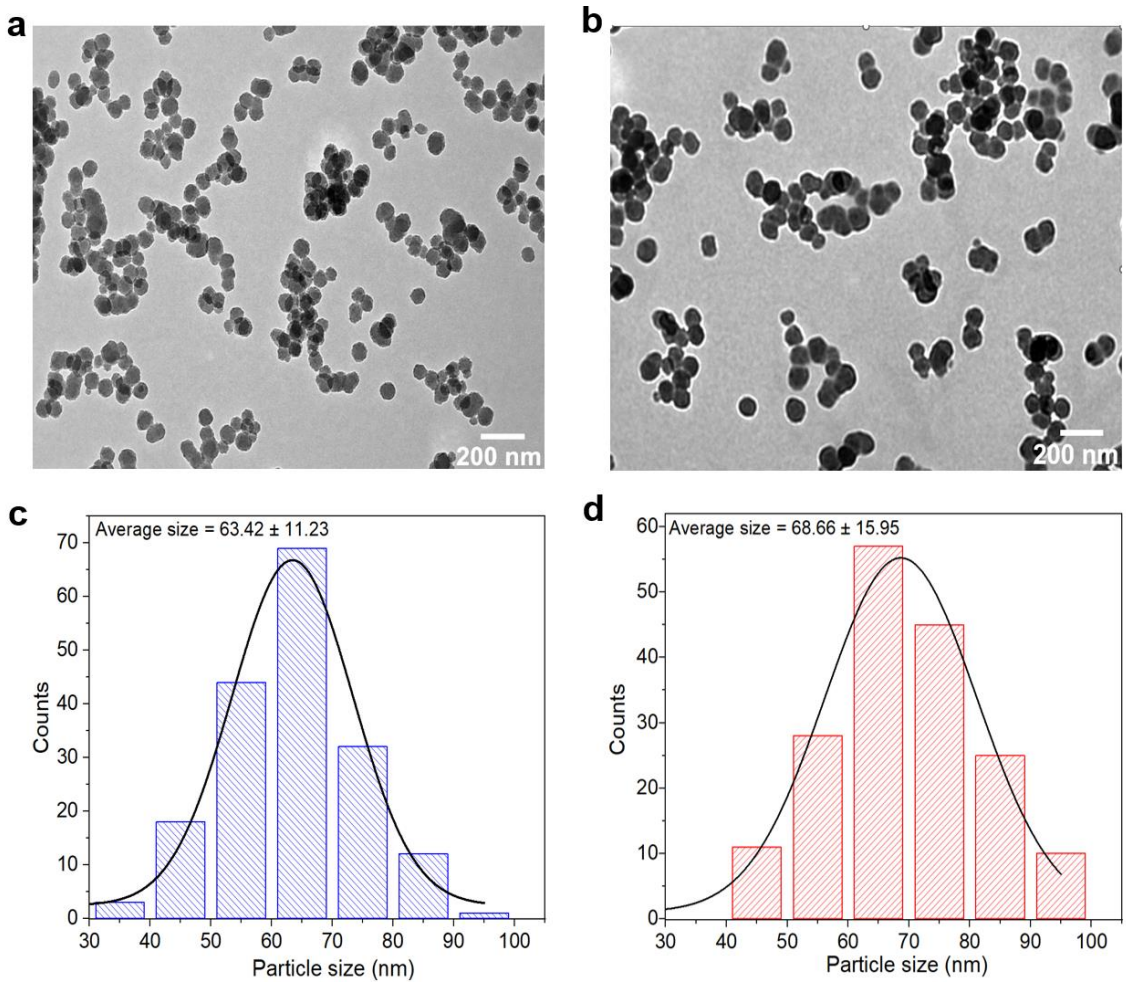

Figure 3.3: Transmission electron microscopy (TEM) images of **(a)** eMIPs and **(b)** eNIPs. Size distribution histogram (from TEM) of synthesised **(c)** eMIPs (63.42 ± 11.23 nm) and **(d)** eNIPs (68.66 ± 15.95 nm).

Additionally, TEM images of eMIPs and eNIPs were captured at higher magnification. TEM images for eMIPs are shown in **Figure 3.4 (i and ii)** and for eNIPs in **Figure 3.4 (iii and iv)**. Comparing the TEM images of eMIPs and eNIPs, lighter areas of lesser electron density can be observed, which are abundant throughout the nanoparticle structure of the eMIPs. These lighter areas correspond to the imprinting cavities of the glucose.

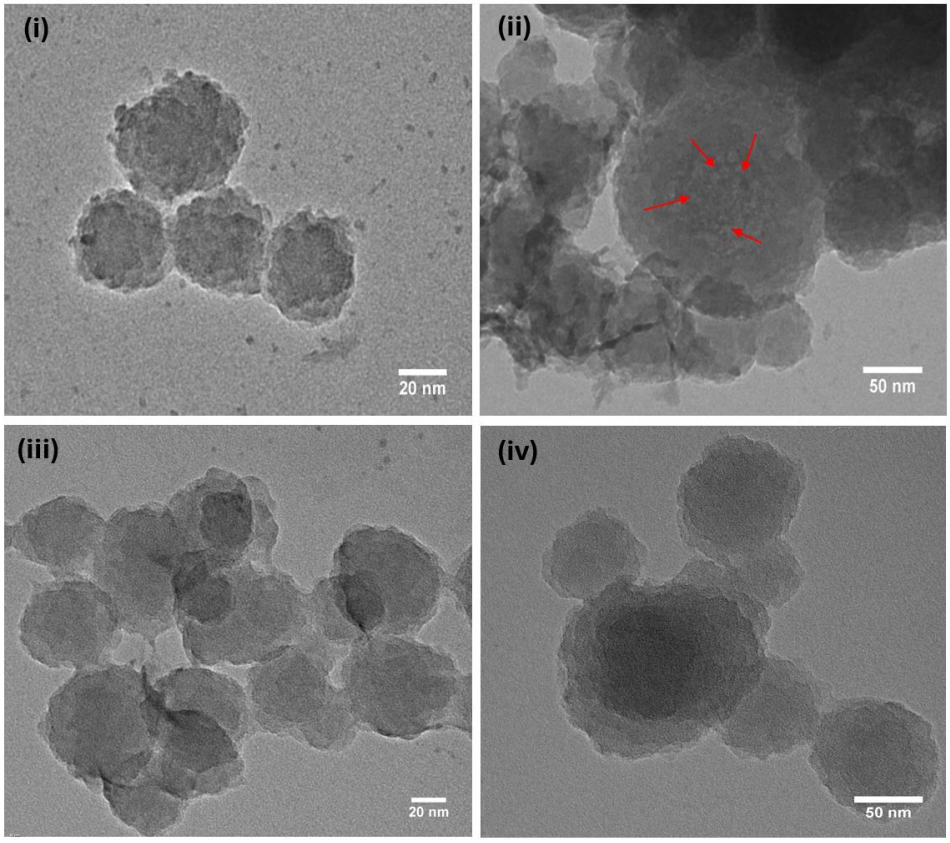

Figure 3.4: TEM images of eMIPs (**i and ii**) and eNIPs (**iii and iv**) at high magnification (scale bar 20 and 50 nm).

eMIPs-functionalised SPEs (eMIPs-SPEs) were developed by drop-casting eMIPs onto the SPEs and eMIPs-SPEs were dried at RT (25 ℃) for 10 min before use (**Figure 3.5a**). Scanning electron microscopy (SEM) was used to investigate eMIP loading on the SPEs. Comparing the SEM images of the bare SPEs (**Figure 3.5b**) and eMIPs-SPEs (**Figure 3.5c**) clearly showed that eMIPs covered the full surface of SPEs, thus confirming the successful deposition of the eMIPs nanoparticles. Additionally, SEM image of different eMIPs-SPEs prepared using another batch of eMIPs and showed similar loadings of eMIPs onto the different SPE which further demonstrated the fabrication stability of our eMIPs-SPEs via drop-casting method.

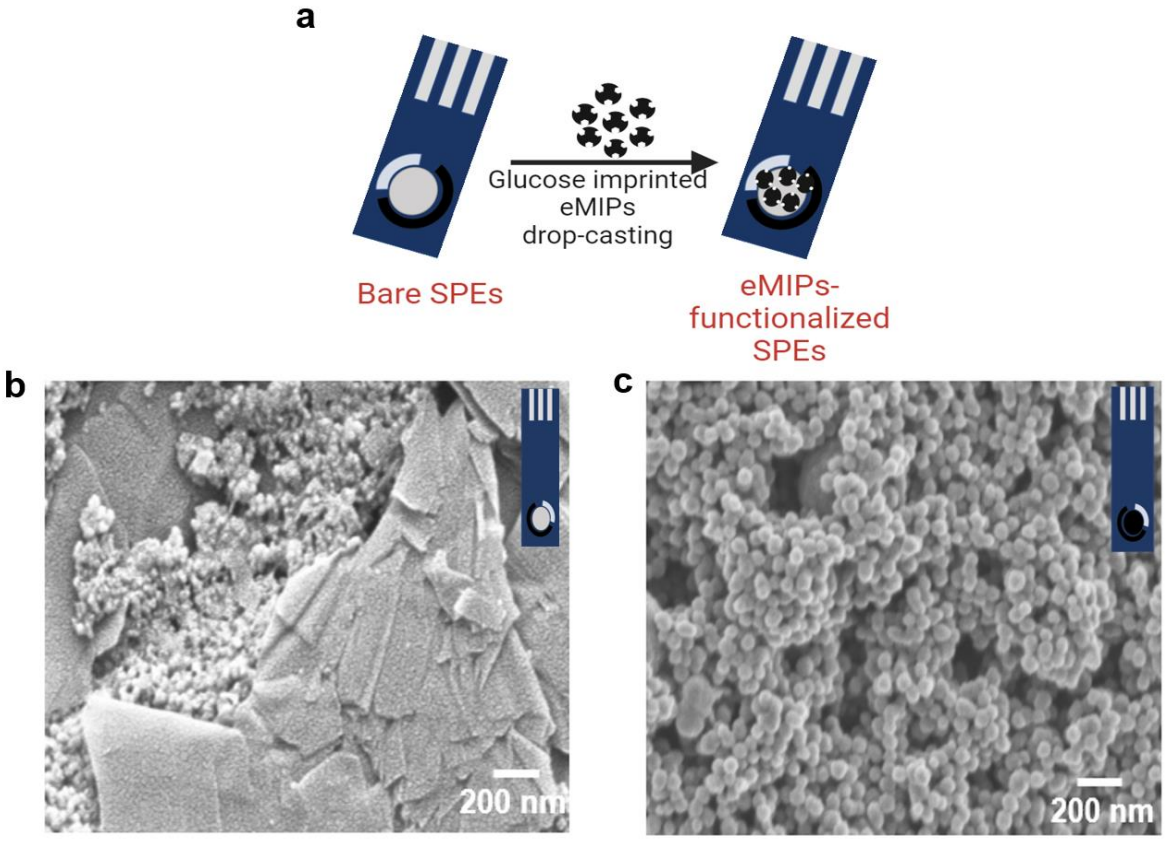

Figure 3.5: (a) schematic representation of the preparation of eMIPs-functionalised SPEs (eMIPs-SPEs). Scanning electron microscopy (SEM) images of **(b)** bare SPE and **(c)** eMIPs-SPEs.

3.4.2 Electrochemical measurements

CV measurements were first conducted to determine the best optimal response of the developed eMIPs-SPEs sensor. Therefore, four different buffer compositions (described in **section 2.2.7**, **Chapter 2)** were tested using eMIPs-SPEs. The oxidation peak of eMIPs was observed to be between +0.7 and +0.8 V in different buffered solutions (buffer 1-4); however, the oxidation peak was not stable in buffer 1-3 since the peak current decreased with every scan in those buffers (**Figure 3.6a-c)**. However, the developed sensor showed a stable response in buffer 4 *i.e.* 0.1 M PBS containing 3.0 mM $[Fe(CN)_6]^{3-/4-}$ and (pH 7.0) 0.1 M KCl as shown in **Figure 3.6d**, therefore, this buffer was chosen as the supporting electrolyte to perform all CV measurements.

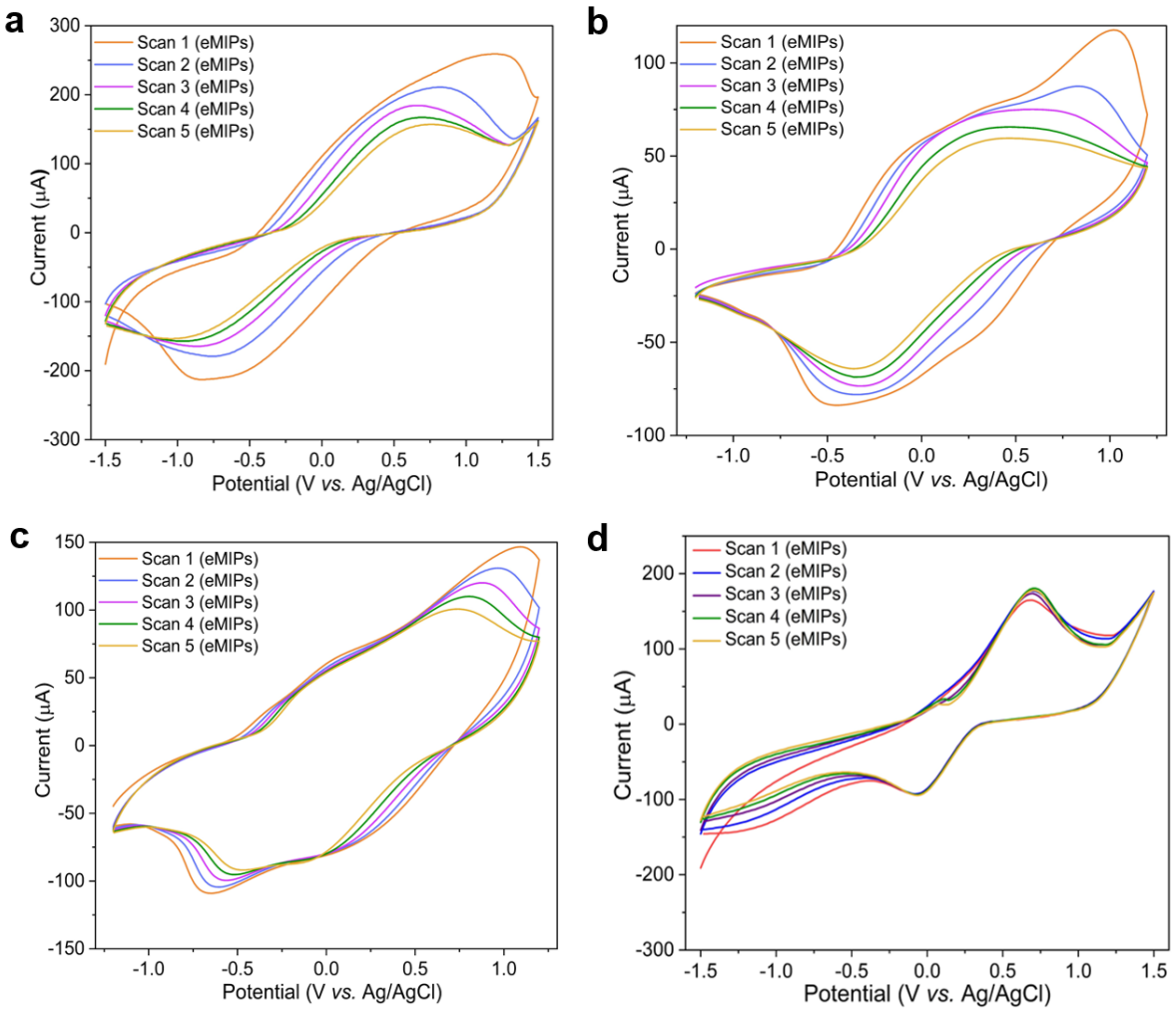

Figure 3.6: Cyclic voltammogram (CV) of eMIPs in **(a)** buffer 1 (0.1 M PBS, pH 7.0). **(b)** buffer 2 (0.1 M PBS containing 0.1M KCl). **(c)** buffer 3 (0.1 M sodium sulphate (Na_2SO_4) aqueous solution). **(d)** buffer 4 (0.1 M PBS containing, 3.0 mM $[Fe(CN)_6]^{3-/4-}$), pH 7.0 and 0.1 M KCl.

3.4.3 Electrochemical detection of glucose with eMIPs sensor

The bare SPE in buffer 4 showed an oxidation peak between +0.4 and +0.5 V for $[Fe(CN)_6]^{3-/4-}$ whereas PPy based eMIPs-SPEs (prepared according to method given in **Chapter 2**) showed an oxidation peak between +0.7 and +0.8 V (**Figure 3.7a**), in agreement with previous literature reports.(Bharath et al., 2022) There was no overlap between oxidation peaks of $[Fe(CN)_6]^{3-/4-}$ and eMIPs, which indicated that the presence of $Fe(CN)_6^{3-/4}$ did not interfere or negatively impact the electrochemical sensor response. eMIPs-SPEs were incubated for 5 min with 5 mL of PBS solutions containing increasing concentrations of glucose from 1 µM to 10 mM and CV measurements were recorded in buffer 4. It was observed that the oxidation peak current (I_p) decreased linearly with

increasing the logarithmic concentration of glucose (n=3) from 1 µM to 10 mM (**Figure 3.7b**). Similar results were observed from the CV measurements on different batches of eMIPs. This could be attributed to the specific recognition of glucose by the complementary binding sites present in the eMIPs. As eMIPs are porous materials, the binding of glucose to the imprinted cavities reduces the permeability of the electrode-nanoparticles interface, leading to a decrease in the current signal of the electroactive PPy as the glucose concentration increases (Ding et al., 2021; Sharif et al., 2022). Similar results were observed by Xu *et al.* who also reported that the differential pulse voltammetry current for the prepared gold nanoparticles/MIPs modified indium/tin oxide (ITO) electrode decreased as the concentration of glyphosate (analyte) increased (Xu et al., 2017). Furthermore, the change in current (ΔI) which is the difference between the CV peak current value detected in the absence ($I_{p\ (eMIPs)}$) and in the presence of glucose ($I_{p\ (glucose)}$) at the relevant concentration was calculated (**Eq. 3.1**).

$$\Delta I = I_{p\ (eMIPs)} - I_{p\ (glucose,\ 1\ mM\ to\ 10\ mM)} \quad \textbf{(Eq. 3.1)}$$

A calibration curve (ΔI vs. Glucose concentration) was plotted by taking the average ΔI values of three experiments (n=3), expressed as mean ± standard deviation (SD). CV results observed that the ΔI increased linearly (40 ± 3 to 105 ± 3 mA) as the glucose concentration increased (1 µM to 10 mM) with a high correlation coefficient (R^2) of 0.99 (**Figure 3.7c**).

Furthermore, the LOD for the developed sensor was ~26 nM (LOD = $3S_b/m$) where S_b is the standard deviation of the blank signal and m is the slope of the calibration curve which suggests that the obtained biosensor exhibited an excellent specificity rivalling the reported or existing sensors (**Table 3.1**). A wide range of methods have been proposed for the electrochemical detection of glucose. However, the method used for sensor development are often labour intensive, not commercially viable, and might require surface modification with nanoparticles to enhance the electrochemical response. For instance, multiple monomers were used to synthesize nanoMIPs for electrochemical sensing of glucose, which resulted in low-yield and is not economically feasible, thereby limiting its commercial potential. Moreover, it required inclusion of ferrocene, a redox probe, which can limit overall affinity and complicates the manufacturing process (Garcia-Cruz et al., 2020).

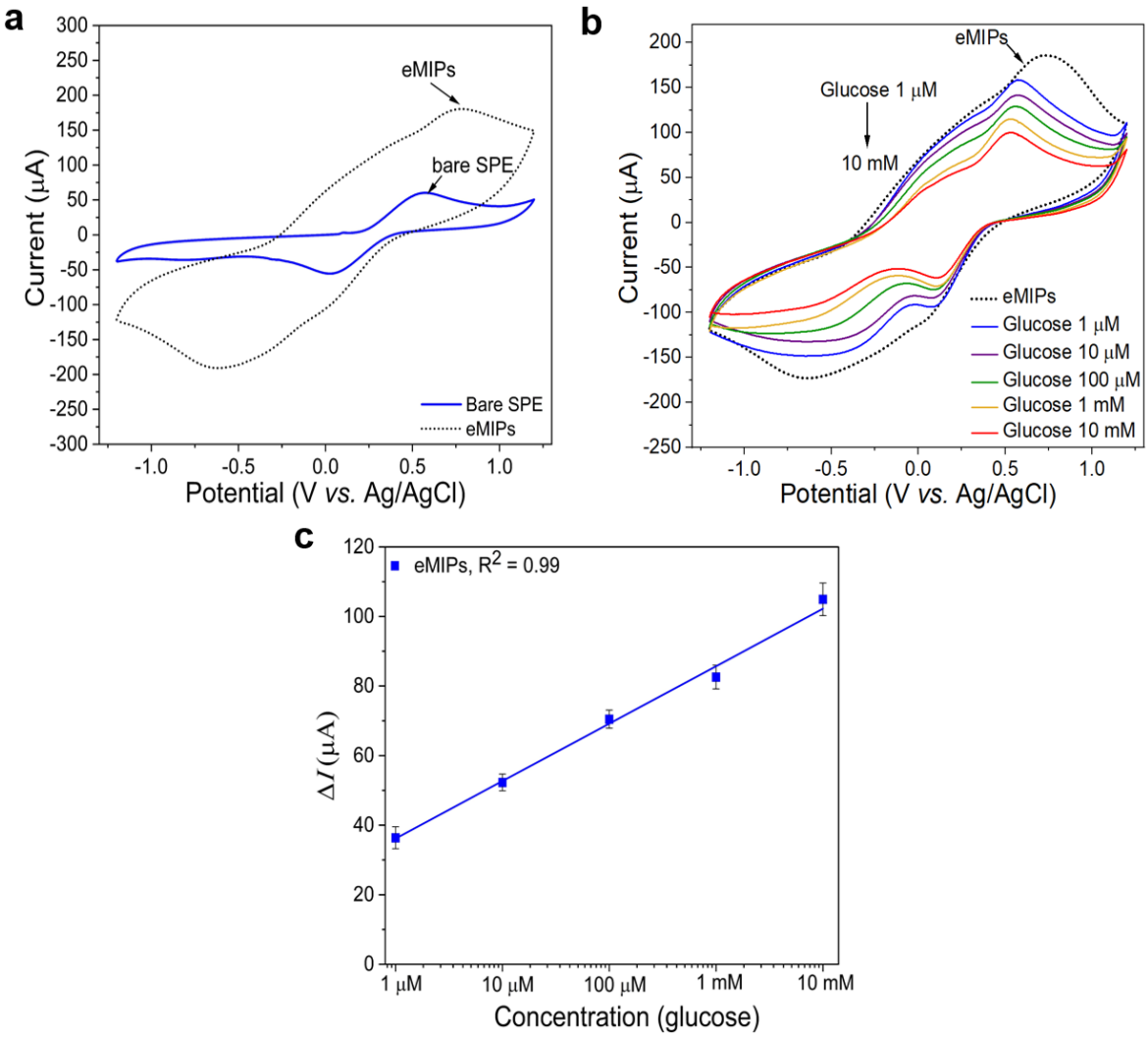

Figure 3.7: Cyclic voltammograms (CV) of **(a)** bare SPE and eMIPs functionalised SPE and **(b)** eMIPs in the presence of glucose at different concentrations in range of 1 µM-10 mM. **(c)** Calibration curve of glucose concentration (1 µM-10 mM) on x-axis vs. average change in current (ΔI) on y-axis (n=3). Results are expressed as mean ± standard deviation (SD) with error bars representing SD (n=3). CV measurements were performed in 0.1 M PBS (pH 7.0) containing 0.1 M KCl and 3.0 mM $[Fe(CN)_6]^{3-/4-}$ (buffer 4) at the scan rate of 50 mV s^{-1}.

The eMIPs sensors developed in this project use a single monomer (Py) for specific binding of glucose, which reduces the overall production cost and facilitates a scalable and straightforward manufacturing process. Other reports require surface modification of either MIPs with AuNPs or glucose oxidase enzyme (GOx) for glucose detection (LOD of 5 mM), such as using of multifunctional bio-nanospheres with boric acid-derived MIPs (Cheng et al., 2022; Sehit et al., 2020). Similarly, an electropolymerized MIP deposited onto Au SPEs was used for the sensing of glucose in saliva samples of healthy volunteers and a LOD was found to be 3.2 µM (Diouf et al., 2019). A glucose imprinted MIP

polymerised on the Au electrode using UV-light radiation showed a LOD 1.1 µM in a linear range of 5.0-120 µM with SWV (Fang et al., 2009). These reports have several drawbacks including tedious polymerisation process, not commercially feasible due to high material or electrode cost (commercial Au electrodes are around £250 or £5 for Au SPEs); and inconsistency in MIP layer homogeneity with each polymerisation. Besides that, these MIP sensors have not been tested with clinical samples of diabetic patients and therefore commercial feasibility and sensor utilisation is unknown.

Table 3.1: Comparison between eMIPs-sensor developed in this work and other glucose sensors reported in the literature.

Sensor	Detection method	Linear range (mM)	LOD (mM)	Reference
PtE/APBA/PPy MIP	Chrono impedimetric	1-45	0.3	(Onur Uygun and Ertuğrul Uygun, 2020)
MIP-micelles/Au electrode	differential pulse stripping voltammetry (DPSV)	0.2-8	10	(Yang et al., 2011)
Au NPs modified MIP film	CV	10^{-6}-10^{-4} and 10^{-4}-1.0^{-4}	3×10^{-8}	(Zhao et al., 2018)
Ferrocene modified eMIPs	DPV	0.8-50	0.43	(Garcia-Cruz et al., 2020)
AuNP-MIPs	SWV and EIS	1.25×10^{-6} - 0.2	1.25×10^{-6}	(Sehit et al., 2020)
Fe_3O_4 nanosphere/Au-GOx/MIPs	CV	0.01-5.0	0.005	(Cheng et al., 2022)
MIPs/Au-SPE	CV, DPV, EIS	0.0027-0.277	0.0032	(Diouf et al., 2019)
MIP/Au-electrode	SWV	0.005-0.12	0.0011	(Fang et al., 2009)
PPy/GOx/AuNPs/GRE	Amperometry	0.99-19.9	0.20	(German et al., 2017)
PVA/MnO_2@GO/CuO MIP	CV	500-4400	53	(Farid et al., 2016)
Ni-NPs/PPy/GRE	Amperometry	0.001-1	0.0004	(Emir et al., 2021)
PPy/GOx/PPy	Amperometry	0.5-24	0.026	(Ayenimo and Adeloju, 2017)
PPy-eMIPs	**CV**	**0.001-10**	**26×10^{-6}**	**This work**

(PPy: polypyrrole, GOx: glucose oxidase, PVA: polyvinyl acetate, GO: graphene oxide, APBA: aminophenylboronic acid, PtE: platinum screen-printed electrode, Ni-NPs: Nickel nanoparticles, GRE: graphite rod electrode, ITO: indium/tin oxide electrode, Au: gold, Au NPs: gold nanoparticles

3.4.4 Specificity of eMIPs sensor

The specificity of the glucose eMIPs sensors was evaluated using eNIPs functionalised SPEs (eNIPs-SPEs). For this, the eNIPs-SPEs were incubated with solutions of PBS with different concentrations of glucose (1 μM to 10 mM) and only a minimal decrease in current was observed (**Figure 3.8a**). The Δ*I* was observed to be negligible (~13μA) at the glucose concentration of 10 mM on eNIPs-SPEs compared to eMIPs (~105 μA) at the same glucose concentration (n=3, **Figure 3.8b**). These results can be attributed to the fact that glucose-complementary imprinted sites were absent in the eNIPs sensor. Therefore, no binding of glucose on eNIPs-SPEs was observed, indicating the high specificity of the eMIPs based glucose sensor. Similar results were reported by Masoudi *et al.* who also observed that there was negligible binding with the eNIPs as compared to glucose imprinted CuO/MnO_2/MIPs (Farid et al., 2016). Furthermore, Sehit *et al.* utilised AuNP-MIPs modified gold electrode for the electrochemical detection of glucose and the prepared sensor showed no significant change in current with glucose in the presence of eNIPs (Sehit et al., 2020).

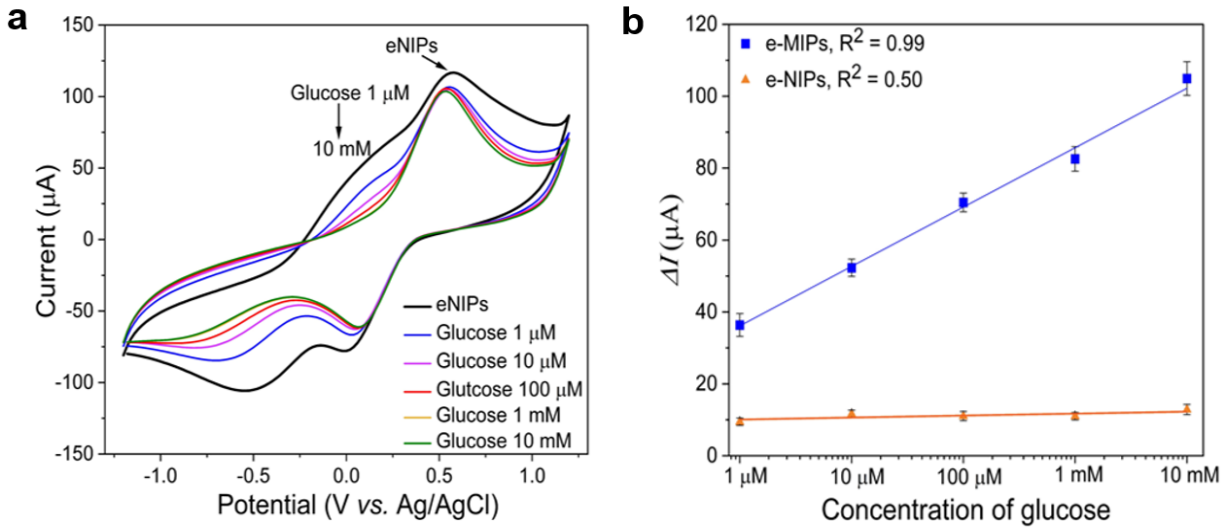

Figure 3.8: (a) CVs of eNIPs at different glucose concentrations (1 μM-10 mM). **(b)** Calibration curve of glucose (1 μM-10 mM) with eNIPs at x-axis vs. change in current (Δ*I*) at y-axis.

Imprinting factor (IF) was calculated by taking the ratio of the slope (Gagliani et al., 2024) (*m*) of the calibration curves of eMIPs (y = 7.273ln(x) + 86.082) and eNIPs (y = 0.266ln(x) + 11.81) as described in **Eq. 3.2**.

$$IF = m_{eMIP}/m_{eNIP} \quad \textbf{(Eq. 3.2)}$$

IF was found to be ~27 for our eMIPs and showed the specificity of eMIPs towards glucose, which indirectly confirm the imprinting of the glucose in the eMIPs. These results are higher or comparable to those reported for other MIP-based sensors, which typically have IF values ranging from 2-23 (Gagliani et al., 2024; Huang et al., 2018; Kugimiya et al., 2001).

3.4.5 Selectivity of eMIPs sensor

Human blood has a complicated matrix that contains ample compounds such as ascorbic acid, sugars, and a mixture of proteins, which can foul the electrode surface and interfere with the sensing mechanism (Qi and Tester, 2019; Salimi and Roushani, 2005). Galactose and fructose are monosaccharides which are present in blood along with glucose and thus impact sensing (Han et al., 2022; Qi and Tester, 2019). Ascorbic acid interference is particularly relevant because it co-exists with glucose in blood and can affect the accuracy of glucose measurements (J. Chen et al., 2008). Therefore, the selectivity of the eMIPs sensors was assessed against possible interferents including galactose, fructose, sucrose, and ascorbic acid using the same concentration range of glucose used in this study (1 µM-10 mM). CV measurements were recorded and the change in peak current was calculated for each sample. CV results showed almost no decrease in current with the incubation of galactose, fructose, and ascorbic acid (1 µM-10 mM) to the eMIP-SPEs (**Figure 3.9a-c**). At the highest (10 mM) concentration, Δ*I* was measured as only ~16, ~14 and ~18 µA for galactose, fructose and ascorbic acid, respectively. These values for Δ*I* were significantly lower compared to the Δ*I* response for glucose (~105 µA). This can be attributed to the incompatibility of the binding sites in the prepared eMIPs sensor with the above interferents. On the other hand, sucrose showed significant binding to the eMIPs at all the investigated concentrations. This is because sucrose is composed of 50 % glucose and 50 % fructose and the presence of glycosyl units in its structure is similar to glucose (**Figure 3.9d**). It is worth mentioning that sucrose binding to the eMIPs sensor will not hinder glucose detection in blood samples since it is not found in human blood. High affinity for sucrose has previously been reported for glucose MIP sensor, in agreement with our observations (Diouf et al., 2019; Sehit et al., 2020). The comparative graph (Δ*I* *vs.* concentration) of interferents (galactose, fructose, and ascorbic acid) and glucose with eMIPs (**Figure 3.9e**) showed that no significant change was observed with other interferents as compared to glucose. These observations highlight the high selectivity of eMIPs sensors towards glucose.

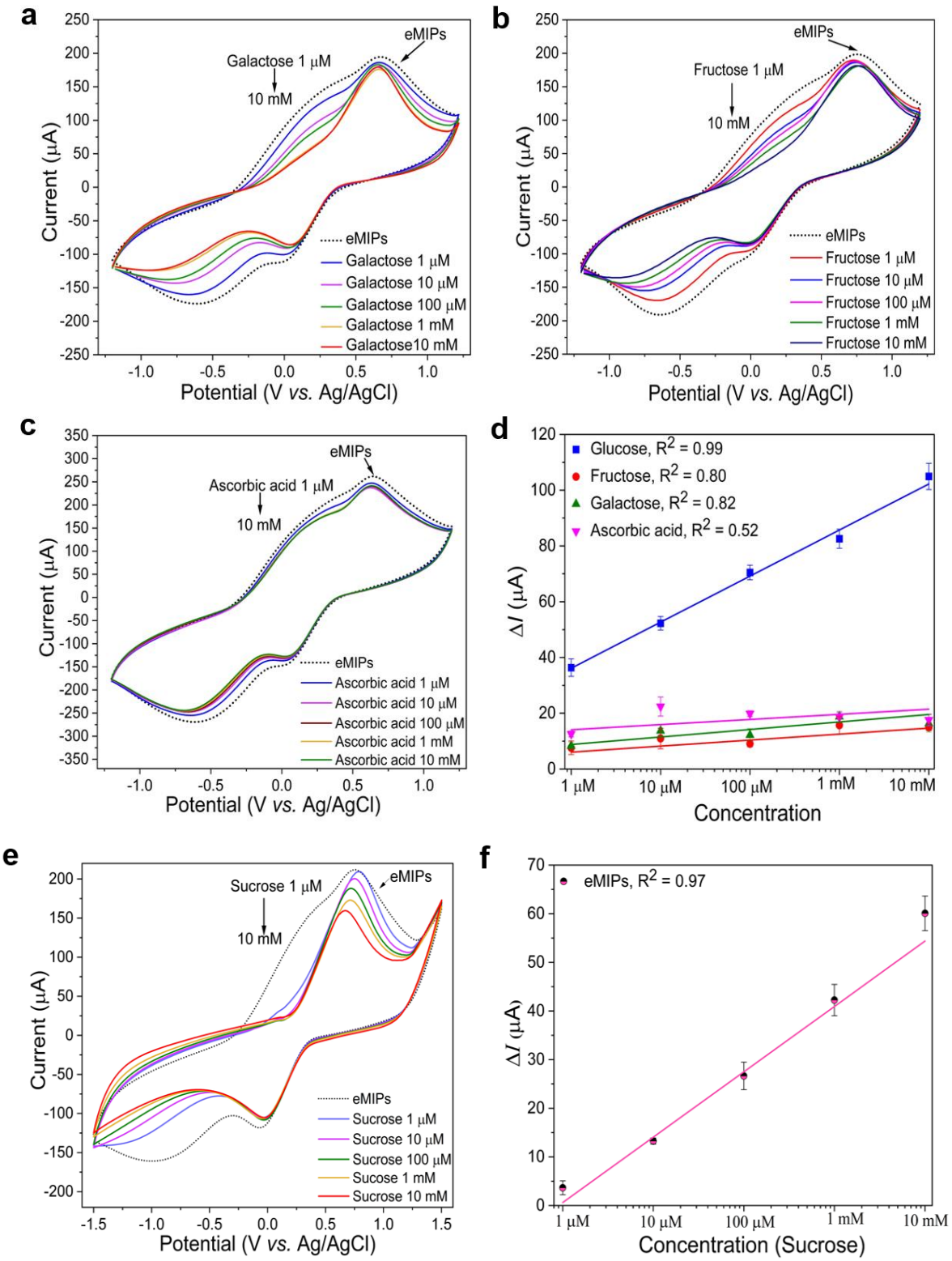

Figure 3.9: Selectivity of glucose imprinted eMIPs sensor with various interferent molecules including **(a)** galactose, **(b)** fructose, **(c)** ascorbic acid and **(d)** Comparison of eMIPs with interferents and glucose at various concentrations (1 µM-10 mM) at x-axis vs. Δ*I* at y-axis. **(e)** sucrose and **(f)** Calibration curve of sucrose (1 µM-10 mM) with eMIPs at x-axis vs. change in current (Δ*I*) at y-axis in buffer 4 at 50 mV s^{-1} scan rate (error bar represents SD, n=3).

3.4.6 Robustness, stability and reproducibility

The robustness of the eMIPs sensor was evaluated by measuring its Δ*I* response with glucose concentration (1 µM) over various temperatures ranging from 20 to 120 ºC. Moreover, the stability of eMIPs was determined over a one-year time (1 to 360 days). The eMIPs sensor retained 98 % of its original sensor response after incubation at 120 ºC **(Figure 3.10a)** and 85 % after 360 days **(Figure 3.10b)**, respectively. Our results were well corroborated with literature reports. For instance, Sehit *et al.* assessed the stability of gold nanoparticles-based eMIP sensor over a 40-day period, revealing a slight signal decrease. Diouf *et al.* also observed the stability of eMIP based glucose sensor for a period of 3 months, with the sensor preserving 85% of its initial response.(Diouf et al., 2019; Sehit et al., 2020) In contrast, our developed sensor demonstrated a very high stability over one year, retaining 85% of the initial response. These results show that our eMIPs sensor is highly robust and stable, even under extreme conditions whereas enzyme-based glucose sensors are only stable at low temperatures (4 ºC). The pH value has a significant role in the electrochemical reaction between the analyte and electrode (Bollella et al., 2019). Therefore, buffered solutions consisting of 0.1 M PBS, $[Fe(CN)_6]^{3-/4-}$ and 0.1 M KCl with different pH values (*i.e.*, pH 5.0, 7.0 and 9.0) were used to observe the effect of pH on binding of glucose to the eMIPs. It was observed that eMIPs incubation with glucose (at 1 µM and 10 mM respectively) showed slightly higher Δ*I* responses at the physiological pH 7.0 compared to pH 5.0 and 9.0, indicating that glucose had higher interactions with imprinted cavities at pH 7.0 **(Figure 3.10c)**. However, pH did not affect the sensing performance significantly and the changes in Δ*I* response was statistically negligible which further confirmed the stability and robustness of our eMIPs sensor.(Uang and Chou, 2003) The developed eMIPs sensor provide a more reliable and practical glucose sensing compared to common enzyme-based sensors that suffer from instability issues as the activity of enzymes (like GOx) can be easily influenced by temperature and buffer pH (Alexander et al., 2017a). Furthermore, to evaluate the reproducibility of eMIPs-SPE sensors, the electrochemical behaviour of six different eMIPs-SPEs (n=6), prepared in two batches (3 SPEs per batch of eMIPs) under identical conditions and the same amount of eMIPs nanoparticles, was studied using CV. The Δ*I* response of different SPEs incubated with 1 µM of glucose (**Figure 3.10d**) showed similar values across all SPEs, with a relative standard deviation (RSD) of 1.96 %, indicating the high reproducibility of the eMIPs-SPE sensors. Similar observations were reported previously on PPy-based

eMIPs for the electrochemical detection of *Klebsiella pneumonia* (RSD of 1.8%) (R. Sharma et al., 2022) and on metal organic framework based PPy-eMIPs for the determination of dopamine in human serum samples (RSD of 2.25 %) (W. Zhang et al., 2018). The prepared sensor exhibited consistent performance, showcasing its ability to maintain a reliable and reproducible response over time. This robust and long-term stable behaviour underscores the durability and long-term effectiveness of the eMIPs sensor, enhancing its potential for practical applications in various sensing scenarios.

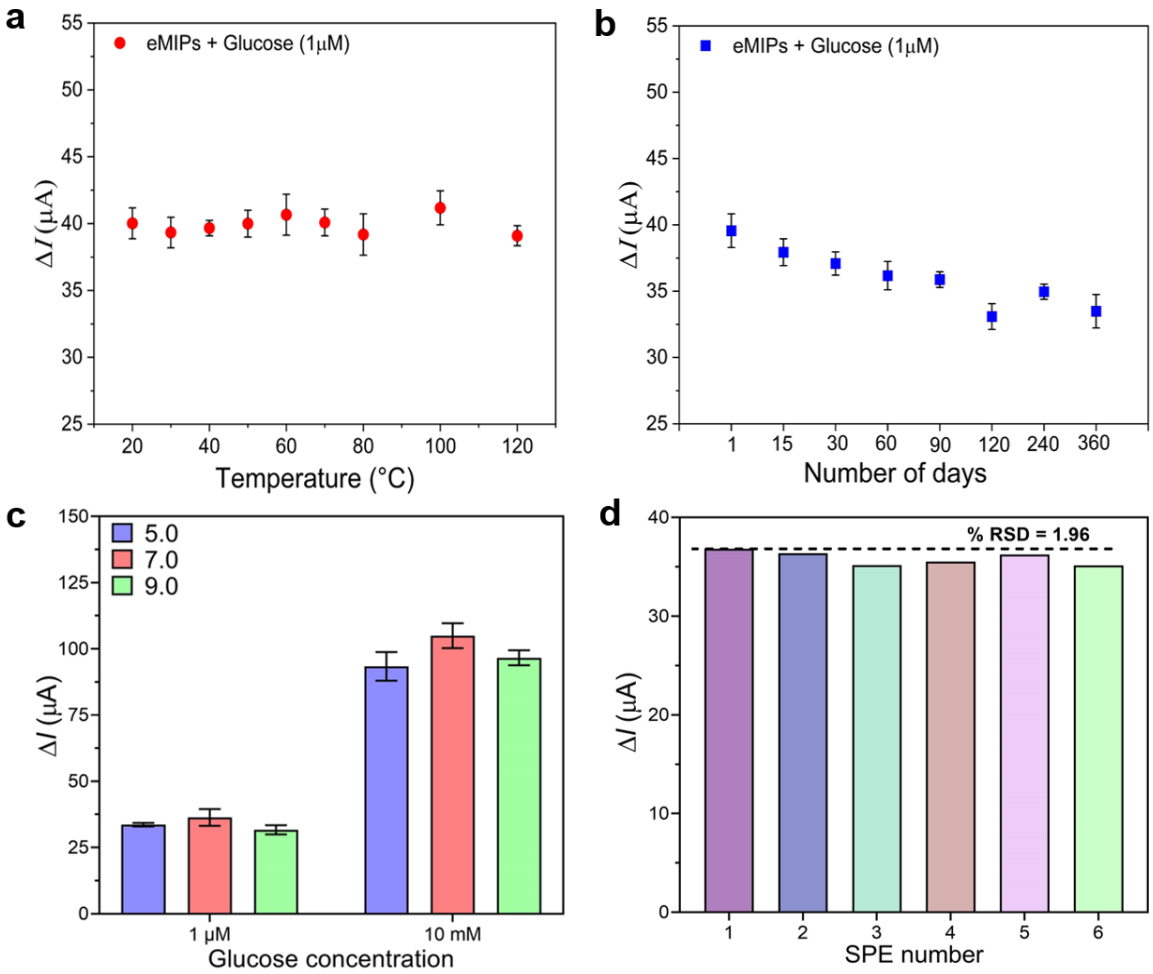

Figure 3.10: (a) Robustness of eMIPs sensor when exposed to temperatures of 20-120 ºC for 30 min. **(b)** Long-term stability study of eMIPs sensor on different days (1-360 days). The eMIPs sensor was tested in a 1 μM glucose concentration in PBS. **(c)** Effect of different pH (5.0, 7.0, and 9.0) on the stability of eMIPs sensor when incubated with glucose at two different concentrations (1 μM and 10 mM). **(d)** Reproducibility study of eMIPs-SPEs sensor (n=6) in the presence of 1 μM glucose. Experiments were performed in triplicates (n=3). Error bars represent SD.

3.4.7 Electrochemical detection of glucose with a two-electrode setup

As a proof of concept, CV measurements were also carried out with a two-electrode setup using eMIPs-SPE as WE and Pt wire as CE. CV results revealed that the incubation of glucose (1 µM-10 mM) with eMIPs sensor had a concentration dependent decrease in current (**Figure 3.11a**). The calibration curve of Δ*I vs.* glucose concentrations (1 µM-10 mM) showed a linear relationship as depicted in **Figure 3.11b.** There was no significant difference in the CV results obtained from the two-electrode and three-electrodes setups (**section 2.2.7, Chapter 2**) and there was a high correlation (0.98) between the data. Compared to the conventional three-electrode systems commonly used for biosensing, the two-electrode setup could be easier and cheaper to make and is more commercially viable since it does not rely on the use of a reference electrode which can be expensive. Additionally, the two-electrode systems eliminate the need for complicated measurement setups as they may be easily used in conjunction with traditional electronics and therefore have relevance towards developing miniaturised wearable sensors. The high correlation of the sensing response between the two-electrode and three-electrode systems opens doors to developing wearable sensors that are tiny, easy to fabricate, scalable, and cost-effective.

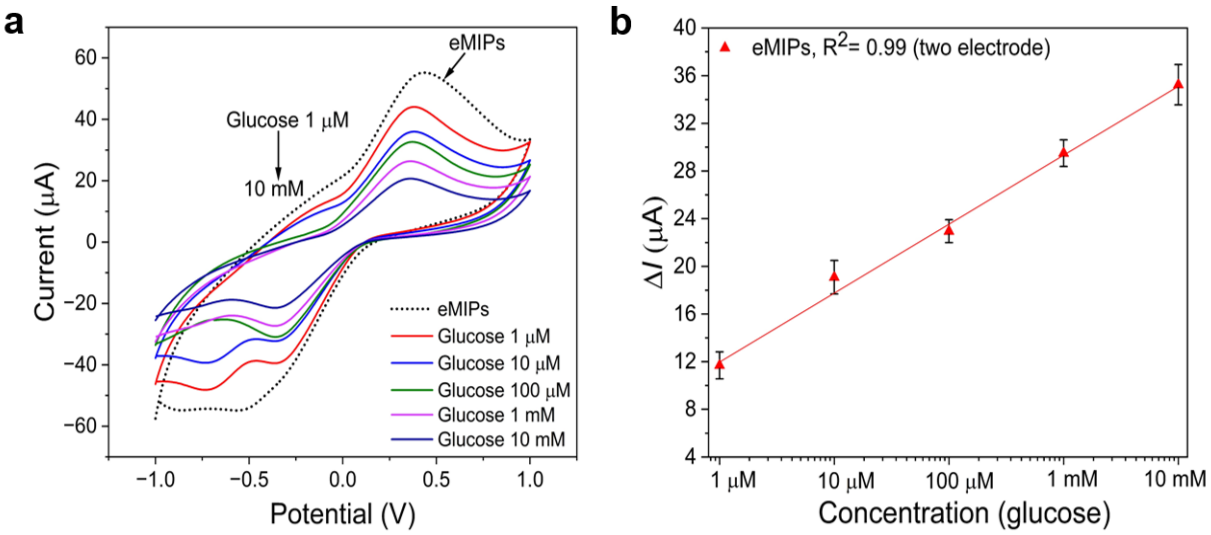

Figure 3.11: (a) CV of eMIPs with glucose (1 µM-10 mM) in two-electrode setup. **(b)** Calibration curves of glucose (1 µM-10 mM) *vs.* Δ*I* (µA) in two-electrode setup.

3.4.8 Electrochemical detection of glucose in real samples

(i) Detection of glucose in spiked human serum samples

The nonspecific adsorption of numerous biomolecules present in complex sample matrix

(serum, blood/plasma, and saliva) can lead to fouling at the electrode interface. This can significantly impede electrochemical performance, a reduction in both the sensitivity and specificity of the biosensor's electrochemical signal (Russo et al., 2021). However, our developed sensor was able to detect glucose concentrations (1 µM-10 mM) with high sensitivity (~2.91 µA and 0.608 µA μM^{-1} mm^{-2},) in spiked human serum (HS) samples using both three-electrode (**Figure 3.12a**) and two-electrode systems (**Figure 3.12b**) respectively. The calibration curve for the three-electrode and two-electrode sensors showed linear relationships between Δ*I* and logarithmic glucose concentration (mM) with a high correlation coefficient (R^2) of 0.99 (**Figure 3.12c**). However, the difference in the Δ*I* of two and three electrode system can be attributed to the fact that in a two-electrode system, the counter electrode is utilised as the reference electrode. Unlike the dedicated reference electrode, the potential of the counter electrode fluctuates during measurement, leading to varying results. Many literature studies have reported the glucose sensing in diluted HS using non-enzymatic electrochemical sensors but those typically require alkaline media (Rajendran et al., 2018; Wu et al., 2016). Our study achieved the glucose detection in the physiological pH range without the need for an expensive and time-consuming preparation process.

(ii) Detection of glucose in diabetic patients' serum samples

A random venous blood (serum) glucose level ≥11 mM or a fasting blood glucose level ≥7 mM on two or more separate occasions, is indicative of a probable diagnosis of diabetes in an individual (Collaboration, 2010; Mathew and Tadi, 2020). Therefore, the real time applicability, reliability, and accuracy of the proposed eMIPs sensors were investigated to determine glucose in serum samples of diabetic patients. The samples from five different patients (Pt.) including males and females with old DM history were tested to measure glucose levels. The glucose concentration (mM) obtained with eMIPs sensor (in both three-electrode and two-electrode setups) showed no significant difference (confidence coefficient 95%) compared to the Roche blood analyser results (data from Newcastle upon Tyne Hospital Trust). The concentration of glucose in the diabetic serum samples was determined using a calibration curve of glucose spiked HS (for both three-electrode and two-electrode systems) and the results (in triplicates) were presented in **Figure 3.12d**. The correlation coefficients for the three-electrode and two-electrode systems with the Roche blood analyser (hospital method) was found to be 0.93 and 0.96, respectively.

Correlation coefficients with magnitudes between 0.9 and 1.0 indicate very high levels of correlation between variables. Thus, these findings demonstrated a significant correlation between the prepared sensors and the established hospital method/Roche blood analyser, affirming the reliability of the developed eMIPs based electrochemical sensor. Notably, the correlation between the results obtained from the two-electrode and three-electrode setups further underscores the robustness of the developed material and sensor platform. These results collectively support the practical application of the prepared sensors in real-time glucose detection.

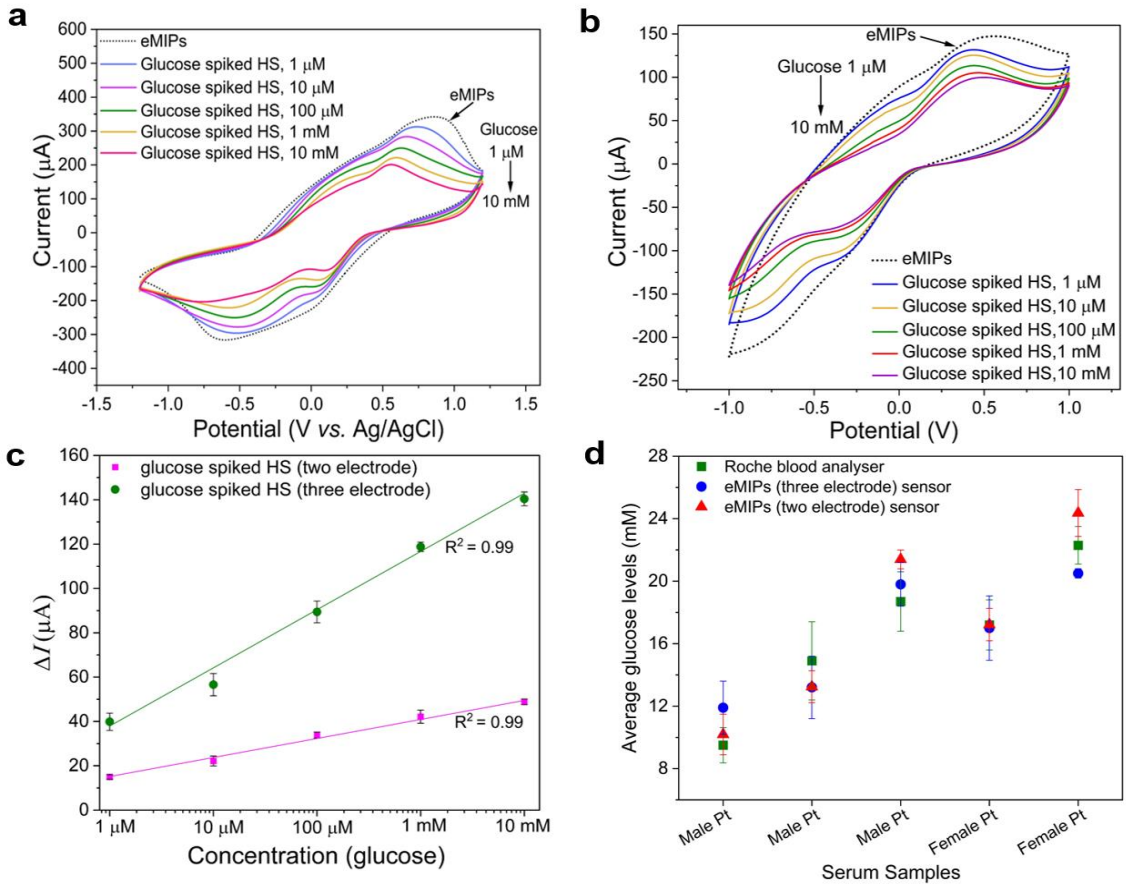

Figure 3.12: CVs of eMIPs with glucose (1 μM-10 mM) spiked human serum (HS, 100X diluted) in a **(a)** three-electrode setup and **(b)** two-electrode setup**. (c)** Calibration curves of glucose concentration in HS (1 μM-10 mM) *vs.* Δ*I* in three-electrode and two-electrode setups (n=3). **(d)** Comparison of average glucose levels in five different (male and female) diabetic patients' (Pt) serum samples determined using Roche blood analyser (hospital method) and eMIPs sensor in three-electrode and two-electrode setups. Error bars represent SD.

(iii) Application of eMIPs sessor in artificial interstitial fluids (AISF)

Wearable monitoring for glucose can be carried out in ISF (the liquid just below the skin) because ISF is very similar in composition to plasma/serum and can be extracted using

non-invasive methods such as reverse iontophoresis and hydrogel microneedle patches (Miller et al., 2018; Samant et al., 2020). Since glucose freely diffuses from capillaries into the interstitial space, the glucose level in the ISF is a reliable indicator of the blood glucose level (Bantle and Thomas, 1997). Understanding the behaviour of glucose in an environment similar to ISF could provide a reliable and practical understanding of the real-life performance of the sensor for diabetes management practices (Saha et al., 2023; Siegmund et al., 2017). We validated the performance of the eMIPs sensor in glucose (1µM to 10 mM) spiked artificial ISF (AISF, pH 7.4). Monitoring the current response revealed a concentration dependent decrease in the peak current (**Figure 3.13a**). Furthermore, the calibration curve of Δ*I* *vs.* glucose spiked AISF (1µM to 10 mM) concentrations (in logarithmic scale) showed a linear relationship (**Figure 3.13b**) with a R^2 of 0.99 (n=3) and a LOD of 44 nM. Notably, a similar trend for Δ*I* response was observed with AISF samples as with Δ*I* response for the three-electrode system and spiked HS samples. The ability of eMIPs sensor to determine the glucose levels in AISF samples (1 µM to 10 mM) and a strong correlation with results from spiked serum samples (~0.99) suggest the suitability of our eMIPs sensor for the development of wearable sensors.

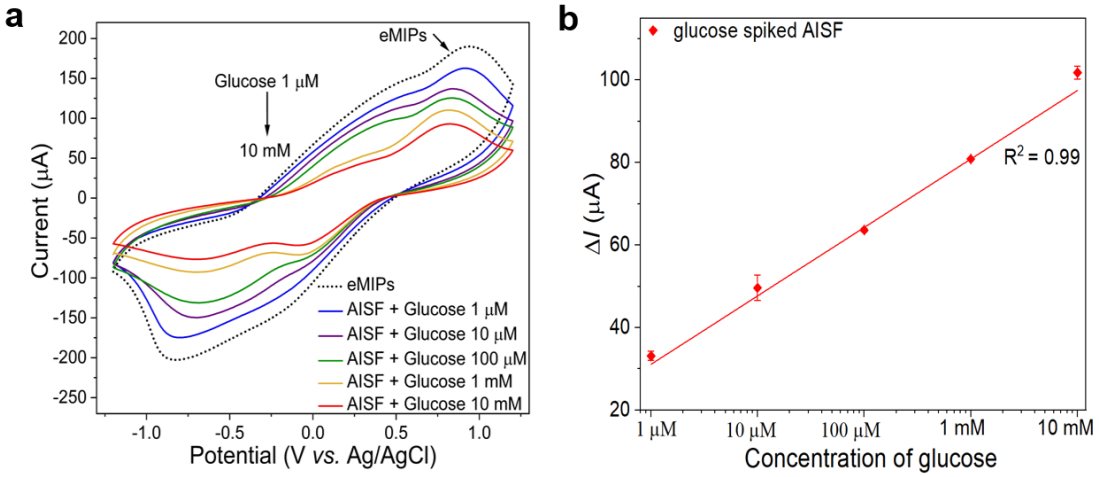

Figure 3.13: (a) CVs of eMIPs with glucose (1 µM-10 mM) spiked artificial interstitial fluid (AISF). **(b)** Calibration curves of Δ*I* vs. glucose concentration (1 µM-10 mM) in AISF (pH 7.4) in three-electrode electrode setup (n=3). Error bars represent SD.

3.5 Conclusion

This is the first report which demonstrate a novel method for the fabrication of PPy based eMIPs sensor for the monitoring of glucose in real samples of diabetic patients. The

production of eMIPs involves a straightforward, cost-effective and facile bulk synthesis process that eliminates the need for lengthy and expensive fabrication steps and materials such as enzymes, AuNPs, and carbon dots. The developed sensor is inexpensive (SPEs<$0.1) and has high robustness (withstanding 120 ^{o}C), long-term stability (12 months), fast response time (<30 s), excellent selectivity, and specificity. CV measurements revealed highly specific binding of glucose with eMIPs based sensor in a wide working range (1 µM-10 mM) with a LOD of ~26 nM (or ~136 nM) and sensitivity of ~2.91 µA μM^{-1} mm^{-2} (or ~0.608 µA μM^{-1} mm^{-2}) when used in a three-electrode (or two-electrode) setup. The clinical potential of the eMIPs sensor as a reliable tool for monitoring glucose levels in diabetic patients was demonstrated by showing a strong correlation (>0.9) of the sensing signal with the data from the common Roche blood analyser. Our eMIPs sensor demonstrated a wide detection range of 1 µM to 10 mM in AISF with a LOD of ~44 nM and strong correlation with serum glucose, highlighting its potential application for non-invasive measurements with wearable technology. Additionally, the use of a two-electrode setup eliminates the need for a reference electrode, enhances the versatility of the sensor, and makes it possible to achieve sensors that are easier and more cost-effective to manufacture. Given the versatility of eMIPs, this technology can extend to detecting other biological molecules like uric acid, dopamine, and creatinine. Utilising dual/triple SPEs enables the simultaneous detection of two or three biological molecules, critical for diabetes patients who have associated co-morbidities that need to be monitored at the same time.

Additional information: The rationale for the simultaneous addition of surfactant and glucose is that Pluronic P84 facilitates glucose solubilisation and micelle formation, ensuring uniform dispersion and effective molecular imprinting. The eMIPs-SPEs were prepared by drop-casting 20 µL of eMIPs (2 mg mL^{-1}) on WE of SPEs. To confirm the repeatability and regenerative performance of a single electrode, the same eMIPs-SPE was subjected to multiple cycles of glucose detection, with DI water washing between cycles. Furthermore, to determine the reproducibility of the developed sensor, CV measurements were performed with six different eMIPs-SPEs (prepared under the same conditions) incubated with 1 µM concentration of glucose. The relative standard deviation (RSD) in percentage was calculated to observe the reproducibility of the developed sensor. The minimum working volume of glucose to be determined with eMIPs sensor was 5 µL for all the experiments. The normal range of glucose in ISF is approximately 3.9-

6.6 mM and 1.99-22.2 in non-diabetic and diabetic individuals respectively (Sun et al., 2024).

This chapter has demonstrated the successful use of single monomer-based eMIPs for the detection of small molecule *i.e.* glucose. However, the detection and analysis of more complex targets, such as proteins, require different monomers to facilitate multiple interactions such as ionic interactions, hydrogen bonding and hydrophobic interactions. To achieve this, a solid-phase synthesis approach will be employed, incorporating various monomers tailored for these complex targets. The detailed methodology and application of this approach will be thoroughly discussed in Chapters 4 and 5.

3.6 References

(IDF), T. I. D. F. (2021). *Diabetes facts & figures*: IDF. Available at: https://idf.org/about-diabetes/diabetes-facts-figures/ (Accessed: 13-02-2024).

Adeel, M., et al. (2020). 'Recent advances of electrochemical and optical enzyme-free glucose sensors operating at physiological conditions' *Biosensors and Bioelectronics*, 165 p. 112331.

Ajjan, R. A., et al. (2018). 'Accuracy of flash glucose monitoring and continuous glucose monitoring technologies: Implications for clinical practice' *Diabetes and Vascular Disease Research*, 15 (3) pp. 175-184.

Alexander, S., Baraneedharan, P., Balasubrahmanyan, S. & Ramaprabhu, S. (2017a). 'Highly sensitive and selective non enzymatic electrochemical glucose sensors based on graphene oxide-molecular imprinted polymer' *Materials Science and Engineering: C*, 78 pp. 124-129.

Alexander, S., Baraneedharan, P., Balasubrahmanyan, S. & Ramaprabhu, S. (2017b). 'Modified graphene based molecular imprinted polymer for electrochemical non-enzymatic cholesterol biosensor' *European Polymer Journal*, 86 pp. 106-116.

Alonso-Lomillo, M. A. & Domínguez-Renedo, O. (2023). 'Molecularly imprinted polypyrrole based electrochemical sensor for selective determination of ethanethiol' *Talanta*, 253 p. 123936.

Ayenimo, J. G. & Adeloju, S. B. (2017). 'Amperometric detection of glucose in fruit juices with polypyrrole-based biosensor with an integrated permselective layer for exclusion of interferences' *Food chemistry*, 229 pp. 127-135.

Bantle, J. P. & Thomas, W. (1997). 'Glucose measurement in patients with diabetes mellitus with dermal interstitial fluid' *Journal of Laboratory and Clinical Medicine*, 130 (4), pp. 436-441.

Bharath, M., et al. (2022). 'Influence of electrochemical co-deposition of bimetallic pt–pd nanoclusters on polypyrrole modified ito for enhanced oxidation of 4-(hydroxymethyl) pyridine' *RSC advances*, 12 (27), pp. 17036-17048.

Bhilare, N. V., Shedge, R., Tambe, P. M. & More, A. (2024). 'Unveiling the potential of prodrug and drug-conjugate strategies in treatment of diabetes mellitus and its complications' *Medicinal Chemistry Research*, pp. 1-17.

Bollella, P., et al. (2019). 'Minimally invasive glucose monitoring using a highly porous gold microneedles-based biosensor: Characterisation and application in artificial interstitial fluid' *Catalysts*, 9 (7), p. 580.

Canfarotta, F., et al. (2018). 'A novel capacitive sensor based on molecularly imprinted nanoparticles as recognition elements' *Biosensors and Bioelectronics*, 120 pp. 108-114.

Chang, T., et al. (2022). 'Highly integrated watch for noninvasive continual glucose monitoring' *Microsystems & Nanoengineering*, 8 (1), p. 25.

Chen, H., et al. (2008). 'Mechanically strong, electrically conductive, and biocompatible graphene paper' *Advanced Materials*, 20 (18), pp. 3557-3561.

Chen, J., Zhang, W.-D. & Ye, J.-S. (2008). 'Nonenzymatic electrochemical glucose sensor based on mno2/mwnts nanocomposite' *Electrochemistry Communications*, 10 (9), pp. 1268-1271.

Chen, Z., et al. (2020). 'A low-cost paper glucose sensor with molecularly imprinted polyaniline electrode' *Sensors*, 20 (4), p. 1098.

Cheng, Y., et al. (2022). 'The construction of molecularly imprinted electrochemical biosensor for selective glucose sensing based on the synergistic enzyme-enzyme mimic catalytic system' *Talanta*, 242 p. 123279.

Collaboration, E. R. F. (2010). 'Diabetes mellitus, fasting blood glucose concentration, and risk of vascular disease: A collaborative meta-analysis of 102 prospective studies' *The lancet*, 375 (9733), pp. 2215-2222.

Corrie, S. R., et al. (2015). 'Blood, sweat, and tears: Developing clinically relevant protein biosensors for integrated body fluid analysis' *Analyst*, 140 (13), pp. 4350-4364.

Crapnell, R. D., et al. (2021). 'Electrospun nylon fibers with integrated polypyrrole molecularly imprinted polymers for the detection of glucose' *Analytical Chemistry*, 93 (39), pp. 13235-13241.

Ding, S., et al. (2021). 'Molecularly imprinted polypyrrole nanotubes based electrochemical sensor for glyphosate detection' *Biosensors and Bioelectronics*, 191 p. 113434.

Diouf, A., Bouchikhi, B. & El Bari, N. (2019). 'A nonenzymatic electrochemical glucose sensor based on molecularly imprinted polymer and its application in measuring saliva glucose' *Materials Science and Engineering: C*, 98 pp. 1196-1209.

Emir, G., Dilgin, Y., Ramanaviciene, A. & Ramanavicius, A. (2021). 'Amperometric nonenzymatic glucose biosensor based on graphite rod electrode modified by ni-nanoparticle/polypyrrole composite' *Microchemical Journal*, 161 p. 105751.

Fang, C., et al. (2009). 'Electrochemical sensor based on molecular imprinting by photo-sensitive polymers' *Biosensors and Bioelectronics*, 24 (10), pp. 3164-3169.

Farid, M. M., et al. (2016). 'Molecular imprinting method for fabricating novel glucose sensor: Polyvinyl acetate electrode reinforced by mno2/cuo loaded on graphene oxide nanoparticles' *Food chemistry*, 194 pp. 61-67.

Gagliani, F., et al. (2024). 'Green synthesis of a molecularly imprinted polymer based on a novel thiophene-derivative for electrochemical sensing' *Molecules*, 29 (7), p. 1632.

Gao, W., et al. (2019). 'Flexible electronics toward wearable sensing' *Accounts of chemical research*, 52 (3), pp. 523-533.

Garcia-Cruz, A., et al. (2020). 'Generic sensor platform based on electro-responsive molecularly imprinted polymer nanoparticles (e-nanomips)' *Microsystems & Nanoengineering*, 6 (1), p. 83.

German, N., Ramanavicius, A. & Ramanaviciene, A. (2017). 'Amperometric glucose biosensor based on electrochemically deposited gold nanoparticles covered by polypyrrole' *Electroanalysis*, 29 (5), pp. 1267-1277.

Gonçalves, M. d. L., Truta, L. A., Sales, M. G. F. & Moreira, F. T. (2021). 'Electrochemical point-of care (poc) determination of interleukin-6 (il-6) using a pyrrole (py) molecularly imprinted polymer (mip) on a carbon-screen printed electrode (c-spe)' *Analytical Letters*, 54 (16), pp. 2611-2623.

Han, Z., et al. (2022). 'Graphene oxide/gold nanoparticle/graphite fiber microelectrodes for directing electron transfer of glucose oxidase and glucose detection' *Journal of Power Sources*, 521 p. 230956.

Hanna, J., et al. (2022). 'Wearable flexible body matched electromagnetic sensors for personalised non-invasive glucose monitoring' *Scientific Reports*, 12 (1), p. 14885.

Harding, J. L., et al. (2019). 'Global trends in diabetes complications: A review of current evidence' *Diabetologia*, 62 pp. 3-16.

Hassan, M. H., Vyas, C., Grieve, B. & Bartolo, P. (2021). 'Recent advances in enzymatic and non-enzymatic electrochemical glucose sensing' *Sensors*, 21 (14), p. 4672.

Healthline *Comparing top glucose monitoring devices*. Available at: https://www.healthline.com/diabetesmine/dexcom-vs-abbott-freestyle-libre-cgm-function-accuracy-and-cost (Accessed: 26 march).

Huang, J., et al. (2018). 'Selective and sensitive glycoprotein detection via a biomimetic electrochemical sensor based on surface molecular imprinting and boronate-modified reduced graphene oxide' *Sensors and Actuators B: Chemical*, 259 pp. 1-9.

Inc., G. M. I. (2023). *Glucose biosensors market size - by type (continuous glucose monitoring, self-monitoring blood glucose), by technology (electrochemical biosensors, optical biosensors), by end-use (hospitals, home care, diagnostic centers & clinics), global forecast, 2023-2032*: Global Market Insights Inc. Available at: https://www.gminsights.com/industry-analysis/glucose-biosensors-market.

Inzucchi, S. E. (2012). 'Diagnosis of diabetes' *New England Journal of Medicine*, 367 (6), pp. 542-550.

K. M, A., et al. (2024). 'Internet of things enabled open source assisted real-time blood glucose monitoring framework' *Scientific Reports*, 14 (1), p. 6151.

Kudva, Y. C., et al. (2018). 'Approach to using trend arrows in the freestyle libre flash glucose monitoring systems in adults' *Journal of the Endocrine Society*, 2 (12), pp. 1320-1337.

Kugimiya, A., Mukawa, T. & Takeuchi, T. (2001). 'Synthesis of 5-fluorouracil-imprinted polymers with multiple hydrogen bonding interactions' *Analyst*, 126 (6), pp. 772-774.

Lee, H., et al. (2018). 'Enzyme-based glucose sensor: From invasive to wearable device' *Advanced healthcare materials*, 7 (8), p. 1701150.

Li, Y., Song, Y.-Y., Yang, C. & Xia, X.-H. (2007). 'Hydrogen bubble dynamic template synthesis of porous gold for nonenzymatic electrochemical detection of glucose' *Electrochemistry Communications*, 9 (5), pp. 981-988.

Luo, J., et al. (2012). 'A novel non-enzymatic glucose sensor based on cu nanoparticle modified graphene sheets electrode' *Analytica chimica acta*, 709 pp. 47-53.

Mathew, T. K. & Tadi, P. (2020). 'Blood glucose monitoring'.

McClements, J., et al. (2022). 'Molecularly imprinted polymer nanoparticles enable rapid, reliable, and robust point-of-care thermal detection of sars-cov-2' *ACS sensors*, 7 (4), pp. 1122-1131.

Miller, P. R., et al. (2018). 'Extraction and biomolecular analysis of dermal interstitial fluid collected with hollow microneedles' *Communications biology*, 1 (1), p. 173.

Olansky, L. & Kennedy, L. (2010). Finger-stick glucose monitoring: Issues of accuracy and specificity. Am Diabetes Assoc.

Omastová, M., et al. (1996). 'Electrical properties and stability of polypyrrole containing conducting polymer composites' *Synthetic Metals*, 81 (1), pp. 49-57.

Onur Uygun, Z. & Ertuğrul Uygun, H. D. (2020). 'A novel chronoimpedimetric glucose sensor in real blood samples modified by glucose-imprinted pyrrole-

aminophenylboronic acid modified screen printed electrode' *Electroanalysis*, 32 (2), pp. 226-229.

Park, S., Boo, H. & Chung, T. D. (2006). 'Electrochemical non-enzymatic glucose sensors' *Analytica chimica acta*, 556 (1), pp. 46-57.

Picconi, F., et al. (2017). 'Retinal neurodegeneration in patients with type 1 diabetes mellitus: The role of glycemic variability' *Acta Diabetologica*, 54 pp. 489-497.

Piletsky, S. A. & Turner, A. P. (2002). 'Electrochemical sensors based on molecularly imprinted polymers' *Electroanalysis: An International Journal Devoted to Fundamental and Practical Aspects of Electroanalysis*, 14 (5), pp. 317-323.

Qi, X. & Tester, R. F. (2019). 'Fructose, galactose and glucose–in health and disease' *Clinical nutrition ESPEN*, 33 pp. 18-28.

Rajendran, S., et al. (2018). 'Influence of mesoporous defect induced mixed-valent nio (ni2+/ni3+)-tio2 nanocomposite for non-enzymatic glucose biosensors' *Sensors and Actuators B: Chemical*, 264 pp. 27-37.

Ramanavičius, S., et al. (2022). 'Electrochemically deposited molecularly imprinted polymer-based sensors' *Sensors*, 22 (3), p. 1282.

Ratautaite, V., et al. (2022). 'Molecularly imprinted polypyrrole based sensor for the detection of sars-cov-2 spike glycoprotein' *Electrochimica acta*, 403 p. 139581.

Russo, M. J., et al. (2021). 'Antifouling strategies for electrochemical biosensing: Mechanisms and performance toward point of care based diagnostic applications' *ACS sensors*, 6 (4), pp. 1482-1507.

Saha, T., et al. (2023). 'Wearable electrochemical glucose sensors in diabetes management: A comprehensive review' *Chemical Reviews*, 123 (12), pp. 7854-7889.

Salimi, A. & Roushani, M. (2005). 'Non-enzymatic glucose detection free of ascorbic acid interference using nickel powder and nafion sol–gel dispersed renewable carbon ceramic electrode' *Electrochemistry Communications*, 7 (9), pp. 879-887.

Samant, P. P., et al. (2020). 'Sampling interstitial fluid from human skin using a microneedle patch' *Science translational medicine*, 12 (571), p. eaaw0285.

Sehit, E. & Altintas, Z. (2020). 'Significance of nanomaterials in electrochemical glucose sensors: An updated review (2016-2020)' *Biosensors and Bioelectronics*, 159 p. 112165.

Sehit, E., et al. (2020). 'Ultrasensitive nonenzymatic electrochemical glucose sensor based on gold nanoparticles and molecularly imprinted polymers' *Biosensors and Bioelectronics*, 165 p. 112432.

Sharif, H. E., et al. (2022). 'Evaluation of electropolymerised molecularly imprinted polymers (e-mips) on disposable electrodes for detection of sars-cov-2 in saliva' *Analytica Chimica Acta*, 1206 p. 339777.

Sharma, R., Lakshmi, G., Kumar, A. & Solanki, P. (2022). 'Polypyrrole based molecularly imprinted polymer platform for klebsiella pneumonia detection' *ECS Sensors Plus*, 1 (1), p. 010603.

Siegmund, T., Heinemann, L., Kolassa, R. & Thomas, A. (2017). 'Discrepancies between blood glucose and interstitial glucose—technological artifacts or physiology: Implications for selection of the appropriate therapeutic target' *Journal of diabetes science and technology*, 11 (4), pp. 766-772.

Silva, B. V., et al. (2016). 'An ultrasensitive human cardiac troponin t graphene screen-printed electrode based on electropolymerised-molecularly imprinted conducting polymer' *Biosensors and Bioelectronics*, 77 pp. 978-985.

Singla, P., et al. (2023a). 'Electrochemical and thermal detection of allergenic substance lysozyme with molecularly imprinted nanoparticles' *Analytical and Bioanalytical Chemistry*, pp. 1-12.

Singla, P., et al. (2023b). 'Enhancing encapsulation of hydrophobic phyto-drugs naringenin and baicalein in polymeric nano-micelles' *Journal of Drug Delivery Science and Technology*, 83 p. 104403.

Singla, P., et al. (2019). 'Temperature-dependent solubilisation of the hydrophobic antiepileptic drug lamotrigine in different pluronic micelles—a spectroscopic, heat transfer method, small-angle neutron scattering, dynamic light scattering, and in vitro release study' *ACS Omega*.

Sun, H., et al. (2022). 'Idf diabetes atlas: Global, regional and country-level diabetes prevalence estimates for 2021 and projections for 2045' *Diabetes research and clinical practice*, 183 p. 109119.

Uang, Y.-M. & Chou, T.-C. (2003). 'Fabrication of glucose oxidase/polypyrrole biosensor by galvanostatic method in various ph aqueous solutions' *Biosensors and Bioelectronics*, 19 (3), pp. 141-147.

Umer, A., Liaqat, F. & Mahmood, A. (2020). 'Moo3 nanobelts embedded polypyrrole/sis copolymer blends for improved electro-mechanical dual applications' *Polymers*, 12 (2), p. 353.

Wilson, R. & Turner, A. (1992). 'Glucose oxidase: An ideal enzyme' *Biosensors and bioelectronics*, 7 (3), pp. 165-185.

Wu, W., et al. (2016). 'A novel nonenzymatic electrochemical sensor based on 3d flower-like ni7s6 for hydrogen peroxide and glucose' *Sensors and Actuators B: Chemical*, 232 pp. 633-641.

Xu, J., et al. (2017). 'A molecularly imprinted polypyrrole for ultrasensitive voltammetric determination of glyphosate' *Microchimica Acta*, 184 pp. 1959-1967.

Xue, J., et al. (2023). 'Partially oxidised carbon nanomaterials with ni/nio heterostructures as durable glucose sensors' *Inorganic Chemistry*, 62 (7), pp. 3288-3296.

Yang, Y., et al. (2011). 'Glucose sensors based on electrodeposition of molecularly imprinted polymeric micelles: A novel strategy for mip sensors' *Biosensors and Bioelectronics*, 26 (5), pp. 2607-2612.

Zeng, Z., et al. (2010). 'Synthetic polymer nanoparticles with antibody-like affinity for a hydrophilic peptide' *ACS nano*, 4 (1), pp. 199-204.

Zhang, W., et al. (2018). 'Metal-organic framework-based molecularly imprinted polymer as a high sensitive and selective hybrid for the determination of dopamine in injections and human serum samples' *Biosensors and Bioelectronics*, 118 pp. 129-136.

Zhao, W., et al. (2018). 'Molecularly imprinted polymeric nanoparticles decorated with au nps for highly sensitive and selective glucose detection' *Biosensors and Bioelectronics*, 100 pp. 497-503.

Chapter 4: Electrochemical and Thermal Detection of Allergenic Substance Lysozyme with Molecularly Imprinted Nanoparticles

*(Published as P. Singla, S. Kaur, O. Jamieson, A. Dann, **S. Garg**, C. Mahon, R.D. Crapnell, C.E. Banks, I. Kaur, M. Peeters, 2023, Analytical and Bioanalytical Chemistry, 415, 4467-78)*

This co-author publication presents the development of molecularly imprinted nanoparticles (nanoMIPs) based dual sensor for the fast and on-site detection of lysozyme protein. This research work was led by Pankaj Singla who designed the work. I have contributed to the synthesis of nanoMIPs as well as electrochemical impedance spectroscopy experiments along with Sarbjeet Kaur and helped in writing the relevant sections of the manuscript. Olliver Jamieson and Ammy Dann assisted with the HTM experiments, Craig E. Banks and Robert Crapnell has provided the SPEs for sensor development. Clare Mahon, Inderpreet Kaur and Marloes Peeters offered their expert advice in conceptualising the work and helped to in review & editing the manuscript.

Monomers with various functional groups interact with the template (target of interest) molecule by self-organising around it and their double bonds or equivalent reactive sites enable polymerisation, forming a structured polymer network. Monomers used in this research work were selected based on their strong interactions with the target epitope and their functional groups facilitate intermolecular interactions such as hydrogen bonding, van der Waals forces, ionic bonding, or metal complexation. Therefore, in this work, a monomer mixture consisting of N-isopropylacrylamide (NIPAM) for hydrogen bonding, N-tert-butylacrylamide (TBAm) for hydrophobic interactions, N-(3-aminopropyl)methacrylamide hydrochloride (APMA) and acrylic acid (AAc) for ionic interactions with N,N′-methylenebisacrylamide (BIS) as a crosslinker was selected to prepare high-affinity nanoMIPs for Lysozyme (LYZ). LYZ, a small allergenic protein found in eggs that triggers allergic reactions, was selected as the template to prepare LYZ-imprinted nanoMIPs. Given the versatility of the nanoMIPs technology, these nanoMIPs can be adopted for other systems containing LYZ or other allergens proteins.

4.1 Abstract

Lysozyme (LYZ) is a small cationic protein which is widely used for medical treatment and in the food industry to act as an anti-bacterial agent; however, since it is an egg protein, it can trigger allergic reactions. In this study, high affinity molecularly imprinted

nanoparticles (nanoMIPs) were synthesised for LYZ using an innovative solid-phase approach. These nanoMIPs were electrografted to Screen-Printed Electrodes (SPEs), disposable electrodes with high commercial potential, to enable electrochemical and thermal sensing. Electrochemical impedance spectroscopy (EIS) facilitated fast measurement (5-10 min) and are able to determine trace levels of LYZ (pM) and can discriminate between LYZ and structurally similar proteins (bovine serum albumin, troponin-I). In tandem, thermal analysis was conducted with the Heat-Transfer Method (HTM), which is based on monitoring the heat-transfer resistance at the solid-liquid interface of the functionalised SPE. HTM as detection technique guaranteed trace level (fM) detection of LYZ but needed longer analysis time compared to EIS measurement (30 min *vs*. 5-10 min). Considering the versatility of the nanoMIPs which can be adapted to virtually any target of interest, these low-cost point-of-care (PoC) sensors hold great potential to improve food safety.

4.2 Introduction

Lysozyme (LYZ), also known as muramidase or N-acetylmuramic hydrolase, is a 14kDa cationic protein. It damages or kills bacteria via lysing peptidoglycan in the bacterial cell wall and disrupting their cell membrane (Ragland and Criss, 2017). Due to its bacterial properties, lytic activation and low molecular weight, LYZ has been widely applied for medical treatment and in the food industry to act as an anti-bacterial agent (Aminlari et al., 2014). Levels in bodily fluids range from µg/L levels in urine to 2.9 mg/L in serum and 1.65 g/L in tears, with increased serum levels being non-specific indicators of leukaemia and liver and kidney diseases (Porstmann et al., 1989; Sen and Sarin, 1986). Since LYZ is an egg protein, it can trigger allergic reactions even when present in trace amounts (Frémont et al., 2007). For instance, the recommended maximum level of LYZ to add during the production process of wine is 0.5 g/L (Weber et al., 2009). Thus, the accurate determination of LYZ in clinical and food samples in a fast and low-cost manner is of paramount importance from a medical and food safety perspective. Moreover, LYZ has long been used as a prominent model system for systematic studies on protein-protein interactions and to evaluate new detection methods.

Traditional detection of LYZ via enzyme-linked immunosorbent assays (ELISA) or chromatographic methods are either expensive, time-consuming, and cannot be used for fast *in-situ* quantification (Kerkaert et al., 2010; Vidal et al., 2005). Therefore, there has

been a drive towards portable devices that can facilitate fast and low-cost measurements. In particular, optical and electrochemical biosensors combined with specific recognition elements have attracted increasing attention (L. Wang et al., 2022). Coupling of Surface Enhanced Raman Spectroscopy with biomimetic receptors and chemometric analysis have demonstrated high sensitivity and selectivity for the detection of LYZ (Banciu et al., 2022). However, these methods cannot be miniaturised and therefore do not offer on-site detection. Electrodes modified with nanomaterials or polymeric films for sensing of proteins offer fast analytical times, high sensitivity and can be easily integrated into portable devices. An electrode modified with a composite of acrylic acid and hollow TiO_2 spheres and embedded aptamers as recognition elements was constructed (Zhang et al., 2015). Electrochemical impedance spectroscopy (EIS) results demonstrated that the aptasensor was able to measure LYZ with a limit of detection of 1.04 pM and a dynamic range between 0.05-100 µg L^{-1}. Aptasensors have been shown to be a promising technology for food allergen detection with an all-field search in Scopus using “allergens” and “aptamers” showing an increasing trend with 789 results in the 2016-2020 period (Melinte et al., 2021). Despite this increasing interest, aptamers can suffer from limited stability and specificity in complex matrices, which remains an issue for industrial development (Menger et al., 2016).

Molecularly Imprinted Polymers (MIPs), porous materials containing high affinity binding sites for the analyte of interest, can rival natural recognition elements in terms of affinity but possess superior thermal and chemical stability (Haupt and Mosbach, 2000; J. W. Lowdon et al., 2020). There are several reports of MIPs for LYZ in literature including MIP gels using acrylamide and methacrylic acid as functional monomers which facilitated complete removal of lysozyme from egg white (Ou et al., 2004). However, MIPs that are traditionally prepared via bulk polymerisation exhibit problems with diffusion limitations in the 3D matrix and resulting slow kinetics due to the large size of proteins (Culver and Peppas, 2017). To overcome these limitations, nanoscale and surface imprinting strategies have been employed which require less protein template to reduce synthesis cost and improve accessibility of the recognition sites (Flavin and Resmini, 2009; Ma et al., 2013). Surface protein imprinted core-shell particles combined with Reversible Additional-Fragmentation Chain Transfer polymerisation enables to improve the kinetics of binding and enhance control over the surface binding sites (Q. Li et al., 2014). As determined by high performance liquid chromatography (HPLC) with UV-vis detection,

these imprinted particles could bind 5.6 mg protein/mg material and could selectively recognise LYZ from a four-protein mixture and an egg white sample. This concept can be further explored when depositing thin MIP layers onto iron oxide particles to facilitate easy separation of LYZ from a complex solution by applying an external magnetic field (Y. Wang et al., 2015). The complication of using molecularly imprinted nanoparticles in the diagnostics and therapeutic sector is their biocompatibility and their integration into portable devices (Tse Bum Sui and Haupt, 2021). In this respect, the preparation of molecularly imprinted nanoparticles (nanoMIPs) from holds great potential. Water-soluble nanoparticles (NPs) were formed by self-assembling γ-glutamic acid with 3-aminothiophene followed by electro-polymerisation to generate a conductive polymer network. A MIP-based biosensor was produced which could arrange LYZ in a range from $1x10^{-10}$ to $1x10^{-5}$ g/L using differential pulse voltammetry as read-out strategy (X. Yang et al., 2022). These nanoparticles can be multifunctional and a “catch and release” system was developed where nanoMIPs can release LYZ, which was chosen as model protein, upon changing the temperature (Yoshimatsu et al., 2012).

Besides biocompatibility, is essential to have a scalable and straightforward nanoMIP production process. Solid-phase imprinting is an innovative technique for the medium scale fabrication of nanoMIPs with a homogenous distribution of binding sites and affinity similar to monoclonal antibodies due to the use of the solid-phase as affinity medium (F. Canfarotta et al., 2016; Moczko et al., 2013). These nanoMIPs have been used to construct highly selective and specific optical, thermal and electrochemical sensors for proteins (Abdin et al., 2015; Alanazi et al., 2021; F. Canfarotta et al., 2018). In this manuscript, we use solid-phase imprinting to develop nanoMIP-based sensors for the electrochemical and thermal detection of LYZ. These nanoMIPs will be electrografted onto screen-printed electrodes (SPEs), which have high potential for commercial use since they are disposable, low-cost, and exhibit high batch-to-batch inconsistency (Crapnell et al., 2022). We demonstrate that it is possible to detect LYZ with high accuracy and selectivity at relevant concentrations using either electrochemical detection or with an in-house developed thermal device. Since the nanoMIPs are highly versatile and adapting this for other targets is straightforward, the technology presented will serve as a platform for food allergen detection.

4.3 Experimental

4.3.1 Materials

Glass beads (53-106 µm diameter, Spheriglass 2429 CP00), N-isopropylacrylamide (NIPAM), N,N'-methylenebisacrylamide (BIS), N-tert-butylacrylamide (TBAm), N-(3-Aminopropyl)methacrylamide hydrochloride (APMA), acrylic acid (AAc), and N,N,N',N'-tetramethylethylenediamine (TEMED), (3-aminopropyl)trimethoxysilane (APTMS), Glutaraldehyde (GA), LYZ (from chicken egg white), PierceTM BCA Protein Assay Kit, ammonium persulfate (APS), methanol, acetone, acetonitrile, sodium hydroxide (NaOH) were used in this study. All chemicals and solvents were high-performance liquid chromatography (HPLC)/analytical grade and were used without any further purification (information provided in **Chapter 2)**. Additionally, dialysis cartridges (Vivaspin® 20, 3 kDa molecular weight cut-off (MWCO) Polyether-sulfone), Supelco polypropylene solid phase extraction tubes (60 mL) were used in the synthesis of nanoMIPs. PBS solutions were prepared with deionised (DI) water with resistivity of ≥18.2 MΩ cm).

4.3.2 Methods and equipment

The LYZ imprinted nanoMIPs were synthesised using solid phase synthesis approach. A protocol followed to manufacture nanoMIPs with high specificity and selectivity for LYZ is described in **Chapter 2**. The size distribution of resulting nanoMIPs were characterised by DLS experiments using a Malvern Zetasizer Nano ZS to measure the D_h at 25 ± 0.1 °C. For SEM measurements, nanoMIPs were drop-casted on the glass slides (1x1 cm) and left for 12 h for evaporation of water. The images were recorded using a Tescan Vega 3LMU SEM (USA) machine.

The LYZ-nanoMIPs were functionalised onto SPEs using an electro-grafting procedure established in our lab for electrochemical measurements (J. McClements et al., 2022). EIS and cyclic voltammetry (CV) were performed with a Reference 3000™ potentiostat/galvanostat (Gamry Instruments, United States). All the measurements were performed in 1 mM $[Fe(CN)_6]^{3-/4-}$ (1:1) mixture in 0.1M KCl in PBS. To construct dose-response curve, a SPE functionalised with nanoMIPs was exposed to PBS solutions with increasing concentrations of LYZ (0 -1 mM). Measurements to construct dose-response curves to monitor the corresponding charge transfer resistance (R_{CT}) values at certain concentrations of LYZ were calculated by fitting equivalent circuits to Nyquist plots

corresponding to each EIS measurement. Thermal measurements were performed according to the method described in **Chapter 2**. LYZ concentrations were measured in a wide range starting at 10 pM, to 1 nM, 0.1 µM, 10 µM, and finally 1 mM. The limit of detection (LoD) was determined via the three-sigma method.

4.4 Results and discussion

4.4.1 NanoMIP and functionalised electrode characterisation

As LYZ is a small protein with low-cost and a monomer structure, we decided to imprint with the whole protein rather than selecting an epitope. The monomer mixture used to manufacture the nanoMIPs was based on previous literature reports and covered a wide range of non-covalent interactions to promote binding, with negatively charged AAc and positively charged APMA able to interact with charged LYZ residues. Furthermore, NIPAM can facilitate hydrogen bonding with lysozyme and hydrophobic TBAm can interact with corresponding hydrophobic amino acids.(Ragland and Criss, 2017) The synthesis process for nanoMIPs for LYZ is shown in **Figure 4.1**.

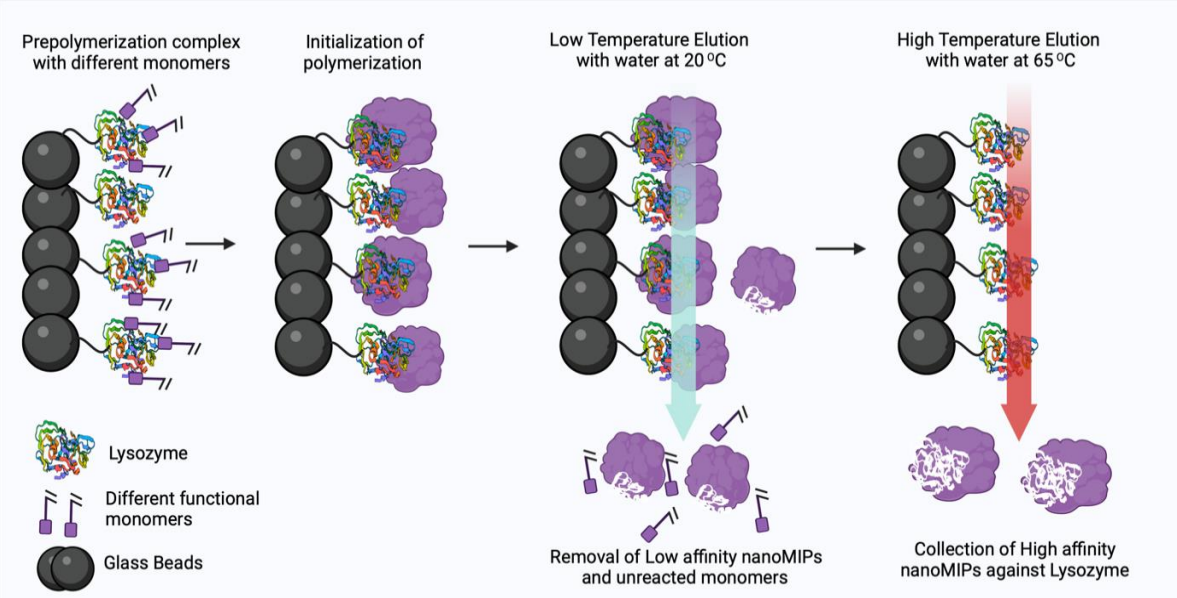

Figure 4.1: Solid-phase imprinting approach to produce high affinity nanoMIPs for lysozyme.

Following complexation of LYZ with the aforementioned monomer mixture, polymerisation was carried out via initiation by APS and TEMED. Low affinity nanoMIPs and unreacted monomers were removed by filtration using SPE tube at low temperature, whereas at high

temperature (65ºC) nanoMIPs with high affinity were collected. The obtained nanoMIPs were dried at 60ºC to determine their concentration, which was 160 µg mL^{-1}. DLS results that the nanoMIPs were monodisperse (PDI = 0.24) and possessed a hydrodynamic diameter of ~158 nm (**Figure 4.2a**). SEM images confirmed that spherical nanoMIPs were formed with an average size range from 40-100 nm (**Figure 4.2b**). It was expected that the size found by DLS was larger as bigger particles have a bigger contribution in the measured intensity. Moreover, monomers used in the synthesis including AAc and NIPAM exhibit significant swelling in liquid and therefore have a bigger size in DLS (conducted in liquid) compared to SEM (conducted in dry state).

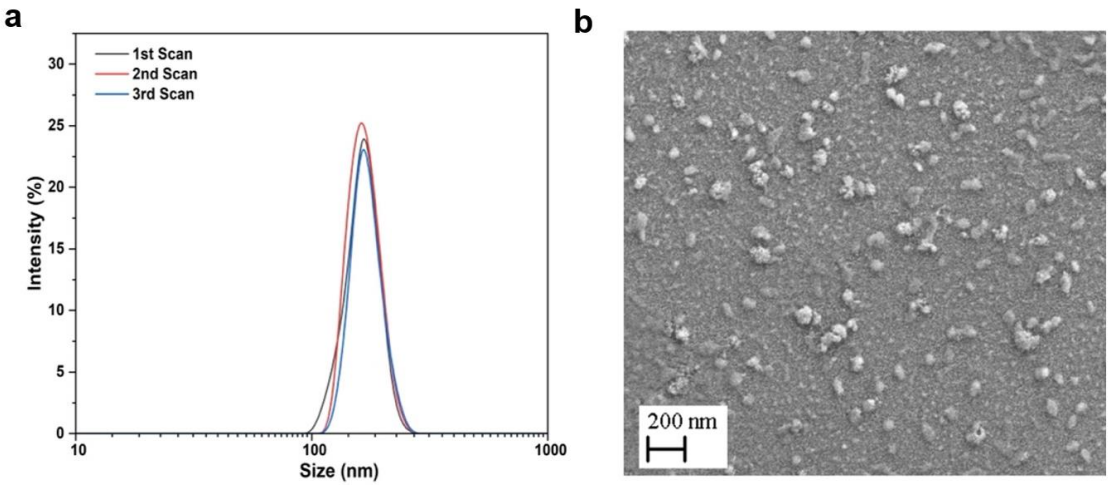

Figure 4.2: (a) Particle size distribution (intensity % vs size nm) for the LYZ specific nanoMIPs as determined by DLS, average hydrodynamic diameter (D_h) 158 nm (n=3). **(b)** SEM images of the nanoMIPs on the surface, demonstrating particles are 40-100 nm when measured in the dry state.

4.4.2 Electrochemical experiments and detection of LYZ

LYZ specific nanoMIPs (c = 300 µg mL^{-1}) were chemically crosslinked onto the surface of SPEs using a previously reported electrografting approach. In short, this involves electrografting of 4-aminobenzoic acid (4-ABA) followed by an EDC/NHS mediated coupling of the carboxylic groups of 4-ABA to the amine groups present in the nanoMIPs. Following the electrografting, the SPEs were washed with double distilled water and used for electrochemistry measurements after drying. EIS was utilised as a quick and straightforward technique to follow the surface functionalisation and nanoMIP attachment using charge transfer resistance (R_{CT}) values of the bare and functionalised SPE as shown in **Figure 4.3a**. A simple Randles circuit (**Figure 4.3a**) was fitted to the respective

Nyquist plots to determine the change in transfer resistance (R_{CT}) throughout the functionalisation process. In **Figure 4.3b**, CV was performed on the functionalised SPEs. Measurements were done with PBS buffered solutions and subsequently with PBS buffered solutions spiked with increasing concentrations (1 pM to 1mM) of LYZ. The same experiment was performed where EIS was used to monitor the influence of LYZ concentration on the R_{CT} value of the nanoMIP-functionalised SPE (**Figure 4.3c**). Finally, a dose-response curve is given in **Figure 4.3d**, which demonstrates the dependence of the R_{CT} value depending on the LYZ concentration. Bare SPEs exhibited a small semicircle at the high frequency regime with a R_{CT} value of 3.7 kOhm. After the self-assembly of 4-ABA on the surface of the SPEs, the Nyquist plot showed an increase in the width of the semicircle and the R_{CT} increased to 6.0 kOhm. Following immobilisation of the polymeric receptors via an organic coupling reaction, a further increase to a R_{CT} = 7.9 kOhm was observed.

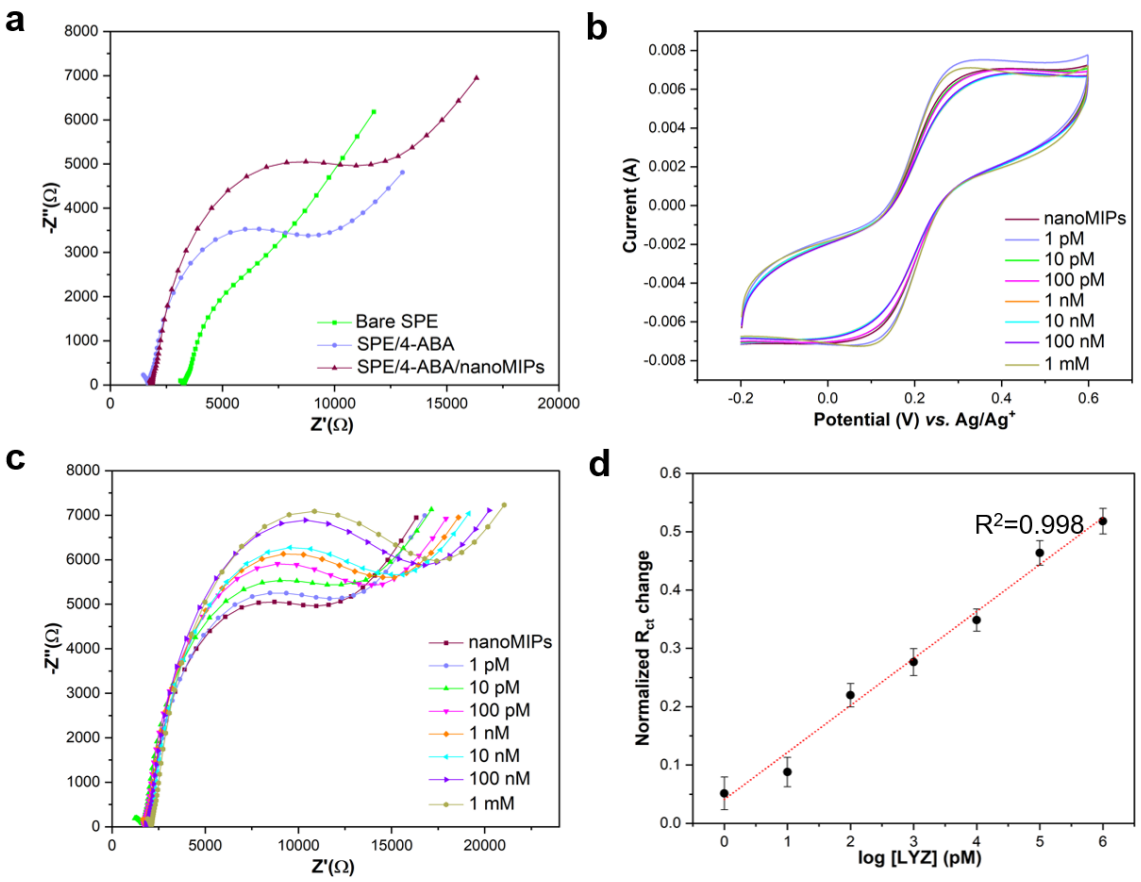

Figure 4.3: (a) EIS measurements with the Nyquist plots for the bare SPE, 4-ABA electrografted onto the SPEs, and nanoMIPs covalently immobilised onto the SPE. **(b)** Representative cyclic voltammograms of nanoMIPs immobilised SPE in the presence of

various concentrations of LYZ (1 pm to 1 µM) in PBS with 1 mM ferrocyanide, 1 mM ferrocyanide, and 0.1 M KCl. **(c)** Nyquist plots for nanoMIP-functionalised SPE in the presence of various concentrations of LYZ (1 pm to 1 µM) in PBS with 1 mM ferrocyanide, 1 mM ferrocyanide, and 0.1 M KCl. **(d)** Calibration curve of R_{ct} vs different LYZ concentrations. Each experiment was performed in duplicate.

This trend in increase in R_{CT} was in line with previous reports, which discussed that all the material deposited onto the SPEs is essentially non-conductive and thereby hampers electron transfer of the $[Fe(CN)_6]^{3-/4-}$ redox couple (McClements et al., 2021). Thus, it confirmed the successful functionalisation of nanoMIPs onto the SPEs using the described preparation method. **Figure 4.3b** shows there was a minimal impact on the $[Fe(CN)_6]^{3-/4-}$ oxidation peak, which reduced from 7.4×10^{-6} in a pure PBS solution to 6.1×10^{-6} when there was 1 µM of LYZ in solution. This was a first indication that there was binding of LYZ to the nanoMIP layer since this was expected to block the electron transfer at the functionalised interface. However, CV is not the most sensitive electrochemical approach, and we are interested in measuring trace amounts of LYZ in samples. Thus, experiments were performed with EIS since this technique has shown promise for highly selective and specific detection of small molecules using gold electrodes modified with nanoMIPs (JyotiGonzato et al., 2021). It was clear there was a significant increase in R_{CT} with increasing concentrations of LYZ, which was due to binding of the LYZ in the cavities of the nanoMIPs which leads to an increase in electrochemical resistance (**Figure 4.3c**). A Randles circuit was used to construct the R_{CT} value at each concentration, with parameters of the circuit for each of the concentrations shown in **Table 4.1**.

Table 4.1: The parameters for the fitted Randles circuit for the nano-MIP functionalised SPEs depending on the concentration of LYZ.

Concentration (pM)	R_s (ohm)	C_{dl} (F)	R_{ct} (ohm)	W ($S*s^{1/2}$)
0	$1.88E^{+03}$	$3.09E^{-05}$	$7.91E^{+03}$	$2.82E^{-04}$
1	$1.90E^{+03}$	$2.73E^{-05}$	$8.31E^{+03}$	$2.74E^{-04}$
10	$1.57\ E^{+03}$	$2.81E^{-05}$	$8.45E^{+03}$	$2.59E^{-04}$
100	$1.77\ E^{+03}$	$2.65E^{-05}$	$9.64E^{+03}$	$2.79E^{-04}$
1000	$1.86\ E^{+03}$	$2.60E^{-05}$	$1.01E^{+04}$	$2.76E^{-04}$
10000	$2.03\ E^{+03}$	$2.56E^{-05}$	$1.06E^{+04}$	$2.76E^{-04}$
100000	$1.92\ E^{+03}$	$2.25E^{-05}$	$1.16E^{+04}$	$2.69E^{-04}$
1000000	$2.14\ E^{+03}$	$2.21E^{-05}$	$1.20E^{+04}$	$2.67E^{-04}$

It was found that there was a significant increase in R_{CT} from 7.9 kOhm in a pure PBS solution to 12 kOhm at a LYZ concentration of 1 µM (19% increase), which can be fitted well with a logarithmic fit. Using the three-sigma method and the slope of the calibration plot in the linear sensor regime (fit formula y = 0.0127x + 8.38, with R^2 = 0.98) to assess sensitivity, it was determined that the nanoMIP-based sensor can detect LYZ with a limit of detection of ~13 pM. This limit of detection is sufficient to measure trace LYZ concentration in food samples, thus confirming high specificity of the sensor. The selectivity of the sensor is further interrogated by exposing the nanoMIP functionalised SPEs to proteins with similar functionality and isoelectric points. BSA was used as interference compound since it belongs to the same protein family as LYZ and is highly abundant in clinical samples such as blood (Peters, 1996). Troponin-I was used since it is similar in molecular weight and, like LYZ, has a high isoelectric point (Peronnet et al., 2007). **Figure 4.4a** demonstrates the response of the nanoMIP-functionalised SPEs to increasing concentrations of BSA (1 pm - 1 µM) in PBS, while **Figure 4.4b** showcases the results when solutions of PBS with increasing concentrations of troponin-I (1 pm - 1 µM) were added. Contrary to when LYZ was added, there was no significant change in the Nyquist plot. This was further confirmed by determining the ΔR_{CT} values for these compounds, as shown in **Figure 4.4c**. At a target concentration of 1 µM LYZ, a significant increase of 4 kOhm (19%) in R_{CT} was found, whereas for BSA this was only 0.6 kOhm and for troponin-I (0.2 kOhm).Thus, these results confirm the selectivity of our sensor system.

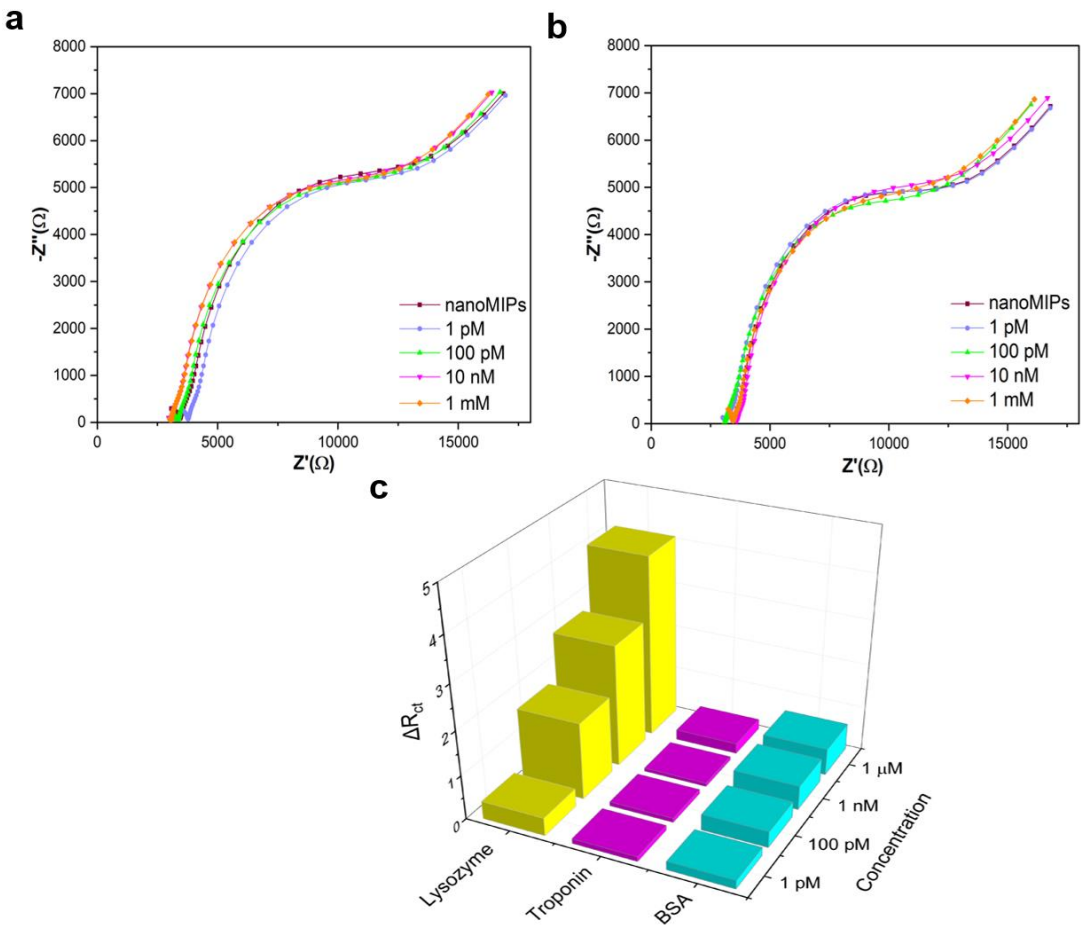

Figure 4.4 (a) EIS measurements with the Nyquist plots for the nanoMIPs immobilised SPE in the presence of various concentrations of BSA (1 pm to 1 µM) in PBS with 1 mM ferrocyanide. **(b)** 1 mM ferrocyanide, and 0.1 M KCl and for troponin-I. **(c)** the absolute change in R_{CT} vs the concentration of analyte is provided for LYZ (yellow), troponin-I (purple) and BSA (blue) as a bar chart.

4.4.3 Thermal detection of LYZ

For benchmarking the results obtained by electrochemical detections, measurements with an in-house build thermal device were performed. LYZ concentrations were thermally detected by mounting nanoMIP-functionalised SPEs into 3D-printed measurement cells to create an interface between the heat sink and the liquid reservoir. At first, the functionalised SPEs were left to stabilize for 15-20 min. Subsequently, PBS buffered solutions spiked with the target LYZ (0, 10 pM, 1 nM, 0.1 µM, 10 µM, and 1 mM), or proteins BSA and troponin-I in the same concentration range to evaluate selectivity, were manually added with a pipette. Following stabilisation, the change in R_{th} was recorded and used to construct the corresponding dose-response curve since attachment of the target to the nanoMIP layer leads to a reduction of heat-transfer at the solid-liquid interface (thus an increase in R_{th}). Each SPE was used to measure the R_{th} at two different concentrations.

After the analysis run, the addition cell was fully deconstructed and washed with DI water to ensure no residual sample solution could affect continuing runs.

Figure 4.5a displays the R_{th} over time from a stabilised PBS signal to an injection of LYZ solution (10 pm). It can be shown that the signal returned to the baseline value since only a small amount of LYZ was present and little binding to the polymer layer occurs. **Figure 4.5b** shows the R_{th} over time when a higher concentration of LYZ was present (10 µM). It can be observed that the PBS thermal signal stabilised at 1500 s, at a baseline of $R_{th} = 4.38 \pm 0.02$ °C/W. The sharp increase witnessed at ~ 1900s was due to the addition of a PBS solution (at RT) spiked with LYZ. The PID feedback corrected for this change in temperature by increasing the voltage, thus leading in a spike of the R_{th}. If no binding of the target would occur to the MIP layer on the surface of the SPE, the R_{th} would return to the same value before the addition of LYZ. However, binding of LYZ to the pores of the nanoMIP layer adds resistance to the surface, which leads to changes in thermal resistance as seen in **Figure 4.5b**. This also confirmed that the higher the concentration of LYZ introduced to the nanoMIPs functionalised onto the surface of the electrode, the higher the response in terms of thermal resistance. At the highest concentration of 1 mM, an increase in nearly 0.7 °C/W was observed (~ 14% increase compared to the baseline value). A log scale was used to plot the absolute response in the mean R_{th} to increasing concentrations of LYZ in **Figure 4.5c** from duplicate results. An individual standard deviation for each sample was calculated over one hundred data points (100 s of data). This standard deviation was derived from duplicate data sets and then used to act as the error for each data point ($n = 2$, mean standard deviation = 0.029). In **Figure 4.5d**, the dose-response curve is shown as the concentration vs the thermal resistance normalised to the starting value from the first individual data set.

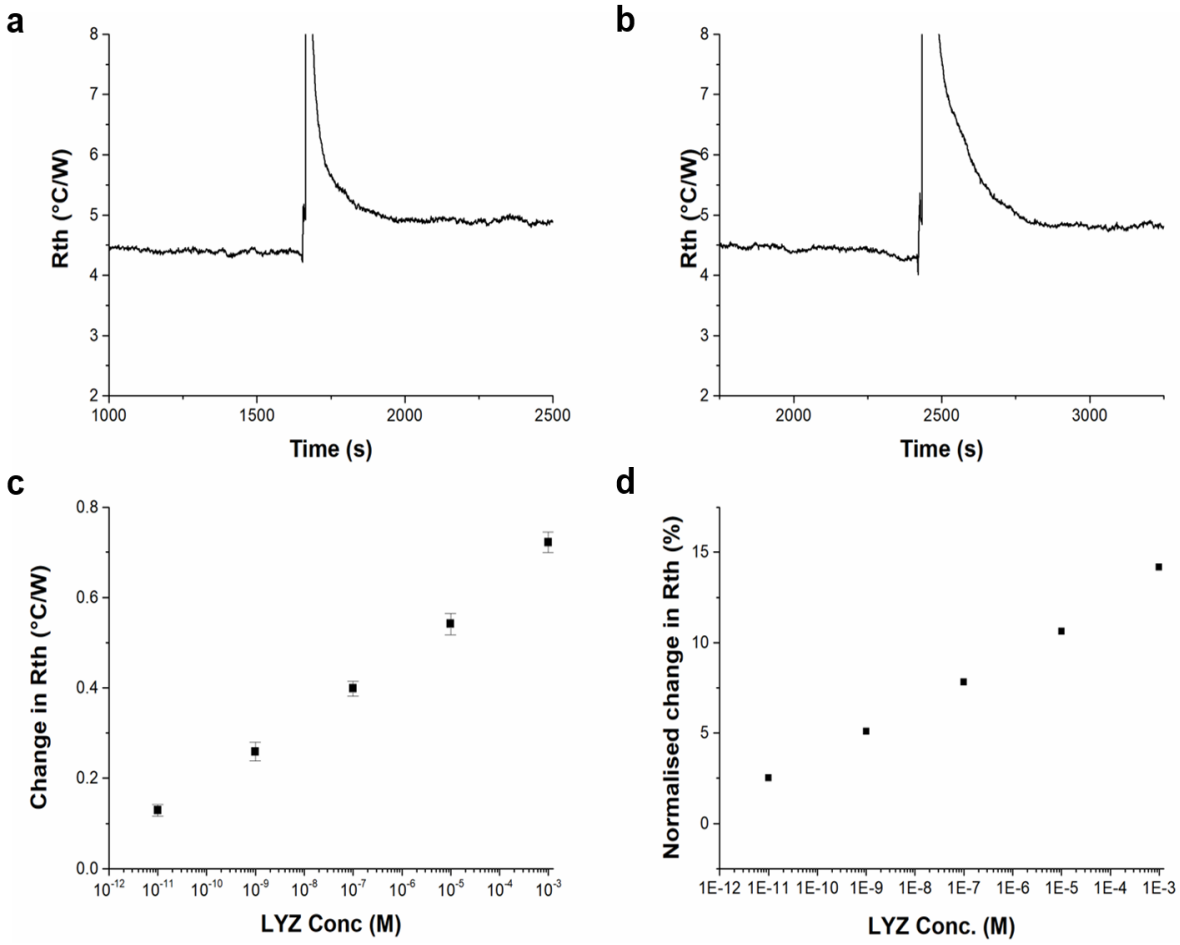

Figure 4.5: (a) Raw HTM data displaying transition from pure PBS to a solution of PBS spiked with 10 µM of LYZ. **(b)** Raw HTM data displaying transition from pure PBS to a solution of PBS spiked with 10 pM of LYZ. **(c)** Absolute change in R_{th} with increasing concentration compared to the R_{th} in pure PBS. **(d)** Normalised change in R_{th} with increasing concentration, which as calculated at R_{th} c=x divided over R_{th} at c=0 and multiplied by 100 to get a percentage.

At 1 mM, the highest concentration of LYZ in PBS, an increase of ~ 14% in R_{th} was observed compared to a 2.5% increase on the injection of 10 pM. This was comparable to changes in R_{th} previously reported in literature.(J. McClements et al., 2022; McClements et al., 2021) Using the linear range of the calibration curve (10 pM to 1 mM) and the standard deviation of the baseline (0.02 °C/W) as an average of all baseline SD values obtained throughout experimentation, a limit of detection of 1 fM was estimated according to the three-sigma method. Stabilisation of a thermal resistance signal was achieved after a minimum of 15 min. A full sample run, composing of a blank and sample injection, was carried out in a duration of 30 min. While this thermal analysis yielded a

lower LOD compared to EIS measurements, it required longer analysis time (30 min vs 5–10 min). In the future, it might be possible to calibrate the system thus only requiring an injection of a sample rather than stabilisation in buffer.

4.4.4 Proof-of-application via impedimetric determination of LYZ concentration in an egg white sample

An egg white sample was prepared as described in the "Proof-of-application impedimetric detection in an egg white sample" section (**Chapter 2, section 2.2.7**), which was measured with a freshly prepared nanoMIP sensor to determine its LYZ content. **Figure 4.6** shows the experimental impedance spectra for the nanoMIP-immobilised SPE in a buffered solution and after incubation in a diluted egg sample. By fitting data to the Randles circuit model, the normalised R_{ct} change was found to be 0.16%. Considering the dilution factor used in sample preparation, the total amount of LYZ found in the egg white was 2.7 mg mL^{-1}. This concentration falls within the 2.5-4.5 mg mL^{-1} range of LYS concentration that is typical in chicken egg white (Vidal et al., 2005). Therefore, these analytical findings demonstrated that the sensor was successfully used to identify LYZ in intricate biological materials.

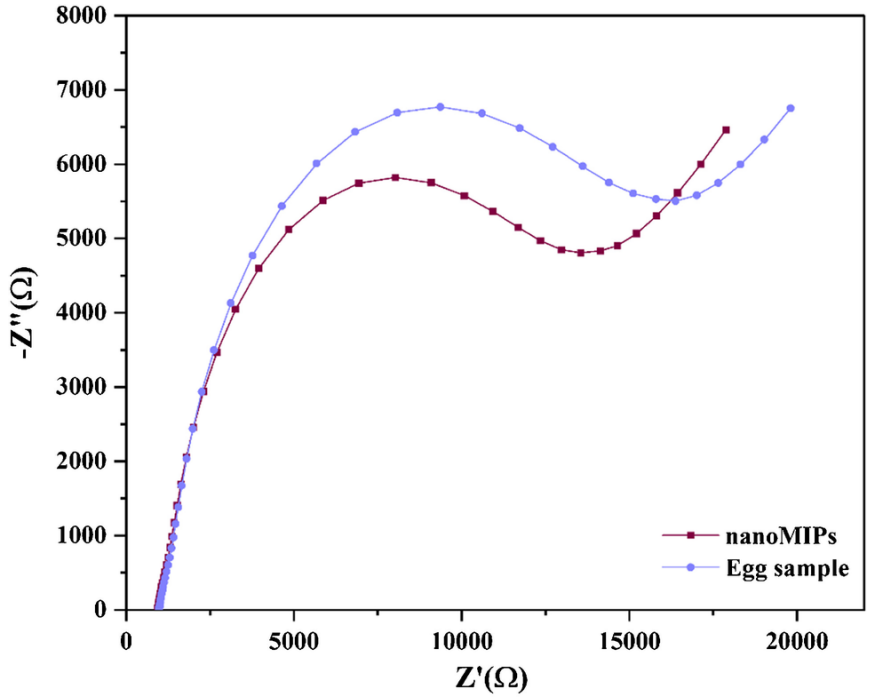

Figure 4.6: EIS measurements with the Nyquist plots for the nanoMIP-immobilised SPE in the presence of diluted egg sample in PBS with 1 mM ferrocyanide, 1 mM ferrocyanide, and 0.1 M KCl.

An overview of the specificity and measurement time of different point-of-care sensors used for LYZ detection is compared in **Table 4.2**. **Table 4.2** demonstrates that both aptamers and nanoMIP-based sensors coupled with electrochemical methods were capable of measuring LYZ at the relevant concentration range. However, LoDs should be compared in real food samples as these are complex matrices and fouling can have a significant impact on sensor specificity. Moreover, sample preparation, often involving dilution or extraction, is an important factor when deciding on the best sensing strategy. Stability should also be considered since nanoMIPs are generally more stable compared to aptamers due to their cross-linked nature, which is advantageous for measuring in complex matrices.

Table 4.2 Comparison of different detection strategies for LYZ based either on aptamers or nanoMIPs. All the LoDs are based on measurements performed in spiked PBS solutions.

Receptors	**Detection technique**	**LoD**	**Measurement time**	**Reference**
Aptamers	EIS	1 pM	5-10 min	(Zhang et al., 2015)
Electroactive nanoMIPs	DPV	100 pM	5 min	(X. Yang et al., 2022)
Electropolymerized scopoletin-based MIPs	EIS	62 nM	5-10 min	(Guilio et al., 2021)
nanoMIPs	EIS	13 pM	5-10 min	**This chapter**
nanoMIPs	Thermal detection	1 fM	30 min	**This chapter**

4.5 Conclusion

We have developed a novel sensor for the electrochemical and thermal detection of LYZ, an allergic substance, using nanoMIP-based sensors. The nanoMIPs were synthesised using an innovative solid-phase approach, yielding uniform particles with a size of ~ 158 nm in the liquid state as determined by DLS in the liquid state and a size of 40–100 nM in the dry state as determined by SEM. Subsequently, these nanoMIPs were electrografted onto SPEs to construct disposable and low-cost sensors. The produced sensors exhibited a LOD of 13 pM for LYZ using EIS as read-out technique and 1 fM when

employing the heat transfer method. Moreover, the nanoMIPs displayed excellent selectivity and no significant response was observed for proteins of similar molecular weight and isoelectric point (*e.g.,* BSA and troponin-I). The obtained LOD values were sufficient to determine trace amounts of LYZ as food allergen and comparable to literature reports, while offering the advantages of fast measurement time (10-min EIS, 30-min thermal detection) and low-cost components. Considering the versatility of the polymeric receptors which can be adapted to virtually any analyte of interest, this creates significant commercial potential for nanoMIP-based test to improve food safety. Apart from applications of nanoMIPs in sensing, their use in drug delivery remains a complex and challenging area of study. The next chapter will focus on addressing this challenge by exploring the potential of MIPs for targeted drug delivery. This research aims to explore how MIPs can be engineered to deliver therapeutic agents with high specificity to targeted sites within the body, potentially enhancing treatment effectiveness.

4.6 References

Abdin, M. J., Altintas, Z. & Tothill, I. E. (2015). 'In silico designed nanomip based optical sensor for endotoxins monitoring' *Biosensors and Bioelectronics,* 67 pp. 177-183.

Alanazi, K., et al. (2021). 'Disposable paracetamol sensor based on electroactive molecularly imprinted polymer nanoparticles for plasma monitoring' *Sensors and Actuators B*, 329 p. 129128.

Aminlari, L., Hashemi, M. M. & Aminlari, M. (2014). 'Modified lysozyme as novel broad spectrum antimicrobial agent in foods' *Journal of food science,* 79(6), pp. R1077-R1090.

Banciu, M., Numan, N. & Vasilescu, A. (2022). 'Optical biosensing of lysozyme' *Journal of Molecular Structure,* 1250 p.131639.

Canfarotta, F., et al. (2018). 'A novel thermal detection method based on molecularly imprinted nanoparticles as recognition elements' *Nanoscale*, 10(4), pp. 2081-2089.

Canfarotta, F., Poma, A., Guerreiro, A. & Piletsky, S. (2016). 'Solid-phase synthesis of molecularly imprinted nanoparticles' *Nature Protocol,* 11(3), pp. 443-455.

Crapnell, R. D., Garcia-Miranda Ferrari, A., Dempsey, N. C. & Banks, C. E. (2022). 'Electroanalytical overview: Screen-printed electrochemical sensing platforms for the detection of vital cardiac, cancer and inflammatory biomarkers' *Sensors & Diagnostics,* 1(3), pp.405-428.

Culver, H. R. & Peppas, N. A. (2017). 'Protein imprinted polymers: The shape of things to come?' *Chemistry of Materials*, 29(14), pp. 5753-5761.

Flavin, K. & Resmini, M. (2009). 'Imprinted nanomaterials: A new class of synthetic receptors' *Analytical and Bioanalytical Chemistry,* 393 pp. 437-444.

Frémont, S., Kanny, G., Nicolas, J. P. & Moneret-Vautrin, D. A. (2007). 'Prevalence of lysozyme sensitisation in an egg-allergic population' *Allergy,1*997, 52(2), pp. 224-228

Guilio, T., Mazzotta, E. & Malitesta, C. (2021). 'Molecularly imprinted polyscopoletin for the electrochemical detection of the chronic disease marker lysozyme' *Biosensors,* 11(1), p.3.

Haupt, K. & Mosbach, K. (2000). 'Molecularly imprinted polymers and their use in biomimetic sensors' *Chemical reviews,* 100(7), pp.2495-2504.

JyotiGonzato, C., et al. (2021). 'Molecularly imprinted polymer nanoparticles-based electrochemical chemosensors for selective determination of cilostazol and its

pharmacologically active primary metabolite in human plasma' *Biosensors and Bioelectronics,* 193 p.113542.

Kerkaert, B., Mestdagh, F. & Meulenaer, B. (2010). 'Detectoin of hen's egg white lysozyme in food: Comparison between a sensitive hplc and a commercial elisa method' *Food Chemistry*,120(2), pp. 580-584.

Li, Q., et al. (2014). 'Surface protein imprinted surface protein imprinted core-shell particles for high selective lysozyme recognition prepared by reversible addition-fragmentation chain transfer strategy'*ACS Applied Materials & Interfaces*, *6*(24), pp.21954-21960.

Lowdon, J. W., et al. (2020). 'Mips for commercial application low-cost sensors and assays – an overview of the current status quo' *Sensors and Actuators B: Chemical,* 325, p.128973.

Ma, Y., et al. (2013). 'Comparative study of the molecularly imprinted polymers prepared by reversible addition-fragmentation chain transfer "bulk" polymerisation and traditional radical "bulk" polymerisation' *Journal of Molecular Recognition,* 26(5), pp.240-251.

McClements, J., et al. (2022). 'Molecularly imprinted polymer nanoparticles enable rapid, reliable, and robust point-of-care thermal detection of sars-cov-2' *ACS sensors,* 7(4), pp.1122-1131.

McClements, J., et al. (2021). 'Immobilisation of molecularly imprinted nanoparticles onto surfaces using different strategies: Evaluating the influence of the functionalised interface on the performance of a thermal assay for the detection of the cardiac biomarker troponin-i'*ACS Applied Materials & Interfaces*, 13(24), pp.27868-27879..

Melinte, G., Selvolini, G., Cristea, C. & Marrazza, G. (2021). 'Aptasensors for lysozyme detection: Recent advances' *Talanta,* 226 p.122169.

Menger, M., et al. (2016). 'Mips and aptamers for recognition of proteins in biomimetic sensing' *Biosensors*, *6*(3), p.35.

Moczko, E., et al. (2013). 'Surface-modified multifunctional mip nanoparticles' *Nanoscale*, 5(9), pp.3733-3741.

Ou, S. H., Wu, M. C., Chou, T. C. & Liu, C. C. (2004). 'Polyacrylamide gels with electrostatic functional groups for the molecular imprinting of lysozyme' *Analytica Chimica Acta,* 504(1), pp.163-166.

Peronnet, E., et al. (2007). 'Isoelectric point determination of cardiac troponin i forms present in plasma from patients with myocardial infarction' *Clinica chimica acta*, 377(1-2), pp.243-247.

Peters, T. (1996). *All about albumin: Biochemisty, genetics and medical applications*. San Diego and London: Academic Press, 1996, 432 pp.

Porstmann, B., et al. (1989). 'Measurement of lysozyme in human bodily fluids: Comparison of various enzyme immunoassay techniques and their diagnostic application' *Clinical Biochemistry,*1989, 22(5), pp. 349-355

Ragland, S. A. & Criss, A. K. (2017). 'From bacterial killing to immune modulation: Recent insights into the functions of lysozyme' *PLoS Pathog*ens, 13 (9), p.e1006512

Sen, D. K. & Sarin, G. S. (1986). 'Biological variations of lysozyme concentration in the tear fluids of healthy persons' *British Journal of Ophthalmology*,1986, 70(4), pp. 246-248.

Tse Bum Sui, B. & Haupt, K. (2021). 'Molecularly imprinted polymer hydrogel nanoparticles: Synthetic antibodies for cancer diagnosis and therapy' *ChemBioChem,* 23(8), p.e202100598.

Vidal, M. L., Gautron, J. & Nys, Y. (2005). 'Development of an elisa for quantifying lysozyme in hen egg white' *Journal of Agricultural and Food Chemistry,* 2005, 53(7), pp. 2379-2385.

Wang, L., Wang, H., Tang, X. & Zhao, L. (2022). 'Molecularly imprinted polymers-based novel optical biosensor for the detection of cancer marker lysozyme' *Sensors and Actuators A: Physical,* 2022, 334 p.113324.

Wang, Y., et al. (2015). 'Preparation of lysozyme imprinted magnetic nanoparticles via surface graft copolymerisation' *Journal of Biomaterials Science, Polymer Edition*, 26(11), pp.644-656.

Weber, P., et al. (2009). 'Lyszoyme in wine: A risk evaluation for the consumers allergic to hen's egg' *Molecular Nutrition & Food Research,* 2009, 53(11) pp.1469-1477.

Yang, X., et al. (2022). 'A molecularly imprinted biosensor based on water-compatible and electroactive polymeric nanoparticles for lysozyme detection' *Talanta,* 236 p.122891.

Yoshimatsu, K., et al. (2012). 'Temperature-responsive "catch and release" of proteins by using multifunctional polymer-based nanoparticles' *Angewandte Chemie,* 51(10), p.2405.

Zhang, Z., et al. (2015). 'Feasible electrochemical biosensor based on plasma polymerisation-assisted composite of polyacrylic acid and hollow tio2 spheres for sensitively detecting lysozyme' *Biosensors and Bioelectronics*, 74 pp.384-390.

Chapter 5. Double Imprinted Nanoparticles for Sequential Membrane-to-Nuclear Drug Delivery

*(Published as P. Singla, T. Broughton, M. V. Sullivan, **S. Garg**, R. Berlinguer-Palmini, P. Gupta, F. Canfarotta, N. W. Turner, E. Velliou, S. Amarnath, M. Peeters, Advanced Science, 2024, 2309976)*

This co-author publication introduces the development of dual functional double imprinted nanoparticles (nanoMIPs) for the imaging and targeted drug delivery to cancer cells. In this work, I contributed to the synthesis of nanoMIPs alongside Pankaj Singla, conducted 2D cell line studies including cytotoxicity assays and confocal microscopy sample preparation, and written the corresponding sections of the manuscript. Tommy Broughton performed the flow cytometry experiments; Mark Sullivan conducted the SPR experiments; R. Berlinguer-Palmini carried out confocal microscopy imaging and assisted with data analysis; Priyanka Gupta was responsible for the 3D scaffold experiments and subsequent data interpretation. Francesco Canfarotta, Eirini Velliou, Nick Turner, and Shoba Amarnath provided expert guidance on experimental design and execution. Marloes Peeters contributed to the conceptualisation of the study and assisted with manuscript review and editing.

As described in Chapter 4, selecting the appropriate monomer composition is crucial for producing high affinity nanoMIPs. Therefore, the same monomer composition from Chapter 4 was used to synthesise double-imprinted nanoMIPs, with the addition of Fluorescein O-methacrylate and the chemotherapy drug doxorubicin (DOX). These modifications allowed the synthesis of fluorescent nanoMIPs for imaging while also providing anticancer properties.

5.1 Abstract

Efficient and site-specific delivery of therapeutics drugs remain a critical challenge in cancer treatment. Traditional drug nanocarriers such as antibody-drug conjugates are not generally accessible due to their high cost and can lead to serious side effects including life-threatening allergic reactions. Here, these problems are overcome via the engineering of supramolecular agents that are manufactured with an innovative double imprinting approach. The developed molecularly imprinted nanoparticles (nanoMIPs) are targeted towards a linear epitope of estrogen receptor alfa (ERα) and loaded with the chemotherapeutic drug doxorubicin. These nanoMIPs are cost-effective and rival the

affinity of commercial antibodies for ERα. Upon specific binding of the materials to ERα, which is overexpressed in most breast cancer (BCs), nuclear drug delivery is achieved via receptor-mediated endocytosis. Consequentially, significantly enhanced cytotoxicity is elicited in BC cell lines overexpressing ERα, paving the way for precision treatment of BC. Proof-of-concept for the clinical use of the nanoMIPs is provided through evaluating their drug efficacy in sophisticated 3D cancer models, which capture the complexity of the tumour microenvironment *in vivo* without requiring animal models. Thus, these findings highlight the potential of nanoMIPs as a promising class of novel drug compounds for use in cancer treatment.

5.2 Introduction

Breast cancer (BC) is the most frequently diagnosed cancer worldwide; with 2.3 million new cases in 2020, this accounts for 1 in 8 cancer diagnoses (Ali and Coombes, 2002; Xu et al., 2021). It is a highly heterogeneous disease that can be caused by a variety of distinct genetic alterations in mammary epithelial cells, requiring a combinatorial evaluation of the histopathology of the primary tumour and of the expression pattern of hormone receptors to determine the optimal patient treatment plan. The majority (70%) of BCs are estrogen receptor positive (ER+), meaning the cancer is fuelled by the estrogen hormone (Ali and Coombes, 2002; Xu et al., 2021). ERα is a central transcription factor that is often overexpressed in BC, but also in ovarian, endometrial and prostate cancers,(Rodriguez et al., 2019) and plays a crucial role in breast tumorigenesis and proliferation of BC cells.

Traditionally, ERs have been considered nuclear receptors, but it has been well-documented that these receptors are also present on the membrane and in the cytoplasm. Nuclear ERα stimulates gene expression changes that promote cell cycle progression (Carroll et al., 2005; P. Chen et al., 2022; Kumar et al., 2021). Moreover, the binding of ligands to plasma membrane ERα triggers rapid cellular changes through second messenger pathways, which also contribute to transcriptional effects of estrogen by regulating processes such as proliferation, cell migration, and development (Acconcia and Marino, 2011; Levin, 2003). Membrane-bound ERα receptors are associated with caveolae that help in their internalisation through dynamin-mediated processes and play a crucial role in initiating ERα signalling (Marczell et al., 2018). Endocrine therapy, consisting of for instance tamoxifen and fulvestrant, is the preferred first line of treatment

for ER positive BC (Utsumi et al., 2007). Chemotherapeutic drugs may also be prescribed alone or in combination with endocrine therapy (Saha Roy and Vadlamudi, 2012). Additionally, chemotherapy may be used after surgical resection or in the case of metastatic BC, with doxorubicin (DOX) being one of the most frequently prescribed chemotherapy drugs for solid breast tumours. However, all current treatment options come with significant challenges and side effects, such as drug resistance, severe toxicity (for example, neurotoxicity and cardiac toxicity including irreversible heart injury) and allergic reactions (fainting, sweating) resulting from chemotherapy's non-selective behaviour (Al-Malky et al., 2019; Moiseenko et al., 2017; Smith et al., 2006).

Nanoparticles are currently being utilised in the field of nanomedicine to enable targeted drug delivery of chemotherapeutic drugs, leading to more effective treatment of cancer while minimising harmful side effects (Davis et al., 2008). To achieve targeted drug delivery, nanoparticles (*e.g.,* gold nanoparticles, liposomes) are functionalised with targeting agents which can be broadly classified as proteins (antibodies and their fragments), nucleic acids (aptamers), or other receptor ligands (peptides, vitamins, and carbohydrates) (Fang et al., 2023; Mitchell et al., 2021). Enhertu® is a prime example of a commercial antibody drug conjugate for BC treatment: this product composed of trastuzumab antibodies conjugated with deruxtecan and are designed to specifically target and treat metastatic HER2 (human epidermal growth factor receptor 2)-positive BC. Another example is Nab-paclitaxel (Abraxane), FDA approved albumin-bound nanoparticles for the delivery of paclitaxel used as second-line treatment for metastatic BC (Peer et al., 2020; Yuan et al., 2020). However, these formulations all rely on biological counterparts, which may encounter significant limitations such as high cost (minimum ~$100,000 per treatment for Enhertu®) limited *in vivo* stability, inherent heterogeneity of biologics which can lead immune intolerance, and inability to recognize altered peptide antigens. These drawbacks are overcome using molecular imprinted polymeric nanoparticles (nanoMIPs), which are highly selective, cost-effective, and robust, and can serve as an alternative for targeted drug delivery. These synthetic receptors are small porous polymeric nanostructures containing specific binding sites for a particular target (Francesco Canfarotta et al., 2018b; Jake McClements et al., 2022; Medina Rangel et al., 2020). These materials possess several advantages such as excellent chemical and biological stability, biocompatibility, versatility, and fast binding kinetics (Francesco Canfarotta et al., 2016b; Cecchini et al., 2017; Poma et al., 2013). Solid phase synthesis

for the manufacturing of nanoMIPs has led to the production of high affinity materials with homogeneous binding distribution and excellent biocompatibility due to the use of the solid-phase as an affinity medium (Francesco Canfarotta et al., 2016a).

There are some examples of hybrid core-shell systems where drug-loaded nanoparticles are coated with MIPs to facilitate targeted drug delivery to cell-specific receptors (Lu et al., 2021; Qin et al., 2020). However, a more scalable and straightforward approach would be to design and synthesize double imprinted nanoMIPs. In this work, we have developed DOX loaded nanoMIPs for its targeted delivery to ERα positive BC cell lines to improve breast cancer treatment via double imprinting with an epitope of ERα in the presence of DOX. Via this innovative synthesis approach, we have streamlined the manufacturing to a one-stage process, which will significantly lower production cost and development time. There is one report on double imprinted nanoparticles where drug delivery of DOX is explored via targeting the membrane receptor epidermal growth factor receptor (EGFR). As this material only bound to the receptor and was not internalised by the cells, the therapeutic effect in this case can be limited (Francesco Canfarotta et al., 2018b). Our work introduces a novel approach by successfully targeting the membrane receptor ERα and facilitating the translocation of nanoMIPs towards the nucleus, which paves the way for the selective drug delivery of traditionally “undruggable” targets with MIPs.

In this context, nanoMIPs have been developed to target ERα and were tested on two different BC cell lines: MCF-7 (ERα positive) and MDA-MB-231 (ERα negative), which represent different subtypes of BC and thus require different treatment in clinical practice. The study showed that nanoMIPs designed for ERα successfully bound to this receptor on the membrane and were subsequently internalised, thus facilitating highly specific intracellular delivery of DOX. By enabling nuclear delivery of DOX, the nanoMIPs elicited significantly higher cytotoxicity (80%) towards the MCF-7 cell line as compared to the negative control cell line MDA-MB-231 (15%).

Furthermore, the efficacy was evaluated in scaffold assisted 3D model of BC cell lines, which provide a better representation of BC progression and response to drugs *in vivo.* 3D cancer models provide a remarkable platform for *in vitro* testing of these nanoparticle formulations by effectively mimicking the complex tumour microenvironment found in living organisms.

There are regulatory demands to move away from traditional animal-based safety assessment studies, and pharmaceutical industries desire to develop alternatives and methodologies to efficiently screen and characterize therapeutic molecules in the pipeline (Wang et al., 2021). However, there is a lack of an appropriate alternative method to study the whole animal's metabolic response, but these methods help to reduce the number of animals needed for research to a certain extent. Even though no animal model can fully replicate the processes within the human body. In the search for alternatives, microphysiological systems, three-dimensional (3D) spheroids, organoids, and scaffolds are being used at singular and multicellular levels to screen drugs (Ko et al., 2024; Ronaldson-Bouchard et al., 2022). 3D cancer models present a significant advancement over traditional two-dimensional (2D) models in the study of human diseases (Gupta et al., 2022; Gupta et al., 2020; Totti et al., 2018). They more accurately replicate various features of the tissue microenvironment, including structural integrity, biochemical composition (mimicking the extracellular matrix), and cellular diversity, offering a robust and personalised approach. This level of detail and specificity renders 3D cancer models superior to animal models, as they enable the creation of patient-specific tissue models *in vitro* (Gupta et al., 2022; Gupta et al., 2020; Totti et al., 2018). Furthermore, 3D cancer models are excellent surrogates for studying tissue penetration, especially when their mechanical properties and cell density closely mimic those of actual human tissues (Gupta et al., 2019; Totti et al., 2018). However, 3D cancer models may not adequately represent the processes of absorption, distribution, metabolism, and elimination (ADME). Therefore, microphysiological systems are continually being explored, utilising multiple organ models to address these limitations and enable effective pharmaceutical testing without the use of animals (Fabre et al., 2020; Van Ness et al., 2022).

The present work builds upon the development of engineered nanoMIPs as a targeted drug delivery vehicle in the field of precision medicine, adhering to the 3Rs (replace, reduce, and refine) principles of animal research. This approach can easily be expanded to other cancer types, given the versatility of the method used to manufacture these engineered nanoparticles.

5.3 Experimental

5.3.1 Materials

Major chemical used in this study were NIPAM, Bis, TBAm, APMA, AA, Fluorescein O-

methacrylate, TEMED, APTMS, DOX, MTT, EDC, dipotassium phosphate, disodium phosphate, ethanolamine, NHS, BCA protein assay kit, glass beads, APS, methanol, acetone, ACN), NaOH, HCl (33%), SIA, KCL, sodium acetate, NaCl, PBS tablets and human recombinant ERα protein, Alexa Fluor™ 594 WGA antibody, a Live/Dead Viability/Cytotoxicity Kit, DAPI, ERα primary monoclonal antibody (MA1-310), Alexa Fluor™ 488 Goat anti-Mouse IgG secondary antibody, ERα epitope (CSHSLQKYYITGEAEGFPATV) and Tween 20. All chemicals and solvents were used without any further purification and their sources information provided in **Chapter 2**. Additionally, dialysis cartridges (Vivaspin® 20, 3 kDa molecular weight cut-off (MWCO) Polyether-sulfone), Supelco polypropylene solid phase extraction tubes (60 mL) were used in the synthesis of nanoMIPs.

5.3.2 Methods and Equipment

All single imprinted nanoMIPs and doubly imprinted DOX loaded nanoMIPs against ERα were synthesised using solid phase synthesis approach. These nanoMIPs named as DOX-nanoMIPs for DOX and ERα double imprinted nanoparticles; FLU-DOX-nanoMIPs for fluorescein tagged DOX-nanoMIPs, FLU-nanoMIPs for Fluorescein tagged nanoMIPs against ERα. UV-visible spectre of DOX and DOX loaded nanoMIPs were recorded between 200 to 600 nm using a Jenway 7200 UV-Visible scanning spectrophotometer. The percent drug loading capacity (DLC) was calculated by taking the ratio of amount of DOX encapsulated and weight of nanoMIPs.

DLS experiments were performed using Malvern Zetasizer Nano ZS to measure the D_h of different nanoMIPs at 25 ± 0.1°C. A nanoMIP solution (40 μg/mL) was drop-casted on the copper grids and images was captured using Hitachi HT7800 120kV TEM machine. For SEM analysis, nanoMIP solutions were drop casted and dried on the glass chips (1x1 cm) and measurements were performed using a Tescan Vega 3LMU SEM machine. The SPR experiment were performed to find out the binding affinity of synthesised nanoMIPs towards their targets and for selectivity study.

In vitro studies: Two different BC cell lines MCF-7 and MDA-MB 231 were used for In vitro studies. *In vitro* cell binding of different nanoMIPs with cancer cells has been determined using a BD LSRFortessa™ X-20 flow cytometry technique. The MTT assay was used to evaluate the *in-vitro* cytotoxicity of various nanoMIPs and pure DOX in MCF-7 and MDA-MB-231 cells(Surapaneni et al., 2018). The nanoMIPs binding as well as

cellular uptake in MCF-7 and MDA-MB-231 cell lines was assessed at different time points (1 and 24 h). The images were taken with a confocal laser scanning microscope Zeiss 880 inverted confocal microscope (Zeiss Europe) and Leica TCS SP8 STED 3X (Leica microsystems, Germany) using the various lasers. The MCF-7 cell lines was seeded onto 3D polyurethane (PU) scaffolds measuring 5 × 5 × 5 mm^3 at a seeding density of 0.5 × 10^6 cells per scaffold to fabricate 3D cancer models (Gupta et al., 2019; Totti et al., 2018; Wishart et al., 2021). After treatment, the scaffolds were characterised through sectioning, staining, and image analysis via CLSM. A live/dead cell analysis was performed on the 3D cancer models and images were taken using a Zeiss 880 inverted confocal microscope (Zeiss Europe).

5.4 Results and discussions

5.4.1 Solid phase synthesis and characterisation of nanoMIPs

We have produced nanoMIPs to target the human ERα receptor protein (595 amino acids) with a molecular weight of 66 kDa (ERα66 wild type). A linear epitope sequence SHSLQKYYITGEAEGFPATV (576-595 amino acids at the C-terminus, corresponding to the binding region of Anti-ERα Antibody F-10, sc-800, Santa Cruz Biotechnology, Inc. USA) on helix 12 of human ERα receptor (UniProtKB-P03372) was selected (Biotechnology, 2021). A cysteine residue was added to the N-terminus of this peptide sequence for binding to the solid support used to produce the nanoMIPs, and its attachment was confirmed via a BCA assay (**Figure 5.1a**). To circumvent the limitations connected with the use of whole proteins, the epitope imprinting approach offers several advantages *viz.* lower costs, compatibility with different synthetic conditions (pH, temperatures, and solvents), selectivity towards target, greater versatility, no need for costly and lengthy protein purification steps (Pasquardini and Bossi, 2021; Teixeira et al., 2021). The epitope-imprinting method is well-established and MIP-based sensors produced with this approach have successfully achieved full protein identification (Francesco Canfarotta et al., 2018b; Ekpenyong-Akiba et al., 2019; Nishino et al., 2006).

A variety of monomers were employed, comprising *N*-Isopropylacrylamide (NIPAM) for hydrogen bonding, *N*-*tert*-Butylacrylamide (nTBA) for hydrophobic interactions, and *N*-(3-Aminopropyl)methacrylamide hydrochloride (APMA), and acrylic acid (AA) for ionic interactions. Fluorescein-o-methacrylate was added in the monomer mixture to obtain fluorescent active nanoMIPs that enable tracking of the nanoparticles in the 2D cell lines and 3D cancer models when imaging of the system. The molecular

structures of the monomers and DOX are depicted in **Figure 5.1b,** while the composition of various batches of nanoMIPs and NIPs produced in this study is presented in **Table A.1**, **Appendix A**. Fluorescein tagged nanoMIPs without DOX (unloaded) are referred to as FLU-nanoMIPs, whereas DOX loaded, and fluorescein tagged DOX loaded double imprinted nanoparticles are named DOX-nanoMIPs and FLU-DOX-nanoMIPs respectively. Non-imprinted nanoparticles (NIPs, named as FLU-NIPs and FLU-DOX-NIPs were also prepared through solid phase synthesis approach using silanized beads and serve as a reference. The solid-phase synthesis method for the manufacturing of the different nanoMIPs is depicted in **Figure 5.1c**.

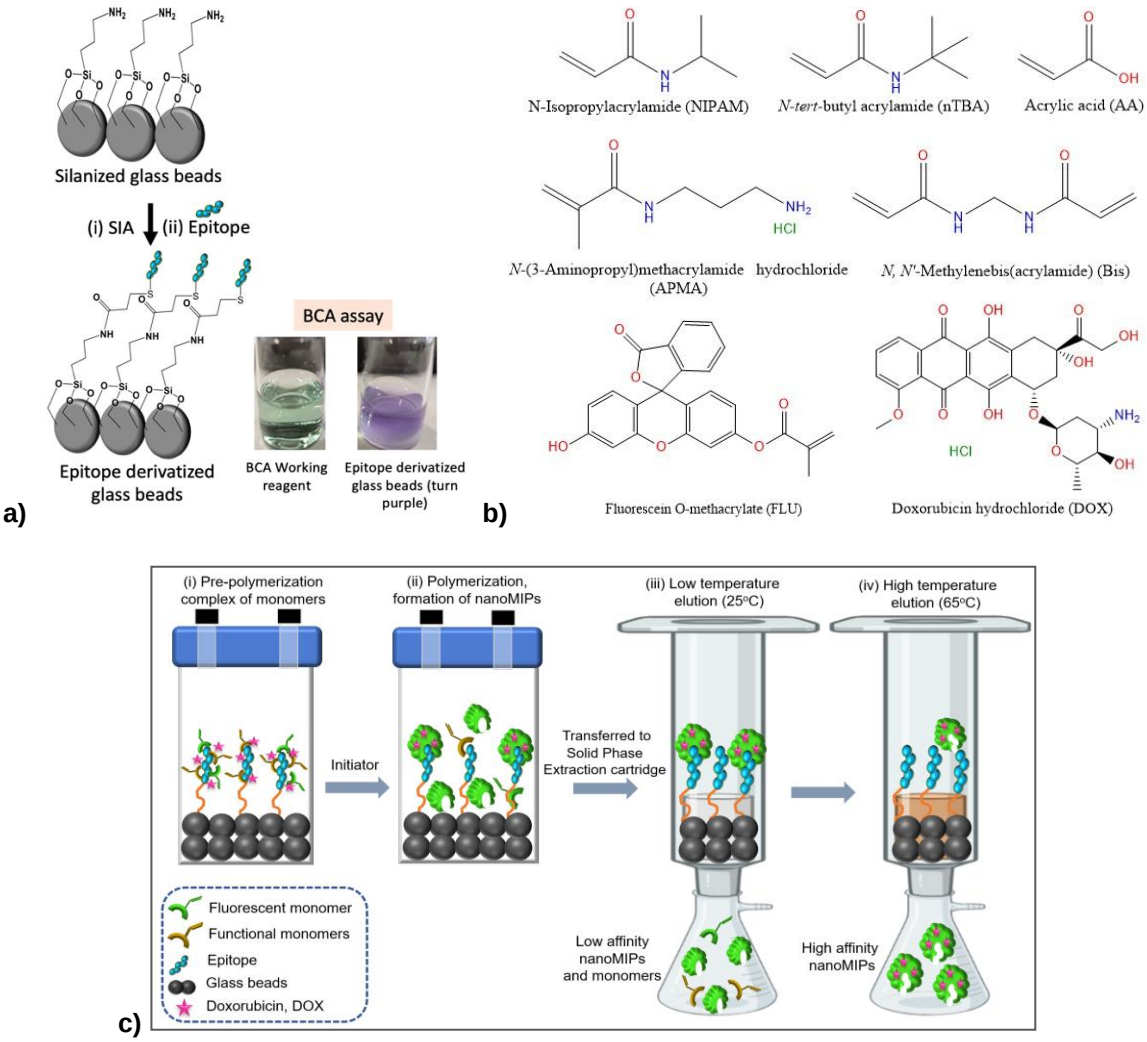

Figure 5.1: a) Molecular structures of different functional monomers, fluorescent monomer (Fluorescein-o-methacrylate), and DOX, **b)** Schematic of conjugation of cysteine modified epitope with silanized glass beads and confirmation through bicinchoninic acid (BCA) assay (green to purple in the presence of epitope modified glass beads), **c)** Schematic of synthesis of double imprinted nanoMIPs: the primary template is

the epitope conjugated on silanized beads, whilst DOX acts as secondary template in solution.

The hydrodynamic diameter (D_h) of FLU-nanoMIPs, DOX-nanoMIPs and FLU-DOX-nanoMIPs were found to be 121 ± 3 nm (PDI=0.115), 141 ± 3 nm (PDI=0.118) and 168 ± 2 nm (PDI=0.127) respectively (**Figure 5.2a**). These results showed that the loading of DOX into nanoMIPs increased D_h of nanoMIPs, due to accommodating fluorescein-o-methacrylate and DOX within the nanoMIPs. PDI values of these nanoMIPs were found to be less than 0.2 suggesting that these nanoparticles are homogeneous. Moreover, the D_h of control nanoMIPs and different NIPs *viz.* control NIPs, FLU-NIPs and FLU-DOX-NIPs is shown in **Table A.2** (Appendix A). The average size from the scanning electron microscopy (SEM) measurements for the FLU-nanoMIPs and FLU-DOX-nanoMIPs were observed to be 46±11 nm and 60±10 nm (**Figure 5.2b,c**) respectively, whereas DOX-nanoMIPs showed the size of 58±6 (**Figure A.1a, Appendix A**). This was in line with the transmission electron microscopy (TEM) results, where the size of FLU-nanoMIPs and FLU-DOX-nanoMIPs was found to 40±6 nm and 58±6 respectively (**Figure 5.2d,e**) and DOX-nanoMIPs showed size of 57±0.9nm (**Figure A.1b,** Appendix A). Moreover, both methodologies confirmed that the nanoMIPs exhibited a spherical morphology. The larger size observed in DLS measurements can be attributed to the swelling of the nanoMIPs, primarily induced by the copolymers of AA and NIPAM monomers, which are highly prone to swelling in the liquid state upon water absorption (Hu et al., 2000). In contrast, the sizes obtained from SEM and TEM reflect the nanoMIPs' dimensions in the dry state, where no water is available to facilitate swelling, and the nanoMIPs exist in a collapsed state (Singla et al., 2023a). Another factor contributing to the discrepancy between the sizes obtained from SEM/TEM and DLS is the potential presence of certain oligomers that adhere to the monodispersed nanoparticles, resulting in an increase in the hydrodynamic diameter (D_h) (Villanueva et al., 2020). This phenomenon can lead to a larger apparent size when measured through DLS. The variation in sizes observed between nanoMIPs and DOX-loaded nanoMIPs was primarily attributed to the incorporation of DOX into the nanoMIPs, resulting in an overall increase in their size.

UV-spectres of different batches DOX loaded nanoMIPs have been shown in **Figure 5.2f** and estimation of DOX loading was performed by determining the amount of imprinted drug using a calibration curve (**Figure A.2,** Appendix A), as well as assessing the loading efficiency and loading capacity (**Table A.3,** Appendix A). The loading of DOX

into DOX-nanoMIPs, FLU-DOX-nanoMIPs, and FLU-DOX-NIPs was found to be 17.28 ± 0.1, 19.33 ± 0.16, and 18.37 ± 0.12 µg/100 µg of nanoMIPs, respectively, with corresponding drug loading efficiencies of 57.6 ± 0.33 %, 64.43 ± 0.53 %, and 61.12 ± 0.40 %. This DOX loading is comparable to the Doxosome™ (DOX 20 µg/ ~160 µg of lipids), which is commercially available liposomal nano formulation specifically designed for research and development purposes (NanoSciences, 2022).

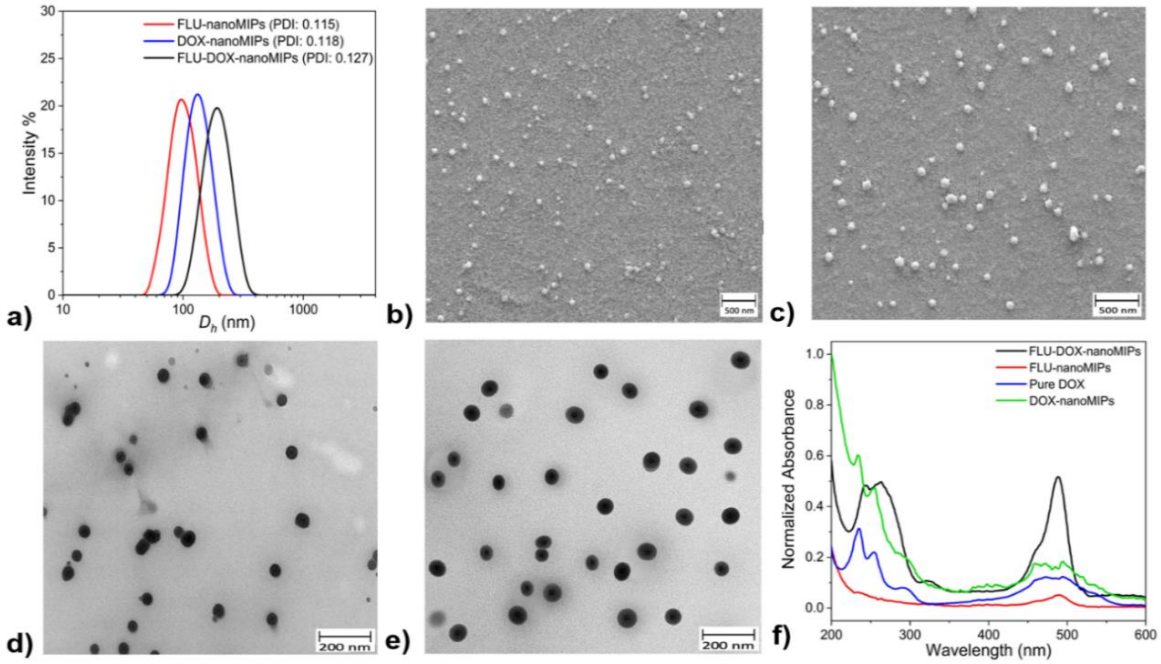

Figure 5.2: Characterisation of different nanoMIPs **a**) Intensity weighted size distribution plot (DLS measurement) FLU-nanoMIPs (D_h = 121.16 ± 2.70), DOX-nanoMIPs (D_h = 141 ± 2.76) and FLU-DOX-nanoMIPs (D_h = 168 ± 2.24) at 25°C. The Z-average D_h of the nanoMIPs was determined using cumulant analysis by the equipment, and the standard deviation was calculated based on 5 measurements, representative SEM images of **b)** FLU-nanoMIPs and **c)** FLU-DOX-nanoMIPs, TEM image (25000x) of **d)** FLU nanoMIPs, **e)** FLU-DOX-nanoMIPs, **f)** UV-spectra of Pure DOX, FLU-nanoMIPs, DOX-nanoMIPs and FLU-DOX-nanoMIPs.

Time-dependent size distribution of nanoMIPs in cell culture media: To understand the size distribution and stability of nanoMIPs in culture media, DLS measurements have been carried out at different time incubations (0, 0.5, 4, 8, 12 and 24 hours) at 37 °C. D_h of various nanoMIPs in DMEM culture media at different time intervals is shown in **Figure A.3**, Appendix A. The size of the nanoMIPs did not vary between incubation points, which indicated that these nanoMIPs are stable and its spherical morphology remains intact.

Meesaragandla and colleagues also reported similar results, where they demonstrated and claimed the stability of dextrin coated gold nanoparticle in protein rich culture media (Meesaragandla et al., 2022). However, there was small increase in D_h of nanoMIPs observed which might be due to the interactions of biomolecules in culture media and nanoMIPs. In addition to that, results from *in vitro* tests such as cytotoxicity, flow-cytometry, confocal microscopy showed that these nanoMIPs remain stable in the complex culture media and performed well. Overall results witness the stability of the nanoMIPs in culture media.

DOX release analysis: In this study, DOX release from different imprinted and non-imprinted polymeric nanoparticles, *viz.* FLU-DOX-nanoMIPs, FLU-DOX-nanoNIPs, and DOX-nanoMIPs, has been assessed at physiological pH (phosphate buffer saline, pH 7.4). All the nanoMIPs and nanoNIPs under investigation showed controlled release of DOX and a similar pattern of drug release because the monomer composition is similar, except for DOX-nanoMIPs, where fluorescein-o-methacrylate is absent (**Figure A.4**, Appendix A). Therefore, complete drug release was shown in both FLU-DOX-nanoMIPs and FLU-DOX-nanoNIPs in 72 hours, whereas DOX-nanoMIPs showed complete DOX release in 68 hours. The controlled release of DOX is ascribed to the protective effect of the MIP layer around the DOX drug, and the DOX is released via a diffusion mechanism. These nanoMIPs showed a pattern of sustained release of DOX, which not only prevents premature DOX release but also helps maintain DOX concentrations at a level to achieve a beneficial therapeutic effect.

5.4.2 Binding performance and selectivity of nanoMIPs

The prepared nanoMIPs were tested for their binding affinity towards the ERα protein (68kDa) and the ERα template epitope used in the imprinting process via surface plasmon resonance (SPR) in a solution of PBS pH 7.4 and 0.01% Tween 20. To compare the effect of DOX loading on nanoMIPs, two different types of nanoMIPs (FLU-nanoMIPs and DOX-FLU-nanoMIPs) were explored for the affinity against both ERα protein and ERα epitope (CSHSLQKYYITGEAEGFPATV). The nanoMIPs were immobilised onto carboxymethyl dextran hydrogel-coated gold (Au) chips through EDC-NHS chemistry, where the amine moiety of nanoMIPs was crosslinked with the carboxymethyl dextran on the Au chip (Sullivan et al., 2021). The sensograms depicted in **Figure 5.3a**, correspond to the

association and dissociation between the ERα protein to FLU-nanoMIPs, with a similar trend observed for the other set of experiments for FLU-nanoMIPs with template epitope (**Figure 5.3b**), FLU FLU-DOX-nanoMIPs with ERα protein and template epitope (**Figure 5.3c,d**) respectively. The increase in signal referred to the association of epitope/ERα protein to the nanoMIPs and the association constant (K_{on}) have been determined. The decrease in the signal showed the dissociation phase by which the dissociation constant was calculated (K_{off}). The binding affinity of a molecular interaction was quantified by the equilibrium dissociation constant (K_D) calculated from the values of K_{off} / K_{on}. Response increases linearly in case of template epitope/ ERα protein (from concentration range of 4 to 64 nM) for both FLU-nanoMIPs and FLU-DOX-nanoMIPs. The K_D values for the entire ERα protein was found to be 10.8 nM and 14.7 nM for FLU-nanoMIPs and FLU-DOX-nanoMIPs, respectively. In case of template epitope, K_D values came out to be 19.2 nM and 16.2 nM for FLU-nanoMIPs and FLU-DOX-nanoMIPs respectively.

Typically, antibodies have K_D values falling within the low micromolar range to nanomolar range, indicating moderate to high affinity for the antigens they bind to. However, antibodies that exhibit even stronger binding affinity are considered to be high-affinity antibodies, with K_D values falling within the low nanomolar to sub-nanomolar range (abcam.com, 2022). Our results revealed that the binding affinity of our nanoMIPs was comparable to that of antibodies. Selectivity is a crucial factor in the development of nanoMIPs as a targeted drug delivery system because it determines the ability of nanoMIPs to selectively bind and deliver drugs to the desired target, such as cancer cells, while minimising their toxicity to healthy tissue (Fei et al., 2011). The selectivity of nanoMIPs was evaluated by using the nontarget epitope SSERIDKQIRYILDGISALR (epitope of interleukin 6), which has a similar molecular weight (M_w) of 2333.64 Da. The results showed that the K_D values for the nontarget epitope were approximately 62 times higher for both FLU-nanoMIPs and FLU-DOX-nanoMIPs as compared to target ERα protein (**Figure 5.3e,f**). Specifically, results found that a 62-fold higher concentration of the nontarget is required to occupy 50% of the nanoMIPs. These results demonstrated the high selectivity of the nanoMIPs for the target ERα protein, which is critical for their effectiveness as a targeted drug delivery system.

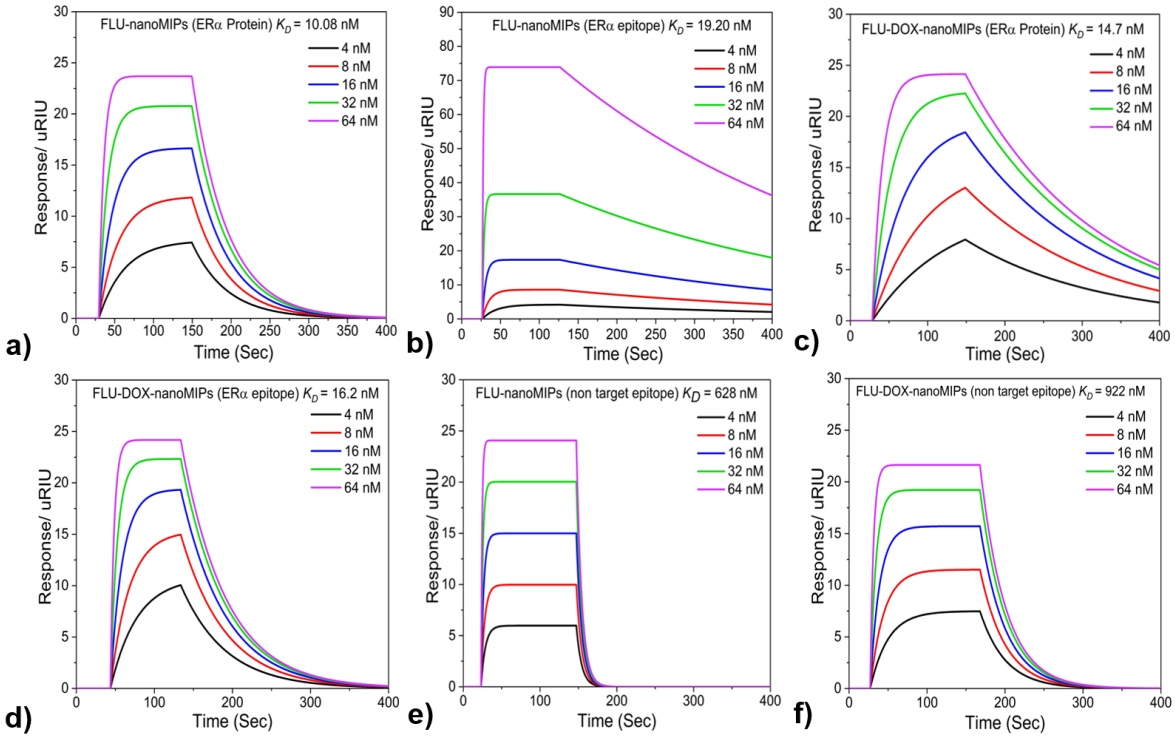

Figure 5.3: Typical sensorgrams depicting binding of different nanoMIPs **a)** FLU-nanoMIPs with ERα protein, **b)** FLU-nanoMIPs with ERα epitope, **c)** FLU-DOX-nanoMIPs with ERα protein, **d)** FLU-DOX-nanoMIPs with ERα epitope, **e)** FLU-nanoMIPs with non-target epitope, and **f)** FLU-DOX-nanoMIPs with non-target epitope.

5.4.3 In-vitro cell binding and specificity of nanoMIPs

Two different BC cell lines MCF-7 (ERα positive) and MDA-MB-231 (ERα negative) have been chosen to visualize the specific binding of nanoMIPs using flow cytometry. Flow cytometry binding for FLU-nanoMIPs, FLU-DOX-nanoMIPs and DOX-nanoMIPs at 10μg/mL concentration with MCF-7 and MDA-MB-231 are represented in **Figure 5.4 a,b,c** respectively. These results demonstrate that there is significantly higher binding of the nanoMIPs (10μg/mL) to MCF-7 cells in comparison to MDA-MB-231 cells. The higher the fluorescence intensity, the higher is the binding of nanoMIPs towards the cells overexpressing ERα. The mean fluorescence intensity (MFI) plots of the FLU-nanoMIPs ($P \leq 0.001$), the FLU-DOX-nanoMIPs ($P \leq 0.0001$), and the DOX-nanoMIPs ($P \leq 0.01$) shown in **Figure 5.4d,e,f** demonstrated that MCF-7 cells exhibited ~4 folds greater number of MFI positive cells than MDA-MB-231 cells. However, low levels of binding with MDA-MB-231 cells have also been encountered, which can occur since some report suggest that there is small amount of ERα present in that cell line (Al-Bader et al., 2011; Ford et al., 2011), in addition to the fact that all nanoparticles have some unavoidable non-

specific binding to the surface of cells.

In addition to that, binding of each nanoMIPs with MCF-7 cells at higher concentration, 40μg/mL was also tested, and the comparison graph is shown in **Figure A.5**, Appendix A. The binding was found to be similar for each nanoMIP type, regardless of concentration. This suggests that the binding is mostly specific, and the lower concentration (10μg/mL) of nanoMIPs was sufficient to occupy most of the ERα. The comparison between FLU-DOX-nanoMIPs and FLU-nanoMIPs revealed that the double imprinting of DOX in these nanoMIPs did not have an adverse effect on their binding performance. In fact, the binding capability was observed to be improved in the double imprinted nanoMIPs.

5.4.4 In vitro cytotoxicity assessment

In vitro cytotoxicity of the different nanoMIPs has been assessed using a MTT assay. After treating MCF-7 cells with different ER-α nanoMIPs (FLU-nanoMIPs, FLU-DOX-nanoMIPs, and DOX-nanoMIPs), an increase in cell cytotoxicity was observed in a time-dependent manner after 24, 48, and 72 hours of incubation. Specifically, nanoMIPs and FLU-nanoMIPs demonstrated significant cytotoxicity (28.29 ± 2.3 % and 30.6 ± 1.2 % respectively) after 24 hour incubation with MCF-7 cells, with only a 9 and 11% increase in cytotoxicity (total 37.22 ± 2.2 % and 41.8 ± 1.2 %) respectively after 72 hours. Conversely, FLU-DOX-nanoMIPs and DOX-nanoMIPs exhibited significant cytotoxicity in MCF-7 cells ($P \leq 0.0001$) even after 24 hours (42.8 ± 0.7 % and 45.5 ± 3.0 %). As FLU-DOX-nanoMIPs and DOX-nanoMIPs contains equal amount of drug, therefore show similar cytotoxicity trend in case of both nanoMIPs. Furthermore, after 72 hours, treatment with FLU-DOX-nanoMIPs and DOX-nanoMIPs resulted in 80.4 ± 0.99 % and 78.3 ± 1.03 % cell death, respectively (**Figure 5.4g**). The similar *in vitro* cytotoxicity observed with both DOX-nanoMIPs and FLU-DOX-nanoMIPs was due to the presence of the equal DOX concentration in these nanoMIPs. The cytotoxicity of FLU-nanoMIPs, FLU-DOX-nanoMIPs, and DOX-nanoMIPs towards MDA-MB-231 cells was found to be only 12.3 ± 2.7 %, 15.0 ± 2.8 %, and 18 ± 2.2%, respectively (as illustrated in **Figure 5.4h**).

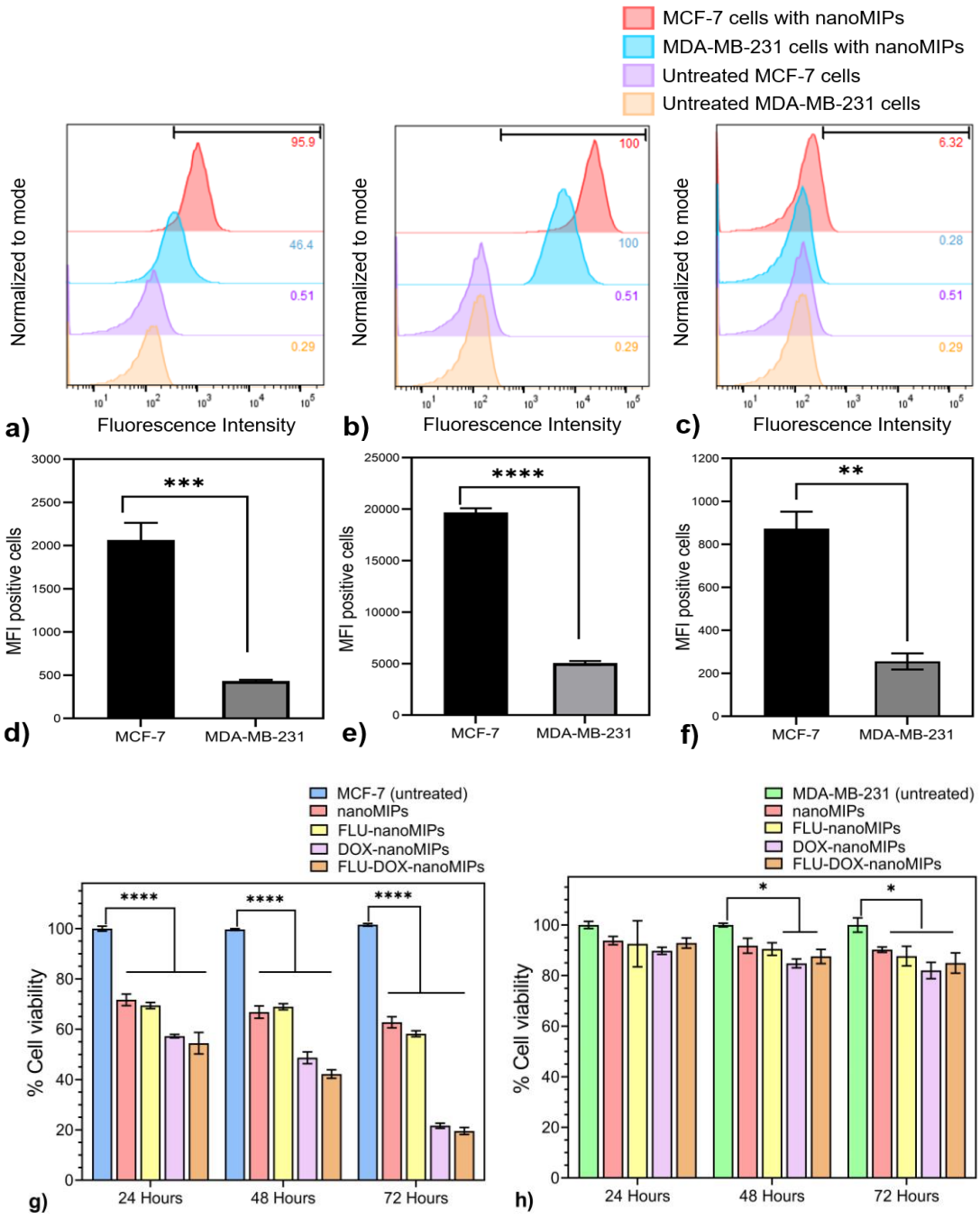

Figure 5.4: *In-vitro* flow cytometry binding assay, cells were incubated with 10 µg/mL of **a)** FLU-nanoMIPs, **b)** FLU-DOX-nanoMIPs, **c)** FLU-DOX-nanoMIPs; Mean Fluorescein intensity (MFI) positive cells (MCF-7 vs MDA-MB-231) with binding of **d)** FLU-nanoMIPs, **e)** FLU-DOX-nanoMIPs, **f)** DOX-nanoMIPs. *In-vitro* cell viability assay, at 10 µg/mL for each treatment of nanoMIPs, FLU-nanoMIPs, DOX-nanoMIPs and FLU-DOX-nanoMIPs in **g)** MCF-7 and **(h)** MDA-MB-231. Data is expressed as mean ± standard error of mean (SEM) of three measurements. ** P ≤ 0.01, *** P ≤ 0.001, **** P ≤ 0.0001 *vs.* MCF-7 **(d-f)**. **** P ≤ 0.0001 *vs.* MCF-7 **(g)**, * P ≤ 0.05 *vs.* MDA-MB-231 **(h).**

Moreover, control nanoMIPs (without FLU and DOX) also induced some cytotoxicity (36 ± 1.8 %) in MCF-7 cells after 72 hours, where no significant cytotoxicity (9.75 ± 0.6 %) with these nanoMIPs was observed in MDA-MB-231 cells (**Figure A.6**, Appendix A). The MTT assay results indicated a marked difference in cytotoxicity between MCF-7 (ERα positive) and MDA-MB-231 (ERα negative) cell lines, which could be attributed to the selective binding and cellular uptake behaviour of these nanoMIPs towards ERα positive cells. The FLU-nanoMIPs exhibited selective cytotoxicity, while FLU-DOX-nanoMIPs and DOX-nanoMIPs show enhanced cytotoxicity to MCF-7 cells. FLU-nanoMIPs also elicited some cytotoxicity to the MCF-7 cells, this could be due to their specific binding to the helix 12 (H12) region of the ER receptor, which plays a crucial role in dimerization and transcriptional activation (Arao and Korach, 2021; Muyan et al., 2015; Yaşar et al., 2017).

We also examined the cytotoxicity of non-imprinted polymeric nanoparticles (NIPs), unloaded and DOX-loaded NIPs (FLU-NIPs and FLU-DOX-NIPs) in MCF-7 and MDA-MB-231 cells. Results showed that NIPs, FLU-NIPs were highly biocompatible as both cell lines demonstrated cell viability of >90% even after 72 hours of exposure. However, treatment with FLU-DOX-NIPs resulted in some cytotoxicity to MCF-7 and MDA-MB-231 cells (20 ± 0.73 % and 25 ± 2.8 % after 72 hours respectively) likely due to the diffusion of DOX from the nanoparticles over time (as seen in **Figure A.6a,b**, Appendix A). In addition, incubation with DOX showed a significant decrease in cell viability in both cell lines, which was consistent with previous literature reports (Abdullah et al., 2014; Minaei et al., 2016). Furthermore, the selected batches of nanoMIPs have been investigated for the live/dead assay in 3D cancer models in the sub-section 2.6.

5.4.5 CLSM imaging

To assess the cellular uptake and internalisation of nanoMIPs in BC cells, CLSM microscopy has been employed. MCF-7 and MDA-MB-231 cells (~80% confluency) were treated with FLU-nanoMIPs and FLU-DOX-nanoMIPs (10 µg/mL) in the chamber plates for 1 and 24 hour at 37 °C. Moreover, a control experiment for ERα expression in both MCF-7 and MDA-MB-231 was also performed and the results are depicted in **Figure A.7a,b**, Appendix A. The mean fluorescence intensity of ERα was observed to be significantly higher in MCF-7 cells as compared to the MDA-MB-231 cells (depicted in **Figure A.7c**, Appendix A) and the results are consistent with the literature reports (Strillacci et al., 2022). Following the nanoMIPs incubation, the wells were washed with PBS (three times) to remove the nanoparticles that were not internalised or bound to the

cells. DAPI and Alexa Fluor™ 594 wheat germ agglutinin (WGA) was used to stain cell nucleus (blue) and plasma membrane (red) respectively. Following 1 hour incubation, FLU-nanoMIPs (**Figure 5.5a**) and FLU-DOX-nanoMIPs (**Figure 5.5b**) were found to specifically bind with the plasma membrane of the MCF-7 cells. On the other hand, minimal binding of FLU-nanoMIPs (**Figure A.8**) and FLU-DOX-nanoMIPs (**Figure 5.5c**) with MDA-MB-231 cells were observed. Moreover, difference in MFI (calculated from confocal images) between MCF-7 cells and MDA-MB-231 cells treated with FLU-nanoMIPs ($P \leq 0.01$) and FLU-DOX-nanoMIPs ($P \leq 0.001$) was found to be statistically significant (**Figure 5.5d**). This signifies that the binding of nanoMIPs is specific to the ERα positive cells.

The 12 hour post-incubation, specifically of FLU-DOX-nanoMIPs (illustrated in **Figure A.9**, Appendix A) and FLU-nanoMIPs and FLU-DOX-nanoMIPs in both MCF-7 and MDA-MB-231 cells after 24 hour incubation, was further examined. It was evident that FLU-nanoMIPs (**Figure 5.6a**) and FLU-DOX-nanoMIPs (**Figure 5.6a**) were able to cross the plasma membrane and get internalised into MCF-7 cells. On the contrary, no significant uptake of nanoMIPs in ERα negative cell line MDA-MB-231 was observed, as shown in **Figure 5.6c,d**. It has been reported that ERα binds with Caveolin-1, which is one of the structural proteins of caveolae, and plays a major role in trafficking of ERα to and from the cell surface and maintaining an environment for cell signalling and endocytosis of Erα (Christensen and Micevych, 2012).Thus, the internalisation of nanoMIPs into MCF-7 cells can likely be attributed to the ERα mediated caveolae dependent endocytosis (Balogh et al., 2013; Carroll et al., 2005). Furthermore, the difference in MFI between MCF-7 cells and MDA-MB-231 cells subjected to 10 µg/mL of FLU-nanoMIPs ($P \leq 0.01$) and FLU-DOX-nanoMIPs ($P \leq 0.001$) was statistically significant (**Figure 5.6e**).

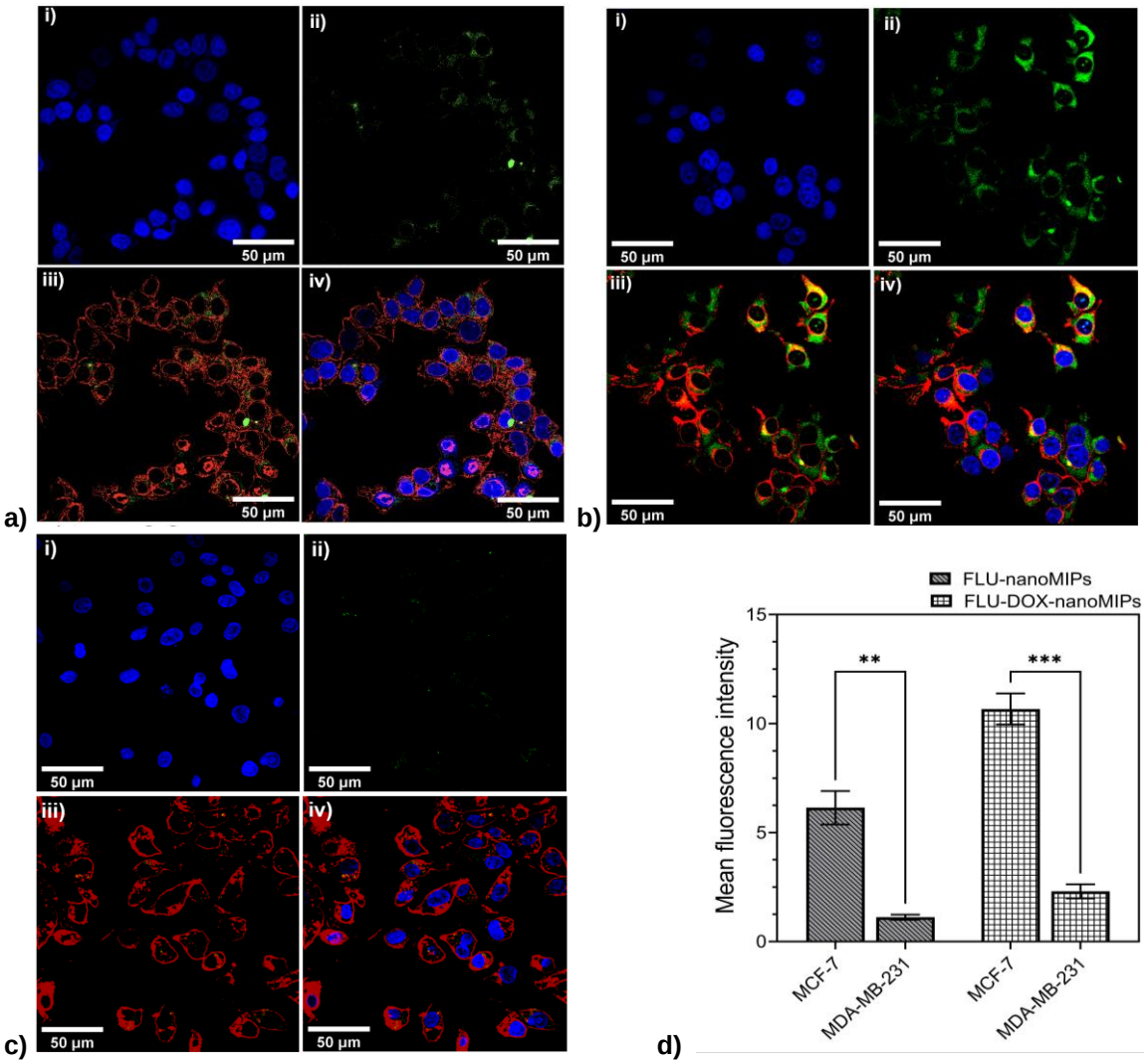

Figure 5.5: CLSM images (40X) of MCF-7 cell line incubated for 1 hour (at 37 °C) with (a) FLU-nanoMIPs and (b) FLU-DOX-nanoMIPs; (c) CLSM images (40X) for MDA-MB-231 incubated with FLU-DOX-nanoMIPs for 1 hour at 37 °C i) DAPI, ii) FLU-DOX-nanoMIPs with green fluorescence, iii) plasma membrane with red fluorescence (WGA Alexa Fluor™ 594) with FLU-DOX-nanoMIPs, iv) merged; (d) The mean fluorescence intensity of FLU-nanoMIPs and FLU-DOX-nanoMIPs in MCF-7 cells and MDA-MB-231 cells. ** $P \leq 0.01$, *** $P \leq 0.001$, vs. MCF-7.

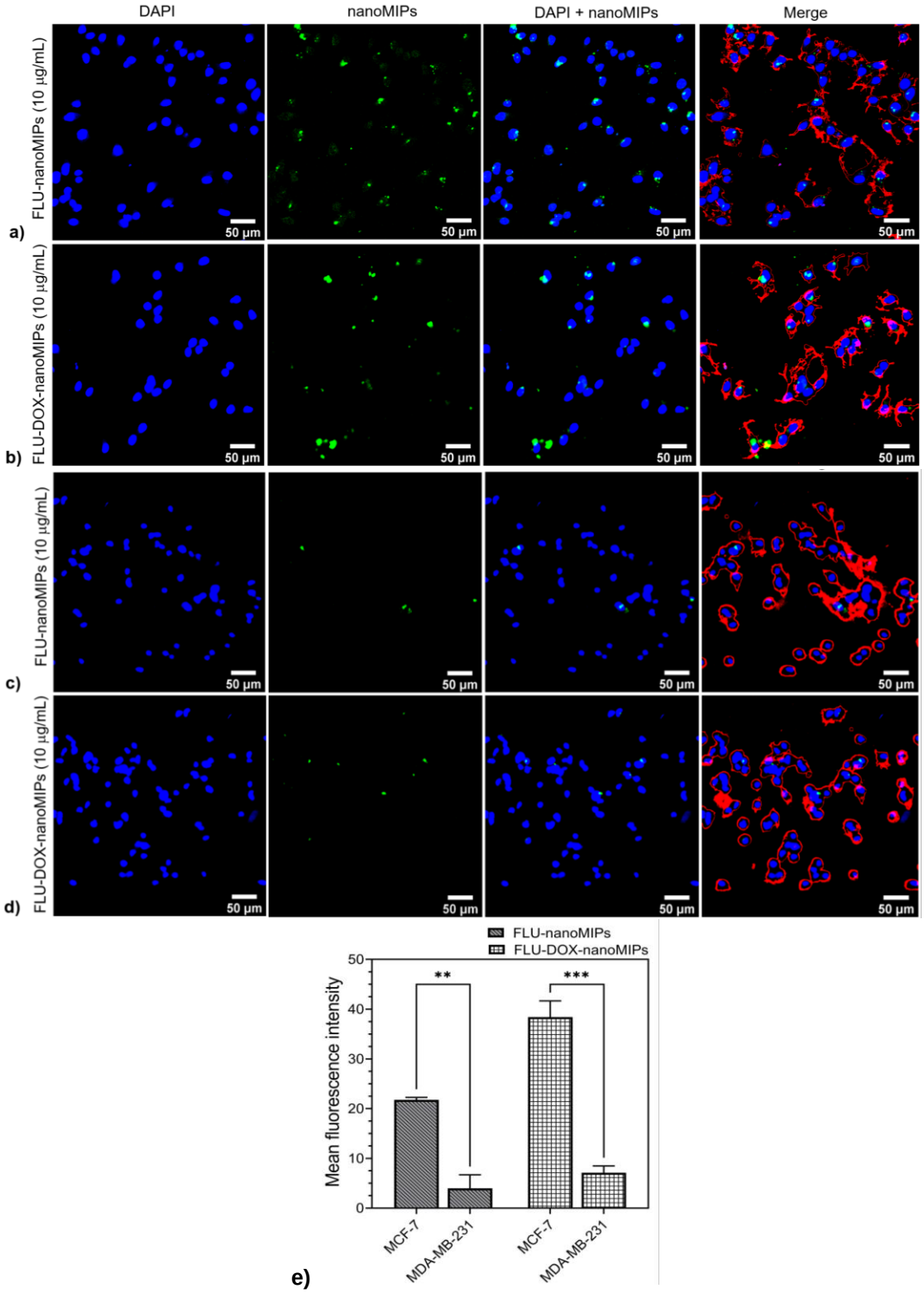

Figure 5.6: CLSM images (20X) for nanoMIPs incubated for 24 hour at 37 °C **(a)** MCF-7 cells incubated with FLU-nanoMIPs, **(b)** MCF-7 cells incubated with FLU-DOX-nanoMIPs, **(c)** MDA-MB-231 cells incubated with FLU-nanoMIPs, **(d)** MDA-MB-231 cells incubated with FLU-DOX-nanoMIPs; Nucleus is stained with blue fluorescence (DAPI), nanoMIPs with green fluorescence, membrane with red fluorescence (WGA Alexa Fluor™ 594), **(e)** The mean fluorescence intensity of FLU-nanoMIPs, FLU-DOX-nanoMIPs in MCF-7 cells and MDA-MB-231 cells. ** $P \leq 0.01$, *** $P \leq 0.001$, *vs.* MCF-7.

After internalisation (as illustrated at 63X in **Figure 5.7a** for FLU-nanoMIPs and **Figure 5.7b** for FLU-DOX-nanoMIPs), the nanoMIPs proceed to translocate into the nucleus, as demonstrated in **Figure 5.7c i**. The 3D CLSM image confirmed the colocalization of the nanoMIPs within the nucleus of ERα positive cells, as evidenced by the overlapping fluorescence signal in yellow (**Figure 5.7c ii**). It has been observed that 3.53% of the volume of the nucleus (in case of **Figure 5.7c ii**) colocalizes with FLU-DOX-nanoMIPs, furthermore, 15.61 % and 1.71 % of the volume of Cluster 1 and Cluster 2 respectively colocalised with the nucleus.

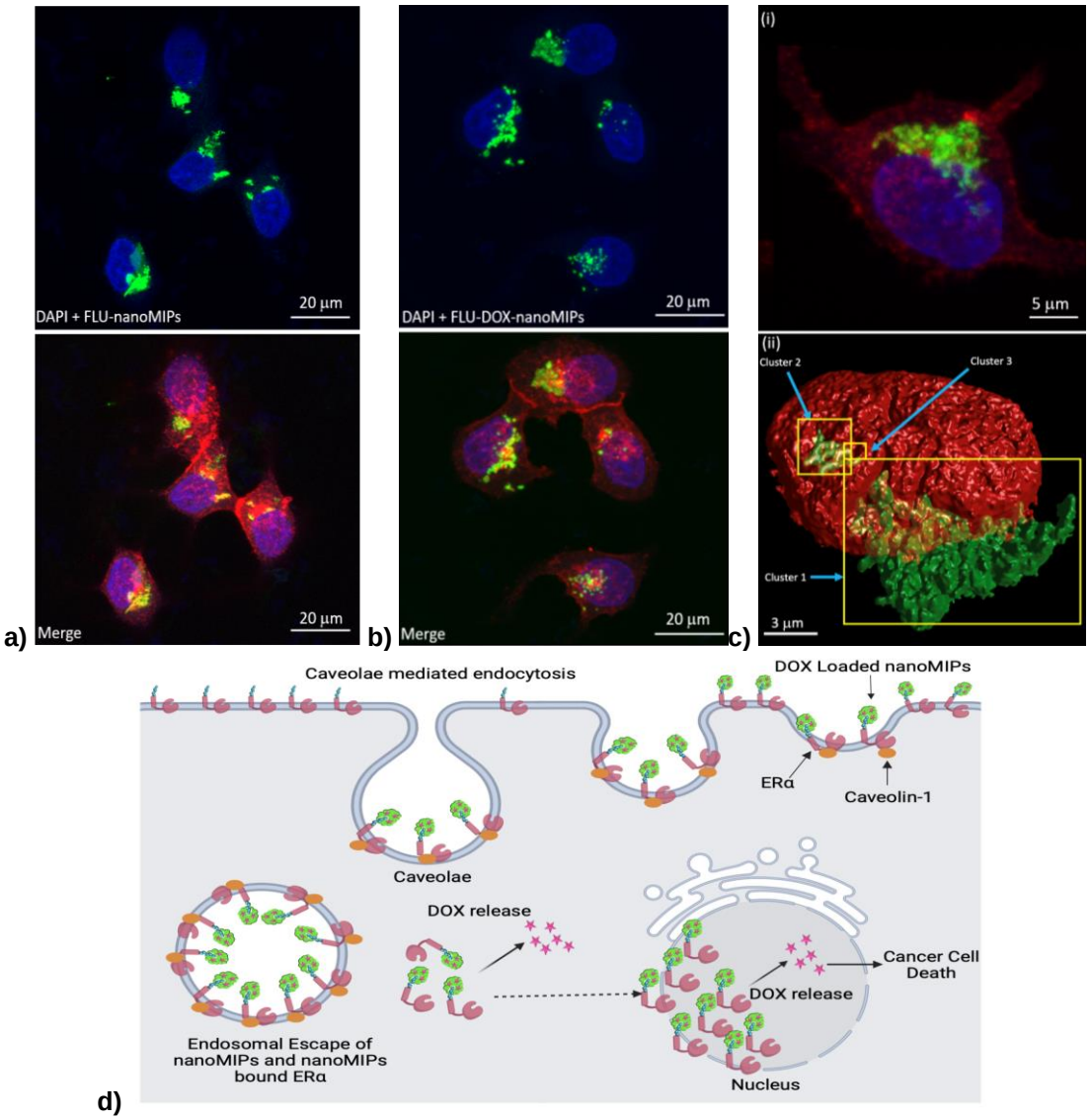

Figure 5.7: CLSM images (63X) of MCF-7 cell line incubated with **(a)** FLU-nanoMIPs, **(b)** FLU-DOX-nanoMIPs for 24 hour at 37 °C, **(c) i)** 3D image of FLU-DOX-nanoMIPs internalisation in MCF-7 cells **ii)** 3D render image showing the yellow areas (indicated by

the blue arrows) are FLU-DOX-nanoMIPs (green) clusters colocalising (hence, inside) the nucleus (red) of ERα positive MCF-7 cells. Nucleus is stained with blue fluorescence (DAPI), nanoMIPs with green fluorescence, membrane with red fluorescence (WGA Alexa Fluor™ 594), **(d)** Schematic representation of internalisation of nanoMIPs through caveolae mediated endocytosis membrane ERα followed by translocation to the nucleus and release of DOX in cytoplasm as well as in nucleus.

The ability of DOX loaded nanoMIPs to specifically bind to ERα positive MCF-7 and its nucleus led to the release of DOX to both cytoplasm and nucleus, thus resulting in higher cytotoxicity compared to MDA-MB-231 cells treated with nanoMIPs. These findings were consistent with our cytotoxicity results observed in MTT assay even at a lower concentration of DOX (~2 μg) in presence of 10 μg/mL nanoMIPs.

5.4.6 Evaluation of nanoMIPs in 3D cancer models

In order to investigate the action of nanoMIPs against MCF-7 cells, in a more tissue biomimetic environment, we conducted experiments in 3D porous polymer poly-urethane (PU) scaffolds, surface modified with Collagen I for extracellular matrix (ECM) mimicry (**Figure 5.8a**) (Gupta et al., 2022; Gupta et al., 2020; Totti et al., 2019). Collagen I is known to influence various factors related to the tumour microenvironment in breast cancer, such as proliferation, survival, migration, and invasion. Changes in the structure of Collagen I have been observed during early BC development and are associated with local invasion. Additionally, the density of Collagen I has been found to correlate with the progression of breast cancer (Badaoui et al., 2018; Provenzano et al., 2008b). Overall, the 3D cancer models are a better mimicry of essential aspects of tumour microenvironment (*in vivo*) in terms of structure, cell-to-cell and cell-to-extracellular matrix interactions and spatial orientation, as compared to the simple 2D culture shown in the previous sections (Gupta et al., 2022; Gupta et al., 2020; Gupta and Velliou, 2023).

More specifically, as described in the methodology section, at week 5 of the 3D culture, the cells were exposed to various treatments for 72 hours after which analysis of their spatial distribution and cell viability was performed. Our results showed that FLU-nanoMIPs successfully penetrated the 3D cancer models of ERα positive MCF-7 cell lines, as indicated by the green fluorescence in **Figure 5.8b i**. Clear binding of FLU-nanoMIPs with the nucleus (DAPI stained) has also been observed (co-localisation). These results demonstrated that these nanoMIPs can penetrate into complex 3D *in vitro* models. In the

case of FLU-DOX-nanoMIPs (**Figure 5.8b ii**), binding to the 3D cancer models of ERα positive MCF-7 cell lines was observed, but a smaller number of cells and lower fluorescence intensity were detected compared to FLU-nanoMIPs. This suggests that after treatment with DOX-loaded nanoMIPs, the cells that have up-taken these nanoMIPs underwent cell death, detached from the scaffolds and were eventually washed away during the washing process. Moreover, the cell viability of MCF-7 cells in 3D cancer models was determined 72 hours post treatment with nanoMIPs, DOX alone and DOX loaded nanoMIPs. **Figure 5.8c and d** demonstrated the confocal images of spatial assessment and quantification of the live/dead staining of multiple sections of different 3D cancer models. It was evidenced from **Figure 5.8c i** that MCF-7 cells were able to proliferate in 3D polyurethane-based scaffolds as can be seen from maximum % of calcein positive (green) area (80 ± 1.82 %) in **Figure 5.8d**. However, a lower cell viability of MCF-7 cells (52.3 ± 4.0 %) in 3D cancer models was observed post FLU-nanoMIPs treatment (72 hours) at 10μg/mL as compared to untreated BC MCF-7 cells (**Figure 5.8c ii,d**). This effect might be attributed to their selective binding to the helix 12 (H12) region of the ER receptor, a region pivotal for dimerization and transcriptional activation. This binding could elucidate the cytotoxicity on MCF-7 cells(Muyan et al., 2015). Furthermore, the cell viability decreased more significantly after treatment with DOX alone (21.4 ± 0.44 %) and DOX-loaded nanoMIPs (26.6 ± 3.60%) at 10 μg/mL compared to MCF-7 control cells (**Figure 5.8c,d**) and was evident from the increased red area (representing dead cells) in **Figure 5.8c iii,iv** for DOX and DOX loaded nanoMIPs respectively. These 3D scaffold findings were in good agreement with the cell viability results obtained from the MCF-7 (2D) cell line and confer that these nanoMIPs can act as a suitable drug carrier for the targeted drug delivery with enhanced activity.

3D cancer models provided the preliminary estimation of the penetration and anticancer activity of DOX-loaded nanoMIPs and mimic better tumour environment than the 2D cell lines. Nonetheless, ADME and toxicity of these materials cannot be addressed using single cellular 3D cancer models. This needs more advanced scaffolds or multi-physiological systems with multiple organs such as liver, kidney, heart, and many more to get more information about the biodistribution, ADME, and toxicity (Fabre et al., 2020; Van Ness et al., 2022). One can also consider xenograft animal models; however, these animal models do not usually possess a complete immune system. These nanoMIPs have been synthesised using a non-degradable crosslinker, and this is a proof-of-concept study

which showed that these double imprinted nanoMIPs can effectively act as a drug delivery vehicle for ER-positive BC and also achieve the nuclear delivery of the anticancer drugs. It is worth mentioning that these nanoMIP compositions are supposed to be excreted through the kidney, and these are not toxic to other organs as supported by previous *in vivo* studies (Kassem et al., 2022). In future studies, we are considering enzyme-cleavable crosslinkers (such as N,N'-Bis(acryloyl)cystamine) which will enable the synthesis of biodegradable nanoMIPs with further optimisation and standardisation. The scope of this work is the development and double imprinted nanoMIPs and their assessment via *in vitro* studies and 3D cancer models; however, for further ADME studies, advanced MPS (animal-free models) or xenograft animal studies might be considered for the further evaluation of such nanomaterials.

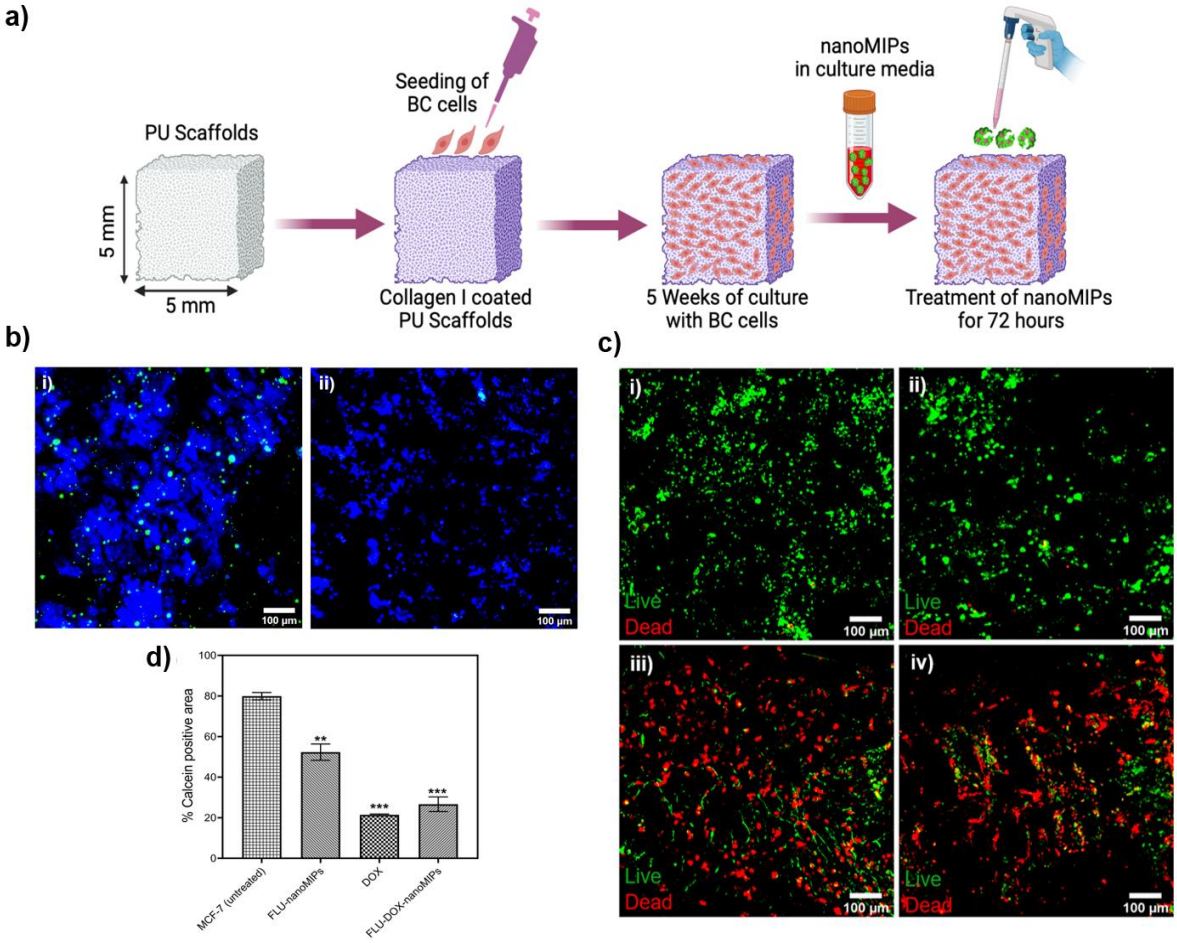

Figure 5.8: (**a)** Schematic of cell culture seeding and treatment of nanoMIPs to 3D scaffold; (**b)** CLSM images (10X) of 3D cancer models (poly-urethane scaffolds coated with Collagen-1) of MCF-7 cell lines treated with **i)** FLU-nanoMIPs, **ii)** FLU-DOX-nanoMIPs (after 72 hour treatment) at 37 °C. Nucleus is stained with DAPI (Blue); nanoMIPs are in green, **(c)** Cell viability (Live/Dead staining) following nanoMIPs and DOX

treatment; Representative images of scaffold sections for Live (green)/Dead (red) staining after 3 days incubation of **i)** MCF-7 control **ii)** FLU-nanoMIPs **iii)** DOX drug **iv)** FLU-DOX-nanoMIPs, (**d)** Quantification of Live (green) image area percentage (% calcein positive) using equivalent image analysis for (i-iv). Analysis included multiple scaffolds (n=3), various scaffold sections (n=3), and a total of 2 images, with average mean values being showcased. The results represent the mean average values.

5.5 Conclusion

A modified solid-phase methodology was used to produce double imprinted nanoMIPs, which enabled the formation of two types of binding sites. The primary site exhibited high specificity towards ER and the secondary site towards DOX, a chemotherapeutic drug, enabling the use of these nanoparticles as targeted drug delivery carriers. The synthesised DOX-loaded nanoMIPs had a spherical morphology with a typical size ranging from 140-170 nm. These materials rival the affinity of commercial antibodies, with a KD of 10 nM for ERα receptor as determined by

measurements. Moreover, these nanoMIPs specifically bound and elicited cytotoxicity (~80%) to ERα positive cancer cells compared to ERα negative cell lines (~15%) via nuclear delivery of DOX. This suggested that these smart nanocarrier systems can minimize off-target side effects while improving on drug efficacy. Furthermore, it was observed that FLU-DOX-nanoMIPs not only penetrated effectively to 3D cancer models of ERα positive BC cell line but also elicited cytotoxicity, as witnessed by live-dead staining. These findings provide strong evidence that these double-imprinted nanoMIPs exhibit similar behaviour in both 2D cell line and complex 3D cancer models that closely resemble the tumour microenvironment. It is worth noting that the membrane to nuclear drug delivery behaviour observed in this work is entirely novel and has not been reported on with molecularly imprinted or other hybrid nanoparticle systems. Importantly, ERα is also highly expressed in other types of cancer, such as endometrial, prostate, and ovarian cancer. Given the versatility of nanoMIPs, it is straightforward to extend this technology to the treatment of other cancers or other drug compounds. However, further studies are needed to explore the potential of these nanoparticles in clinical settings, their *in vivo* biodistribution and biocompatibility, and optimize their efficacy and safety. Overall, the use of targeted drug delivery systems such as nanoMIPs hold great promise for the future of cancer treatment due to their cost-effective nature, robustness, high selectivity, and scalable production process.

This study successfully demonstrated the use of nanoMIPs for targeted drug delivery. However, the application of nanoMIPs in delivering hydrophobic drugs remains a significant challenge due to their poor solubility in aqueous environments. To address this issue, we explored the use of commercially available polymers called Pluronics, to enhance the solubilization and loading of these hydrophobic drugs. By leveraging the amphiphilic properties of Pluronics, we aimed to improve drug bioavailability and enable more efficient delivery of hydrophobic drugs with details discussed in Chapters 6 and 7.

5.6 References

abcam.com (2022). *KD value: a quantitative measurement of antibody affinity, retrieved from* https://www.abcam.com/primary-antibodies/kd-value-a-quantitive-measurement-of-antibody-affinity.

Abdullah, A.-S. H., et al. (2014). 'Cytotoxic effects of mangifera indica l. Kernel extract on human breast cancer (mcf-7 and mda-mb-231 cell lines) and bioactive constituents in the crude extract' *BMC Complementary and alternative medicine*, 14 (1), pp. 1-10.

Acconcia, F. & Marino, M. (2011). 'The effects of 17β-estradiol in cancer are mediated by estrogen receptor signaling at the plasma membrane' *Frontiers in PHYSIOLOGY*, 2 p. 30.

Al-Bader, M., Ford, C., Al-Ayadhy, B. & Francis, I. (2011). 'Analysis of estrogen receptor isoforms and variants in breast cancer cell lines' *Experimental and therapeutic medicine*, 2 (3), pp. 537-544.

Al-Malky, H. S., et al. (2019). 'Modulation of doxorubicin-induced expression of the multidrug resistance gene in breast cancer cells by diltiazem and protection against cardiotoxicity in experimental animals' *Cancer Cell International*, 19 (1), pp. 1-10.

Ali, S. & Coombes, R. C. (2002). 'Endocrine-responsive breast cancer and strategies for combating resistance' *Nature Reviews Cancer*, 2 (2), pp. 101-112.

Arao, Y. & Korach, K. S. (2021). 'The physiological role of estrogen receptor functional domains' *Essays in biochemistry*, 65 (6), pp. 867-875.

Badaoui, M., et al. (2018). 'Collagen type 1 promotes survival of human breast cancer cells by overexpressing kv10. 1 potassium and orai1 calcium channels through ddr1-dependent pathway' *Oncotarget*, 9 (37), p. 24653.

Balogh, P., et al. (2013). 'Estrogen receptor alpha is expressed in mesenteric mesothelial cells and is internalized in caveolae upon Freund's adjuvant treatment' *PLoS One*, 8 (11), p. e79508.

Biotechnology, S. C. (2021). Estrogen Receptor alpha Antibody (F-10), retrieved from https://www.scbt.com/p/estrogen-receptor-alpha-antibody-f-10.

Canfarotta, F., et al. (2018). 'Specific drug delivery to cancer cells with double-imprinted nanoparticles against epidermal growth factor receptor' *Nano letters*, 18 (8), pp. 4641-4646.

Canfarotta, F., Poma, A., Guerreiro, A. & Piletsky, S. (2016a). 'Solid-phase synthesis of molecularly imprinted nanoparticles' *Nature protocols*, 11 (3), pp. 443-455.

Canfarotta, F., et al. (2016b). 'Biocompatibility and internalization of molecularly imprinted nanoparticles' *Nano Research*, 9 pp. 3463-3477.

Carroll, J. S., et al. (2005). 'Chromosome-wide mapping of estrogen receptor binding reveals long-range regulation requiring the forkhead protein foxa1' *Cell*, 122 (1), pp. 33-43.

Cecchini, A., et al. (2017). 'In vivo recognition of human vascular endothelial growth factor by molecularly imprinted polymers' *Nano letters*, 17 (4), pp. 2307-2312.

Chen, P., Li, B. & Ou-Yang, L. (2022). 'Role of estrogen receptors in health and disease' *Frontiers in Endocrinology*, 13 p. 839005.

Christensen, A. & Micevych, P. (2012). 'Cav1 siRNA reduces membrane estrogen receptor-α levels and attenuates sexual receptivity' *Endocrinology*, 153 (8), pp. 3872-3877.

Davis, M. E., Chen, Z. & Shin, D. M. (2008). 'Nanoparticle therapeutics: An emerging treatment modality for cancer' *Nature reviews Drug discovery*, 7 (9), pp. 771-782.

Ekpenyong-Akiba, A. E., et al. (2019). 'Detecting and targeting senescent cells using molecularly imprinted nanoparticles' *Nanoscale Horizons*, 4 (3), pp. 757-768.

Fabre, K., et al. (2020). 'Introduction to a manuscript series on the characterisation and use of microphysiological systems (mps) in pharmaceutical safety and ADME applications' *Lab on a Chip*, 20 (6), pp. 1049-1057.

Fang, R. H., Gao, W. & Zhang, L. (2023). 'Targeting drugs to tumours using cell membrane-coated nanoparticles' *Nature Reviews Clinical Oncology*, 20 (1), pp. 33-48.

Fei, Y., et al. (2011). ‘Fluorescent labeling agents change binding profiles of glycan-binding proteins’ *Molecular BioSystems*, 7 (12), pp. 3343-3352.

Ford, C. H., Al-Bader, M., Al-Ayadhi, B. & Francis, I. (2011). ‘Reassessment of estrogen receptor expression in human breast cancer cell lines’ *Anticancer research*, 31 (2), pp. 521-527.

Gupta, P., et al. (2022). ‘A systematic comparative assessment of the response of ovarian cancer cells to the chemotherapeutic cisplatin in 3d models of various structural and biochemical configurations—does one model type fit all?’ *Cancers*, 14 (5), p. 1274.

Gupta, P., et al. (2020). ‘A novel scaffold-based hybrid multicellular model for pancreatic ductal adenocarcinoma—toward a better mimicry of the in vivo tumor microenvironment’ *Frontiers in Bioengineering and Biotechnology*, 8 p. 290.

Gupta, P., et al. (2019). ‘Chemoradiotherapy screening in a novel biomimetic polymer based pancreatic cancer model’ *RSC advances*, 9 (71), pp. 41649-41663.

Gupta, P. & Velliou, E. G. (2023). 'A step-by-step methodological guide for developing zonal multicellular scaffold-based pancreatic cancer models’, Cancer *cell culture: Methods and protocols*: Springer, pp. 221-229.

Hu, T., Gao, J. & Wu, C. (2000). ‘Swelling and shrinking of poly (n-isopropylacrylamide) chains adsorbed on the surface of polystyrene nanoparticles’ *Journal of Macromolecular Science, Part B*, 39 (3), pp. 407-414.

Kassem, S., et al. (2022). ‘Assessing the in vivo biocompatibility of molecularly imprinted polymer nanoparticles’ *Polymers*, 14 (21), p. 4582.

Ko, J., Song, J., Choi, N. & Kim, H. N. (2024). ‘Patient-derived microphysiological systems for precision medicine’ *Advanced Healthcare Materials*, 13 (7), p. 2303161.

Kumar, S., Freelander, A. & Lim, E. (2021). ‘Type 1 nuclear receptor activity in breast cancer: Translating preclinical insights to the clinic’ *Cancers*, 13 (19), p. 4972.

Levin, E. R. (2003). ‘Bidirectional signaling between the estrogen receptor and the epidermal growth factor receptor’ *Molecular endocrinology*, 17 (3), pp. 309-317.

Lu, H., et al. (2021). 'Redox-responsive molecularly imprinted nanoparticles for targeted intracellular delivery of protein toward cancer therapy' *ACS nano*, 15 (11), pp. 18214-18225.

Marczell, I., et al. (2018). 'Membrane-bound estrogen receptor alpha initiated signaling is dynamin dependent in breast cancer cells' *European Journal of Medical Research*, 23 (1), pp. 1-10.

McClements, J., et al. (2022). 'Molecularly imprinted polymer nanoparticles enable rapid, reliable, and robust point-of-care thermal detection of sars-cov-2' *ACS sensors*, 7 (4), pp. 1122-1131.

Medina Rangel, P. X., et al. (2020). 'Chemical antibody mimics inhibit cadherin-mediated cell–cell adhesion: A promising strategy for cancer therapy' *Angewandte Chemie International Edition*, 59 (7), pp. 2816-2822.

Meesaragandla, B., et al. (2022). 'The impact of cell culture media on the interaction of biopolymer-functionalised gold nanoparticles with cells: Mechanical and toxicological properties' *Scientific Reports*, 12 (1), p. 16643.

Minaei, A., et al. (2016). 'Co-delivery with nano-quercetin enhances doxorubicin-mediated cytotoxicity against mcf-7 cells' *Molecular biology reports*, 43 pp. 99-105.

Mitchell, M. J., et al. (2021). 'Engineering precision nanoparticles for drug delivery' *Nature reviews drug discovery*, 20 (2), pp. 101-124.

Moiseenko, F., et al. (2017). 'Resistance mechanisms to drug therapy in breast cancer and other solid tumors: An opinion' *F1000Research*, 6.

Muyan, M., et al. (2015). 'Modulation of estrogen response element-driven gene expressions and cellular proliferation with polar directions by designer transcription regulators' *PLoS One*, 10 (8), p. e0136423.

NanoSciences, E. (2022). Doxosome™-Doxorubicin Liposomes (PEGylated), retreived from https://encapsula.com/products/liposomal-doxorubicin/non-surface-reactive-doxorubicin-liposomes/pegylated-non-surface-reactive-doxorubicin-liposomes-pegylated-doxosome/doxosome-doxorubicin-liposomes-pegylated/.

Nishino, H., Huang, C. S. & Shea, K. J. (2006). 'Selective protein capture by epitope imprinting' *Angewandte Chemie*, 118 (15), pp. 2452-2456.

Pasquardini, L. & Bossi, A. M. (2021). 'Molecularly imprinted polymers by epitope imprinting: A journey from molecular interactions to the available bioinformatics resources to scout for epitope templates' *Analytical and Bioanalytical Chemistry*, 413 (24), pp. 6101-6115.

Peer, D., et al. (2020). 'Nanocarriers as an emerging platform for cancer therapy' *Nano-enabled medical applications*, pp. 61-91.

Poma, A., et al. (2013). 'Solid-phase synthesis of molecularly imprinted polymer nanoparticles with a reusable template– "plastic antibodies"' *Advanced functional materials*, 23 (22), pp. 2821-2827.

Provenzano, P. P., et al. (2008). 'Collagen density promotes mammary tumor initiation and progression' *BMC medicine*, 6 (1), pp. 1-15.

Qin, Y.-T., et al. (2020). 'Tumor-sensitive biodegradable nanoparticles of molecularly imprinted polymer-stabilised fluorescent zeolitic imidazolate framework-8 for targeted imaging and drug delivery' *ACS applied materials & interfaces*, 12 (22), pp. 24585-24598.

Rodriguez, A. C., Blanchard, Z., Maurer, K. A. & Gertz, J. (2019). 'Estrogen signaling in endometrial cancer: A key oncogenic pathway with several open questions' *Hormones and Cancer*, 10 pp. 51-63.

Ronaldson-Bouchard, K., et al. (2022). 'A multi-organ chip with matured tissue niches linked by vascular flow' *Nature Biomedical Engineering*, 6 (4), pp. 351-371.

Saha Roy, S. & Vadlamudi, R. K. (2012). 'Role of estrogen receptor signaling in breast cancer metastasis' *International journal of breast cancer*, 2012.

Singla, P., et al. (2023). 'Electrochemical and thermal detection of allergenic substance lysozyme with molecularly imprinted nanoparticles' *Analytical and Bioanalytical Chemistry*, pp. 1-12.

Smith, L., et al. (2006). 'The analysis of doxorubicin resistance in human breast cancer cells using antibody microarrays' *Molecular cancer therapeutics*, 5 (8), pp. 2115-2120.

Strillacci, A., et al. (2022). 'Erα-lbd, an isoform of estrogen receptor alpha, promotes breast cancer proliferation and endocrine resistance' *NPJ Breast Cancer*, 8 (1), p. 96.

Sullivan, M. V., et al. (2021). 'Hybrid aptamer-molecularly imprinted polymer (aptamip) nanoparticles from protein recognition—a trypsin model' *Macromolecular bioscience*, 21 (5), p. 2100002.

Surapaneni, S. K., Bashir, S. & Tikoo, K. (2018). 'Gold nanoparticles-induced cytotoxicity in triple negative breast cancer involves different epigenetic alterations depending upon the surface charge' *Scientific reports*, 8 (1), p. 12295.

Teixeira, S. P., et al. (2021). 'Epitope-imprinted polymers: Design principles of synthetic binding partners for natural biomacromolecules' *Science Advances*, 7 (44), p. eabi9884.

Totti, S., et al. (2018). 'A 3d bioinspired highly porous polymeric scaffolding system for in vitro simulation of pancreatic ductal adenocarcinoma' *RSC advances*, 8 (37), pp. 20928-20940.

Totti, S., et al. (2019). 'A novel versatile animal-free 3D tool for rapid low-cost assessment of immunodiagnostic microneedles' *Sensors and Actuators B: Chemical*, 296 p. 126652.

Utsumi, T., Kobayashi, N. & Hanada, H. (2007). 'Recent perspectives of endocrine therapy for breast cancer' *Breast Cancer*, 14 (2), pp. 194-199.

Van Ness, K. P., et al. (2022). 'Microphysiological systems in absorption, distribution, metabolism, and elimination sciences' *Clinical and Translational Science*, 15 (1), pp. 9-42.

Villanueva, M. E., et al. (2020). 'Oligomer-stabilised silver nanoparticles for antimicrobial coatings for plastics' *Nano-Structures & Nano-Objects*, 24 p. 100610.

Wang, H., et al. (2021). '3d cell culture models: Drug pharmacokinetics, safety assessment, and regulatory consideration' *Clinical and translational science*, 14 (5), pp. 1659-1680.

Wishart, G., et al. (2021). 'On the evaluation of a novel hypoxic 3d pancreatic cancer model as a tool for radiotherapy treatment screening' *Cancers*, 13 (23), p. 6080.

Xu, Y., et al. (2021). 'Erα is an RNA-binding protein sustaining tumor cell survival and drug resistance' *Cell*, 184 (20), pp. 5215-5229. e17.

Yaşar, P., et al. (2017). 'Molecular mechanism of estrogen–estrogen receptor signaling' *Reproductive medicine and biology*, 16 (1), pp. 4-20.

Yuan, H., et al. (2020). 'Albumin nanoparticle of paclitaxel (abraxane) decreases while taxol increases breast cancer stem cells in treatment of triple negative breast cancer' *Molecular pharmaceutics*, 17 (7), pp. 2275-2286.

Chapter 6. Loading of Hydrophobic Drug Silymarin in Pluronic and Reverse Pluronic Mixed Micelles

*(Published as **S. Garg**, M. Peeters, R. K. Mahajan, P. Singla, Journal of Drug Delivery Science and Technology, 2022, 75, 103699)*

This first-author publication focuses on the development of Pluronic mixed micellar based drug delivery vehicles to enhance the solubilisation and loading of poorly water-soluble drugs. I have designed this work, performed most of the experiments and written the manuscript. Marloes Peeters and Rakesh Kumar Mahajan contributed to the conceptualisation of the study and helped in reviewing and editing the manuscript. Pankaj Singla co-designed this work and provided expert guidance on the experimental design and methodology.

In this work, two different types of Pluronics viz. normal Pluronics (P84, P85, F127 and F108) and reverse Pluronic 10R5 were explored as drug delivery vehicles. Normal Pluronics consist of two hydrophilic (polyethylene oxide, PEO) and one hydrophobic (polypropylene oxide, PPO) blocks and forms micelles in water with a hydrophobic core (PPO) and a hydrophilic shell (PEO). These typically form conventional spherical micelles and are well-suited for encapsulating hydrophobic drugs in aqueous environments. On the contrary, reverse Pluronic with two hydrophobic (PPO) and one hydrophilic (PEO) blocks forms micelles with two hydrophilic core (PEO) and a hydrophobic shell (PPO). These tend to form reverse micelles or other non-spherical aggregates such as rod-like, flower-like or worm-like micelles, especially in non-aqueous or low-polarity environments, making them more suitable for hydrophilic drug encapsulation.

6.1 Abstract

Poor water solubility of drugs is a significant challenge in pharmaceutical research and industry. A key strategy to overcome this issue is to improve the formulations of existing drugs. In this context, Pluronic micelles offer a promising approach for delivering hydrophobic (poor water soluble) drugs. Pluronics (tri-block copolymers) are already approved by the US FDA as excipients in various marketed formulations and are widely used in parenteral injections. In the presented work, pure Pluronic and mixed micelles of normal Pluronics (F108, F127, P85 and P84) with reverse Pluronic (10R5) have been studied to enhance the solubilisation of the hydrophobic drug silymarin (SLY) at different

% w/v proportions (4:1, 2:5, 1:4 and 5:0). Solubilisation capacity of SLY in the mixed micelles was found to be higher than pure Pluronic micelles. Drug solubilisation parameters including drug loading efficiency (*DL*), partition coefficient (*P*) and Gibbs free energy of solubilisation (ΔG°) were calculated. SLY loaded mixed micellar formulation of P84:10R5 (4:1% w/v) showed maximum solubility and drug loading efficiency as compared to other mixed micellar formulations. The *cmc* of pure as well as mixed micellar systems has been evaluated using fluorescence measurements. The locus of SLY in these micelles was evaluated by micropolarity measurements. After solubilisation, increase in hydrodynamic size evidenced by DLS measurements confirmed the solubilisation of SLY in the mixed micelles. *In vitro* drug release study was also performed for mixed micellar formulations with maximum SLY solubilisation, and it was found to exhibit sustained release drug behaviour. Different kinetics models were also applied and the best fitted model for the optimum SLY loaded mixed micellar formulation was found to be the Korsmeyer-Peppas model. To investigate the anti-oxidative potential of SLY drug and SLY loaded mixed micellar formulation of P84:10R5 (4:1% w/v),1,1-diphenyl-2-picryl-hydrazyl free radical (DPPH·) scavenging, ferrous ions (Fe^{2+}) chelating activities, total reducing ability determination by Fe^{3+} to Fe^{2+} transformation method, 2,2′-azino-bis(3-ethylbenzthiazoline-6-sulfonic acid) (ABTS) radical scavenging and nitric oxide assay were undertaken. The SLY loaded mixed micellar formulation of P84:10R5 (4:1% w/v) exhibited appreciably enhanced anti-oxidative activity as compared to SLY alone.

6.2 Introduction

Silymarin (SLY), a well-known flavolignan, has been isolated from *Silybum marianum* L. (Asteraceae) and is one of the most widely used drug of ancient times (Hellerbrand et al., 2017). SLY is known for its use as hepatoprotective (Saller et al., 2001), anti-diabetic**,** anti-nociceptive, anticancer, anti-inflammatory, and potential anti-oxidative activities (Agarwal et al., 2006; Al-Enazi, 2013; Gharagozloo et al., 2013; Karimi et al., 2011; Malekinejad et al., 2011; Shaker et al., 2010). Poor solubility of SLY is a major challenge to its bioavailability, since only 23-47% of the drug is documented to be absorbed on oral administration (Ghosh et al., 2010).

In recent years, various strategies have been employed to increase SLY solubilisation and bioavailability with different formulations such as Pluronic-lecithin-organogels (Mady et al., 2016), Pluronic nano micelles (El-Far et al., 2016), nanoparticles, liposomes, SLY lipid

emulsion (Abrol et al., 2005) and complexation of SLY with cyclo-dextrin-clathrate (Morazzoni et al., 1993). Pluronics [polyethylene oxide (PEO)-polypropylene oxide (PPO)-polyethylene oxide (PEO)] or micellar systems including normal Pluronic micelles, mixed micelles have been employed to increase the solubility of many poorly soluble drugs (Kwon and Kataoka, 1995). Pluronics have attracted attention as drug delivery system in pharmaceutical formulations due to their core-shell structure which allows the incorporation of drugs with poor solubility and prevents their degradation in biological media (Naskar et al., 2012). Pluronics are available commercially and are well documented as non-toxic, biocompatible polymers that have been approved by the US-FDA (Danson et al., 2004; Fda, 2019; Singla et al., 2019b). Micelles formed by reverse Pluronics have gained significant attention as drug carrier with different configurations of PPO-PEO-PPO units (Ma et al., 2007a). The prominent feature of reverse Pluronic is to self-assemble in water to form aggregates having different shapes such as flower, rod-like or lamellar (Noolandi et al., 1996). Although reverse Pluronics have high potential, studies conducted on these are sparse as compared to normal Pluronics. However, high critical micelle concentration (*cmc*) value of these polymers may be unfavourable since it can affect the stability of micelles. Furthermore, vesicles formed by reverse Pluronics have large size and exhibit phase separation (Larrañeta and Isasi, 2013). Therefore, an alternative approach for the efficient loading of poorly water-soluble drugs is to use a binary mixture of reverse Pluronic with normal Pluronic to achieve an increased drug loading, higher solubilisation capacity and enhanced stability (Hassanzadeh et al., 2015). Studies have revealed that mixtures of different types of surfactant solutions provide better surface activities and low *cmc* values as compared to single Pluronic solutions (Oh et al., 2004). Moreover, polymeric mixture can overcome the problems of low drug loading capacity and high *cmc* and fast release rate associated with normal Pluronic micelles.

The combination of normal Pluronic with reverse Pluronic 10R5 is reported to stabilise micelles and decreases the *cmc*. Naskar et al. studied the solution behaviour of binary mixture of Pluronic L44, 10R5 and suggested that a mixture of these two Pluronics has ability to serve as template for the synthesis of nanoparticles (Naskar et al., 2014). Zhang et al. reported increased drug loading capacity and significant increase in the anti-cancer activity of Pluronic P123-F127 mixed micelles of paclitaxel (Zhang et al., 2010). Singla et al. have also documented enhanced solubilisation of hydrophobic drugs clozapine and oxcarbazepine in mixed micelles of low molecular weight Pluronics (L64 and L35) and

high molecular weight (P84, F127, F68 and P123) Pluronics (Singla et al., 2020).

To the best of our knowledge, the current investigation is the first to explore the formulation characteristics of SLY loaded mixed micellar formulation using Pluronic mixtures for solubilisation of otherwise poorly soluble SLY with respect to its *in vitro* release profile and anti-oxidative activity.

6.3 Experimental

6.3.1 Materials

Silymarin (SLY), Pluronics P84, P85, F127, F108 and reverse Pluronic 10R5, 1,1-diphenyl-2-picryl-hydrazyl (DPPH·), 3-(2-pyridyl)-5,6-bis (4-phenyl-sulfonic acid)-1,2,4-triazine (Ferrozine), ABTS, tri-chloroacetic acid (TCA) were purchased from Sigma Aldrich, USA. All the materials were of analytical grade and used without any further purification. The molecular structure of SLY, normal Pluronics F108, F127, P85 and P84 and reverse Pluronic 10R5 depicted in **Figure 6.1**.

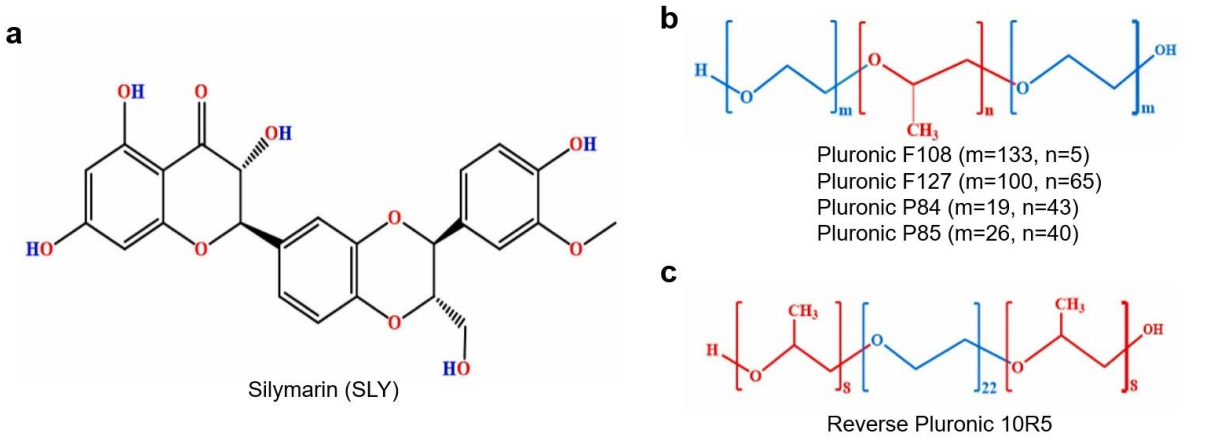

Figure 6.1 Chemical Structures of **(a)** Silymarin; **(b)** Normal Pluronics (F108, F127, P84 and P85) and **(c)** Reverse Pluronic 10R5.

6.3.2 Methods and equipment

The solubilisation of SLY in Pluronic, reverse Pluronic 10R5 micelles and Pluronics (F108, F127, P85, and P84)-reverse Pluronic 10R5 mixed micelles was studied using the direct dissolution method. To determine the amount of SLY solubilised in mixed micelles of 10R5 with different normal Pluronics and SLY *in vitro* release from these formulations, UV-visible double beam spectrophotometer (Shimadzu, UV-1800) was employed. The critical

micellar concentration (*cmc*) and locus of solubilised SLY in above mentioned Pluronic micelles and Pluronic-reverse Pluronic mixed micelles at different % w/v concentration (37 °C) was performed employing Fluorescence spectrophotometer F-4600 (Hitachi Tokyo, Japan). Pyrene was used as a standard fluorescent probe for fluorescence studies as reported earlier (Singla et al., 2020). DLS (Malvern Zetasizer Nanoseries Nano-ZS) measurements were performed to observe the D_h of SLY loaded and unloaded mixed micelles of normal Pluronics with reverse Pluronic 10R5 were determined for at 37 ± 0.1 °C, which operated with He-Ne laser (λ = 632.8 nm) at a scattering angle of 173°. The formulations were filtered through 0.2 µm millipore filters to remove the contaminants prior to sample measurements. To observe the antioxidant activity of Pluronic mixed micellar formulations, DPPH free radical scavenging activity, metal chelating activity, nitric oxide (NO) scavenging activity, $ABTS^{\cdot+}$ radical scavenging and ferric cyanide (Fe^{3+}) reducing activity assays were performed.

6.4 Results and discussion

6.4.1 Solubilisation of SLY into pure and mixed polymeric micelles

The solubilisation capacity of the pure and mixed micelles of normal Pluronic (F108, F127, P85 and P84) with reverse Pluronic 10R5 was determined at different (% w/v) copolymer concentrations, and the total ratio of Pluronic mixed system was 5% w/v. The UV-visible spectrum of SLY at various concentrations was recorded in methanol and λ_{max} was found to be 288 nm (**Figure 6.2**). The linear calibration curve for the absorbance versus concentration of SLY was plotted. The molar absorption coefficient was found to be 11.85×10^3 L mol^{-1} cm^{-1} determined using the slope of the calibration curve. This molar absorption coefficient was used to calculate the solubilisation of SLY in water and binary mixture of 10R5 with different Pluronics. The solubilisation of SLY in aqueous media was found to be less than 0.008 mg mL^{-1} , in accordance with literature value (Ghosh et al., 2010).

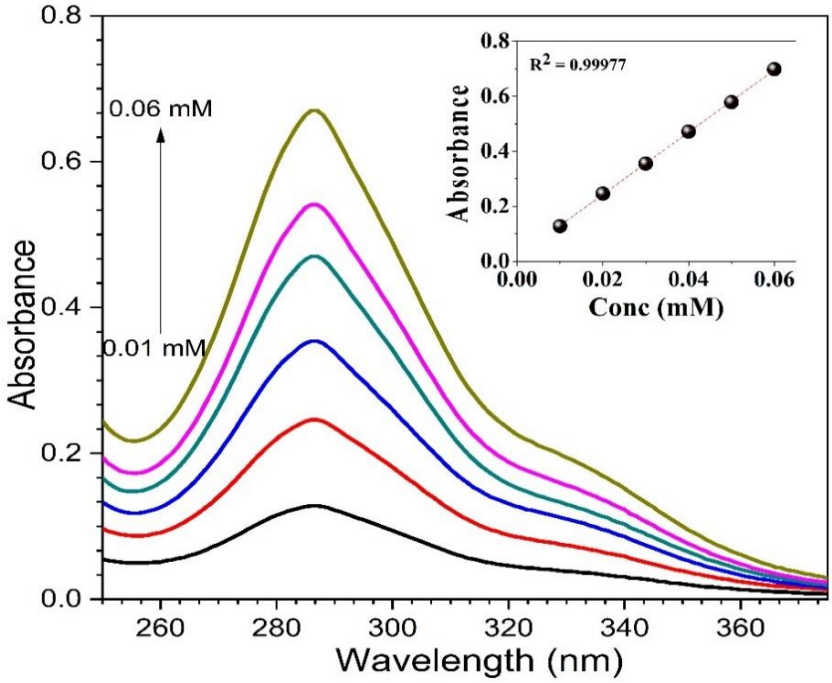

Figure 6.2: UV spectra of SLY at different concentrations (0.01-0.06 mM), **inset:** Calibration curve of SLY at 288 nm.

The micelles comprised of normal Pluronic exhibited highest solubility, while 10R5 Pluronics micelles showed the lowest solubility, at the same concentration. The lower solubility for 10R5 (3.08 mg/5 mL) could be corroborated to the fact that 10R5 reverse Pluronic form the different types of micellar structures such as flower-type, rod-like or lamellar micelle. These are spherical aggregates having PEO block at the outer layer and the core forming PPO blocks that penetrate more water resulting in lower solubilisation capacity (Naskar et al., 2012). The loading efficiency of the investigated individual normal Pluronics and reverse Pluronic 10R5 was found to be low.

Several studies have revealed improved solubilisation, stability as well as loading efficiency of hydrophobic drugs using mixed micellar systems (Hassanzadeh et al., 2015; Wei et al., 2009; Zhao et al., 2012). To increase the solubilisation capacity and loading efficiency of SLY, the mixed micelles of normal Pluronics with reverse Pluronic 10R5 were explored. Three different proportions of Pluronic (F108, F127, P85 and P84) with reverse Pluronic 10R5 (4:1; 2.5:2.5 and1:4) were selected to study the solubilisation of SLY. The results indicated that after addition of 1% w/v concentration of reverse Pluronic 10R5 to normal Pluronics (F108, F127, P85 and P84), the aqueous solubility of SLY was increased with improved loading efficiency. Further addition of reverse Pluronic 10R5 at

concentration of 2.5 and 4% w/v resulted in a decrease in solubilisation compared to that of 1% 10R5 in normal Pluronics micelles. The reason behind the decrease in solubilisation of the SLY with increasing concentration of 10R5 may be that higher concentration of 10R5 results in the formation of more random micellar structure which results in the penetration of more water in Pluronic:10R5 mixed micelles. This hypothesis was further confirmed by *cmc* measurements (section 6.4.4), as increasing concentration of 10R5 resulted in the higher *cmc* values. The penetration of more water in the mixed micelles forms more hydrophilic micellar structures which do not favour the penetration of hydrophobic SLY. This trend was observed in all investigated normal Pluronics (F108, F127, P85 and P84) comprising mixed micelles with 10R5.The SLY solubility pattern in normal and reverse Pluronic mixed micelles followed the order P84:10R5 > F127:10R5 > P85:10R5 >F108:10R5 at all different % w/v proportions (**Figure 6.3a**). Solubility values for the mixed micelles comprising P84:10R5 (4:1), (2.5:2.5) and (1:4) was 3.929 mg mL^{-1}, 2.890 mg mL^{-1} and 2.741 mg mL^{-1} representing more than 491, 361 and 342-fold increase respectively as compared to the aqueous solubility of SLY. This higher solubilisation and loading efficiency for P84:10R5 mixed micelles may be attributed to the more hydrophobic nature of Pluronic P84 as compared to other investigated Pluronics (Singla et al., 2016). Mixture of F127:10R5 at variable concentrations (4:1), (2.5:2.5) and (1:4) was found to increase the SLY solubility by 389 and 337 and 327 times than SLY aqueous solubility and found to be 3.116 mg mL^{-1} , 2.700 mg mL^{-1} and 2.622 mg mL^{-1} respectively. As observed in **Figure 6.3a,** in case of P85:10R5 at 4:1, 2.5:2.5 and 1:4 (% w/v) concentration, the solubility of SLY increased 365, 326 and 313-fold as compared to the water solubility of SLY and observed to be 2.922 mg mL^{-1} , 2.614 mg mL^{-1} and 2.506 mg mL^{-1} respectively. The least increase in solubility of SLY was observed in case of F108:10R5 was observed, the solubility of SLY was found to be 2.704 mg/mL (338 folds), 2.516 mg mL^{-1} (314 folds) and 2.288 mg mL^{-1} (286 folds) at 4:1, 2.5:2.5 and 1:4 respectively.

Interestingly, the solubilisation of SLY was found to be higher in case of F127:10R5 mixed micelles as compared to that of P85:10R5 micelles. This may be attributed to F127 Pluronic having more hydrophobic blocks (65 PPO units) than Pluronic P85 (40 PPO units) which likely resulted in the formation of more hydrophobic core of the F127:10R5 mixed micelle ideal for accommodation and incorporation of SLY (Singla et al., 2016). The least solubility in case of F108:10R5 may be due to the longer corona region comprising of 133

PEO units making it more hydrophilic and unfavourable for the solubilisation of hydrophobic SLY. As described in previous reports, the solubility of the hydrophobic drug molecules is improved by the hydrophobic nature of the Pluronic micelles through hydrophobic-hydrophobic interactions between the drug and Pluronics resulting in higher solubilisation in P84:10R5, F127:10R5 and P85:10R5. In case of F108:10R5 mixed micelles, there insufficient interaction between SLY and the hydrophilic core of Pluronic F108 which results in the lower solubilisation of SLY drug (Singla et al., 2020).

The Drug loading efficiency (*DLE*) was defined as the %age of SLY loaded from the SLY fed initially in mixed micelles during formulation process and has been computed from **Eq. 2.6 (Chapter 2).** SLY in a concentration of 20 mg was chosen to incorporate in these Pluronic micelles because the commercial product (Milk Thistle) by Purolabs Natural Science company, claimed that the active amount of SLY is 20 mg/capsule. Drug loading efficiency of P84:10R5 mixed micelles was found to be higher than other investigated Pluronic:10R5 mixed micelles (**Figure 6.3b**).

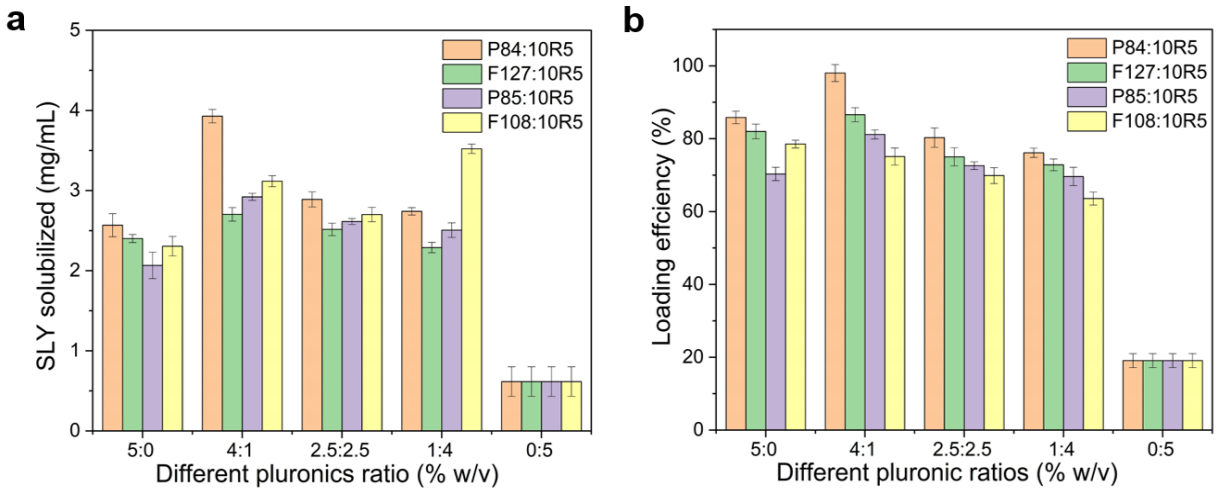

Figure 6.3: (a) Amount of SLY solubilised and **(b)** Loading efficiency in mixed micelles (5% w/v in total) of normal Pluronics (F108, F127, P85 and P84) with reverse Pluronic 10R5 at different concentrations (5:0, 4:1, 2.5:2.5, 1:4 and 0:5 %w/v).

6.4.2 Partition coefficient (P)

The partition coefficient (*P*) is an important parameter for the evaluation of micellar systems for their potential as drug carrier (Sun et al., 2018). UV-visible solubilisation results can be used to calculate the micellar/water partition coefficient and is described as the ratio of SLY in the Pluronic micelles to the SLY solubilised in water for a particular

Pluronic concentration as represented in **Eq. 2.8 (Chapter 2)**.

P value was found to be increased by addition of 1% of 10R5. A marked increase in partition coefficient in case of P84:10R5 mixed micelles was observed whereas the addition of the 10R5 (2.5 and 4% w/v) resulted in a decrease in the partition coefficient (**Figure 6.4a**). These results are in agreement with our UV–visible results that revealed higher solubilisation occurred in the case of Pluronic:10R5 at the proportion of 4:1. These results can be explained by the phenomenon of hydrophobic interaction between the SLY drug and core of the Pluronic:10R5 (4:1) mixed micelles resulting a more hydrophobic environment than other investigated proportions of Pluronic:10R5 (2.5:2.5, 1:4) mixed micelles.

6.4.3 Gibbs free energy of solubilisation (ΔG°)

The *ΔG°* value is described as the Gibbs free energy of transfer of 1 mol of the drug in the micellar phase. As mentioned in the partition coefficient section, the solubilisation can be considered as a normal partitioning of the drug between micelle and aqueous phases, and *ΔG°* was calculated from **Eq. 2.9 (Chapter 2)**.

The negative values of *ΔG°* showed (**Figure 6.4b**) that SLY solubilisation process in these mixed micelles of normal Pluronics (F108, F127, P85 and P84) with reverse Pluronic 10R5 is spontaneous and transfer of water molecules from the micellar core make a more hydrophobic environment (Desai et al., 2001; Ingram et al., 2013; Kadam et al., 2010; Parekh et al., 2011). However, an increase in the concentration of 10R5 from 1% w/v to 2.5 and 4% w/v resulted in less negative *ΔG°* values. This may be due to the penetration of the water in the mixed micelles which further resulted in the proportional decrease in the hydrophobic nature of these mixed micelles. Therefore, these results conferred that the increasing proportion of 10R5 in the mixed micellar system makes the SLY solubilisation less spontaneous.

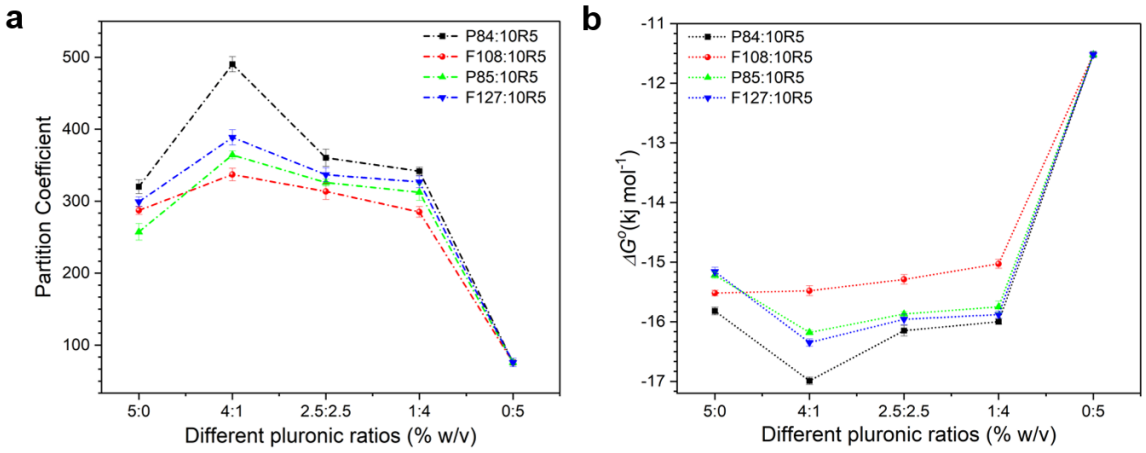

Figure 6.4: (a) Micellar/water Partition coefficient (*P*) and **(b)** Gibbs free energy of solubilisation (*ΔG°*) of mixed micelles (5% w/v in total) of normal Pluronic (F108, F127, P85 and P84) with reverse Pluronic 10R5 at 37 °C.

6.4.4 Fluorescence measurements

The critical micelle concentration (*cmc*) is an important parameter which influences the stability of micelles *in vitro* and *in vivo*. In this work, fluorescence measurements were employed to determine the *cmc* of the Pluronic mixed micelles using pyrene as a hydrophobic probe. The fluorescence emission spectra were plotted taking intensities ratio of I_{374}/I_{393} (I_1/I_3) versus copolymer concentration (see **Figure B.1, Appendix B**). The *cmc* values of different mixed micellar formulations *viz.* F108, F127, P85 and P84 with reverse Pluronic 10R5 at different % w/v concentrations are shown in **Table 6.1**. It was observed that upon addition of the reverse Pluronic 10R5 into the solution of normal Pluronics that is F108, F127 and P85, there was a slight increase in the *cmc* values as compared to pure normal Pluronic solutions. The pronounced decrease in the *cmc* values in case of P84:10R5 mixtures is ascribed to the hydrophobicity of P84 leads to increase in the interactions between them (Liu et al., 2011). Surprisingly, *cmc* values were very less than the 10R5 (3.551), which may be due to the intercalation of 10R5 monomers with the normal Pluronic micelles that are able to form micelles at that concentration. Renu et al., reported the similar results when they studied the interactional behaviour of 0.5 mM 10R5 with Surface active ionic liquids ([C8mim][Cl], [C10mim][Cl], and [C12mim][Cl]) in aqueous medium (Sharma et al., 2015). It is anticipated that the PPO segments of 10R5 undergo dehydration from the water phase and interact with the PPO segment of the normal Pluronics (F108, F127, P85 and P84), which is further followed by interaction of PEO region of 10R5 with normal Pluronics (Dai et al., 2001).

Table 6.1: Critical micelle concentration (*cmc*) values determined from Fluorescence measurements: pure and mixed micelles of different Pluronics (F108, F127, P85 and P84) with reverse Pluronic 10R5 at different % w/v at 37 °C.

Concentration	**Systems**			
(% w/v)	P84+10R5	P85+10R5	F127+10R5	F108+10R5
5:0	3.551	3.551	3.551	3.551
4:1	0.027	0.063	0.040	0.043
2.5:2.5	0.044	0.067	0.047	0.046
1:4	0.048	0.068	0.049	0.050
0:5	0.150	0.058	0.039	0.040

The ratio of the first (373 nm) and third (384 nm) vibronic peak intensities (I_1/I_3) of pyrene emission spectra senses the polarity of the medium in the immediate vicinity of the probe known as micropolarity (Chaudhuri et al., 2009; Hugerth, 2001). Therefore, location of SLY is adjudged in selected SLY loaded micellar system by observing the change in the micropolarity of pyrene probe (Ridell et al., 1999; Singla et al., 2018a). SLY loaded reverse Pluronic 10R5 micelles and four best performing mixed micelles *viz.* P84:10R5 (1:4, 4:1 % w/v) and F127:10R5 (1:4, 4:1 % w/v) have been studied for the micropolarity measurements.

Micropolarity values for reverse Pluronic 10R5 are depicted in **Figure 6.5a**, but R^2 value is 0.847 for linear fit regression. This suggests that the SLY is not experiencing same environment by each addition of SLY loaded 10R5 micelles, this means micropolarity is dynamic and SLY is exposed to both hydrophobic and hydrophilic environments. Moreover, the SLY drug is not fully shielded within the micelles due to the presence of water, which results from the loose micellar structure of reverse Pluronic 10R5 (Naskar et al., 2012). In contrast, micropolarity decreased linearly with increasing concentrations of SLY loaded P84:10R5 and F127:10R5 at a 4:1% w/v ratio, as shown in **Figures 6.5b,c**. A similar linear trend was observed at a higher 10R5 ratio in both P84:10R5 (1:4) and F127:10R5 (1:4) (**Figures 6.5d,e**). This linear decrease in the micropolarity (I_1/I_3) is referred to the hydrophobic environment of pyrene provided by more defined SLY loaded mixed micelles, consisting of and dominated by P84 and F127.

Singla and colleagues previously reported similar behaviour in pure Pluronic systems where P84 micelles showed a linear decrease in micropolarity with increasing clozapine concentration, while F127 micelles exhibited a linear trend followed by a plateau (Singla

et al., 2018). Reference micropolarity data from Singla et al. for pure F127 and P84 micelles with clozapine are included in Appendix B (**Figure B.2**). In the current study, the presence of reverse Pluronic 10R5 having longer PPO segments, appears to contribute additional hydrophobicity which results in linear decrease in the micropolarity in case of mixed micelles of F127:10R5.

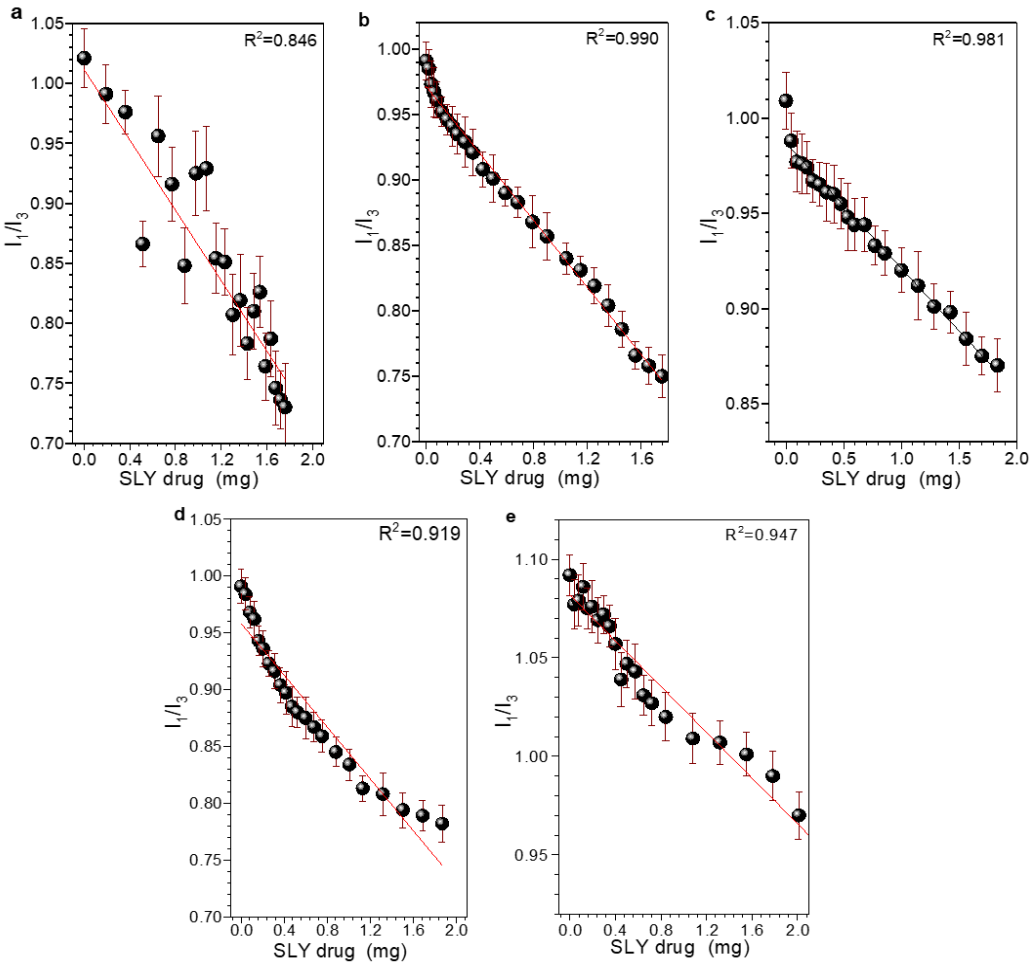

Figure 6.5: Variation of micropolarity ratio (I_1/I_3) as a function of SLY to determine solubilisation locus in different Pluronic and Pluronic-reverse Pluronic10R5 mixed micelles (5% w/v in total) at 37 °C (linear regression was fitted on obtained data). Each point represents average ± SD (n = 3). **(a)** 5% w/v 10R5, **(b)** P84:10R5 (4:1), **(c)** F127:10R5 (4:1), **(d)** P84:10R5 (1:4), **(e)** F127:10R5 (1:4) % w/v.

6.4.5 DLS measurements

The size and change in the size of the colloidal particles can be determined by DLS (Suh and Jun, 1996). The smaller particle size of nanoparticles facilitates the EPR (enhanced permeability and retention) effect results in the enhanced penetration (Ganguly et al.,

2012). Hydrodynamic diameter (D_h) of normal Pluronic F108, F127, P85 and P84 (at 5% w/v) was 24.36, 21.04, 15.7 and 13.54 ± 0.1 nm respectively. At the concentration of 4% of F108, F127, P85 and P84 with 1% reverse Pluronic 10R5, the D_h found to be 32.70, 24.4, 18.2 and 15.7 ± 0.1 respectively **(Figure 6.5)**. This increase in size of mixed micellar system was due to the formation of less arranged structure than pure micelles because pure reverse Pluronic 10R5 is only able to form random coils in aqueous solution (Sharma et al., 2015). Upon the solubilisation of SLY at the concentration ratio of 4%, normal Pluronics F108, F127, P85 and P84 with of 1% 10R5, the D_h value of different SLY loaded mixed micelles was observed to be 37.75, 28.2, 18.2 and 21 ± 0.1 nm respectively **(Figure 6.6)**. The increase in the D_h after the solubilisation of SLY confirmed the penetration of drug in these mixed micelles. The addition of 1% 10R5 in normal Pluronic micelles intervene the structure that can absorb the more cargo (SLY) molecule, may be due to the less compact structure than the pure micellar system (J. Wang et al., 2015). This is confirmed from the solubilisation results in which the higher solubility of SLY was found to be at 4:1 %w/v (normal Pluronic: reverse Pluronic 10R5) ratio. On the other hand, at concentration ratio of 2.5:2.5 %w/v of 10R5 with normal Pluronics F108, F127, P85 and P84 showed polydispersity with two D_h 36.56 and 113.73, 24.44 and 262.34, 20.96 and 228.75,19.2 and 147.73 respectively (**Figure B.2,** Appendix B)**.** At the higher concentration of 10R5 (4%) with 1% normal Pluronics F108, F127, P85 and P84, the D_h was found to be 330.8, 20.59 and 174.39, 19.97 and 194.29, 61.18, respectively (**Figure B.3,** Appendix B)**.** The polydispersity observed in case of higher concentration of 10R5 is attributed the structure of this reverse Pluronic which self-assemble into random structure (larger D_h) and normal Pluronics which form the smaller micelles (lower D_h values). Moreover, there may be intercalation of both reverse Pluronics 10R5 and normal Pluronic at both D_h values. SLY loaded mixed micellar formulation of normal Pluronics F108, F127, P85 and P84 with 10R5 at ratio 2.5:2.5 (% w/v), the D_h values were observed to be 50.48 and 152.29, 27.15 and 301.69, 24.86 and 297.13, 24.4 and 164.79 nm respectively **(Figure B.1)**. At higher concentration of 10R5 with normal Pluronics F108, F127, P85 and P84 with 10R5, the D_h values were increased after SLY loading into mixed micelles and found to be 386.49, 29.96 and 270.4, 521.58 and 195.91, 97.40 nm respectively **(Figure B.2)**.

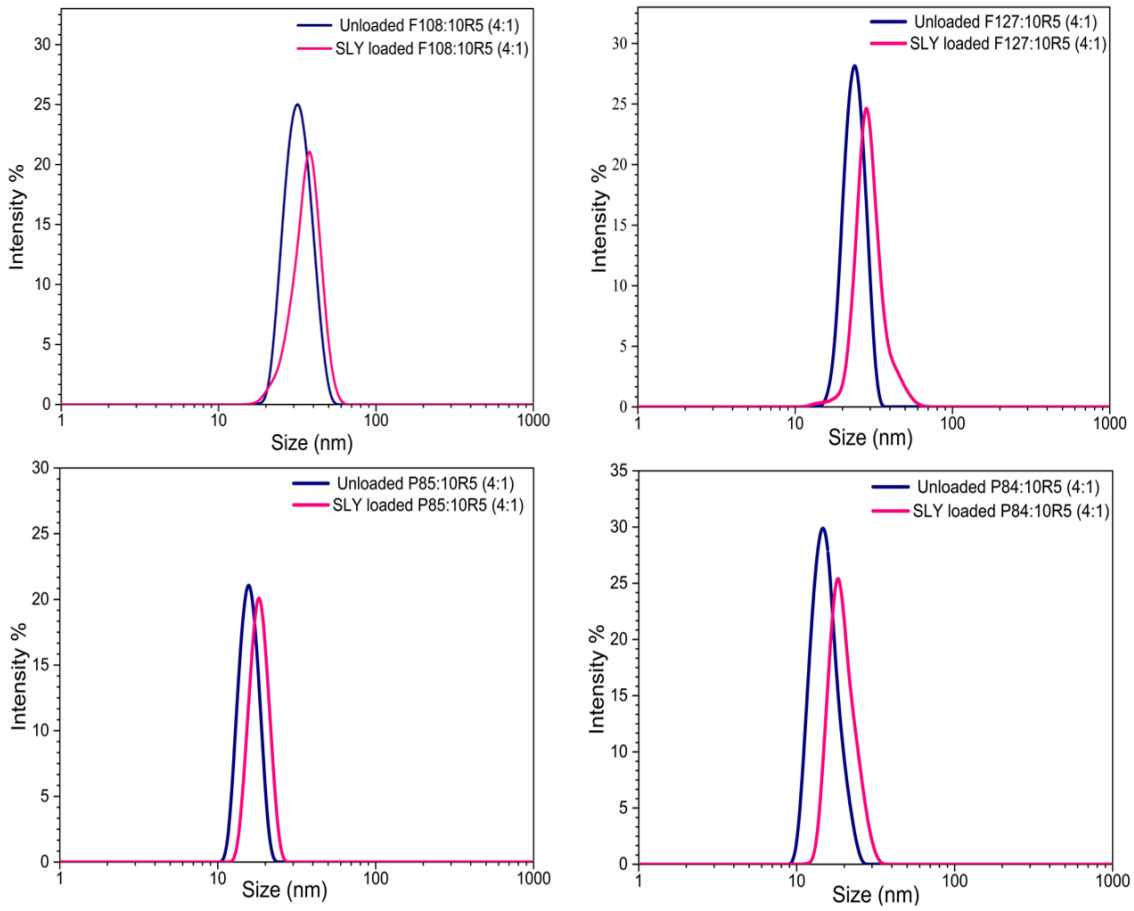

Figure 6.6. Intensity weighed size distribution profiles for unloaded and SLY loaded mixed micelles of normal Pluronics F108, F127, P85 and P84 with 10R5 at concentration ratio of 4:1% w/v.

6.4.6 In vitro drug release

In vitro drug release from the micellar medium has great significance since it provides an idea about their behaviour *in vivo* (Singla et al., 2018a). The dialysis method was employed to determine the SLY release from different mixed micelle system of normal Pluronics (F108, F127, P85 and P84) with reverse Pluronic 10R5. The cumulative %age release of SLY from mixed micelles of F108:10R5, P84:10R5, P85:10R5, F127:10R5 at 4:1% w/v was found to be 98%, 43%, 44%, 65% respectively after 5 h. After 6 h, 100% of SLY was released from the mixed micelles of F108:10R5 at 4:1%w/v. In the case of mixed micelles of F127:10R5 and P85:10R5, almost 100% SLY was found to be released after 12 h and 20 h respectively while the mixed micelles of P84:10R5 (4:1 %w/v) took 24 h to release almost 95% drug as shown in **Figure 6.7**.

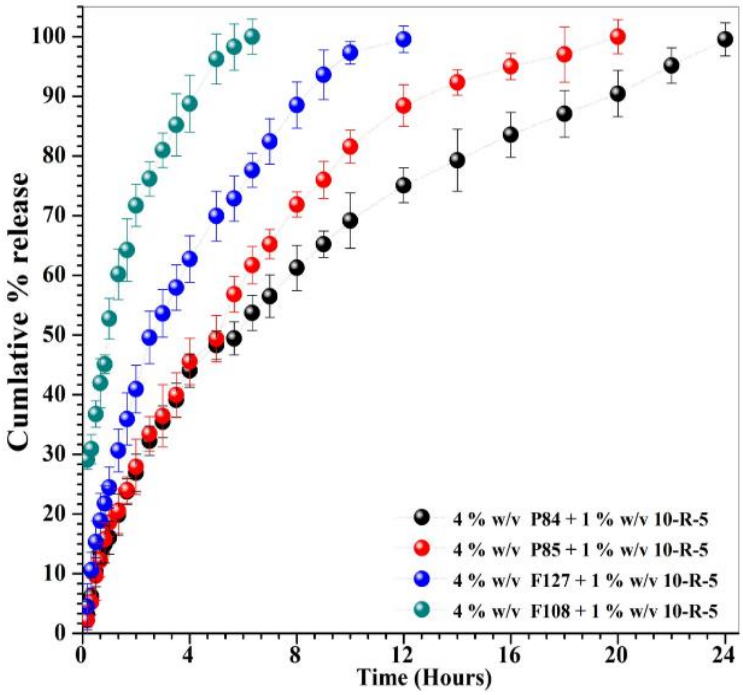

Figure 6.7: *In vitro* release of SLY from mixed micelles of different normal Pluronics (F108, F127, P85 and P84) with 10R5 at concentration of 4:1% w/v.

The *in vitro* drug release study results showed the slower release of SLY from the mixed micelles of P84 with 10R5 which is due to the hydrophobic nature of P84 (Singla et al., 2020). Singla et al. previously reported that change in the length of corona region (PEO units) affect the drug release, if drug solubilisation locus in the Pluronic micelles is corona region, faster will be the drug release (Singla et al., 2016). Due to concentration gradient provided by release medium, drug first leaves the solubilisation site of the Pluronic micelles and reaches the solution where micelles were suspended within dialysis bag. Afterwards, through the pore of dialysis membrane drug comes to the release medium. Moreover, various kinetic models have been applied to elucidate the release mechanism from mixed micelles of 10R5 with F108, F127, P85 and P84 and correlation coefficient (R^2) and rate constant (K) values were calculated for all five models (**Table 6.2**). The most appropriate model was chosen based on the best goodness of fit. In the binary mixtures of P84:10R5, P85:10R5, F127:10R5 and F108:10R5, the highest R^2 values were obtained with the Korsmeyer-Peppas (KP) Model. Furthermore, the release exponent NNN derived from the KP model provides insight into the underlying drug release mechanism. Specifically: (i) when N≤0.45N, drug release occurs via Fickian diffusion (simple diffusion), (ii) when N=1, release is governed by polymer relaxation or

erosion, characteristic of zero-order kinetics, and (iii) when 0.45<N<0.89, the drug release follows a non-Fickian (anomalous) transport mechanism, involving a combination of diffusion and change in polymer matrix (swelling or relaxation). From **Table 6.2**, it is observed that the mixed micellar formulations P84:10R5, P85:10R5, and F127:10R5 (4:1 %w/v) exhibited N values below 0.89, indicating that drug release followed a non-Fickian diffusion mechanism. This suggests that the release of SLY from these mixed micellar systems is influenced by both diffusion and polymer matrix relaxation or swelling. In contrast, the formulation F108:10R5 exhibited an N value below 0.45, suggesting that SLY release from this system is predominantly governed by Fickian diffusion.

Table 6.2: Rate constants and correlation coefficient calculated using different kinetic model for the release behaviour of SLY from Pluronic: Pluronic10R5 mixed micelles (5% w/v in total).

System	**Zero order kinetics**		**First order kinetics**		**Higuchi kinetics**		**KP model**		
(4:1 %w/v)	R^2	K_0 (h^{-1})	R^2	K (h^{-1})	R^2	K_H (-h^1)	R^2	K_H (h^{-1})	N
P84:10R5	0.908	19.38	0.857	2.038	0.967	24.23	0.986	1.191	0.639
P85:10R5	0.902	17.59	0.738	2.184	0.961	23.47	0.965	1.171	0.733
F127:10R5	0.918	19.34	0.903	2.105	0.961	20.68	0.975	1.360	0.679
F108:10R5	0.901	37.90	0.739	2.191	0.957	17.51	0.982	1.712	0.385

6.4.7 DPPH radical scavenging assay

DPPH free radical scavenging method has gained popularity as an anti-oxidative assay due to its high sensitivity and accuracy (Mazhari et al., 2018).The total radical scavenging activity for the mixed micellar formulation of SLY loaded P84:10R5 (4:1%w/v), SLY loaded 5% w/v Pluronic P84 micelles and SLY alone was evaluated using **Eq. 2.10 (**described in **Chapter 2)** (Oktay et al., 2003). The SLY loaded mixed micelles of P84:10R5 showed the DPPH radicals scavenging activity in a concentration (20-100 µg mL^{-1}) dependent manner (**Figure 6.8a**). Addition of SLY resulted in consumption of free radicals and was directly proportional to the disappearance of DPPH radicals present in test sample. DPPH radicals scavenging activity at all concentrations followed the order of SLY loaded P84:10R5 (4:1%w/v) > SLY loaded P84 micelles (5%w/v) >SLY alone.

At 100 µg/mL concentration of SLY, radical scavenging activity of P84:10R5 (4:1%w/v), P84 micelles (5%w/v) and SLY alone was found to be 61%, 35% and 18% respectively.

These results evidenced that these micellar formulations improved the radical scavenging activity of the SLY. Moreover, SLY loaded mixed micellar formulation comprising P84:10R5 (4:1%w/v) exhibited highest anti-oxidative potential and the IC_{50} of SLY loaded mixed micelles of P84:10R5 (4:1%w/v) and SLY was found to be 60.94 µg mL^{-1} and 91.57 µg mL^{-1} respectively (**Figure 6.8b)**. Enhanced DPPH radical scavenging was observed for the prepared formulations so these can be used as potential drug carriers for neurodegenerative diseases where radicals are majorly involved (Noipa et al., 2011).

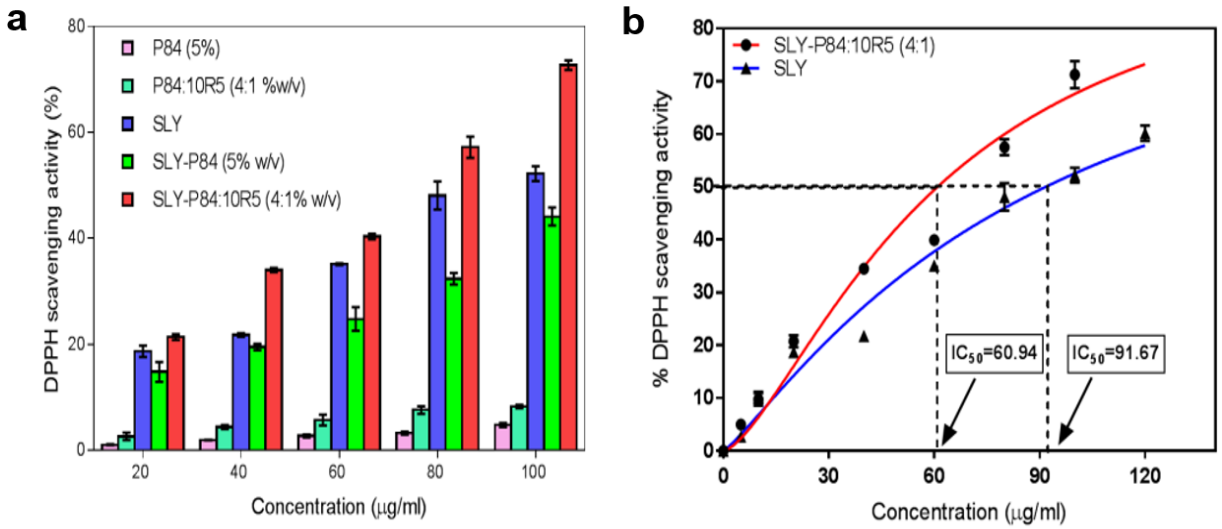

Figure 6.8: (a) DPPH scavenging activity (%) of bare P84 (5% w/v), P84:10R5 (4:1% w/v), SLY alone, SLY loaded P84 (5% w/v) and SLY loaded P84:10R5 (4:1% w/v) mixed micellar formulation; **(b)** IC_{50} of SLY and SLY loaded P84:10R5 (4:1%w/v) mixed micellar formulation in DPPH assay. Data is expressed as mean ± SD of three parallel measurements. $^{a}p<0.05$ compared with SLY and $^{b}p < 0.05$ compared to P84 (5%).

6.4.8 Metal chelating activity

The percentage of metal scavenging activity at the concentration of 100 µg/mL of mixed micellar formulation of SLY loaded P84:10R5 (4:1% w/v), SLY loaded P84 (5% w/v), SLY in water were found as 79%, 31%, 29% respectively (**Figure 6.8a)**. The metal scavenging activity was calculated using the **Eq. 2.11** (**Chapter 2**). The IC_{50} of SLY loaded mixed micelles of P84:10R5 (4:1% w/v) was five times lower than SLY alone and was found to be 29.3 µg mL^{-1} and 157.4 µg mL^{-1} respectively (**Figure 6.8b)**. A significant difference in the ferrous ions chelating capacity for the mixed micellar formulation of SLY was observed as compared to the drug (SLY) alone. The ferrozine-Fe^{2+} complex formation was disrupted in the presence of the mixed micelles of SLY, indicating its anti-oxidative

potential (Moon and Shibamoto, 2009). A linear decrease in the absorbance of Fe^{2+}-ferrozine complex in concentration dependent manner (20-100 µg mL^{-1}) was observed. The SLY loaded mixed micellar formulation of P84:10R5 (4:1% w/v) showed the higher metal chelating activity as compared to SLY loaded micelles of P84 and SLY alone.

It has been documented in literature that various metals and free radicals are associated with the pathogenesis of several neurodegenerative disorders, such as Schizophrenia (SZ), Alzheimer disease (AD) and neuropathic pain, and have also been implicated in the development of cardiovascular disorders, cancer, cataract, and inflammation (Oktay et al., 2003). Our results revealed the efficient iron binding capacity of the mixed micellar formulation of SLY, suggesting the anti-oxidative potential may be associated with the chelation of metal ions. Thus, due to the better antioxidant activity of mixed micellar formulation of SLY, these formulations can be used as potential drug carrier for the drugs used to treat neurodegenerative disorders.

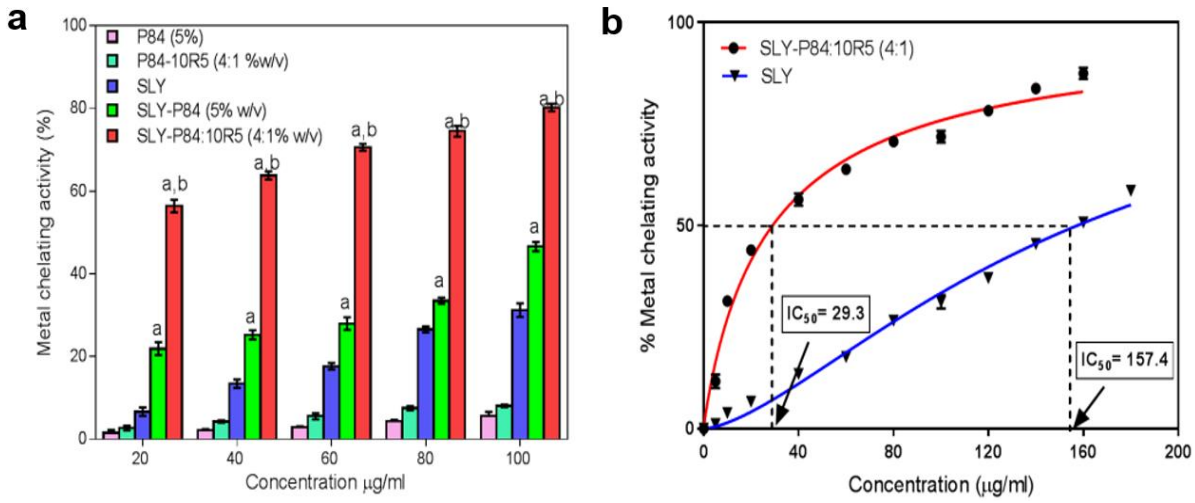

Figure 6.9: Metal chelating activity (%) of bare P84 (5% w/v), P84:10R5 (4:1), SLY alone, SLY loaded P84 (5% w/v) and SLY loaded P84:10R5 (4:1% w/v) mixed micellar formulation; (b) IC_{50} of SLY and SLY loaded P84:10R5 (4:1% w/v) micellar formulation in Metal chelating assay. Data is expressed as mean ± SD of three parallel measurements. $^{a}p<0.05$ compared with SLY and $^{b}p < 0.05$ compared to P84 (5%).

6.4.9 Nitric oxide (NO) scavenging activity

The release of nitric oxide (NO) can change the function and structure of many cellular components. The comparative NO scavenging activity of the SLY loaded mixed micellar formulations in concentration dependent manner with highest scavenging at 100 µg mL^{-1} was observed (calculated using **Eq. 2.12, Chapter 2**). Nitrite is a stable oxidation

product of NO produced by the incubation of sodium nitroprusside in phosphate buffer saline at 25 °C for 2 h, was scavenged by 69.74%, 49% and 38% with SLY loaded P84:10R5 (4:1% w/v) mixed micelles, SLY loaded micelles of P84 (5% w/v) and bare SLY respectively (**Figure 6.10a**). IC_{50} of SLY loaded mixed micelles of P84:10R5 (4:1% w/v) and was found to be 25.06 µg mL^{-1} and 93.28 µg mL^{-1} (**Figure 6.10b**). The role of nitric oxide (NO) in pathophysiology of variety of diseased conditions including asthma, myocarditis, Parkinsonism, Alzheimer's disease and inflammation is well documented (Asanuma et al., 2001; Auddy et al., 2003). Therefore, from these results, it can be suggested that mixed micellar formulation of P84:10R5 (4:1% w/v) can be an effective drug delivery system for drugs used for the treatment of above-mentioned diseases

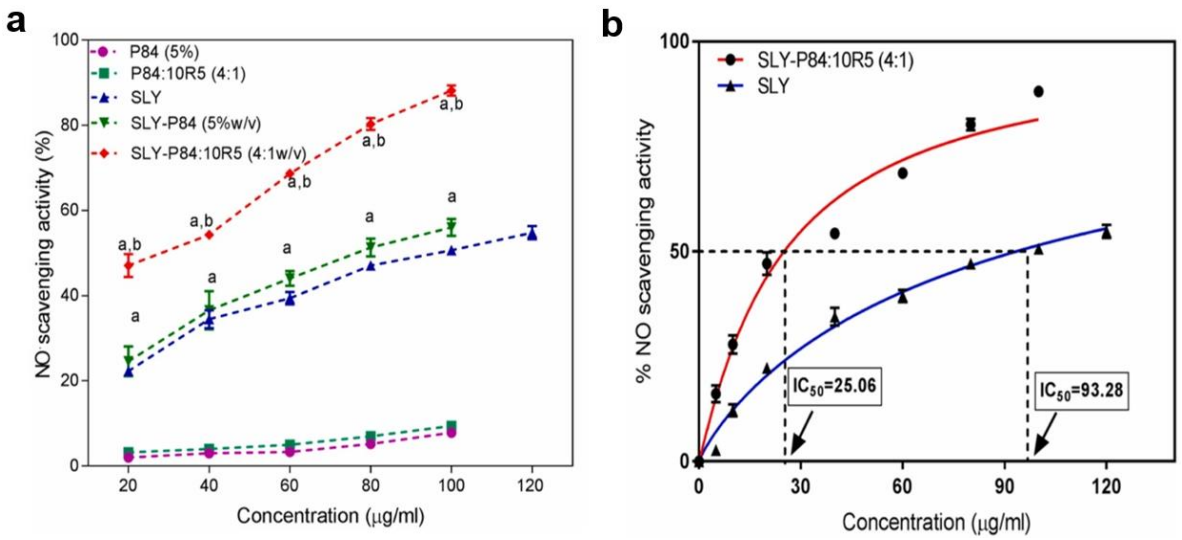

Figure 6.10: (a) NO scavenging activity (%) of bare P84 (5%w/v), P84:10R5 (4:1%w/v), SLY alone, SLY loaded P84 (5%w/v) and SLY loaded P84:10R5 (4:1%w/v) mixed micellar; (b) IC_{50} of SLY and SLY loaded P84:10R5 (4:1%w/v) mixed micellar formulation in NO scavenging assay. Data is expressed as mean ± SD of three parallel measurements. $^{a}p<0.05$ compared with SLY and $^{b}p < 0.05$ compared to P84 (5%).

6.4.10 ABTS•+ radical scavenging assay

Anti-oxidative potential of mixed micellar formulation of SLY-10R5:P84 (1:4 %w/v) was evaluated by the well-known method called the ABTS•+ radical scavenging assay. Percentage inhibition is measured as the reduction in radical cation absorbance (734 nm). Mixed micellar formulation, SLY loaded pure micelles of P84 and SLY alone at higher concentration (100 µg mL^{-1}) showed the percentage inhibition of ABTS•+ radical (**Eq. 2.13, Chapter 2**) in the following order: 10R5:P84-SLY (80%) >P84-SLY (69%) > SLY

(40%) respectively (Ak and Gülçin, 2008). Similar to other free radical scavenging assays, a statistically significant ($p < 0.05$) results were obtained for the mixed micellar formulation as compared to those of free drug (**Figure 6.10a**). Results of this study revealed that SLY loaded mixed micellar formulation of P84:10R5 (4:1% w/v) displayed an eminent scavenging activity in a concentration dependent manner and maximum scavenging was observed to be at a concentration of 40 µg mL^{-1} .

6.4.11 Reducing power assay

The anti-oxidative activity of different formulations viz. P84:10R5 (4:1% w/v) mixed micellar formulation of SLY (P84:10R5-SLY) and SLY loaded P84 (5% w/v) Pluronics was further quantified by using a reducing power assay (calculated using **Eq. 2.14, Chapter 2)**. A linear increase in the reducing power of SLY and SLY loaded mixed micellar formulation was observed at concentrations ranging from 20 to 100 µg mL^{-1} as shown in **Figure 6.11b**. Reducing power activity at all concentration follows the order SLY loaded P84:10R5 (4:1% w/v) >SLY loaded 5% w/v P84> bare SLY. The SLY-mixed micellar formulation showed highest reducing ability ($p < 0.05$) was observed as compared to SLY loaded 5% w/v P84, SLY alone. The results indicated that the mixed micellar formulation has maximum electron donor properties which neutralize the higher numbers of free radicals by the formation of stable intermediates and products (Prathapan et al., 2011).

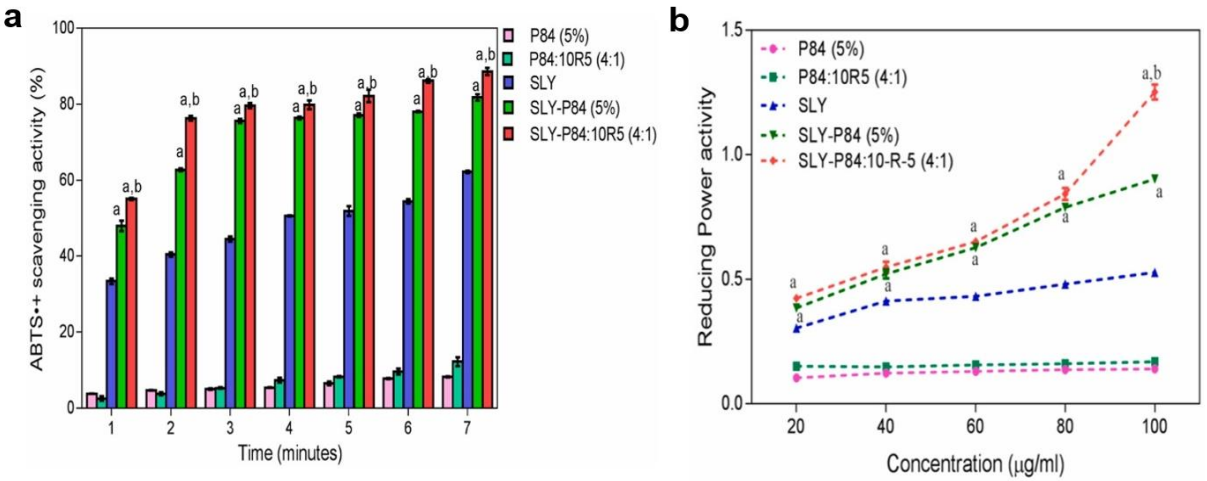

Figure 6.11: (a) ABTS·**+** scavenging activity (%) and **(b)** Reducing power activity, of bare P84 (5%), P84:10R5 (4:1% w/v), SLY alone, SLY loaded P84 (5% w/v) and SLY loaded P84:10R5 (4:1% w/v) mixed micellar formulation. Data is expressed as mean ± SD of three parallel measurements. [a]$p<0.05$ compared with SLY and [b]$p < 0.05$ compared to P84 (5%).

6.5 Conclusion

In summary, we have presented the SLY solubilisation in mixed micelles of normal Pluronics (F108, F127, P85 and P84) with reverse Pluronic 10R5. It was observed that mixed micellar Pluronic formulations can solubilize appreciably higher amount of SLY in comparison to pure Pluronic micelles. The best mixed micellar formulation P84:10R5 (4:1 %w/v) exhibited the solubilisation of 3.929 mg mL^{-1} and DL efficiency 98.03% for SLY, enhanced antioxidative activity as well as sustained release behaviour. Comparison with previously reported formulations that are Pluronic-lecithin organogels (Mady et al., 2016), Pluronic nano micelles (El-Far et al., 2016), SLY lipid emulsion (Abrol et al., 2005) and SLY-cyclo-dextrin-clathrate complex (Morazzoni et al., 1993), our explored micellar systems are easy to fabricate without use of any sophisticated techniques and 4-5 folds lesser amounts of Pluronic/polymers and surfactants needed. Although there are number of reports focused on Pluronic/non-ionic surfactants for the drug delivery applications (Kaur et al., 2022; Singla et al., 2022a; Singla et al., 2022b), but in this report, we showed that mixing of reverse Pluronic 10R5 can also enhance the solubility of hydrophobic drug SLY as compared to pure Pluronic micelles. Furthermore, D_h of mixed micelles at ratio 4:1% w/v of F108, F127, P85 and P84 with 10R5 showed little increment ranging from 4 to 6 nm than pure normal Pluronic micelles, so, this mixing ratio would be appropriate for fabricating nano-formulation systems. Micropolarity results clearly evidenced that mixed micelles provided a better hydrophobic environment for SLY drug. Therefore, it can be suggested that SLY loaded mixed micellar formulations at ratio 4:1% w/v (Pluronics F108, F127, P85 and P84:10R5) can be used as an efficient drug delivery carrier for SLY drug, however, there is still a need to explore their biological and biocompatibility performances in vivo.

Future work for Pluronic formulations would involve advancing to in vivo studies to assess safety and efficacy, optimising the formulations for better performance, and potentially scaling up for clinical trials if results are promising. This chapter has seen the preparation of Pluronic mixed micellar formulations using direct dissolution method) as drug delivery vehicle for poorly water-soluble natural drug SLY. Building on this work, Chapter 7 will demonstrate the development of Pluronic formulations for other plant-derived drugs, employing two different solubilisation methods to further enhance the solubilisation capacity of these formulations.

6.6 References

Abrol, S., Trehan, A. & Katare, O. P. (2005). 'Comparative study of different silymarin formulations: Formulation, characterisation and in vitro/in vivo evaluation' *Current drug delivery*, 2 (1), pp. 45-51.

Agarwal, R., et al. (2006). 'Anticancer potential of silymarin: From bench to bed side' *Anticancer research*, 26 (6B), pp. 4457-4498.

Ak, T. & Gülçin, I. (2008). 'Antioxidant and radical scavenging properties of curcumin' *Chemico-biological interactions*, 174 (1), pp. 27-37.

Al-Enazi, M. M. (2013). 'Neuroprotective effect of silymarin by modulation of endogenous biomarkers in streptozotocin induced painful diabetic neuropathy' *British journal of pharmacology and toxicology*, 4 (3), pp. 110-120.

Asanuma, M., et al. (2001). 'Neuroprotective effects of non-steroidal anti-inflammatory drugs by direct scavenging of nitric oxide radicals' *Journal of neurochemistry*, 76 (6), pp. 1895-1904.

Auddy, B., et al. (2003). 'Screening of antioxidant activity of three indian medicinal plants, traditionally used for the management of neurodegenerative diseases' *Journal of ethnopharmacology*, 84 (2-3), pp. 131-138.

Chaudhuri, A., Haldar, S. & Chattopadhyay, A. (2009). 'Organisation and dynamics in micellar structural transition monitored by pyrene fluorescence' *Biochemical and biophysical research communications*, 390 (3), pp. 728-732.

Dai, S., Tam, K. & Li, L. (2001). 'Isothermal titration calorimetric studies on interactions of ionic surfactant and poly (oxypropylene)− poly (oxyethylene)− poly (oxypropylene) triblock copolymers in aqueous solutions' *Macromolecules*, 34 (20), pp. 7049-7055.

Danson, S., et al. (2004). 'Phase i dose escalation and pharmacokinetic study of pluronic polymer-bound doxorubicin (sp1049c) in patients with advanced cancer' *British journal of cancer*, 90 (11), pp. 2085-2091.

Desai, P., Jain, N., Sharma, R. & Bahadur, P. (2001). 'Effect of additives on the micellisation of peo/ppo/peo block copolymer f127 in aqueous solution' *Colloids and Surfaces A: Physicochemical and Engineering Aspects*, 178 (1-3), pp. 57-69.

El-Far, Y. M., et al. (2016). 'A newly developed silymarin nanoformulation as a potential antidiabetic agent in experimental diabetes' *Nanomedicine*, 11 (19), pp. 2581-2602.

Fda, U. (2019). Inactive ingredient search for approved drug products. FDA White Oak, MD, USA.

Ganguly, R., et al. (2012). 'Phenol solubilisation in aqueous pluronic® solutions: Investigating the micellar growth and interaction as a function of pluronic® composition' *Journal of colloid and interface science*, 378 (1), pp. 118-124.

Gharagozloo, M., Karimi, M. & Amirghofran, Z. (2013). 'Immunomodulatory effects of silymarin in patients with β-thalassemia major' *International immunopharmacology*, 16 (2), pp. 243-247.

Ghosh, A., Ghosh, T. & Jain, S. (2010). 'Silymarin-a review on the pharmacodynamics and bioavailability enhancement approaches' *Journal of Pharmaceutical Science and Technology*, 2 (10), pp. 348-355.

Hassanzadeh, S., Feng, Z., Pettersson, T. & Hakkarainen, M. (2015). 'A proof-of-concept for folate-conjugated and quercetin-anchored pluronic mixed micelles as molecularly modulated polymeric carriers for doxorubicin' *Polymer*, 74 pp. 193-204.

Hellerbrand, C., et al. (2017). 'The potential of silymarin for the treatment of hepatic disorders' *Clinical Phytoscience*, 2 pp. 1-14.

Hugerth, A. M. (2001). 'Micropolarity and microviscosity of amitriptyline and dextran sulfate/carrageenan-amitriptyline systems: The nature of polyelectrolyte–drug complexes' *Journal of pharmaceutical sciences*, 90 (10), pp. 1665-1677.

Ingram, T., et al. (2013). 'Prediction of micelle/water and liposome/water partition coefficients based on molecular dynamics simulations, cosmo-rs, and cosmomic' *Langmuir*, 29 (11), pp. 3527-3537.

Kadam, Y., et al. (2010). 'Thermodynamic of micelle formation of nonlinear block co-polymer tetronic® t904 in aqueous salt solution' *Colloids and Surfaces A: Physicochemical and Engineering Aspects*, 369 (1-3), pp. 121-127.

Karimi, G., et al. (2011). '"Silymarin", a promising pharmacological agent for treatment of diseases' *Iranian journal of basic medical sciences*, 14 (4), p. 308.

Kaur, J., Singla, P. & Kaur, I. (2022). 'Labrasol mediated enhanced solubilisation of natural hydrophobic drugs in pluronic micelles: Physicochemical and in vitro release studies' *Journal of Molecular Liquids*, 361 p. 119596.

Kwon, G. S. & Kataoka, K. (1995). 'Block copolymer micelles as long-circulating drug vehicles' *Advanced drug delivery reviews*, 16 (2-3), pp. 295-309.

Larrañeta, E. & Isasi, J. R. (2013). 'Phase behavior of reverse poloxamers and poloxamines in water' *Langmuir*, 29 (4), pp. 1045-1053.

Liu, J., et al. (2011). 'Interaction between two homologues of cationic surface active ionic liquids and the peo-ppo-peo triblock copolymers in aqueous solutions' *Colloid and Polymer Science*, 289 pp. 1711-1718.

Ma, J.-h., et al. (2007). 'Salt-induced micellisation of a triblock copolymer in aqueous solution: A 1h nuclear magnetic resonance spectroscopy study' *Langmuir*, 23 (6), pp. 3075-3083.

Mady, F. M., et al. (2016). 'Formulation and clinical evaluation of silymarin pluronic-lecithin organogels for treatment of atopic dermatitis' *Drug design, development and therapy*, pp. 1101-1110.

Malekinejad, H., Taheri-Broujerdi, M., Moradi, M. & Tabatabaie, S. H. (2011). 'Silymarin potentiates the antinociceptive effect of morphine in mice' *Phytotherapy research*, 25 (2), pp. 250-255.

Mazhari, S., Razi, M. & Sadrkhanlou, R. (2018). 'Silymarin and celecoxib ameliorate experimental varicocele-induced pathogenesis: Evidences for oxidative stress and inflammation inhibition' *International urology and nephrology*, 50 pp. 1039-1052.

Mehta, S. & Jindal, N. (2013). 'Mixed micelles of lecithin–tyloxapol as pharmaceutical nanocarriers for anti-tubercular drug delivery' *Colloids and Surfaces B: Biointerfaces*, 110 pp. 419-425.

Moon, J.-K. & Shibamoto, T. (2009). 'Antioxidant assays for plant and food components' *Journal of agricultural and food chemistry*, 57 (5), pp. 1655-1666.

Morazzoni, P., Montalbetti, A., Malandrino, S. & Pifferi, G. (1993). 'Comparative pharmacokinetics of silipide and silymarin in rats' *European journal of drug metabolism and pharmacokinetics*, 18 pp. 289-297.

Naskar, B., Ghosh, S. & Moulik, S. P. (2012). 'Solution behavior of normal and reverse triblock copolymers (pluronic l44 and 10r5) individually and in binary mixture' *Langmuir*, 28 (18), pp. 7134-7146.

Naskar, B., Ghosh, S. & Moulik, S. P. (2014). 'Interaction of normal and reverse pluronics (l44 and 10r5) and their mixtures with anionic surfactant sodium n-dodecanoylsarcosinate' *Journal of colloid and interface science*, 414 pp. 82-89.

Noipa, T., Srijaranai, S., Tuntulani, T. & Ngeontae, W. (2011). 'New approach for evaluation of the antioxidant capacity based on scavenging dpph free radical in micelle systems' *Food research international*, 44 (3), pp. 798-806.

Noolandi, J., Shi, A.-C. & Linse, P. (1996). 'Theory of phase behavior of poly (oxyethylene)− poly (oxypropylene)− poly (oxyethylene) triblock copolymers in aqueous solutions' *Macromolecules*, 29 (18), pp. 5907-5919.

Oh, K. T., Bronich, T. K. & Kabanov, A. V. (2004). 'Micellar formulations for drug delivery based on mixtures of hydrophobic and hydrophilic pluronic® block copolymers' *Journal of Controlled Release*, 94 (2-3), pp. 411-422.

Oktay, M., Gülçin, İ. & Küfrevioğlu, Ö. İ. (2003). 'Determination of in vitro antioxidant activity of fennel (foeniculum vulgare) seed extracts' *LWT-Food Science and Technology*, 36 (2), pp. 263-271.

Parekh, P., Singh, K., Marangoni, D. & Bahadur, P. (2011). 'Micellisation and solubilisation of a model hydrophobic drug nimesulide in aqueous salt solutions of tetronic® t904' *Colloids and Surfaces B: Biointerfaces*, 83 (1), pp. 69-77.

Prathapan, A., et al. (2011). 'Antiperoxidative, free radical scavenging and metal chelating activities of boerhaavia diffusa l' *Journal of Food Biochemistry*, 35 (5), pp. 1548-1554.

Ridell, A., Evertsson, H., Nilsson, S. & Sundelöf, L. O. (1999). 'Amphiphilic association of ibuprofen and two nonionic cellulose derivatives in aqueous solution' *Journal of pharmaceutical sciences*, 88 (11), pp. 1175-1181.

Saller, R., Meier, R. & Brignoli, R. (2001). 'The use of silymarin in the treatment of liver diseases' *Drugs*, 61 pp. 2035-2063.

Shaker, E., Mahmoud, H. & Mnaa, S. (2010). 'Silymarin, the antioxidant component and silybum marianum extracts prevent liver damage' *Food and Chemical Toxicology*, 48 (3), pp. 803-806.

Sharma, R., Kang, T. S. & Mahajan, R. K. (2015). 'Complexation of triblock reverse copolymer 10r5 with surface active ionic liquids in aqueous medium: A physico-chemical study' *RSC Advances*, 5 (21), pp. 16349-16360.

Singla, P., Chabba, S. & Mahajan, R. K. (2016). 'A systematic physicochemical investigation on solubilisation and in vitro release of poorly water soluble oxcarbazepine drug in pluronic micelles' *Colloids and Surfaces A: Physicochemical and Engineering Aspects*, 504 pp. 479-488.

Singla, P., et al. (2020). 'Solubilisation of hydrophobic drugs clozapine and oxcarbazepine in the lower and higher molecular weight pluronic mixed micelles-a

physicochemical, in vitro release and in vitro anti-oxidant study' *Journal of Molecular Liquids*, 317 p. 113816.

Singla, P., et al. (2022a). 'Unusual solubilisation capacity of hydrophobic drug olanzapine in polysorbate micelles for improved sustained drug release' *Journal of Molecular Liquids*, 359 p. 119256.

Singla, P., et al. (2022b). 'Advances in the therapeutic delivery and applications of functionalised pluronics: A critical review' *Advances in Colloid and Interface Science*, 299 p. 102563.

Singla, P., et al. (2018). 'Sodium deoxycholate mediated enhanced solubilisation and stability of hydrophobic drug clozapine in pluronic micelles' *Spectrochimica Acta Part A: Molecular and Biomolecular Spectroscopy*, 191 pp. 143-154.

Singla, P., et al. (2019). 'Temperature-dependent solubilisation of the hydrophobic antiepileptic drug lamotrigine in different pluronic micelles—a spectroscopic, heat transfer method, small-angle neutron scattering, dynamic light scattering, and in vitro release study' *ACS omega*, 4 (6), pp. 11251-11262.

Suh, H. & Jun, H. W. (1996). 'Physicochemical and release studies of naproxen in poloxamer gels' *International journal of pharmaceutics*, 129 (1-2), pp. 13-20.

Sun, F., et al. (2018). 'Mixed micellar system stabilised with saponins for oral delivery of vitamin k' *Colloids and Surfaces B: Biointerfaces*, 170 pp. 521-528.

Wang, J., et al. (2015). 'The role of micelle size in tumor accumulation, penetration, and treatment' *ACS nano*, 9 (7), pp. 7195-7206.

Wei, Z., et al. (2009). 'Paclitaxel-loaded pluronic p123/f127 mixed polymeric micelles: Formulation, optimisation and in vitro characterisation' *International journal of pharmaceutics*, 376 (1-2), pp. 176-185.

Zhang, W., et al. (2010). 'Enhanced antitumor efficacy by paclitaxel-loaded pluronic p123/f127 mixed micelles against non-small cell lung cancer based on passive tumor targeting and modulation of drug resistance' *European journal of pharmaceutics and biopharmaceutics*, 75 (3), pp. 341-353.

Zhao, L., et al. (2012). 'Curcumin loaded mixed micelles composed of pluronic p123 and f68: Preparation, optimisation and in vitro characterisation' *Colloids and Surfaces B: Biointerfaces*, 97 pp. 101-108.

Chapter 7: Enhancing Encapsulation of Hydrophobic Phyto-drugs Naringenin and Baicalein in Polymeric Nano-micelles

*(Published as P. Singla, G. Parokie, **S. Garg**, S. Kaur, I. Kaur, R.D. Crapnell, C.E. Banks, U. Rinner, C. Wills, M. Peeters, Journal of Drug Delivery Science and Technology, 2023, 83, 104403)*

This co-author publication explores and compares two different methods (solvent evaporation and direct dissolution) for producing polymeric (Pluronic) micelles to improve the solubilisation of two different phyto-drugs with poor water solubility. Pankaj Singla designed this work, wrote and proofread the manuscript. Gloria Parokie experiments such as UV-visible, DLS, antioxidant assays and did data acquisition. I (Saweta Garg) contributed to the development and characterisation of Pluronic formulations as well as assisted in writing the manuscript. Sarbjeet Kaur, Inderpreet Kaur Corinne Wills performed ^{1}H NMR experiments; Robert D. Crapnell and Craig E. Banks performed and discussed the SEM measurements. Dr Uwe Rinner proofread the manuscript and Marloes Peeters designed and conceptualised the work and proofread the manuscript.

7.1 Abstract

In this chapter, I will move from a single method (direct dissolution method) used for the SLY Pluronic based formulation to two different methods including solvent evaporation method (S.Ev.M) and Direct dissolution method (D.D.M.) for two different phyto-drugs naringenin (NAR) and baicalein (BAC). This is the first report that describes the solubilisation and loading of phyto-drugs NAR and BAC in different Pluronics F108, F127 and P84 (as drug delivery vehicles) using S.Ev.M and D.D.M. Pluronic P84 micelles were able to encapsulate significantly higher amount of both phyto-drugs as compared to other Pluronic micelles. S.Ev.M appreciably enhanced the encapsulation of NAR (19.2 ± 0.438 mg/mL) and BAC (2.593 ± 0.223 mg/mL) compared to D.D.M. (NAR, 10.95 ± 0.212 mg/mL, and BAC, 1.058 ± 0.049 mg/mL) in 5% w/v and 12% w/v Pluronic P84, respectively. Scanning Electron Microscopy (SEM) results showed a spherical morphology after the incorporation of NAR into Pluronic micelles and evidenced that S.Ev.M did not affect the morphology. Sustained release behaviour of phyto-drugs was observed from the loaded Pluronic micelles, which was confirmed via *in vitro* release studies. Finally, antioxidant activity was analysed by $ABTS^{\bullet+}$ scavenging assays, with both NAR and BAC loaded P84 micelles (IC_{50} 7.185 and 28.90 μg/mL) showcasing a marked increase in antioxidant activity compared to the pure phyto-drugs NAR and BAC

(IC_{50} 13.25 and 53.68 μg/mL) or other Pluronic formulations. Interaction of phyto-drugs and Pluronic P84 has been screened using ^{1}H-NMR (proton nuclear magnetic spectroscopy) spectroscopy and revealed that whole NAR molecule was encapsulated within the Pluronic micelles. These phyto-drugs hold great potential for use as nutraceuticals and other pharmaceutical applications but currently can't be used due to poor solubilisation. Therefore, it can be suggested that the preparation of drug loaded Pluronic formulations using S.Ev.M. would be a more convenient, fast, and efficient method over D.D.M.

7.2 Introduction

Nutraceuticals (NUTs) are bioactive compounds commonly found in foods, which provide certain health benefits when taken orally (Peng et al., 2018). Naringenin (NAR) and baicalein (BAC) are phyto-drugs belonging to the class of flavonoids and have been reported to possess several pharmacological properties including anticancer, antioxidant, anti-inflammatory, neuroprotection, antibacterial, antiviral, antiallergic and many more (Liu et al., 2016; Peng et al., 2018). In addition to that, both NUTs are known to have protective effects on cardiovascular and microvascular diseases, hyper-tension, parkinsonism and alzheimer's diseases (Moghaddam et al., 2020; You et al., 2021). NAR (4,5,7-trihydroxyflavanone) is a colourless and flavourless flavanone mainly found in grapes and other citrus fruits like tomatoes (*Solanum lycopersicum*), bergamot (*Citrus bergamia*), oranges (Citrus sinensis), beans (*Phaseolus vulgaris*), water mint (*Mentha aquatica*), grapefruits (*Citrus paradise*) and tart cherries (*Prunus cerasus*) (Jabbari and Jabbari, 2016). BAC (5,6,7-trihydroxyflavone) is a glycone baicalin (baicalein-7-O-glucoside), present in the roots of *Scutellaria baicalensis* (Chinese skullcap), *Scutellaria lateriflora,* as well as in *Oroxylum indicum* (Indian trumpet flower) (Lin Wang et al., 2022). However, the latent health benefits and advantages of NAR and BAC flavonoids in functional food and pharmaceutical goods is restricted because of their hydrophobicity and poor bioavailability (Gong et al., 2017; Shulman et al., 2011). Liang and colleagues have reported the nanocomposites consisting of carbon quantum dots for the delivery of NAR to improve the drug's solubility and its biological properties (Liang et al., 2022). Additionally, glycyrrhizin nano-micelles, polymeric (Pluronic F68) micelles, cellulose based solid dispersions, and liposomes have also been explored to enhance the water solubility, bioavailability and stability of NAR (Choi et al., 2015). Similarly, there are some literature reports in which cyclodextrin complexes, nano-formulations and glycyrrhizin

nano-micelles have been investigated to improve the poor water solubility of BAC (J. Sun et al., 2022; You et al., 2021). Nonetheless, alternatives are required to ameliorate the physical and chemical properties of NAR and BAC and other poorly soluble flavonoids.

Pluronics, also known as poloxamers, are surface-active tri-block copolymers comprised of polyethylene oxide (PEO)-polypropylene oxide (PPO)-polyethylene oxide (PEO). These materials are non-ionic, biocompatible, non-toxic, non-immunogenic and are commercially available (Singla et al., 2016). They can self-assemble into nano-micelles ranging from 15-50 nm depending upon the type of Pluronic at/or above *cmc* (critical micelle concentration) and *cmt* (critical micelle temperature) (Singla et al., 2022b). Typically, PEO forming corona region of Pluronic micelles can accommodate hydrophilic drugs and PPO-forming core region solubilise hydrophobic drug molecules (Van Thoai et al., 2020).[16] Pluronics are extensively studied for the solubilisation and loading of hydrophobic and hydrophilic drugs. Moreover, these are being used in targeted delivery for various drugs, gene delivery as well as for small interfering RNA (Singla et al., 2016; Singla et al., 2022b). Pluronics are being exploited for the different food formulations including micellar formulations, nano emulsions, hydrogels and many more. It was found that the hydrophobic core of Pluronics acts as a microenvironment to improve drug loading efficacy (Arango-Ruiz et al., 2018; Van Thoai et al., 2020). Curcumin encapsulated inside Pluronic micelles were found to have a very low hydrolytic breakdown rate as compared to curcumin in aqueous solution, making it a promising drug delivery agent (Ganguly et al., 2017). Kadam and colleagues used Pluronics P103, P123, P84, and F127 for the testing its solubilisation capacity for the hydrophobic drug Carbamazepine. Pluronic P103 was found to be the most effective Pluronic for solubilising carbamazepine, because P103 is more hydrophobic than the other copolymers, resulting in increased hydrophobic-hydrophobic interaction between the drug and P103 (Kadam et al., 2009). On the other hand, Raval *et al.* examined six different Pluronics (F88, P84, F127, P105, P103, and P123) for the solubilisation of three widely used hydrophobic anticancer drugs, genistein, paclitaxel and quercetin. P103 and P123 showed a higher solubilisation capacity as compared to other Pluronics employed in this study. The *in vitro* cytotoxicity results evidenced the improved anticancer activity of drug loaded P103 and P123 micelles as compared to free drugs on breast cancer cells (MCF-7) (Raval et al., 2017).

There is no report till date in which solubility of hydrophobic drugs in Pluronic systems has been compared using solvent evaporation method (S.Ev.M) and direct dissolution

method (D.D.M.). Thus, phyto-drugs NAR and BAC were evaluated for their loading into different Pluronics F108, F127 and P84 to improve their water solubility and other properties including antioxidant potential. These phyto-drug loaded formulations are intended to administer through intravenous (IV) route as this is most convenient and well explored route for nano-formulations till date for examples Vyxeos™ in chemotherapy (by Jazz Pharmaceuticals) and Onivyde® (Ipsen) (Lorscheider et al., 2021). Pluronics formulations are the series of Pluronic chosen in this study was based on the hydrophobicity of the Pluronics; Pluronic F108, F127 and Pluronic P84 have 20%, 30% and 60% PPO (hydrophobic units) content respectively. The objective of selecting this set of Pluronics, is to decipher the impact of the hydrophobicity of Pluronic micelles on the encapsulation of the hydrophobic drugs (NAR and BAC). The locus of solubilisation was determined using proton nuclear magnetic spectroscopy (^{1}H-NMR). Formulations were screened employing DLS and SEM to gain insight into the size and structure of these formulations respectively. Moreover, NAR and BAC loaded Pluronic formulations were screened for *in vitro* drug release and antioxidant activity using $ABTS^{\bullet+}$ scavenging assays. The obtained results showed the significantly higher encapsulation of both phyto-drugs in Pluronic P84 micelles as compared to other investigated Pluronics. Moreover, S.Ev.M method enhanced the loading of NAR and BAC in these Pluronic micelles as compared to D.D.M. Overall, the current study delineated that Pluronic P84 micelles can be employed for the loading of hydrophobic phyto-drugs as well as in pharmaceutical drug delivery applications.

7.3 Experimental

7.3.1 Materials

Pluronics P84, F127 and F108 were kindly provided as gift samples by BASF (Germany). Naringenin (NAR) and baicalein (BAC) were purchased from Alfa-Aesar Thermo Fisher Scientific, Heysham, UK. All other chemicals used were of analytical grade and used without further purification.

7.3.2 Methods and equipment

Pluronic formulations were prepared and characterised in a similar manner as described in **Chapter 2**. Briefly, two different methods S.Ev.M. and D.D.M. were employed to prepare the unloaded and NAR/BAC loaded micellar formulations. UV-visible spectrophotometer (Jenway 7200, UK) was used to measure phyto-drugs (NAR and BAC)

in micellar formulations. *In vitro* drug release and $ABTS^{\bullet+}$ assay was also performed using UV-visible spectrophotometer. DLS (Malvern Zetasizer Nano ZS) was performed to determine the hydrodynamic diameter (D_h) of Pluronic, and phyto-drugs loaded Pluronic micelles at 25 ± 0.1 °C. The ^{1}H-NMR studies were performed with Bruker Avance III HD 700 MHz nuclear magnetic resonance spectrometer to observe the binding and interactional behaviour of phyto-drugs with Pluronics.

7.4 Results and discussion

7.4.1 Loading and estimation of NAR and BAC

The molecular structure of NAR, BAC and Pluronics, in addition to schemes of the different drug loading methods, are depicted in **Figure 7.1a**. To explore the effect of the encapsulation process on loading capacity and efficiency of NAR and BAC phyto-drugs in Pluronic (F108, F127 and P84) micelles, two different methods *viz.* solvent evaporation method (S.Ev.M) and Direct dissolution method (D.D.M.) were employed (**Figure 7.1b)**.

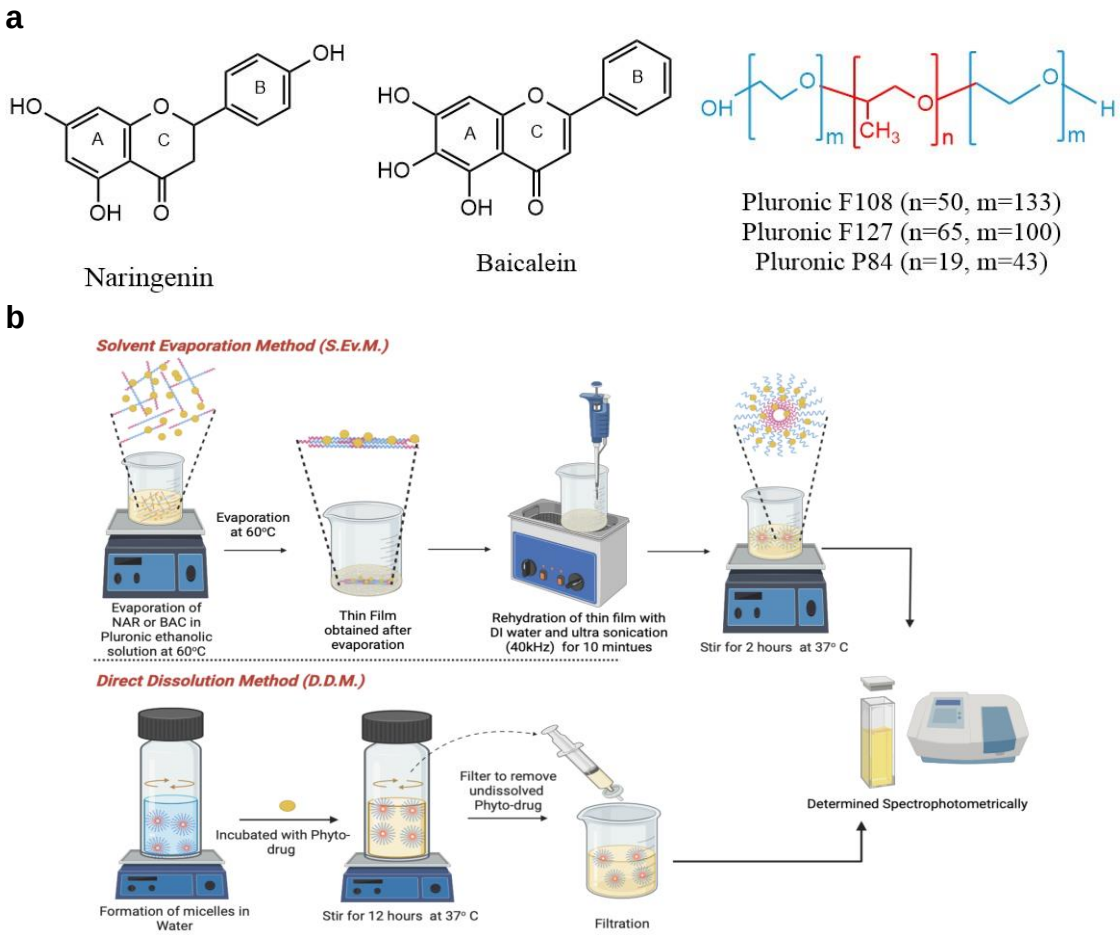

Figure 7.1: (a) The molecular structure of naringenin (NAR), baicalein (BAC), and Pluronics P84, F108, and F127, **(b)** Method of drug solubilising using Solvent evaporation

method (S.Ev.M.) and Direct dissolution method (D.D.M.).

The λ_{max} of NAR and BAC were obtained at 292 nm and 275 nm using a Jenway 7200 UV-visible scanning spectrophotometer. The stock solution of NAR and BAC was prepared in the ethanol and further diluted to the desired concentration with deionised water. Calibration curves of NAR and BAC were plotted at different concentrations (see **Figure C.1a and b, Appendix C**)**,** the molar absorption coefficient of NAR and BAC was determined to be 13.42 and 20.84 L mol^{-1} cm^{-1} respectively. These molar absorption coefficients were used to estimate the loading of phyto-drugs into different concentration of Pluronic (F108, F127 and P84) micelles. It was observed that encapsulation of NAR was increased upon increasing the concentration of Pluronic micelles from 1 to 5 % w/v (**Figure 7.2a)**. Unexpectedly, encapsulation of BAC was less pronounced, therefore, concentration from Pluronic micelles were increased and screened for 6-12% w/v (**Figure 7.2b)**. The solubilisation of both NAR and BAC was found to be higher in Pluronic P84 as compared to other screened Pluronic micellar systems due to its hydrophobic nature (Van Thoai et al., 2020). The hydrophilic–lipophilic balance (HLB) value for Pluronic P84, F127 and F108 is 14, 22 and 27 respectively, higher the HLB values greater the hydrophilicity, and these balance values are an indicative that the encapsulation efficiency of P84 for hydrophobic phyto-drugs (NAR and BAC) would be better than that of F127, F108 (Jindal and Mehta, 2015; Senthilkumar et al., 2022; Singla et al., 2016). In 5% w/v and 12% w/v Pluronic P84, S.Ev.M. significantly improved ($P < 0.05$) the encapsulation of NAR (19.2 ± 0.438 mg/mL) and BAC (2.593 ± 0.223 mg/mL) when compared to D.D. M. (NAR, 10.95 ± 0.212 mg/mL, and BAC, 1.058 ± 0.049 mg/mL) and other screened Pluronic micellar systems. The loading of BAC in Pluronic micelles was found to be significantly lower in comparison to NAR, this may be due to the structural differences between them. NAR is 4′,5,7-Trihydroxyflavanon, and BAC is 5,6,7-trihydroxyflavon; the major difference between flavanones and flavones is a saturated C ring (see **Figure 7.1a**) while in flavones there is a double bond between the 2,3 positions of the C ring. Another difference between NAR and BAC is that there is no hydroxyl group present on the B ring of BAC (all three hydroxyl moieties are positioned on the A ring). In the case of NAR, two hydroxyl groups are present on the A ring and one hydroxyl group is present on the B ring (Tu et al., 2015). Additionally, the results showed significantly higher solubilisation of NAR and BAC with S.Ev.M. as compared to D.D.M. The possible reason behind higher solubilisation is the energy input used during the S.Ev.M. and enthalpic and entropic contribution. After the

evaporation of organic solvent (ethanol), the molecules of phyto-drug and Pluronic closely interacted with each other, on the other hand, this was missing in D.D.M. During the rehydration, the use of sonication at frequency of 40 kHz facilitated the formation of micelles in a Pluronic solution that consisted of a complex between phyto-drug and PPO and PEO region of Pluronic molecule. Additionally, the corona region of the Pluronic molecules played a role in stabilising and dispersing the micelles in the solvent system. The energy input also helps to obtain smaller micelles from the thin film aggregates. Other reason is enthalpic and entropic contribution, during the solvent evaporation of Pluronic and phyto-drugs, there were enthalpic and entropic interactions between drug and chains of Pluronics which facilitates the solubilisation of phyto-drugs. This mechanism has been proposed by Xu and colleagues, where solvent evaporation induced and facilitated the formation of polymer patch nanoparticles by exquisite balance between enthalpic interaction and conformational entropy of grafted chains of polymers (L. Yu et al., 2021). The solubility of NAR was found to be ~2100 and ~1200 folds higher in Pluronic P84 micelles (5% w/v) with S.Ev.M. and D.D.M. method respectively, as compared to NAR solubility in pure water. In the case of BAC, aqueous solubility was increased ~3200 and ~1300 in Pluronic P84 (12% w/v) with S.E.M and D.D.M. method respectively.

The percent (%) drug loading capacity (DLC) was calculated by taking the ratio of amount of Phyto-drug encapsulated and weight Pluronic used as mentioned in **Eq. 2.7**. DLC of Pluronic micelles at higher concentration of both formulations were calculated (**Figure C.2**, Appendix C). DLC was observed to be ~40% for NAR loaded P84 (at 5% w/v) micellar formulation, however, only ~2% DLC in 12% P84 micelles was observed for BAC. DLC for other Pluronic systems was lower than when the drug was loaded into Pluronic P84 micelles (**Figure C.2,** Appendix C). Thermodynamics of phyto-drugs (NAR and BAC) encapsulation was determined in terms of the partition coefficient (*P*) and Gibbs free energy (ΔG°). *P* is the ratio of the drug encapsulated in the micellar phase to the drug solubilised in aqueous phase (**Eq. 2.8**). From the partition coefficient, the Gibbs free energy of drug encapsulation has been calculated using the **Eq. 2.9** (**Chapter 2**). *P* values for NAR (1-5%) and BAC (6-12%) in the different Pluronics at various concentrations were calculated using solubilisation data **(Figure 7.2c,d).** The higher values of *P* confirmed that Pluronic P84 micelles at concentration of 5% w/v and 12% w/v for NAR and BAC respectively provided a better hydrophobic environment to solubilize these phyto-drugs (Singla et al., 2018a). In addition to that, ΔG° was more negative in the case of Pluronic

P84 at concentrations of 5% w/v and 12% w/v for NAR and BAC respectively **(Figure 7.2e,f)**.

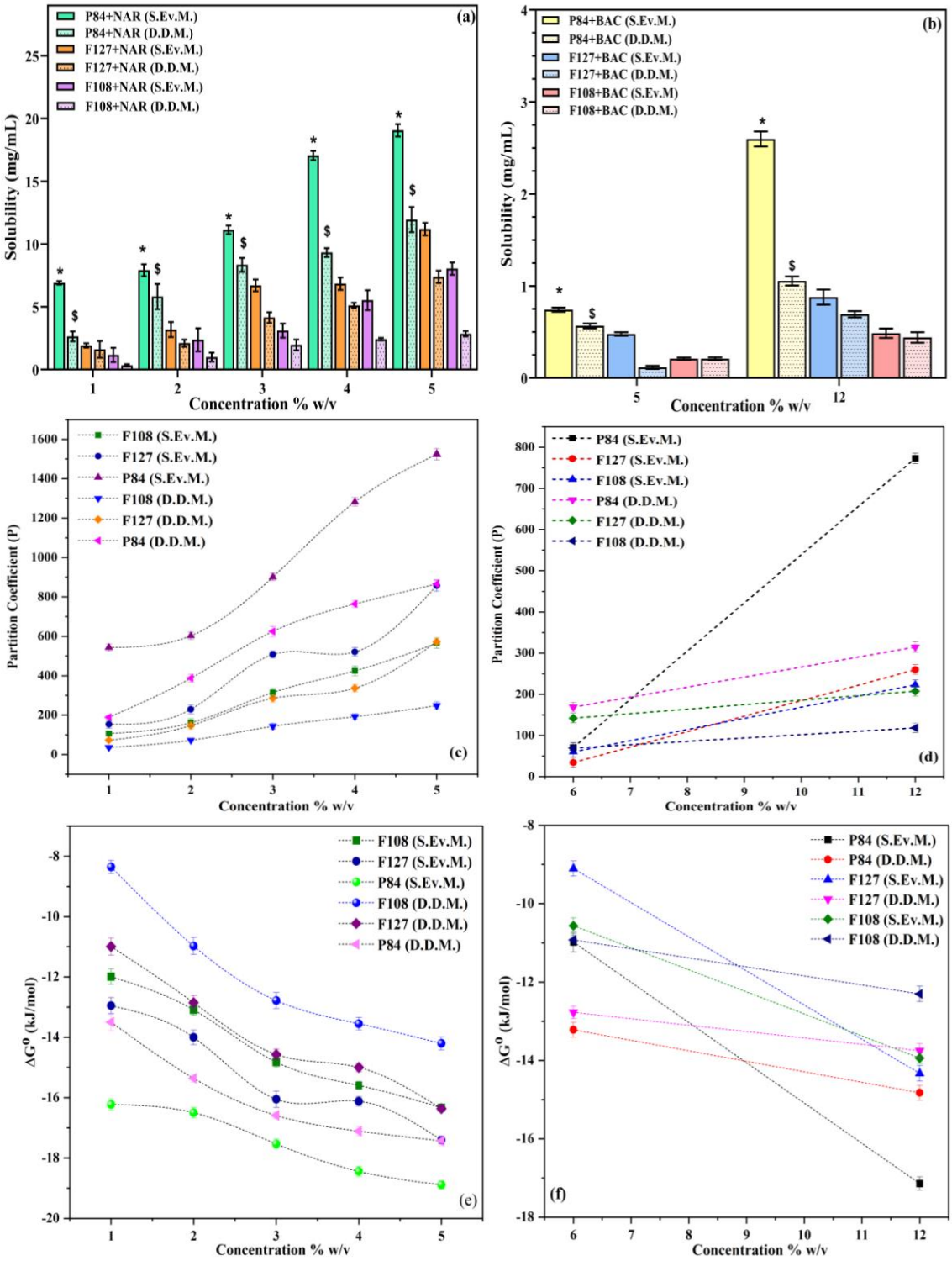

Figure 7.2: Solubility of different nutraceuticals in different Pluronics (P84, F127 and F108) **(a)** NAR and **(b)** BAC; Partition coefficient (P) of **(c)** NAR and **(d)** BAC; Gibbs free energy ΔG^o (kJ/mol) of **(e)** NAR and **(f)** BAC.

7.4.2 Dynamic light scattering (DLS) and zeta potential (ζ) measurements

Hydrodynamic diameter *(D_h)* of the optimal micellar formulation produced using S.Ev.M. was measured by employing DLS measurements. D_h values of empty micelles of Pluronic P84, F127 and F108 (5% w/v) at 25 ± 0.1 °C were found to 28.58, 32.39 and 51.30 nm respectively (see **Figure C.3a-c,** Appendix C). After NAR loading, the D_h values for Pluronic P84, F127 and F108 (5% w/v) micellar aggregates were found to be 50.66, 59.11 and 108.23 nm respectively. The increase in the D_h was observed at 12 % w/v concentration of Pluronic P84, F127 and F108 i.e. 33.27, 44.06 and 62.78 nm respectively. The D_h values were measured to be 42.83, 44.06 and 62.78 nm (**Figure C.3d-f,** Appendix C) for Pluronic P84, F127 and F108 (12% w/v) respectively after the encapsulation of BAC drug. The polydispersity index (PDI) values for all formulations were given in captions of **Figure C3** and found to be between 0.2 to 0.3, this means that formulations are moderately homogeneous. There was a higher increase in D_h upon the loading of NAR as compared to BAC, which indicates the higher interactions between the NAR and Pluronic micelle surface and encapsulating the higher amount of NAR within the Pluronic micelle core and corona (Braga et al., 2020; Callari et al., 2017). Zeta potential (ζ) measurements were also performed to probe the surface charge and stability of Pluronics, and phyto-drug loaded Pluronic micelles, values for ζ potential as well as pH of the formulations have been tabulated in **Table C.1 (Appendix C)**. Unloaded Pluronic micelles of 5% w/v P84, F127 and F108 exhibited ζ values (in mV) of − 8.82 ± 0.43, − 10.57 ± 0.58 and − 11.94 ± 0.50, respectively, whereas for 12% w/v P84, F127 and F108 unloaded micelles ζ values for found to be − 11.82 ± 0.43, − 12.57 ± 0.58, and − 12.94 ± 0.50 respectively. The loading of NAR to 5% w/v Pluronic P84, F127 and F108 increased the ζ values to − 9.93 ± 0.65, − 11.44 ± 1.52, − 12.09 ± 0.79, respectively, on the other hand, loading of BAC in 12% w/v Pluronic P84, F127 and F108 increases the ζ to − 12.03 ± 0.65, − 12.73 ± 0.52, − 13.04 ± 0.22. Pluronics, despite being non-ionic, exhibit negative zeta potentials, indicating the presence of repulsive interactions among the micelles. These interactions prevent aggregation among the Pluronic micelles, resulting in their stability (Abdelbary et al., 2013). **Table C.1** demonstrates that phyto-drug loaded Pluronics an increase in ζ values, confirming the stability of the micelles. Moreover, to evaluate the stability of Pluronic formulations the Phyto-drug loaded Pluronic P84 micellar formulations (5% w/v P84 for NAR and 12% w/v P84 for BAC) were

stored for 1, 4 and 8 weeks at 25 °C and size and visual turbidity was determined. There were no visual turbidity or size changes of the formulations (data not shown), for the storage of 8 weeks, but after that it showed little turbidity. It witnessed that Pluronic P84 micelles formulations were stable for 8 weeks during storage. This information can be important in the development of drug delivery systems, as the size and stability of the delivery vehicle can impact the efficacy and safety of the drug.

7.4.3 In vitro drug release

In vitro drug release is highly valuable for uncovering essential information about formulation structure and behaviour, potential interactions between the drug and carrier composition, and how they impact the rate and mechanism of drug release (D'Souza and DeLuca, 2006; Higuchi, 1963). The Pluronic formulation was examined using the dialysis release method in phosphate-buffered saline (PBS) with a pH of approximately 7.4, which is isotonic to blood. After 6 h, NAR loaded Pluronic P84, F127, and F108 micelles (at 5% w/v) showed a fast release of 32.55 ± 2.19%, 66.76 ± 1.93%, and 50.55 ± 1.97% respectively, followed the release rate slowed down (**Figure 7.3a**). NAR was fully released from P84 micelles after 34 h, whereas, from F127 and F108 micelles, NAR took 26 h to be released completely. In the case of BAC, Pluronics P84, F127, and F108 (12% w/v) exhibited a faster drug release compared to NAR. BAC complete release was observed to be in 5 and 8 h in case of F127 and F108 micelles (**Figure 7.3b**) respectively as compared to P84 micelles (16 h). Pluronic P84 is composed of 60% PPO component, and most of the drug is located within the PPO core. Therefore, the phyto-drugs must first pass through the PEO corona region before leaving the micelles and ultimately passing through the pores of the dialysis membrane to be released in the medium. This is the reason slower release of phyto-drugs in the P84 micelles was observed as compared to other F127 and F108 micelles. Sahu and colleagues noticed the slow and sustained release of Curcumin in Pluronic F127 and F68 micelles (Sahu et al., 2011). Zhao et al. also observed the sustained release behaviour of Curcumin (phyto-drug) loaded from the Pluronic P123 and F68 mixed micelles (Zhao et al., 2012). In addition to that the phyto-drugs release of both NAR and BAC has been showed in the insets of respective **Figure 7.3a,b**. Four different release kinetics were conducted which are zero-order, first-order, Korsmeyer-Peppas, and Higuchi to analyse the release study, the theoretical background and equations of these kinetic release models is provided in the **in the section C.1** of

Appendix C. The highest R^2 value indicated the best release kinetics followed by these formulations and kinetics data is tabulated in **Table C.2** (Appendix C)**.** NAR loaded with P84, F108 (5% w/v) and BAC loaded with P84, F127 (12% w/v) followed the Higuchi release kinetics implying that that the drug release was diffusion controlled at this concentration (Higuchi, 1963). Besides, NAR loaded F127 showed the first order release kinetics, confirming that the release was independent of concentration of NAR entrapped (Gibaldi and Feldman, 1967). BAC loaded F108 micelles followed the Zero order release kinetics which revealed that the drug is released at a constant rate (Costa and Lobo, 2001).

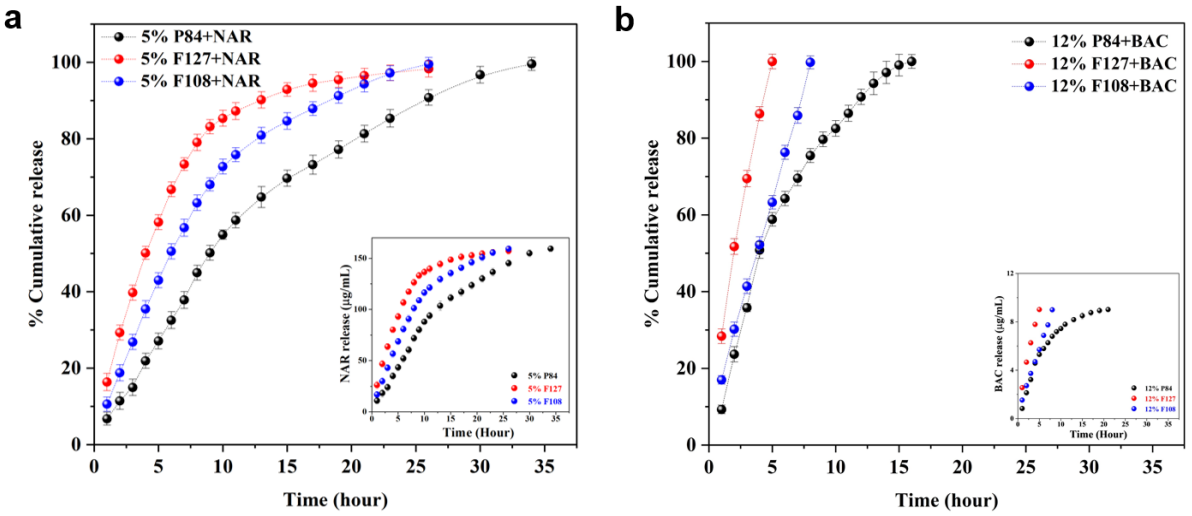

Figure 7.3: *In vitro* release of **(a)** NAR and **(b)** BAC from different Pluronic micelles at concentration 5% w/v and 12 % w/v, respectively, at 37 ℃ ± 0.2, SD (n = 3).

7.4.4 In vitro antioxidant activity

The antioxidant activity of pure phyto-drugs NAR and BAC and their different Pluronic micellar formulations was deciphered through experiments with $ABTS^{\bullet+}$ radical scavenging assays (calculated using **Eq. 2.13, Chapter 2**). The antioxidant potential of pure drugs and drug loaded Pluronic micellar formulations was found to be increased in a concentration dependent manner. Pluronic formulations of NAR and BAC exhibited higher $ABTS^{\bullet+}$ scavenging activity as compared to the pure drug. However, higher $ABTS^{\bullet+}$ scavenging was observed in NAR and BAC loaded P84 micelles with 98.58 ± 1.36% and 95.6 ± 0.11% inhibition respectively as compared to NAR (81.92 ± 0.985%) and BAC (70.41 ± 2.71%) drugs (**Figure 7.4a and 7.4a**). However, NAR-P84 micellar formulation was found to be a better antioxidant than BAC loaded Pluronic P84 micelles because it

showed higher antioxidant activity at a very low concentration of 25 μg/mL. On the other hand, BAC loaded Pluronic P84 micelles showed the highest inhibition of $ABTS^{\bullet+}$ at 80 μg/mL. IC_{50} was also calculated for all systems mentioned above and depicted in **Figures 7.4c and 7.4d** for NAR and BAC respectively.

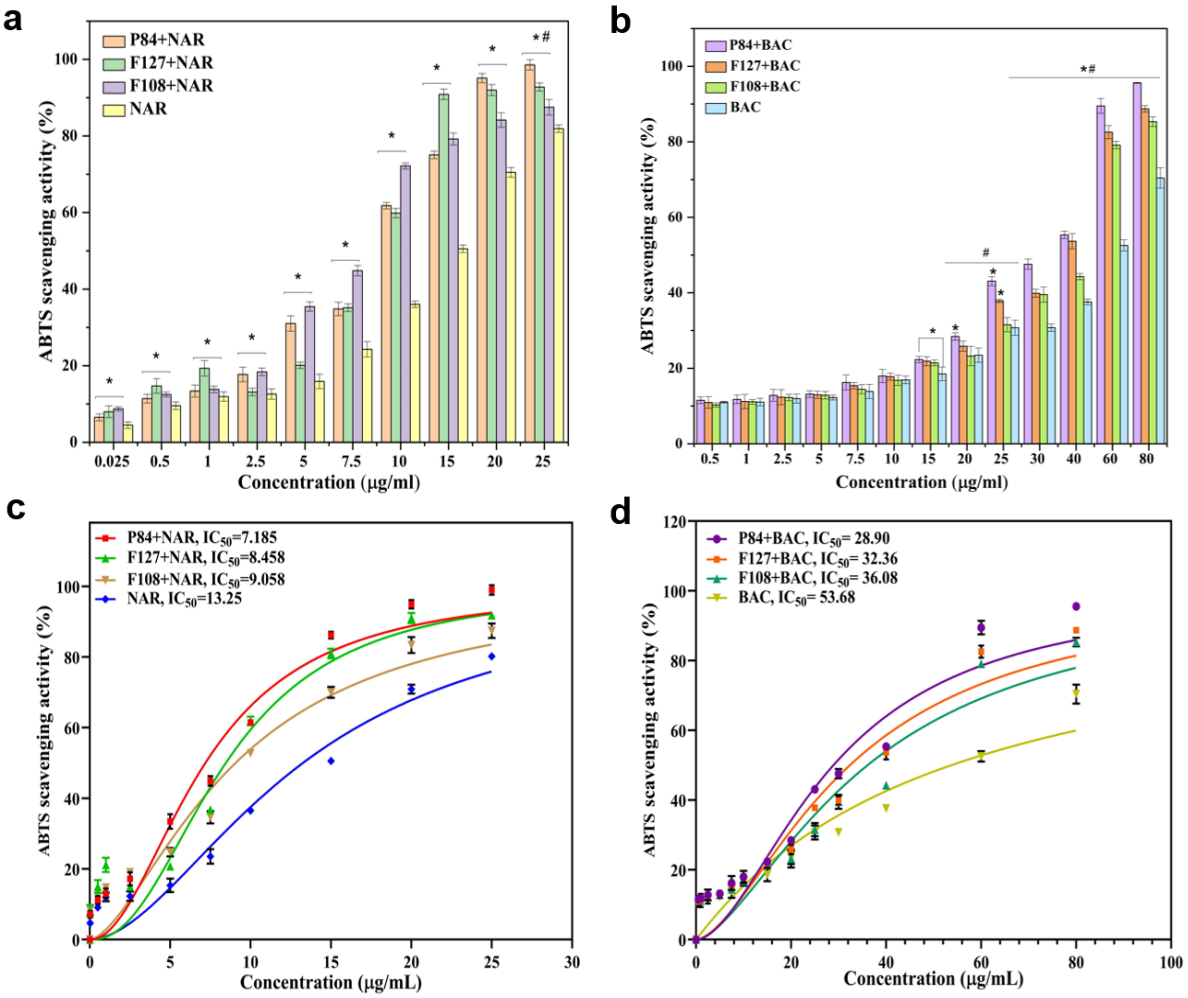

Figure 7.4: $ABTS^{\bullet+}$ scavanging activity of different Pluronic formulations of **(c)** NAR and **(d)** BAC; IC_{50} of **(e)** NAR **(f)** BAC different Pluronic formulations in $ABTS^{\bullet+}$ assay.

Results showed that the IC_{50} values of Pluronic formulations of NAR (7.185 μg/mL) and BAC (28.90 μg/mL) were lower than the pure phyto-drugs NAR and BAC with IC_{50} of 13.25 and 53.68 μg/mL respectively. Therefore, these results implied that encapsulation of these drugs in Pluronic formulations improved the overall antioxidant potential. Moreover, the ABTS•+ scavenging activity of unloaded Pluronic P84, F127 and F108 micelles (as a blank) at 5% w/v was found to be 3.235 ± 0.36%, 2.93 ± 0.12% and 2.165

± 0.26% respectively and at 12% w/v values were observed to be 3.88 ± 0.33%. 3.285 ± 0.47% and 2.865 ± 0.26% respectively (as shown in **Figure C.4,** Appendix C)**.** These results confers that the enhancement in the antioxidant was due to the overall improvement and solubilisation of the Phyto-drugs (NAR and BAC).

The increase in $ABTS^{\bullet+}$ scavenging with NAR and BAC loaded Pluronic P84 micelles can be attributed to the improved water solubility of these drugs in Pluronic micelles, which imparts the better contact of these drugs with free radicals of $ABTS^{\bullet+}$. These results corroborated with our previous studies in which Pluronic mixed micellar formulations of clozapine and oxcarbazepine improved the antioxidant activity of pure drugs (Singla et al., 2020). Similar results were observed by Sun *et al.,* who also observed improved $ABTS^{\bullet+}$ scavenging activity of flavonoid Myricetin with polymeric micellar formulation as compared to the free drug (Sun et al., 2019). As evidenced in literature, antioxidant activities of these phyto-drugs play an important role in several drug pathways including cancer, liver diseases and brain diseases (Y. Wang et al., 2019). Therefore, it can be suggested that these formulations could provide a better formulation system for such type of drugs being used for the treatment of various diseases in which antioxidant activity plays a major protective role.

7.4.5 Morphology of the micelles

To check whether S.Ev.M. technique for NAR loading had any impact on the morphology of Pluronic micelles, SEM measurements were performed. Drug loading is higher in the case of Pluronic P84 and Pluronic F127; thus, these two micellar systems were subjected to perform SEM measurements. Pluronic F127 and P84 micelles showed spherical morphology at 5% w/v concentration with average size of 58.33 nm and 40.33 nm respectively (**Figure 7.5a and b**). Further, after NAR loading, the average sizes of Pluronic F127 and P84 micelles were found to be increased with average sizes of 75.66 nm and 61.66 nm (**Figure 7.5c and d**) respectively. Moreover, SEM measurement evidenced that S.Ev.M. did not affect the morphology of Pluronic micelles, it is reported in the literature that Pluronic micelles exhibited spherical morphology (Nasehi et al., 2020).

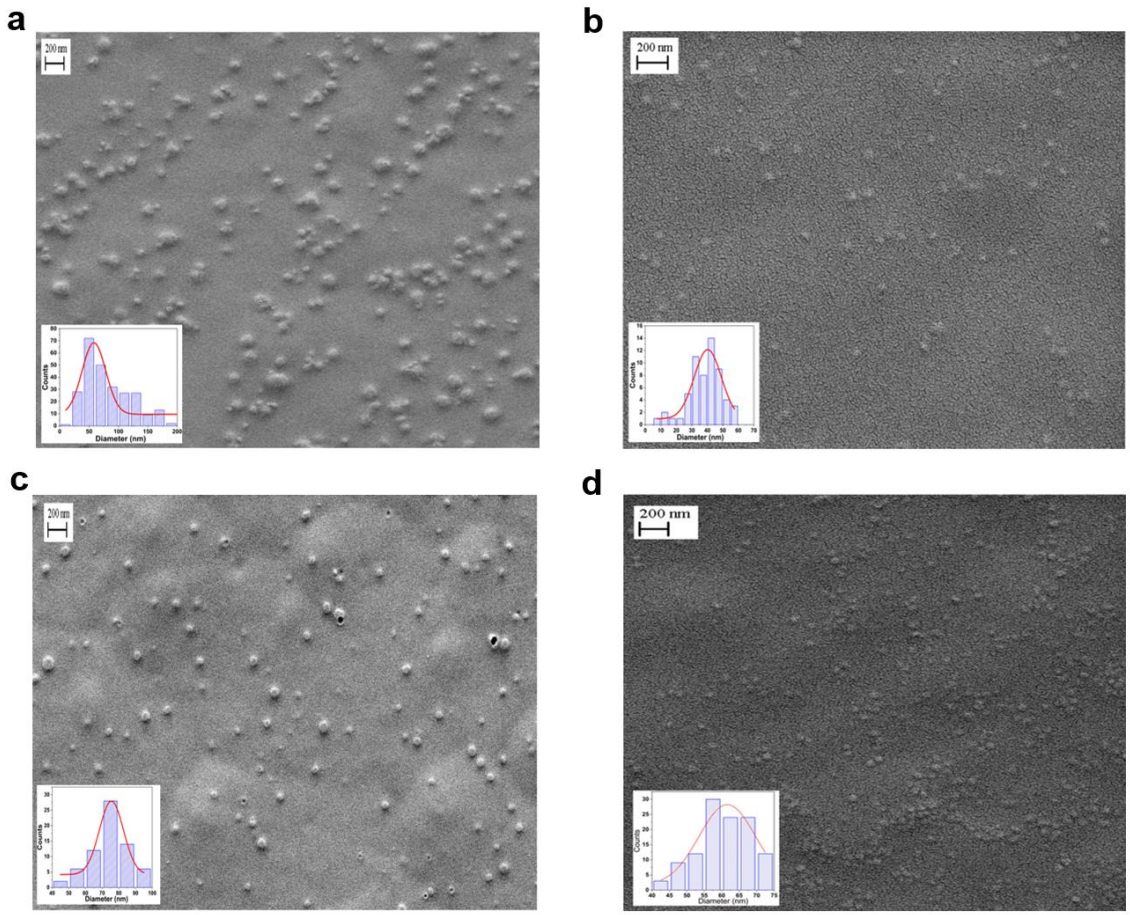

Figure 7.5: SEM images of 5% w/v Pluronic micelles prepared by Solvent evaporation method (S.Ev.M.) **(a)** Empty Pluronic F127 micelles **(b)** Empty Pluronic P84 micelles **(c)** NAR loaded Pluronic F127 micelles **(d)** NAR loaded Pluronic P84 micelles.

7.4.6 Interactional behaviour of NAR and BAC with Pluronic micelles

^{1}H-NMR spectroscopy was employed to understand the binding interactions and solubilisation locus of NAR and BAC within Pluronic 84 micelles, which had the highest solubilisation capacity. Stock solutions of NAR and BAC were prepared in DMSO-d6 and further diluted in D_2O with final concentration of 1 mM NAR/BAC in solvent ratio of 5% v/v DMSO-D_2O. These solutions were recorded for their NMR spectra using TMSP-d4 (Trimethylsilylpropanoic acid) as internal standard (0.0 ppm) and titrated against Pluronic P84. Water suppression was used to remove the water signal. The hydrophobic drug BAC was observed to precipitate out in the chosen solvent system and therefore measurements were not possible with BAC. The typical NMR spectra of 1 mM NAR showed doublets at 7.45 and 6.97 ppm due to aromatic H's H-12, H-16 and H-13, H-15, respectively along with a singlet at 5.87 ppm due to H-2 and H-6 (**Figure C.5,** Appendix

C). The peaks at 5.50 and 3.25 ppm correspond to H-9 and H-8, respectively. The peaks due to –OH hydrogens (H-18, H-19 and H-20) were resolved in pure DMSO-d6 at 9.59, 10.80 and 12.16 ppm. However, no peaks corresponding to –OH groups were observed in the chosen solvent system which was likely due to rapid exchange of OH protons with deuterium which is not observable in a ^{1}H NMR spectrum **(Figure 7.6)** (Alexandridis et al., 1994; Shriky et al., 2020). Upon sequential additions of P84 solution (up to 0.05 mM), the Ar–H's peaks showed upfield shifts to 7.41, 6.95 and 5.81 ppm along with broadening of signals. Also, the resonance signals at 5.50 and 3.25 ppm showed upfield shifts to 5.45 and 3.20 ppm, respectively. With each addition of P84, the peaks corresponding to protons of NAR are increasingly broadened while the peaks at 1.17 ppm belong to PPO-CH3. The broad peaks at 3.50–3.65 ppm and the sharp peak at 3.71 ppm correspond to PPO-CH2 and PEO-CH2 groups of P84. Broadening of the peak evidenced that the protons of NAR molecule were in close proximity with PEO and PPO blocks of Pluronic P84 (Vekariya et al., 2014). These NMR results emphasised that the probable solubilisation locus (location of the NAR within micelles) is both PEO forming Corona and PPO forming core region (Ma et al., 2007b).

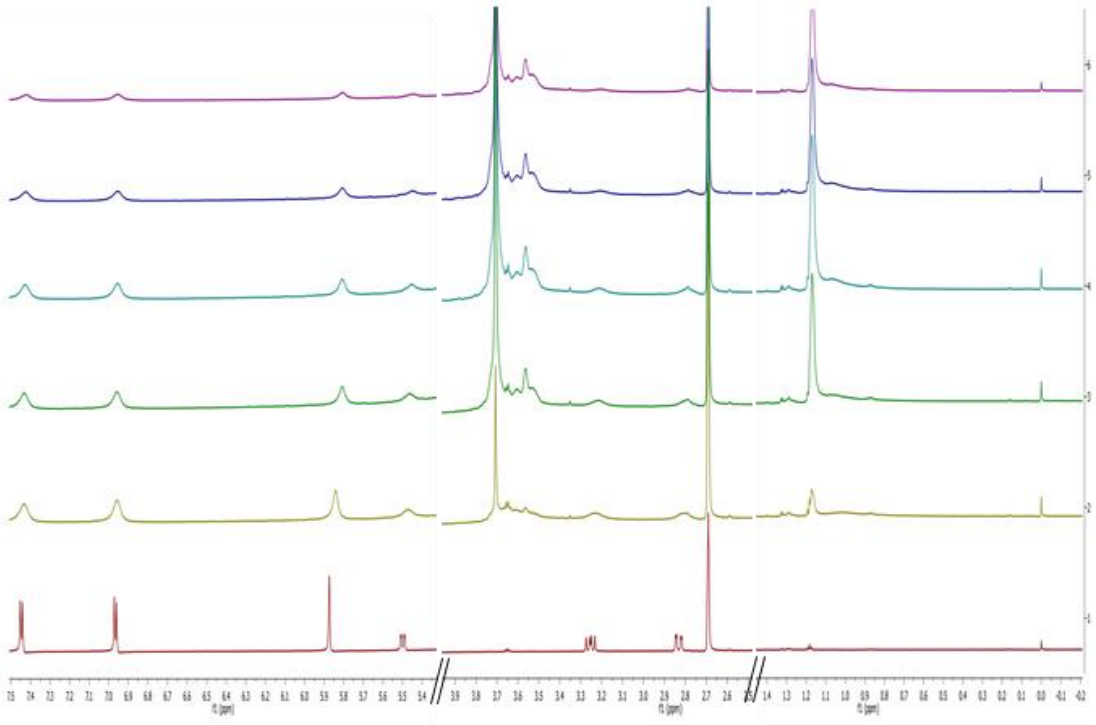

Figure 7.6: ^{1}H-NMR spectra of NAR and titrated with different concentrations of Pluronic P84.

7.4.7 Effect of temperature on the solubilisation of NAR in Pluronic micelles

NAR loaded Pluronic P84 micelles at 1% w/v were selected to scrutinise the effect of temperature using ^{1}H NMR in a 9:1 H_2O:D_2O solution (**Figure 7.7**). It is worth mentioning that we selected 1% w/v of Pluronic P84 instead of 5% w/v (which have highest solubilisation capacity) for this study. Because at higher concentration of Pluronic P84, the signals from its protons were much stronger than NAR even at higher temperature screening, making it difficult to distinguish the NAR signals. At temperature of 283 K, the singlet at ~ 1.17 ppm was attributed to protons of PPO CH_3 groups and the additional peaks at ~3.36 and ~3.58 ppm belong to the protons of PPO CH groups and PPO CH_2 groups respectively. A sharp peak at ~3.72 ppm belongs to the protons of PEO CH_2 group. However, peaks of NAR could not be seen at this temperature. The micellar system was then subjected to an increase in temperature and the spectra were recorded. It was observed that the peak at 1.17 ppm was suppressed after increasing temperature from 283 to 293 K. Further increasing the temperature resulted in the formation of a new peak at 1.06 ppm, which intensified with sequential rise in temperature. This could be attributed to the change in microenvironment around the PPO-CH_3 region of Pluronic P84 due to interaction with hydrophobic NAR molecules. The signals at 1.17 and 1.06 ppm are due to hydrated and anhydrous state of the PPO-CH_3 groups. At lower temperatures, the chemical exchange rate between the two states was low, resulting in two well defined peaks while with increased temperature the chemical exchange rate accelerated, leading to unresolved signals (Ma et al., 2007b). In addition, peaks attributed to NAR were observed with the rise in temperature, thus leading to the conclusion that the signal of NAR solubilised in P84 can be seen at higher temperature due to higher chemical exchange rate.

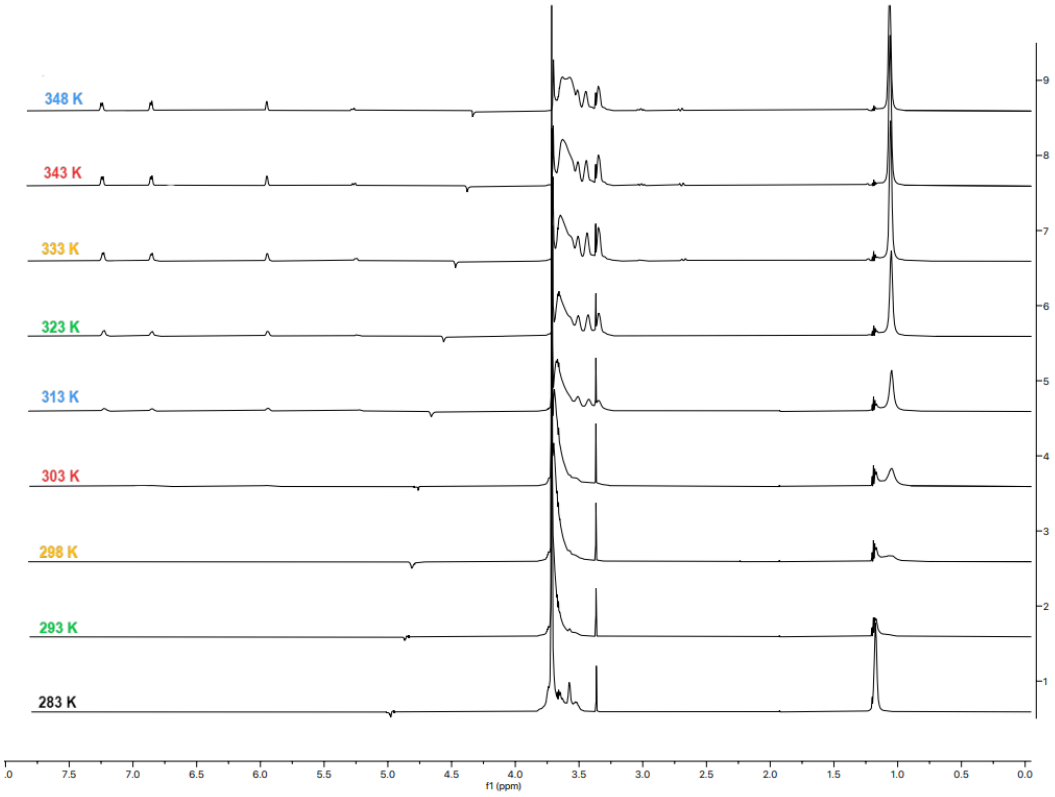

Figure 7.7: ^{1}H-NMR spectra of NAR loaded Pluronic P84 (1% w/v) micelles with temperature variation from 283-348 K.

7.5 Conclusion

This study demonstrated that the S.Ev.M. is a better method compared to D.D.M. for loading hydrophobic flavonoids NAR and BAC without compromising the size and morphology of Pluronic micelles. The results delineated that S.EV.M. method would be a greater alternative to solubilize the hydrophobic drugs over D.D.M. and can be employed in pharmaceutical industries as it is more efficient, less processing time and easy deployable method. Pluronics were more favourable for the loading of NAR than BAC, as confirmed by encapsulation studies. DLS results showed that the loading of phyto-drugs resulted in swelling of the Pluronic micelles. *In vitro* sustained release behaviour and higher antioxidant potential was evaluated for NAR and BAC loaded Pluronic formulation. It was demonstrated that Pluronic P84 exhibited greater sustained release (100% release in 36 h) and higher antioxidant potential for NAR and BAC. Furthermore, ^{1}H NMR results evidenced that NAR interacts with both core and corona regions of Pluronic P84 micelles. From these results, it can therefore be suggested that this approach could be used for a wider range of other water insoluble phyto and pharmaceutically important molecules.

7.6 Refernces

Abdelbary, A. A., et al. (2013). 'Effect of fixed aqueous layer thickness of polymeric stabilizers on zeta potential and stability of aripiprazole nanosuspensions' *Pharmaceutical Development and Technology*, 18 (3), pp. 730-735.

Alexandridis, P., Holzwarth, J. F. & Hatton, T. A. (1994). 'Micellisation of poly (ethylene oxide)-poly (propylene oxide)-poly (ethylene oxide) triblock copolymers in aqueous solutions: Thermodynamics of copolymer association' *Macromolecules*, 27 (9), pp. 2414-2425.

Arango-Ruiz, Á., et al. (2018). 'Encapsulation of curcumin using supercritical antisolvent (sas) technology to improve its stability and solubility in water' *Food chemistry*, 258 pp. 156-163.

Braga, G., et al. (2020). 'Tautomeric and aggregational dynamics of curcumin-supersaturated pluronic nanocarriers' *ACS Applied Polymer Materials*, 2 (11), pp. 4493-4511.

Callari, M., De Souza, P. L., Rawal, A. & Stenzel, M. H. (2017). 'The effect of drug loading on micelle properties: Solid-state nmr as a tool to gain structural insight' *Angewandte Chemie*, 129 (29), pp. 8561-8565.

Choi, Y. A., et al. (2015). 'Enhanced oral bioavailability of morin administered in mixed micelle formulation with pluronicf127 and tween80 in rats' *Biological and Pharmaceutical Bulletin*, 38 (2), pp. 208-217.

Costa, P. & Lobo, J. M. S. (2001). 'Modeling and comparison of dissolution profiles' *European journal of pharmaceutical sciences*, 13 (2), pp. 123-133.

D'Souza, S. S. & DeLuca, P. P. (2006). 'Methods to assess in vitro drug release from injectable polymeric particulate systems' *Pharmaceutical research*, 23 pp. 460-474.

Ganguly, R., et al. (2017). 'Heat-induced solubilisation of curcumin in kinetically stable pluronic p123 micelles and vesicles: An exploit of slow dynamics of the micellar restructuring processes in the aqueous pluronic system' *Colloids and surfaces B: Biointerfaces*, 152 pp. 176-182.

Gibaldi, M. & Feldman, S. (1967). 'Establishment of sink conditions in dissolution rate determinations. Theoretical considerations and application to nondisintegrating dosage forms' *Journal of pharmaceutical sciences*, 56 (10), pp. 1238-1242.

Gong, W.-y., et al. (2017). 'Exploring the chemopreventive properties and perspectives of baicalin and its aglycone baicalein in solid tumors' *European Journal of Medicinal Chemistry*, 126 pp. 844-852.

Higuchi, T. (1963). 'Mechanism of sustained-action medication. Theoretical analysis of rate of release of solid drugs dispersed in solid matrices' *Journal of pharmaceutical sciences*, 52 (12), pp. 1145-1149.

Jabbari, M. & Jabbari, A. (2016). 'Antioxidant potential and dpph radical scavenging kinetics of water-insoluble flavonoid naringenin in aqueous solution of micelles' *Colloids and Surfaces A: Physicochemical and Engineering Aspects*, 489 pp. 392-399.

Jindal, N. & Mehta, S. (2015). 'Nevirapine loaded poloxamer 407/pluronic p123 mixed micelles: Optimisation of formulation and in vitro evaluation' *Colloids and Surfaces B: Biointerfaces*, 129 pp. 100-106.

Kadam, Y., Yerramilli, U. & Bahadur, A. (2009). 'Solubilisation of poorly water-soluble drug carbamezapine in pluronic® micelles: Effect of molecular characteristics, temperature and added salt on the solubilising capacity' *Colloids and Surfaces B: Biointerfaces*, 72 (1), pp. 141-147.

Liang, Y., et al. (2022). 'Preparation, characterisation of naringenin, β-cyclodextrin and carbon quantum dot antioxidant nanocomposites' *Food Chemistry*, 375 p. 131646.

Liu, Y., An, W. & Gao, A. (2016). 'Protective effects of naringenin in cardiorenal syndrome' *Journal of Surgical Research*, 203 (2), pp. 416-423.

Lorscheider, M., et al. (2021). 'Challenges and opportunities in the delivery of cancer therapeutics: Update on recent progress' *Therapeutic delivery*, 12 (1), pp. 55-76.

Ma, J.-h., et al. (2007). 'Probing paeonol− pluronic polymer interactions by 1h nmr spectroscopy' *The Journal of Physical Chemistry B*, 111 (47), pp. 13371-13378.

Moghaddam, R. H., et al. (2020). 'Naringenin and naringin in cardiovascular disease prevention: A preclinical review' *European Journal of Pharmacology*, 887 p. 173535.

Nasehi, N., et al. (2020). 'Sorafenib loaded pluronic f127-lithocholic acid micelles for prostate cancer therapy: Formulation, optimisation, and in vitro evaluation against lncap cells' *International Journal of Polymeric Materials and Polymeric Biomaterials*, 69 (3), pp. 158-172.

Peng, S., et al. (2018). 'Enhancement of curcumin bioavailability by encapsulation in sophorolipid-coated nanoparticles: An in vitro and in vivo study' *Journal of agricultural and food chemistry*, 66 (6), pp. 1488-1497.

Raval, A., Pillai, S. A., Bahadur, A. & Bahadur, P. (2017). 'Systematic characterisation of pluronic® micelles and their application for solubilisation and in vitro release of some hydrophobic anticancer drugs' *Journal of Molecular Liquids*, 230 pp. 473-481.

Sahu, A., Kasoju, N., Goswami, P. & Bora, U. (2011). 'Encapsulation of curcumin in pluronic block copolymer micelles for drug delivery applications' *Journal of biomaterials applications*, 25 (6), pp. 619-639.

Senthilkumar, M., Dash, S., Vigneshwari, R. & Paulraj, E. (2022). 'Aceclofenac-loaded pluronic f108/l81 mixed polymeric micelles: Effect of hlb on solubilisation' *Designed monomers and polymers*, 25 (1), pp. 1-11.

Shriky, B., et al. (2020). 'Pluronic f127 thermosensitive injectable smart hydrogels for controlled drug delivery system development' *Journal of colloid and interface science*, 565 pp. 119-130.

Shulman, M., et al. (2011). 'Enhancement of naringenin bioavailability by complexation with hydroxypropoyl-β-cyclodextrin' *PloS one*, 6 (4), p. e18033.

Singla, P., Chabba, S. & Mahajan, R. K. (2016). 'A systematic physicochemical investigation on solubilisation and in vitro release of poorly water soluble oxcarbazepine drug in pluronic micelles' *Colloids and Surfaces A: Physicochemical and Engineering Aspects*, 504 pp. 479-488.

Singla, P., et al. (2020). 'Solubilisation of hydrophobic drugs clozapine and oxcarbazepine in the lower and higher molecular weight pluronic mixed micelles-a physicochemical, in vitro release and in vitro anti-oxidant study' *Journal of Molecular Liquids*, 317 p. 113816.

Singla, P., et al. (2022). 'Advances in the therapeutic delivery and applications of functionalised pluronics: A critical review' *Advances in Colloid and Interface Science*, 299 p. 102563.

Singla, P., et al. (2018). 'Sodium deoxycholate mediated enhanced solubilisation and stability of hydrophobic drug clozapine in pluronic micelles' *Spectrochimica Acta Part A: Molecular and Biomolecular Spectroscopy*, 191 pp. 143-154.

Sun, F., et al. (2019). 'New micelle myricetin formulation for ocular delivery: Improved stability, solubility, and ocular anti-inflammatory treatment' *Drug delivery*, 26 (1), pp. 575-585.

Sun, J., et al. (2022). 'Chitosan binding to a novel alfalfa phytoferritin nanocage loaded with baicalein: Simulated digestion and absorption evaluation' *Food Chemistry*, 386 p. 132716.

Tu, B., et al. (2015). 'Study of the structure-activity relationship of flavonoids based on their interaction with human serum albumin' *RSC advances*, 5 (89), pp. 73290-73300.

Van Thoai, D., et al. (2020). 'Lipophilic effect of various pluronic-grafted gelatin copolymers on the quercetin delivery efficiency in these self-assembly nanogels' *Journal of Polymer Research*, 27 pp. 1-12.

Vekariya, R. L., Aswal, V. K., Hassan, P. A. & Soni, S. S. (2014). 'Influence of n-alkylpyridinium halide based ionic liquids on micellisation of p123 in aqueous solutions: A sans, dls, and nmr study' *Langmuir*, 30 (48), pp. 14406-14415.

Wang, L., et al. (2022). 'Latest research progress on anticancer effect of baicalin and its aglycone baicalein' *Archives of Pharmacal Research*, 45 (8), pp. 535-557.

Wang, Y., et al. (2019). 'Construing the biochemical and molecular mechanism underlying the in vivo and in vitro chemotherapeutic efficacy of ruthenium-baicalein complex in colon cancer' *International Journal of Biological Sciences*, 15 (5), p. 1052.

You, G., et al. (2021). 'Preparation, optimisation, characterisation and in vitro release of baicalein-solubilising glycyrrhizic acid nano-micelles' *International journal of pharmaceutics*, 601 p. 120546.

Yu, L., et al. (2021). 'Solvent-evaporation induced and mechanistic entropy-enthalpy-balance controlled polymer patch formation on nanoparticle surfaces' *The journal of physical chemistry letters*, 12 (30), pp. 7100-7105.

Zhao, L., et al. (2012). 'Curcumin loaded mixed micelles composed of pluronic p123 and f68: Preparation, optimisation and in vitro characterisation' *Colloids and Surfaces B: Biointerfaces*, 97 pp. 101-108.

Chapter 8. General Conclusion and Outlook

This chapter contains key findings of the research work completed and the conclusions presented in this thesis, with the goal of providing and explaining future workings as well as the expected scope of the work detailed. The research work produced has resulted in the five scientific publications in international journals of repute (including Small and Advanced Science) and conference contributions articulated in section **8.3** and **8.4**.

8.1 Key findings

Electroactive MIPs (eMIPs) were developed for glucose detection, achieving a LOD of 26 nM and 44 nM in PBS and artificial ISF (AISF) respectively (objective 1, Chapter 3). The eMIPs based sensor demonstrated strong clinical potential by showing a high correlation (>0.9) with the state-of-the-art Roche analyser in serum samples of diabetic patients. Moreover, the sensor can be used for continuous monitoring of glucose with a wearable, as evidenced by its ability to detect AISF samples with a two-electrode system.

Further advances in MIPs, particularly in nano-format which are referred to as nanoMIPs, present intriguing opportunities for their application in biosensors and drug delivery. NanoMIPs exhibit high surface area and have the ability to be engineered to recognise virtually any target (including proteins, peptides, small and large molecules), with high binding specificity and sensitivity. The work conducted to achieve objective 2 (Chapter 4) has provided insight into the use of nanoMIPs for the sensing of protein for food safety applications. These nanoMIPs prepared using solid-phase synthesis present several advantages over other nanoparticle system including high affinity, better selectivity, specificity, uniform sized particles, easy and cost-effective fabrication process. Chapter 4 focussed on the development of novel, low cost nanoMIPs based sensor for the electrochemical and thermal detection of LYZ, achieving a low LOD of 13 pM via EIS and 1 fM with thermal detection. This sensor showed high selectivity against different proteins such as BSA and troponin-I. Moreover, nanoMIPs sensor successfully detected Lysozyme (a protein present in eggs and tend to cause the allergic reactions) in hen egg samples. Lysozyme is a model protein and due to the versatility of these nanoMIPs (prepared using solid phase) to imprint any target, can be easily expanded to other proteins and small to large molecules. In Chapter 5 (objective 3), dual functionality of nanoMIPs was explored by combining specific recognition of proteins with localised drug delivery. This chapter

highlights the progress made in designing double imprinted nanoMIPs for the targeted delivery of anticancer drug doxorubicin (DOX) to ERα positive breast cancer (BC). The binding affinity of these nanoMIPs (K_D of 10 nm) for ERα receptors rival the affinity of commercial antibodies. Moreover, DOX loaded nanoMIPs exhibited selective cytotoxicity to ERα positive BC cells (~80%) while showing a minimal toxicity to ERα negative cell lines (~15%). Similar results were observed in complex 3D cancer models that mimic the tumour microenvironment, thus demonstrating the clinical potential of these advanced materials. These characteristics show the potential of nanoMIPs for developing next-generation diagnostic tools for the detection of disease biomarkers such as cancer and diabetes. Further, advancements in nanoMIPs technology will open the door to 'personalized' medicines. These nanoMIPs have shown promising results for delivering hydrophilic drugs; however, challenges could emerge when employing this technique to deliver hydrophobic drugs or molecules. It might be due to the hydrophilic nature of the monomers and washing steps employed in solid phase synthesis approach where hydrophobic drugs typically have poor solubility. As a results, these drugs struggle to effectively interact with and imprint onto the polymer matrix, highlighting the challenges that remaining developing systems capable to deliver hydrophobic drugs.

Phyto-drugs (nutraceuticals) are widely used due to their biocompatibility, safety and therapeutic properties such as anti-oxidant and anti-inflammatory. However, hydrophobic nature of these drugs results in their poor absorption and bioavailability limiting their usage in pharmaceutical industry. To improve the solubility of hydrophobic drugs, polymer-based drug delivery carriers are being explored from decades. Surface active polymers, particularly Pluronics (commercial polymers) have gained widespread attention as potential drug delivery vehicle due to their core-shell structure which allows for the incorporation of drugs with poor solubility and prevents their degradation in biological media. Therefore, the incorporation of mixed polymeric systems, such as Pluronics, offers a potential solution by improving drug solubility and bioavailability, paving the way for more effective treatment options. Therefore, objective 4 (Chapter 6 and 7) were designed to prepare the Pluronic micelles using different methods for the solubilisation and drug delivery of hydrophobic phyto-drugs SLY, NAR and BAC). Mixed micellar formulations (Chapter 6) of Pluronic and reverse Pluronic demonstrated higher SLY solubility of 3.929 mg mL^{-1} and drug loading efficiency of 98.03 % as compared to pure Pluronics.

Further in Chapter 7, two different methods were explored for the solubilisation of two phyto-drugs NAR and BAC. The solvent evaporation method showed better solubilisation of NAR (19.2 mg mL^{-1}) and BAC (2.593 mg mL^{-1}) as compared to direct dissolution methods (NAR, 10.95 mg mL^{-1}, and BAC, 1.058 mg mL^{-1}) in Pluronic P84, respectively. Moreover, SLY, NAR and BAC polymeric micelles (mixed and pure Pluronics) significantly enhanced the anti-oxidant activity as compared to pure phyto-drugs. Therefore, it can be suggested that Pluronic formulations can be potentially used as drug delivery vehicle for poorly water-soluble drugs in the pharmaceutical industry.

8.2 Final conclusion and future outlook

This thesis explored the use of advanced polymer materials for cutting-edge healthcare applications, using a range of technologies. Each of these methods offer distinct advantages in sensors and drug delivery and can be tailored for range of biomarkers/targets or different drugs. Firstly, the eMIPs developed in this thesis are more robust, versatile and affordable compared to current enzyme-based systems, enabling label-free and PoC detection that can be integrated into a wearable system. Moreover, they have other advantages including easy fabrication, high selectivity and specificity over the currently widely used glucose oxidase enzyme and emerging receptors such as aptamers and cyclic peptides. Secondly, I demonstrated that nanoMIPs enable the development of efficient and robust impedimetric sensors for protein biomarker detection in egg samples, highlighting their significant commercial potential of nanoMIPs-based sensor to enhance food safety testing. Due to the nanoMIPs advantages such as high stability, cost-effectiveness, easy fabrication and potential reusability of nanoMIPs over natural counterparts like Abs, nanoMIPs can be used for the imprinting of other proteins. Fluorescent and anticancer drug (DOX) loaded double imprinted nanoMIPs against ERα have showed the targeted drug delivery to the ER+ BC. Moreover, these nanoMIPs were able to translocate from membrane to nucleus of BC cells, which emphasise that this novel approach can be used to deliver drugs and genes directly to the nucleus of cells. Moreover, nanoMIPs platform can be tailored to other anticancer drugs and new targets for targeted therapeutics with additional potential for use in imaging of cancer cells and tumours. Lastly, Pluronic (surface active polymers) micellar approach demonstrated that this can be utilised to improve the therapeutic values of natural agents (SLY, NAR and BAC). Given the commercial availability and versatility, these Pluronics can be employed

to the range of hydrophobic natural drugs.

The differences in access to modern diagnostic tools and costly treatments have significantly impacted the healthcare system and these concerns underscores the critical need for the development of affordable and approachable theragnostic solutions. The future scope of the developed polymer systems, including MIPs and surface-active polymers, offers promising healthcare applications, especially in diagnosis and therapeutics, due to their straightforward and low-cost approach. The established eMIPs based sensor platform is highly novel and can be adapted for broader range of biomarkers, including proteins, hormones, and disease-related markers using multi-marker techniques. Therefore, these electrochemical sensing approaches leading towards the diagnostics, wearable sensing, and food safety monitoring. The integration of MIPs based sensors into wearable and PoC devices can revolutionise real-time health monitoring of chronic illnesses including diabetes and cardiovascular problems. Furthermore, the versatility of MIPs in terms of surface modification and flexibility enable the simultaneous detection of different disease markers in a multiplexed system. To use nanoMIPs for drug delivery to its fullest potential, conducting rigorous preclinical and clinical trials will be critical for demonstrating their safety and efficacy to achieve breakthroughs in this field. Further advances in research are likely to be around the combination of nanoMIPs with cleavable linkers and cell penetrating peptides for healthcare applications. Ultimately, identifying specific therapeutic areas for application and the partnerships with pharmaceutical industries will allow the successful introduction of nanoMIPs in the drug delivery market. Pluronic micellar formulations due to their easy fabrication without use of any sophisticated techniques, can be easily used for other drugs of hydrophobic nature. Pluronics can be engineered for controlled and sustained release, ensuring drugs are delivered more efficiently over time, reducing the frequency of dosing and enhancing patient compliance. Additionally, advancements in stimuli-responsive Pluronic systems, such as those triggered by temperature or pH changes, could allow for highly specific drug release at targeted sites, improving therapeutic outcomes. Their ability to form NPs makes them ideal for encapsulating a wide range of drugs, including small molecules and biologics, offering enhanced stability and reduced toxicity. Pluronics also hold promise in combination therapies, where they could synergize with other treatments like gene therapy or immunotherapy. As personalised medicine continues to grow, Pluronics could be tailored to meet individual patient needs, further enhancing the

precision and effectiveness of treatments. The future of combination delivery using MIPs for hydrophilic drugs and Pluronics for hydrophobic drugs offers a powerful approach for enhancing drug efficacy and overcoming solubility challenges. By integrating these systems, it's possible to develop versatile, targeted therapies with improved bioavailability and controlled release profiles for a wide range of drugs. Finally, the future advancements in polymer-based diagnostics and therapeutics are expected to provide more accessible, cost-effective, and efficient healthcare solutions, addressing disparities and improving health outcomes in both developed and developing countries.

8.3 Publications

1. **S. Garg,** P. Singla, F. Canfarotta, E. Velliou, J. Dawson, N. Kapur, N. Warren, S. Amarnath, M. Peeters, Analysis and future perspectives on the automation and biocompatibility of molecularly imprinted polymers for healthcare applications (invited perspective), *Macromolecules*, 2025, 58, 1157−1168 **(Editor's Choice)** [IF:5.5]. (https://doi.org/10.1021/acs.macromol.4c01621)

2. **S. Garg**, P. Singla, S. Kaur, R.D. Crapnell, C.E. Banks, S. Seyedin, M. Peeters, Electroactive Molecularly Imprinted Polymer Nanoparticles (eMIPs) for Label-free Detection of Glucose: Toward Wearable Monitoring, *Small***,** 2024, 2403320. [IF: 13.3]. (https://doi.org/10.1002/smll.202403320)

3. P. Singla, T. Broughton, M. V. Sullivan, **S. Garg**, R. Berlinguer-Palmini, P. Gupta, F. Canfarotta, N. W. Turner, E. Velliou, S. Amarnath, M. Peeters, Double Imprinted Nanoparticles for Sequential Membrane-to-Nuclear Targeted Drug Delivery of Chemotherapeutic Drugs, *Advanced Science,* 2024, 2309976. [IF: 15.1] (https://doi.org/10.1002/advs.202309976)

4. **S. Garg**, A. Sachdeva, M. Peeters, J. McClements, Point-of-Care Prostate Specific Antigen Testing: Examining Translational Progress toward Clinical Implementation, 2023, *ACS Sensors,* 8(10), 3643-58. [IF: 8.9] (https://doi.org/10.1002/smll.202403320)

5. P. Singla, S. Kaur, O. Jamieson, A. Dann, **S. Garg**, C. Mahon, R.D. Crapnell, C.E. Banks, I. Kaur, M. Peeters, Electrochemical and thermal detection of allergenic substance lysozyme with molecularly imprinted nanoparticles, *Analytical and Bioanalytical Chemistry*, 2023, 415(18), 4467-78. [IF: 4.3] (https://doi.org/10.1007/s00216-023-04638-2)

6. P. Singla, H. Kaur, **S. Garg**, N. Kaur, F. Canfarotta, R. K. Mahajan, M. Peeters, Early detection of SARS-CoV-2 with functionalized gold and molecularly imprinted polymeric nanoparticles: a mini review, 2023, Molecular Systems Design & Engineering, 8, 1337-1354. [IF:3.6] (https://doi.org/10.1002/advs.202309976)

7. P. Singla, G. Parokie, **S. Garg**, S. Kaur, I. Kaur, R.D. Crapnell, C.E. Banks, U. Rinner, C. Wills, M. Peeters, Enhancing encapsulation of hydrophobic phyto-drugs naringenin and baicalein in polymeric nano-micelles, *Journal of Drug Delivery Science and Technology*, 2023, 83,104403. [IF: 5.0] (https://doi.org/10.1016/j.jddst.2023.104403)

8. **S. Garg**, M. Peeters, R. K. Mahajan, P. Singla, Loading of Hydrophobic Drug Silymarin in Pluronic and Reverse Pluronic Mixed Micelles, *Journal of Drug Delivery Science and Technology*, 2022, 75: 103699. [IF: 5.0] (https://doi.org/10.1016/j.jddst.2022.103699)

8.4 Conference contributions

1. Poster Presentation (in person) on “Non-invasive detection of glucose with electroactive molecularly imprinted polymers (MIPs)” at ASN 2022, Kettering, Northamptonshire,13-15th May 2022.
2. Poster Presentation (online) on “Wearable sensor for the non-invasive detection of D-glucose with electroactive molecularly imprinted polymers (eMIPs)” at UK-Poland-Ukraine Bioinspired Materials Conference, 29-30th November 2022. **(Best poster award).**
3. Poster (in person)- “Wearable sensor for the non-invasive detection of D-glucose with electroactive molecularly imprinted polymers (e-MIPs) at 16th International conference on materials chemistry (MC16), 3-6th July 2023, Dublin, Ireland. **(Best poster award with £200 prize money).**
4. Oral (in person)- Non-invasive detection of glucose with electroactive molecularly imprinted polymers (e-MIPs): Application in wearable sensors“ at MIP2024, Verona University, Italy, 19-21st June 2024.
5. Oral presentation on Double imprinted MIPs for drug delivery to lung cancer at Drug Delivery to the Lungs Conference, Scotland, 11-13th December 2024

Appendices

Appendix A supplementary data for Chapter 5

Table A.1: Composition of different batches of the nanoMIPs and NIPs fabricated in this study.

Batch	ERα epitope	NIPAM	nTBA	AA	APMA	Bis	FLU	DOX
nanoMIPs	+	+	+	+	+	+	-	-
FLU-nanoMIPs	+	+	+	+	+	+	+	-
FLU-DOX-nanoMIPs	+	+	+	+	+	+	+	+
DOX-nanoMIPs	+	+	+	+	+	+	-	+
NIPs	-	+	+	+	+	+	-	-
FLU-NIPs	-	+	+	+	+	+	+	-
FLU-DOX-NIPs	-	+	+	+	+	+	+	+

A.1 DLS measurement of control nanoMIPs and non-imprinted polymeric nanoparticles (NIPs)

The hydrodynamic diameter (D_h) of nanoMIPs, NIPs, FLU-NIPs and FLU-DOX-NIPs were determined to be 110 ± 2 nm (PDI=0.112), 108 ± 3 nm (PDI=0.116), 121 ± 4 nm (PDI=0.110) and 143 ± 3 nm (PDI=0.131) respectively (**Table A.2**). These results indicate that the loading of fluorescein-o-methacrylate and DOX within the NIPs led to the increased D_h of FLU-NIPs and FLU-DOX-NIPs as compared to NIPs (control). Furthermore, PDI values of nanoMIPs and different NIPs were observed to be less than 0.2 suggesting the homogeneity of these nanoparticles.

Table A.2: Intensity weighted size (hydrodynamic diameter) of control nanoMIPs and NIPs.

Sample	Hydrodynamic diameter (D_h), nm	Polydispersity index (PDI)
nanoMIPs	110 ± 2	0.112
NIPs	108 ± 3	0.116
FLU-NIPs	121 ± 4	0.110
FLU-DOX-NIPs	143 ± 3	0.131

Table A.3: DOX loading, loading efficiency and loading capacity of different batches of DOX loaded nanoMIPs and NIPs.

Sample	Loading DOX concentration (μg/100 μg)	Loading efficiency (%)	Loading Capacity (%)
DOX-nanoMIPs	17.28 ± 0.1	57.6 ± 0.33	17.28 ± 0.1
FLU-DOX-nanoMIPs	19.33 ± 0.16	64.43 ± 0.53	19.27 ± 0.16
FLU-DOX-NIPs	18.37 ± 0.12	61.12 ± 0.40	18.21 ± 0.12

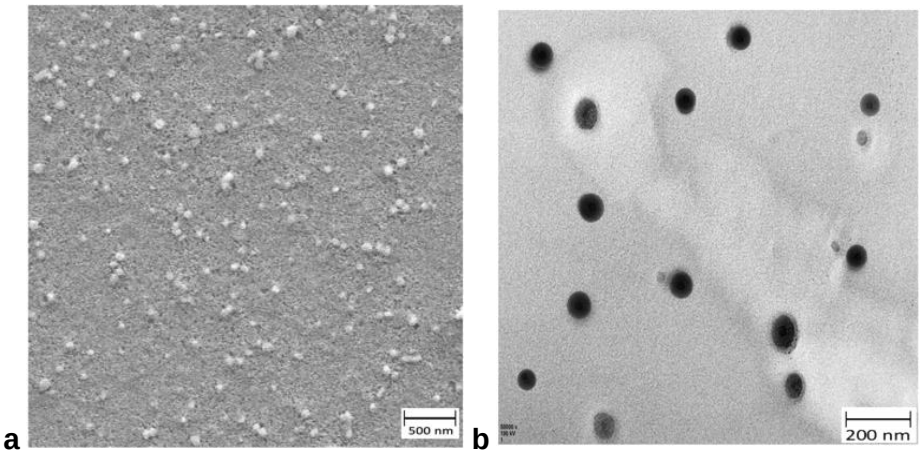

Figure A.1: Characterization: **a)** representative SEM images of DOX-nanoMIPs; **b)** TEM image (25000x) DOX-nanoMIPs

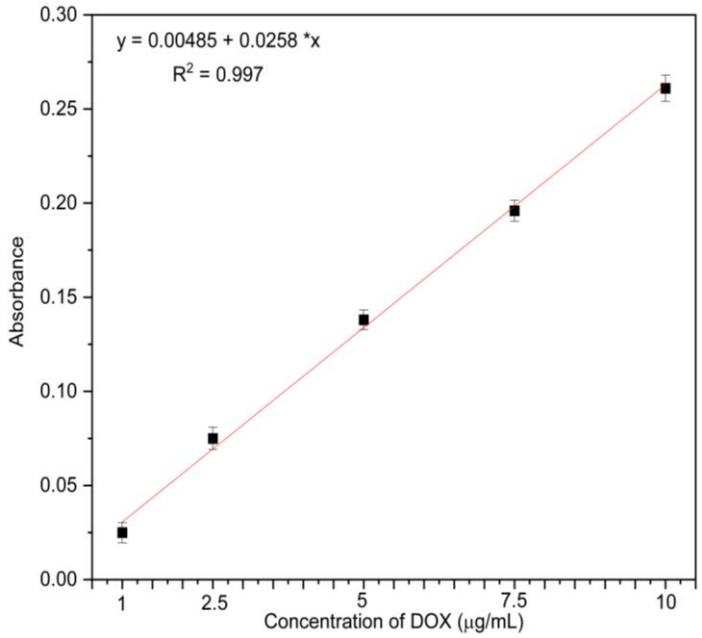

Figure A.2: Calibration curve of DOX absorbance (l_{max} 254 nm) *vs.* concentration (1, .5, 7.5 and 10 μg/mL) obtained from UV-visible spectres.

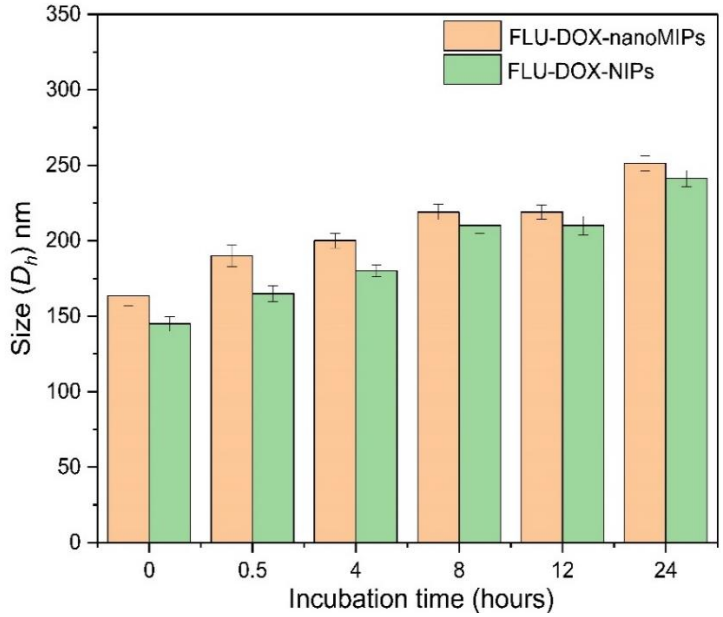

Figure A.3: Time dependent stability of nanoMIPs (FLU-DOX-nanoMIPs and FLU-DOX-NIPs) in DMEM culture media.

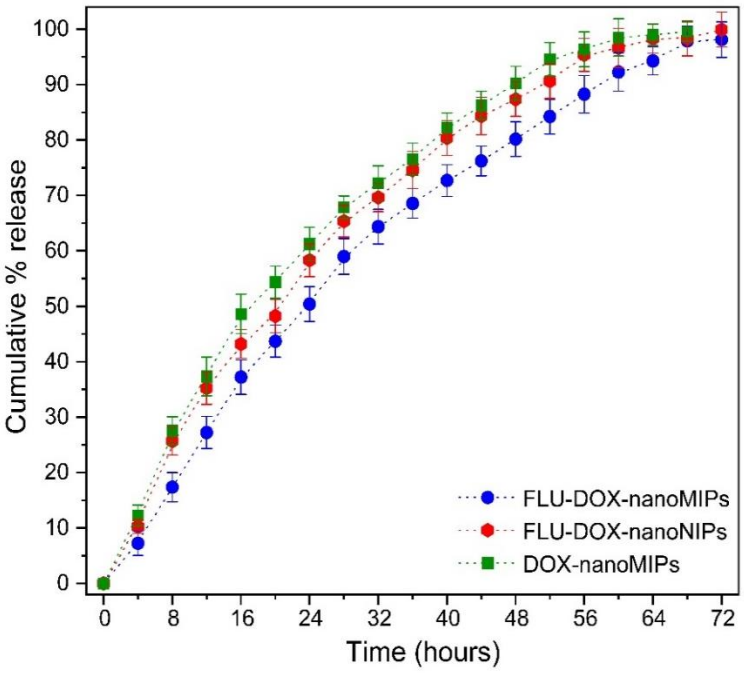

Figure A.4: The cumulative % release of DOX by FLU-DOX-nanoMIPs, FLU-DOX-nanoNIPs and DOX-nanoMIPs in phosphate buffer saline (pH = 7.45). Data are shown as mean ± SD.

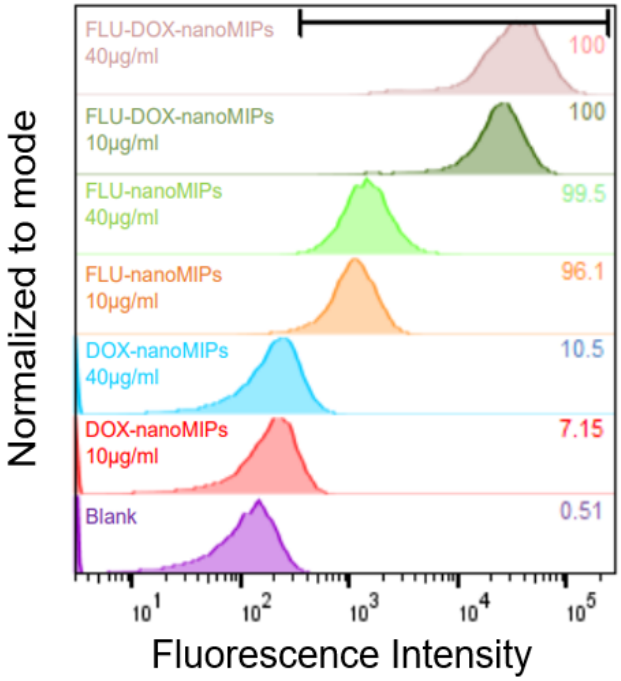

Figure A.5. *In vitro* flow cytometry binding assay, MCF-7 cells were incubated with 10 µg/mL and 40 µg/mL of DOX-nanoMIPs, FLU-nanoMIPs and FLU-DOX-nanoMIPs.

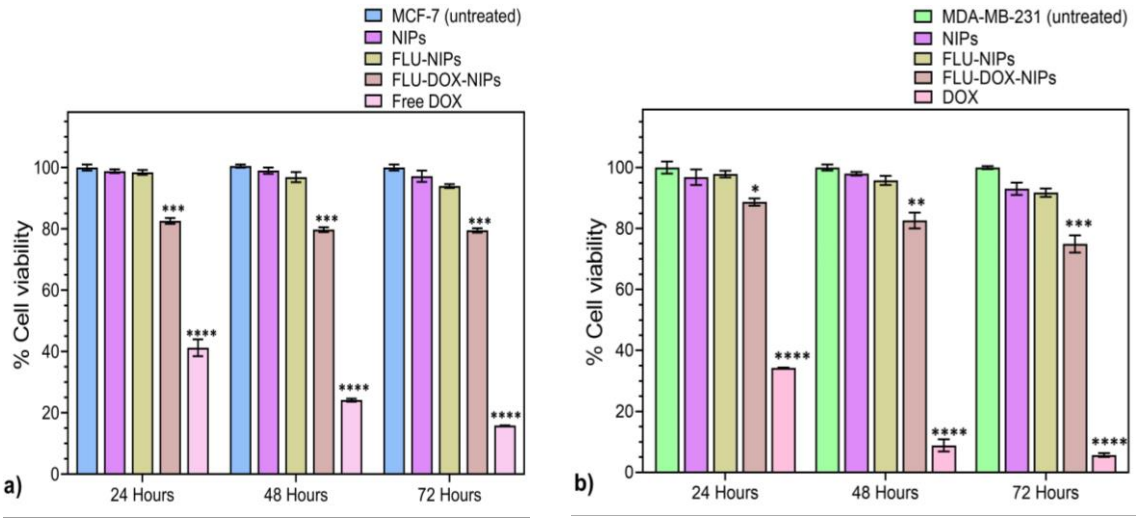

Figure A.6. *In vitro* cell viability assay, at 10 µg/mL for each treatment with NIPs, FLU-NIPs, FLU-DOX-NIPs and Free DOX, **a)** MCF-7 and **b)** MDA-MB-231. Data is expressed as mean ± SEM of three measurements. *** P ≤ 0.001, **** P ≤ 0.0001 *vs.* MCF-7 control (**a**), *P ≤ 0.05, ** P ≤ 0.01, *** P ≤ 0.001, **** P ≤ 0.0001 *vs.* MDA-MB-231 control (**b**).

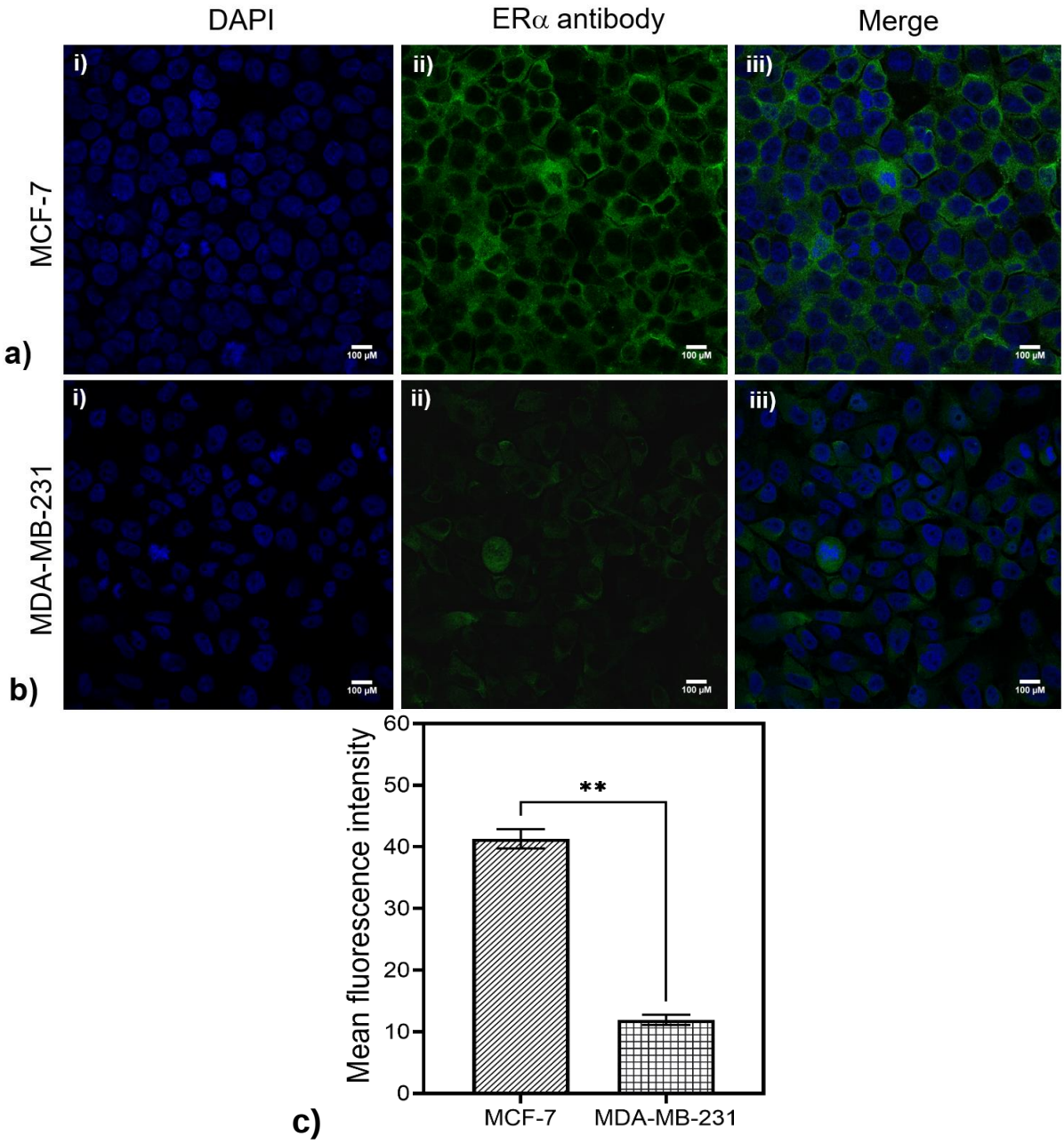

Figure A.7: CLSM images (40X) for **a)** MCF-7, **b)** MDA-MB-231 stained with ERα primary antibody incubated overnight at 4°C, and subsequently stained with anti-mouse Alexa Fluor 488 secondary antibody for 30 min at room temperature and DAPI nuclear staining for 5 min at room temperature. **(i)** DAPI (blue), **(ii)** ERα antibody (green), **(iii)** merged, **c)** The mean fluorescence intensity of ERα antibody in MCF-7 cells and MDA-MB-231 cells. Data is expressed as mean ± SEM of three measurements, ** $P \leq 0.01$ *vs.* MCF-7 control.

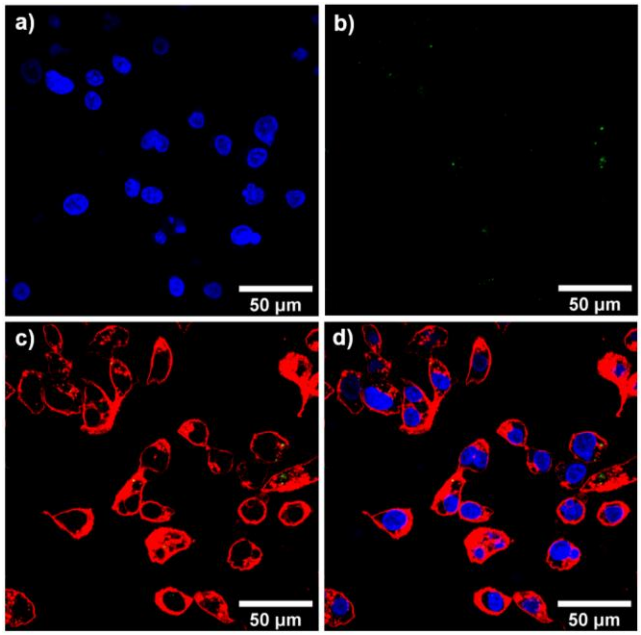

Figure A.8: CLSM images (40X) for MDA-MB-231 incubated with FLU-DOX-nanoMIPs for 1 hour at 37 °C **(a)** DAPI, **(b)** FLU-DOX-nanoMIPs with green fluorescence, **(c)** plasma membrane with red fluorescence (WGA antibody Alexa Fluor™ 594) with FLU-DOX-nanoMIPs, **(d)** merged.

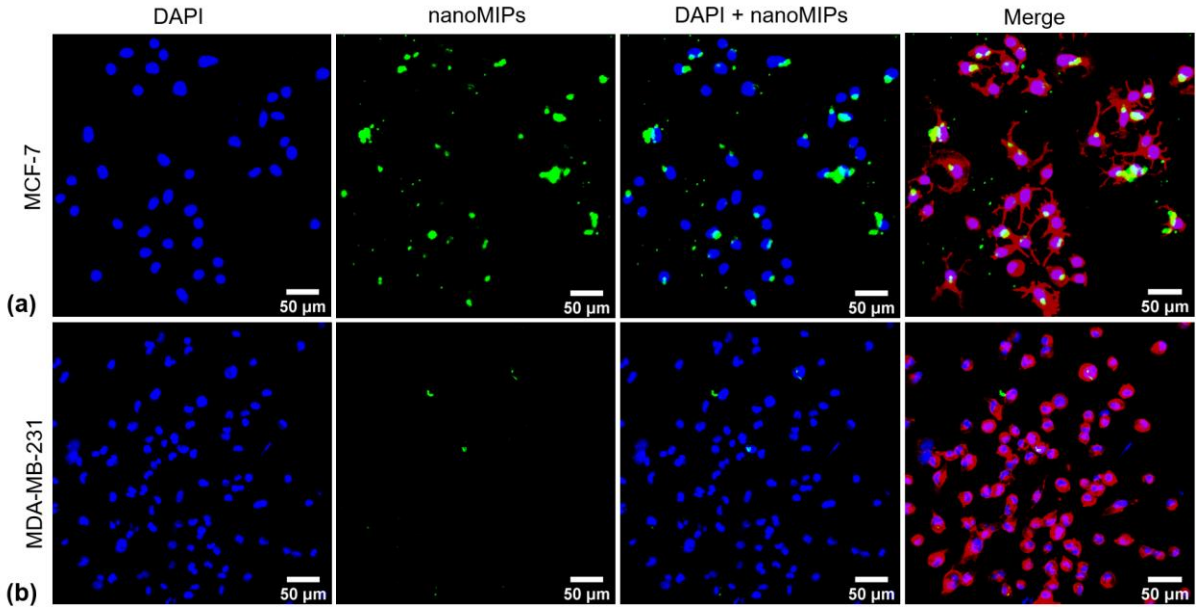

Figure A.9: CLSM images (20X) for FLU-DOX-nanoMIPs incubated for 12 hours at 37 °C with **(a)** MCF-7 cells, **(b)** MDA-MB-231 cells. Nucleus is stained with blue fluorescence (DAPI), nanoMIPs with green fluorescence, plasma membrane with red fluorescence (WGA antibody Alexa Fluor™ 594).

Appendix B supplementary data for Chapter 6

a

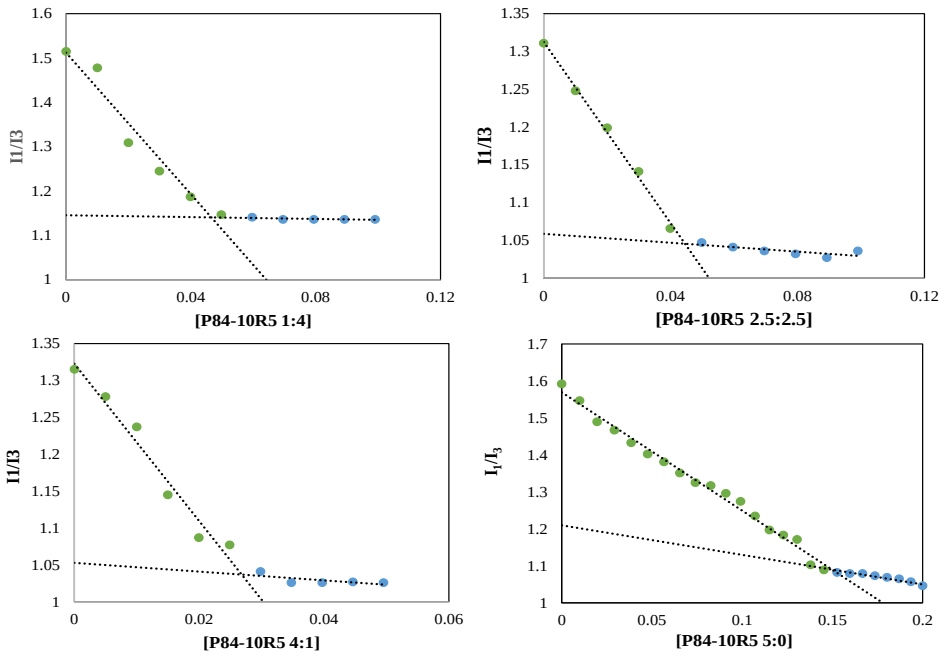

b

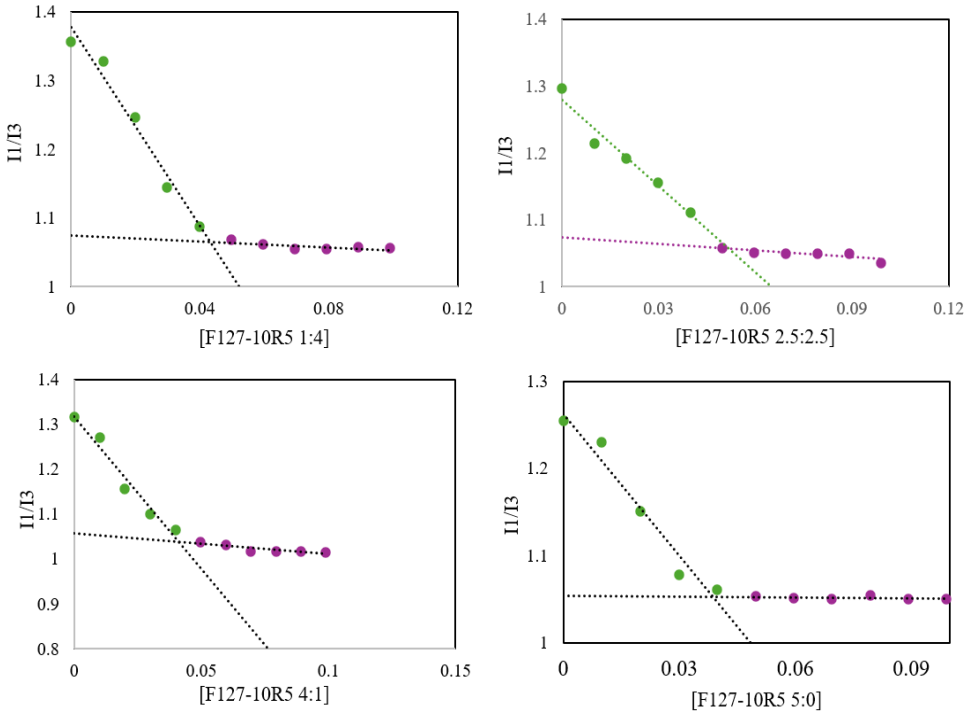

c

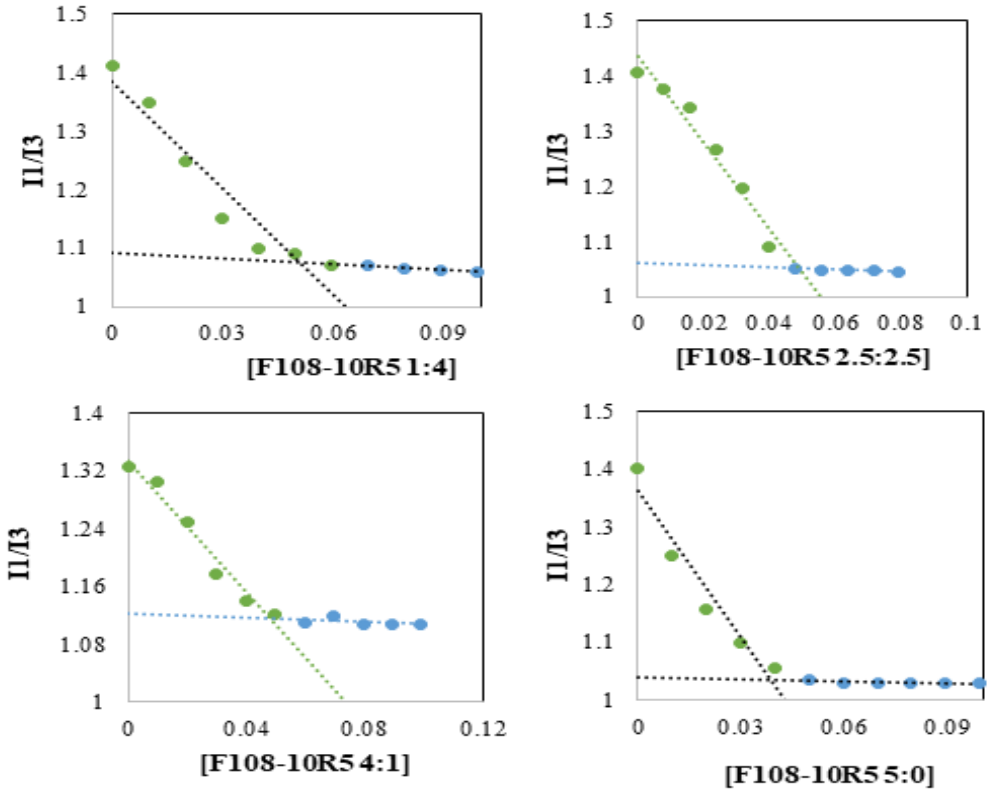
I1/I3
[F108-10R5 1:4]
[F108-10R5 2.5:2.5]
[F108-10R5 4:1]
[F108-10R5 5:0]

d

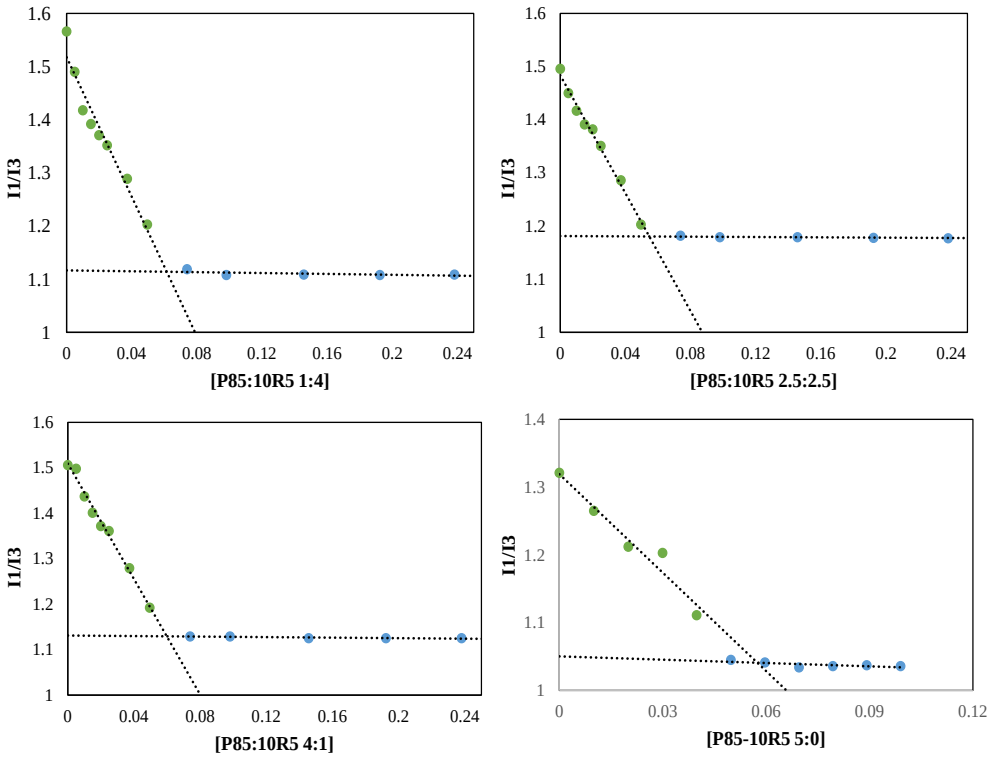
I1/I3
[P85:10R5 1:4]
[P85:10R5 2.5:2.5]
[P85:10R5 4:1]
[P85-10R5 5:0]

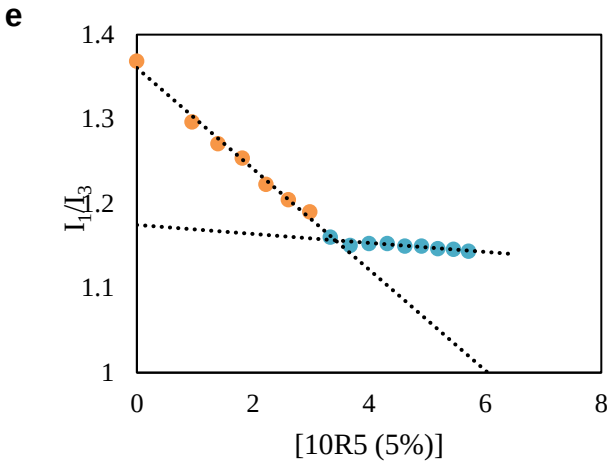

Figure B.1*: cmc's* of Pluronic mixed systems at different concentrations (1:4, 2.5:2.5, 4:1 and 5:0); **(a)** Pluronic P84-10R5, **(b)** Pluronic F127-10R5, **(c)** Pluronic F108-10R5, **(d)** Pluronic P85:10R5 and **(e)** Pluronic 10R5.

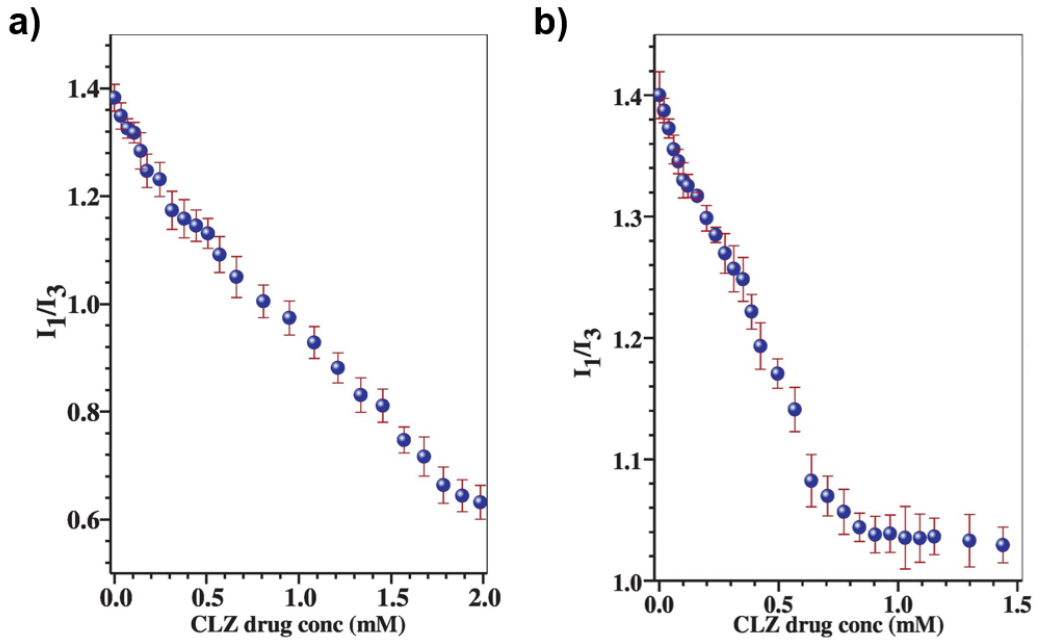

Figure B.2*:* Representative graphs for variation of micropolarity ratio (I_1/I_3) as a function of clozapine (CLZ) to determine its location **(a)** 12 % w/v P84, **(b)** 12 % w/v F127.

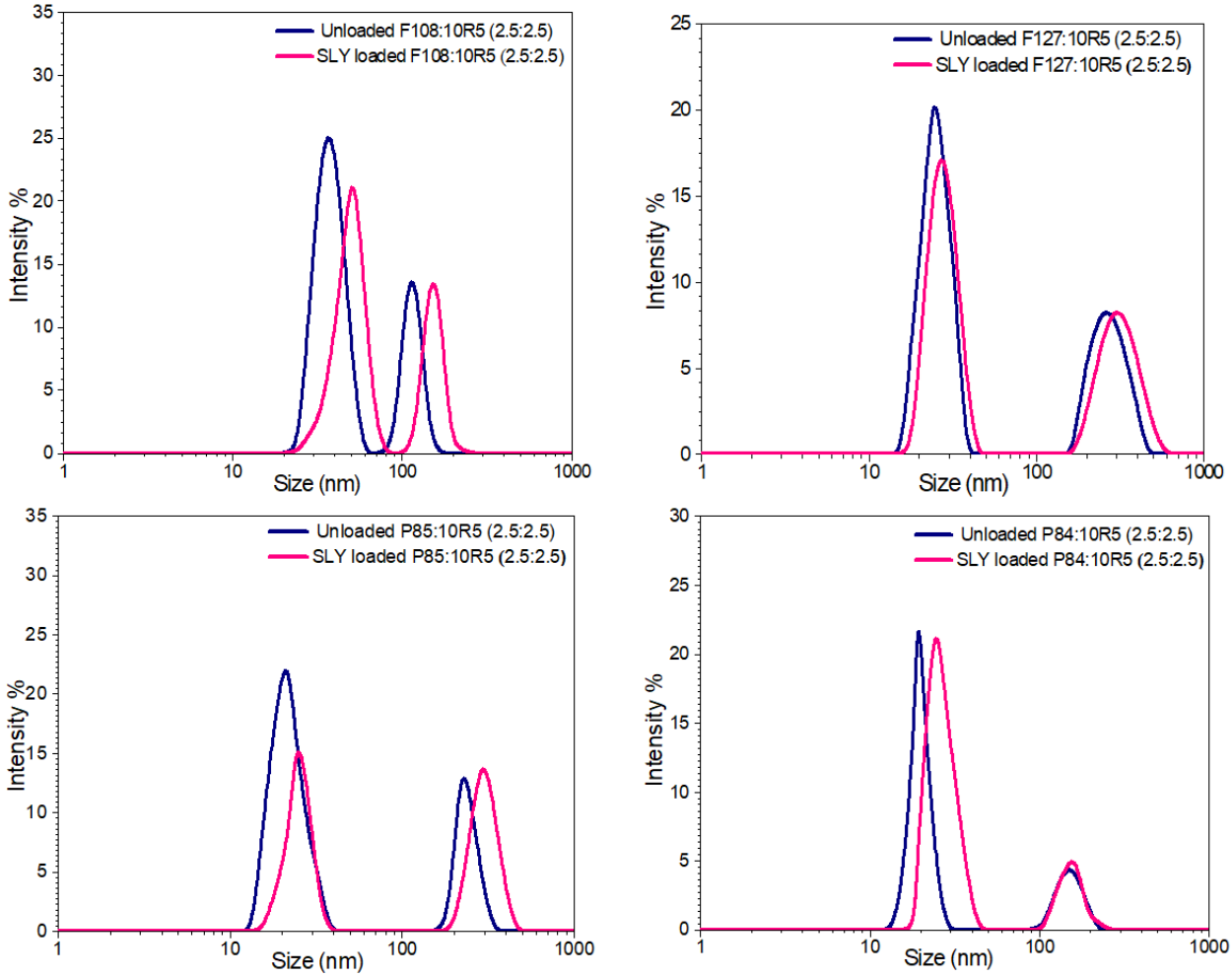

Figure B.3: Intensity weighed size distribution profiles for unloaded and SLY loaded mixed micelles of normal Pluronics F108, F127, P85 and P84 with 10R5 at concentration ratio of 2.5:2.5 % w/v.

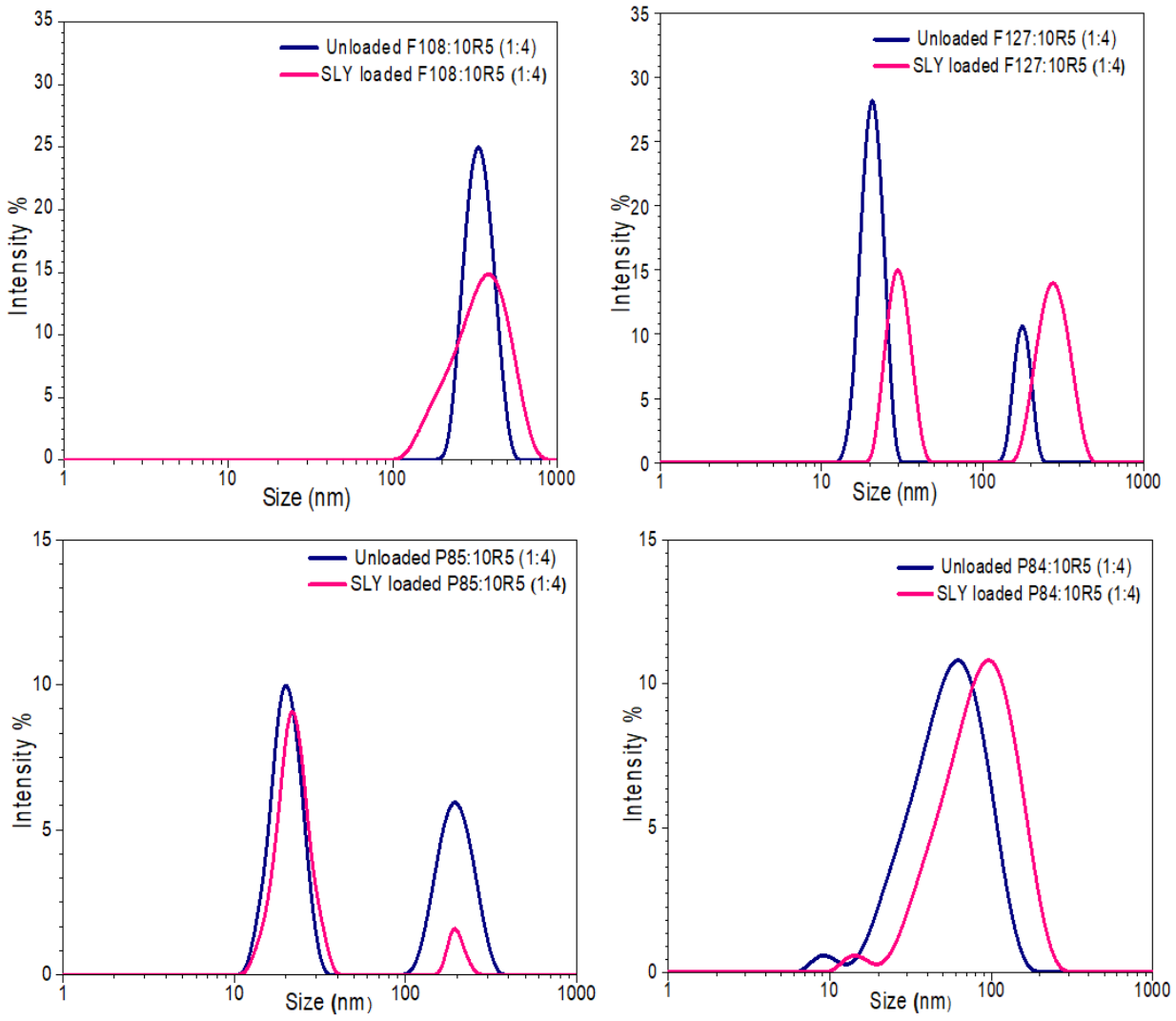

Figure B.4: Intensity weighed size distribution profiles for unloaded and SLY loaded mixed micelles of normal Pluronics F108, F127, P85 and P84 with 10R5 at concentration ratio of 1:4 % w/v.

Appendix C supplementary data for Chapter 7

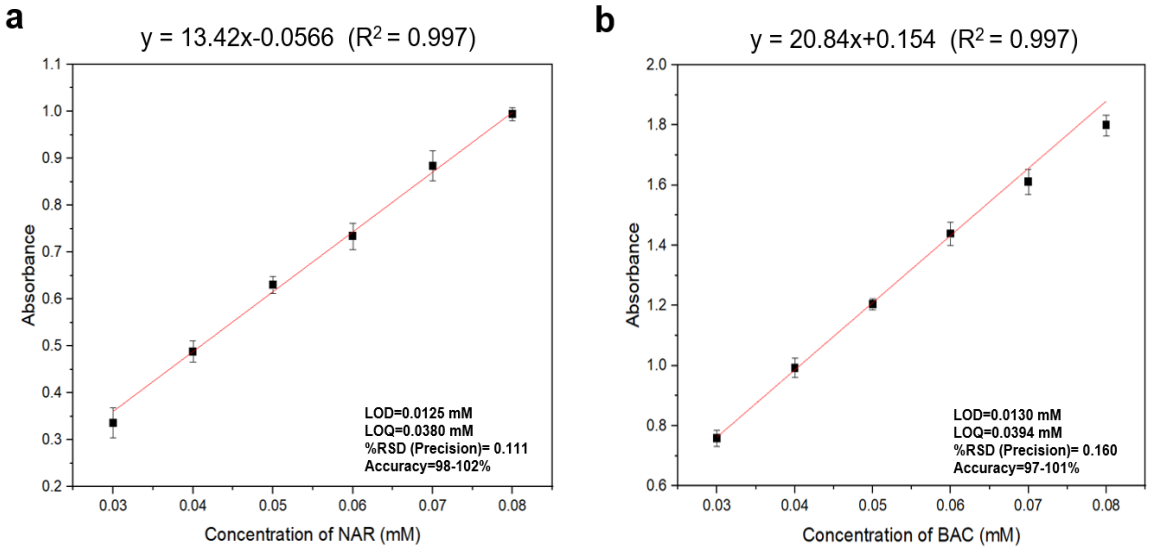

Figure C.1: Calibration curve of **(a)** NAR and **(b)** BAC, in a linear range of 0.03 mM to 0.08 mM (R^2 = 0.997).

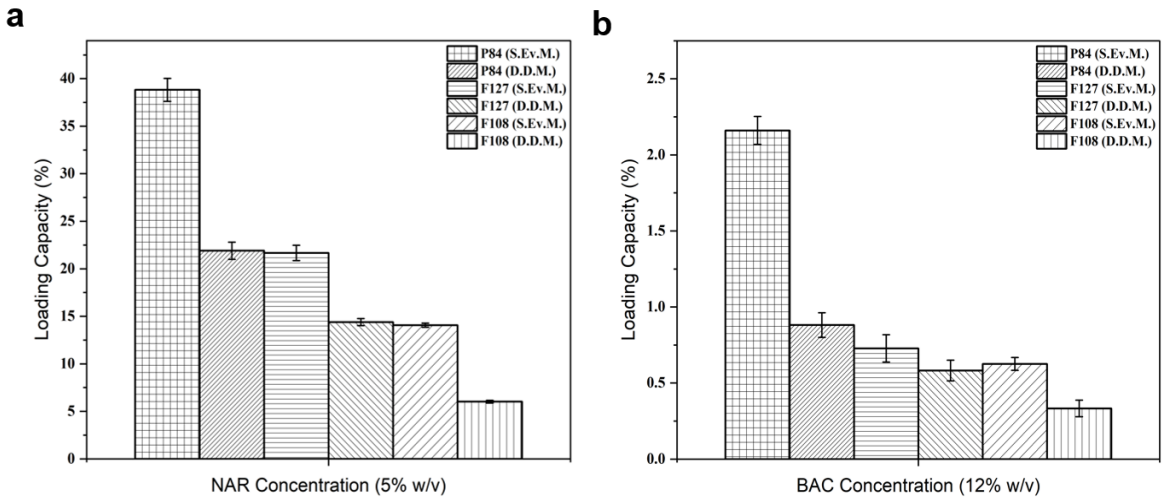

Figure C.2: Drug Loading Capacity (DLC) of **(a)** NAR and **(b)** BAC in different Pluronic micelles (P84, F127, F108) in D.D.M and S.Ev.M.

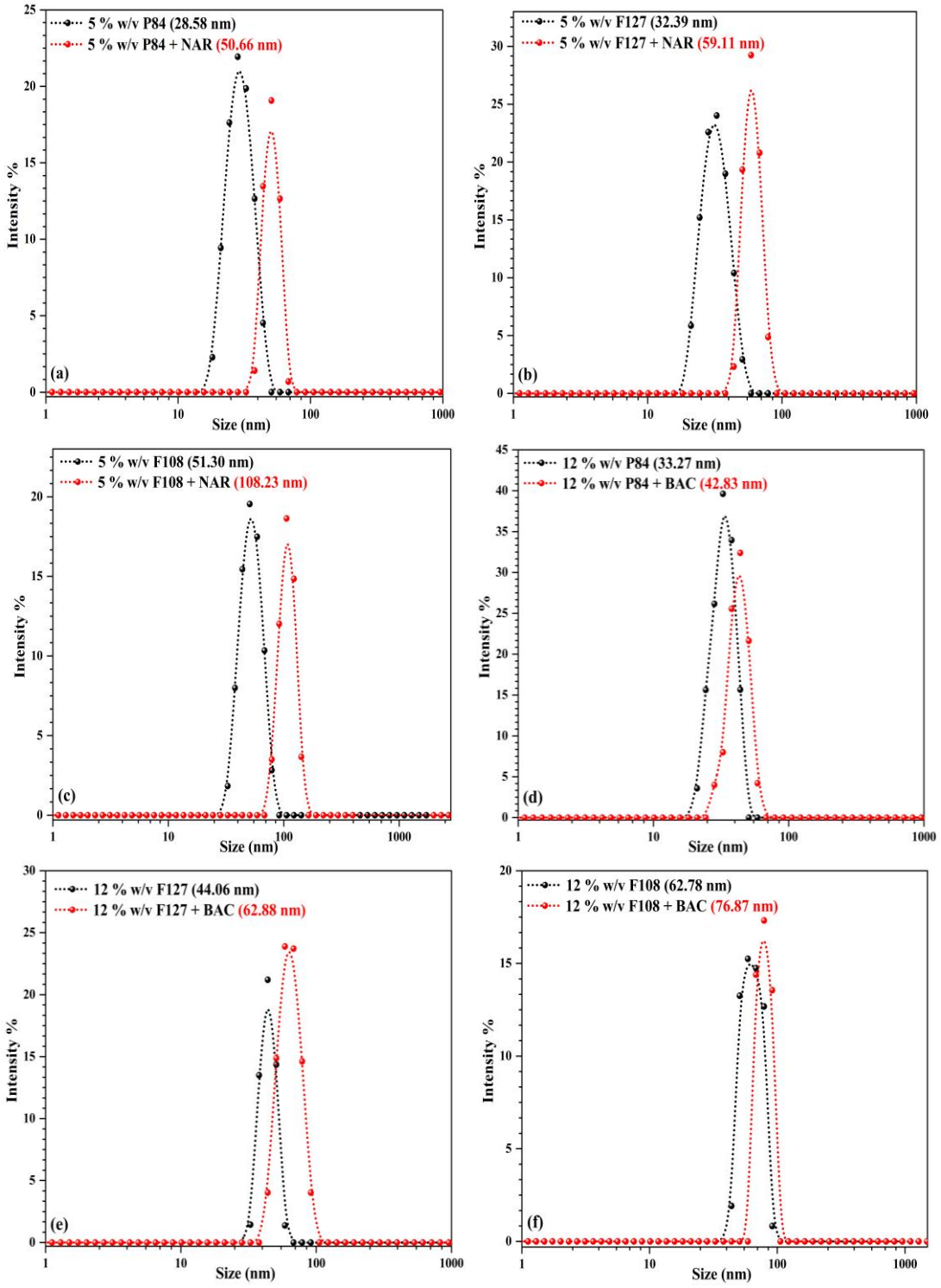

Figure C.3: Dynamic light scattering (DLS) measurements, Intensity weighted size distribution plot for 5% w/v Pluronic micelles before and after loading NAR at 37°C **(a)** P84 **(b)** F127 and **(c)** F108;12 % w/v Pluronic micelles before and after loading BAC at 37°C **(d)** P84 **(e)** F127 and **(f)** F108. **Polydispersity index** (PDI) for Pluronic micelles before and after loading NAR **(a)** P84, PDI: 0.232 and 0.242 respectively **(b)** F127 PDI: 0.22 and 0.243 respectively and **(c)** F108 PDI: 0.256 and 0.263 respectively;12 % w/v Pluronic micelles before and after loading BAC at 37°C **(d)** P84 PDI: 0.213 and 0.207 respectively **(e)** F127 PDI: 0.321 and 0.33 respectively and **(f)** F108 PDI: 0.343 and 0.371 respectively.

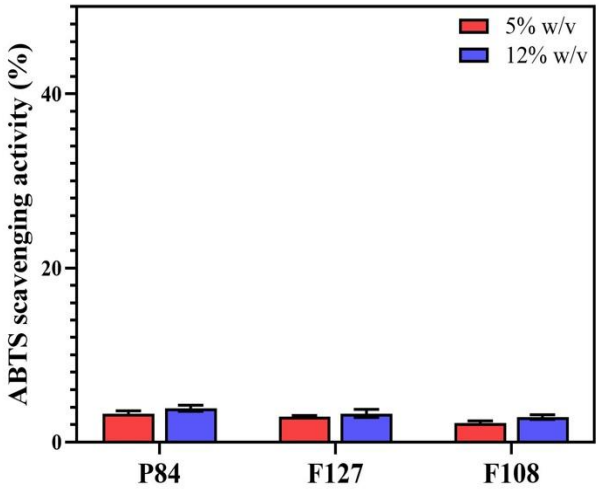

Figure C.4: ABTS$^{\bullet+}$ scavenging activity of pure Pluronics *viz.* P84, F127 and F108 at different concentrations (5 and 12% w/v).

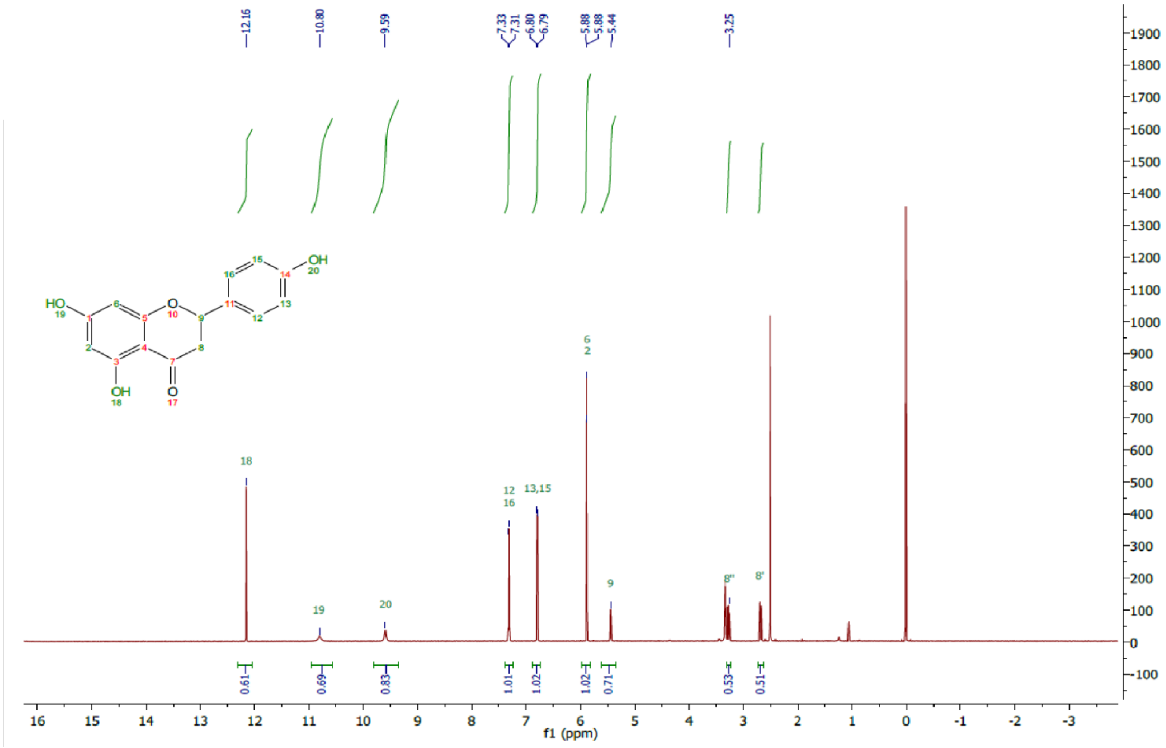

Figure C.5: ^{1}H-NMR spectra of Naringenin (NAR) in DMSO-d6.

Table C.1 Zeta potential (ζ) and pH values of unloaded Pluronics and Pluronics loaded with drugs.

	Zeta Potential (mV)		**pH values**
	Unloaded Pluronic	**Pluronic loaded with NAR**	**Pluronic loaded with NAR**
5% P84	-8.82±0.43	-9.93±0.65	7.00±0.3
5% F127	-10.57±0.58	-11.44±1.52	7.07±0.4
5% F108	-11.94±0.50	-12.09±0.79	7.02±0.3
	Unloaded Pluronic	**Pluronic loaded with BAC**	**Pluronic loaded with BAC**
12% P84	-11.82±0.43	-12.03±0.65	7.01±0.8
12% F127	-12.57±0.58	-12.73±0.52	7.06±0.6
12% F108	-12.94±0.50	-13.04±0.22	7.23±0.5

Table C.2: Rate constants and corelation coefficients (R^2) using different kinetic models for release behaviour of NAR and BAC from Pluronic micelles (P84, F127, F108) at concentration 5% w/v and 12 % w/v, respectively.

Pluronic System	**Higuchi**		**First Order**		**Korsmeyer-peppas**			**Zero Order**	
% w/v	**R^2**	**K_H (h^{-1})**	**R^2**	**K (h^{-1})**	**R^2**	**K_H (h^{-1})**	**N**	**R^2**	**K_0 (h^{-1})**
P84 +NAR 5%	0.984	21.185	0.865	-0.05	0.974	1.130	0.787	0.915	2.920
F127 + NAR 5%	0.862	19.744	0.986	-0.067	0.903	1.463	0.783	0.709	2.854
F108 + NAR 5%	0.960	22.933	0.911	-0.074	0.958	1.223	0.841	0.861	3.449
P84 + BAC 12%	0.976	30.218	0.689	-0.162	0.936	0.869	0.799	0.902	5.564
F127 + BAC 12%	0.999	58.052	0.567	-0.765	0.996	1.350	0.525	0.987	17.785
F108 + BAC 12%	0.977	44.773	0.566	-0.268	0.998	1.116	0.688	0.998	11.592

Section C1: *In vitro* drug release kinetic models

Korsmeyer-Peppas (KP) model

A simple relationship which described drug release from a polymeric system was derived by Korsmeyer *et al* in 1983. The release of the drug which follows Korsmeyer-Peppas model can be expressed by the **Eq. C.1.**

$$M_t/M_\infty = Ktn \ (\boldsymbol{C.1})$$

where M_t/ M_∞ is fraction of drug released at time "t", n is the release exponent, K is a kinetic constant characteristic of the drug/polymer system (Korsmeyer et al., 1983).

Higuchi model kinetics

It is a mathematical model showed drug release from matrix devices, proposed by Higuchi in 1961. Drug release is determined by diffusion in the Higuchi equation (Higuchi, 1963) and expressed by the **Eq. C.2**.

$$Q_t = K_H.\ t^{1/2} \quad (\mathbf{C.2})$$

where Q_t the cumulative amount of drug release at time "t" and K_H is the Higuchi release constant.

Zero order release kinetics

The pharmaceutical dosage forms following zero order release profile release the same amount of drug by unit of time and is given by Eq. C.3.

$$Q^t = Q^0 + K^0 t \quad (\mathbf{C.3})$$

Q^t is the cumulative drug release at time "t", Q^0 is the initial amount of drug and K^0 is the zero-order release constant. The formulations which follow the first order release kinetics implies that the drug release rate is independent of the concentration of the dissolved drug (Costa and Lobo, 2001).

First order release kinetics:

Gibaldi and Feldman in 1967 described the application of this kinetic model in drug dissolution studies (Gibaldi and Feldman, 1967). The drug release that follows first order kinetics can be expressed by the **Eq. C.4.**

$$logQ_t = LogQ_0 - K_t 2.303 \quad (\mathbf{C.4})$$

where Q_t is the cumulative amount of drug release at time "t", Q_0 is the initial amount of drug and K_t is the first order release constant.

References:

1. Korsmeyer, R.W., Gurny, R., Doelker, E., Buri, P. and Peppas, N.A., 1983. Mechanisms of solute release from porous hydrophilic polymers. *International journal of pharmaceutics*, *15*(1), pp.25-35.
2. Higuchi, T., 1963. Mechanism of sustained-action medication. Theoretical analysis of rate of release of solid drugs dispersed in solid matrices. *Journal of pharmaceutical sciences*, *52*(12), pp.1145-1149.
3. P. Costa, J.M.S. Lobo, Eur. J. Pharm. Sci., 13 (2001), pp. 123-133.
4. M. Gibaldi, S. Feldman, J. Pharm. Sci., 56 (1967), pp. 1238-1242